THE UNIVERSITY OF
SYDNEY

Design and Topology Optimisation of Tissue Scaffolds

Che-Cheng Chang

A thesis submitted in fulfilment of the requirements for the degree of Doctor of Philosophy

Schoold of Aerospace, Mechanical and Mechatronic Engineering
Faculty of Engineering & Information Technologies

University of Sydney

2015

Abstract

Tissue reconstruction and restoration by tissue scaffolding is a promising technique. Over the past few decades, research in tissue engineering and scaffold has been carried out extensively and mostly experimentally in search of ideal scaffold design, and design criteria are being established. Even though some design criteria can be derived empirically from experimentation, it remains unclear how the microstructure of a scaffold affects cell proliferation and how it can be optimised for specific tissue applications. Meanwhile computational modelling is emerging as a new design method, and has demonstrated significant potential in predicting cell response and has augmented experimental design approaches.

This thesis presents a computational investigation of scaffold design. It is hypothesised that the material properties of tissue scaffolds and the cell viability can be improved by means of structural design and optimisation. This study proposes an isosurface-based characterisation and optimisation technique for the design of periodic microscopic architecture, and a porosity-based design approach for the design of macroscopic structure. The goal of this study is to physically define the optimal tissue scaffold structures, and to establish any link between cell proliferation outcome and scaffold architecture.

Single-objective and multi-objective topology optimisation was conducted at microscopic scale to determine the ideal scaffold structures. To create and to present unambiguous design models, a high quality isosurface modelling technique was formulated and automated to define scaffold microstructure in stereolithography format. Periodic structures with optimised permeability, and theoretically optimal diffusivity and bulk modulus were found using modified level set method. Microstructures with specific effective diffusivity were also

created by means of inverse homogenisation. Cell viability simulation was subsequently conducted to provide evidence that the optimised microstructures offered a more viable environment than those with random microstructure. The resultant isosurface models of tissue scaffolds exhibited superior model quality and improved numerical accuracy when compared to results obtained from conventional topology optimisation approaches. The results also showed that the multiobjective solutions closely resembled the Schwarz's primitive surface though they appeared to be not exactly the same.

The macroscopic porosity and material distribution of scaffolds were also subjected to topology optimisation. Biological design criteria were incorporated into the optimisation process to allow direct investigation of the relationship between physical structures and cell growth. This part of research demonstrated the possibility of improving cell proliferation outcome, in terms of cell number and survivability, through the manipulation of the porosity profile of tissue scaffolds. The resultant porosity patterns depended on a number of technical factors including seeding density, seeding uniformity, perfusion rate and the design objective.

Artificial vascular systems were also designed and optimised to enhance nutrient transport. In this modelling process, a clear relationship between optimality and fractality of material distribution was established in the steady-state diffusion simulations, where the scaffold material was virtually non-conductive and the volumetric oxygen consumption was the primary driving force. The results supported the conjecture that natural vascular systems acquire their fractal shapes through the process of self-optimisation. Additionally, partially fractal and non-fractal optimised designs were found in other design scenarios.

Acknowledgement

I would like to thank my supervisor Professor Qing Li for his support and guidance over the past few years. I am also grateful for Dr Shiwei Zhou's support in technical matters. I would like to express my gratitude to many unnamed individuals in the research community for sharing their knowledge and insight. I would also like to acknowledge the Australian government, the University of Sydney and Qing Li for scholarships.

List of Publications

Published:

Li, E., Zhang, Z.P., **Chang, C.C.**, Liu, G.R. & Li. Q. 2015. Numerical homogenization for incompressible materials using selective smoothed finite element method. *Composites Structures* 123, 216–232.

Accepted:

Li, E., **Chang, C.C.**, Zhang, Z.P. & Li, Q. 2015. Characterization of Tissue Scaffolds for Time-Dependent Biotransport Criteria – A Novel Computational Procedure. *Computer Methods in Biomechanics and Biomedical Engineering*.

Li, E., Zhang, Z.P., **Chang, C.C.**, Zhou, S.W., Liu, G.R. & Li, Q. 2015. A New Homogenization Formulation for Multifunctional Composites. *International Journal of Computational Methods* .

Submitted:

Chen, J.N., Chen, L.J., **Chang, C.C.**, Zhang, Z.P., Li, W., Swain, M.V., Li, Q. 2015. Injection-Moulded Porous Titanium Dental Implant and Characterization Modeling. *Journal of Biomedical Materials Research: Part B - Applied Biomaterials* (JBMR-B-15-0070).

Conference proceedings:

Li, E., Zhang, Z.P., **Chang, C.C.**, Liu, G.R. & Li, Q. 2014. Homogenization for composite material properties using smoothed finite element method. *Proceedings of the 5th International Conference on Computational Methods*, 28th – 30th July 2014, Cambridge, G.R. Liu and Z.W. Guan Eds., Paper ID. ScienTech Publisher. Conference paper (Best paper award in ICCM 2015).

Table of Contents

Table of Figures

Table of Tables

Nomenclature

BC	Boundary condition
BESO	Bi-directional Evolutionary Structural Optimisation
CAD	Computer-aided design
CFD	Computational fluid dynamics
CFL	Courant–Friedrichs–Lewy
CT	Computed tomography
DoF	Degree of freedom
ESO	Evolutionary Structural Optimisation
FE	Finite element
FEA	Finite element analysis
FEM	Finite element method / Finite element model
LS	Level set
LSF	Level set function
MMA	Method of moving asymptote
RVE	Representative volume element
SDF	Signed-distance function
SIMP	Solid isotropic material penalisation
ρ	Solid volume fraction

1 Introduction

1.1 Motivation

Tissue scaffolding is a treatment technique developed to restore lost tissues [1]. The principle of tissue scaffolding is to fill the space that was originally occupied by tissue with special materials, for example, replacing a partially broken jaw with hypoxia appetite that is shaped like the original jaw. In addition to providing structural support, these materials are typically porous and are designed to allow host cells to recolonise, regenerate and mature. The ideal outcome of this treatment is the full regeneration of function tissue.

Tissue engineering is a multidisciplinary research area that involves material engineering, cells biology and biomechanics [2-5]. Maintaining even oxygen supply and achieving uniform cell distribution are two major challenges in this field of research [6, 7]. Hypoxia in particular is frequently encountered in non-vascularised tissue scaffolds, and is responsible for low cell survival rate [8, 9]. Hypoxia and the subsequent cell death are typical of static culture, in which the viable living space is limited to the region near the scaffold boundary, where high oxygen concentration is maintained [10, 11]. Cell viability in the core region can experience an ongoing deterioration when the cells living near the scaffold boundary proliferate and form an oxygen transport barrier [12], which prevents oxygen from reaching the core region [13].

It is known that diffusion transport alone is insufficient at maintaining an adequate oxygen level in large tissue scaffolds [14, 15]. A direct solution to this problem is the use of perfusion system, which has been proven highly effective in boosting oxygen concentration and improving uniform cell distribution [16, 17]. However, perfusion also induces wall shear stress and subsequently threatens the stability of cell attachment on the material surface [16,

18]. When the flow rate is increased above a certain point, the risk of cell detachment can negate the benefit of elevated oxygen level to cell colonisation. For this reason, perfusion must be applied with caution and under certain constraints. To improve the perfusion efficiency and to minimise the adverse wall shear stress, high permeability structure and artificial vasculature may be used to guide the fluid flow through pores in a more desirable manner.

The porous structure of tissue scaffolds has been shown to play a critical role in nutrient transport [19] as well as cell infiltration and migration [10, 11, 13, 20]. A range of structural recommendations and requirements ranging from porosity [7, 13, 20], pore size [21] to connectivity [13] have been suggested since. However, meeting these basic requirements does not guarantee successful tissue regeneration outcome [22-25]. Increasing porosity also reduces structural strength [26, 27]. Therefore a direct investigation and characterisation of diffusivity [6, 28], fluid flow behaviour [18, 29] as well as other characteristics is necessary to critically assess the suitability of any structures for tissue scaffold applications.

The structural design of tissue scaffolds can be carried out computationally [30, 31]. Past computational studies have encompassed structural properties [8, 19, 32], nutrient supply [33-35], mechanical stimuli and the resultant biological response as design criteria [36-43]. The idea of building tissue scaffolds with microscopic periodic blocks known as the representative volume element (RVE) is especially popular. Unlike the conventional scaffolds, models created from computational design process are expected to be fabricated by means of solid freeform fabrication, which has a strong emphasis on structural details.

Despite the successful computational application, most computational techniques are not customised and tailored for this design purpose and results are often flawed in a practical sense. Firstly, the topology optimisation methods used in the past studies utilised fixed-mesh

and voxelised modelling processes, which results in the formation of numerical artefacts. Secondly, the ambiguous nature of voxelised models makes it difficult to accurately fabricate the physical products. Additionally, there are unassessed potential designs and unverified claims of optimality. There is a strong need to properly define the porous architectures to enable more robust examination, and to bridge the gap between computational design and actual fabrication.

1.2 Aims

This study was set to overcome past design limitations and develop better, definitive structures of tissue scaffold with reasonably predictable outcome. The aims of this study can be summarised as follows:

1. To determine the optimal porous structures for maintaining nutrient transport and cell viability in tissue scaffolds. These two prominent problems will be resolved by means of topology optimisation.
2. To develop more accurate modelling techniques for structural characterisation. The optimal shapes of tissue scaffold structures must be unambiguously defined.
3. To incorporate biological design criteria into the optimisation process and to directly investigate the relationship between physical structures and cell proliferation outcome.
4. To examine popular design ideas and conjectures, and assess their potential as tissue scaffold structures. Past claims and design suggestions will be scrutinised, in particular the optimality of minimal surface models and natural vascular transport systems.

To achieve these, a new topology optimisation method has been proposed along with some other modified methods for the design tasks. The goal was not only to obtain the optimal results, but also to outperform conventional methods such as Bidirectional Evolutionary Structural Optimisation, Solid Isotropic Material with Penalisation, and the level set method.

1.3 Structure and scope of the thesis

This thesis is a five-part study. It begins with the development of new modelling techniques, and then the topology optimisation, and finishes with the construction and examination of fractal architectures. Each part of study introduces one core computational concept and solves a set of related problems. The first part of this study is the development of a high quality modelling technique. This modelling technique along with the level set method creates the foundation for topology optimisation to be used in the next two parts of study. The second and the third parts of the study focus on single-objective and multi-objective topology optimisation, respectively. Here, both conventional methods and the proposed approach are presented and compared. The last two parts of study take on the manipulation of the porosity of tissue scaffolds. In general, the earlier chapters focus on design at microscopic scale, and the later chapters cover macroscopic problems.

Chapter 2 is the literature review. The first section of this chapter looks into the current development of tissue scaffolding techniques with a strong emphasis on structural design, and the second section surveys recent computational studies that present possible approaches to various design problems. The first section covers structural characterisation, common materials and fabrication techniques, mechanical and fluid dynamics behaviour, and general biological responses. In the second section, the merits and issues of existing computational topology optimisation methods are discussed.

Chapter 3 introduces the concept of smooth 3D isosurface modelling. This chapter provides detailed formulation and programming instructions required to automate the creation of isosurface as well as finite element mesh. Improving the robustness of mesh generation and the mesh quality is the primary objective.

Chapter 4 presents the design and optimisation of the microstructure of tissue scaffolds. This is the single-objective topology optimisation that attempts to maximise effective bulk modulus, effective diffusivity and effective permeability. This chapter introduces the concepts of homogenisation for the characterisation of material properties, and boundary tracking for modelling of microstructure. Here it is demonstrated how isosurface modelling can be implemented in a level set based topology optimisation method and presents the optimisation results in such format. Detailed programming instructions of finite element analysis and the level set method are provided. The optimisation results are compared to those obtained from BESO method, conventional level set method and the SIMP method.

Chapter 5 presents the multi-objective topology optimisation of the microstructure of tissue scaffolds. The goal is to maximise effective diffusivity and effective bulk modulus concurrently. The idea of design by inverse homogenisation is also explained. In addition to the topology optimisation, a steady-state cell viability test is presented to compare the optimised model with a model constructed from a CT-scanned tissue scaffold, which has random microstructure.

Chapter 6 moves onto the optimisation of macrostructure. In this chapter, the possibility of improving cell proliferation outcome, in terms of cell number and survivability, is explored through using scaffolds with non-uniform porosity. An optimisation formulation based on biological outcome is introduced. Diffusion and advection transport scenarios are presented separately and the results are compared.

Chapter 7 introduces the concept of fractal and scale-independency. This chapter focuses on the design and optimisation of artificial vascular systems of tissue scaffolds for nutrient transport. This part of study explains how fractal vascular patterns develops in the process of topology optimisation in a steady-state, diffusion-driven system. This work attempts to establishes any potential relationship between optimality and fractality, which will help elucidate the much speculated self-optimising nature of vascular system [44]. Partially fractal and non-fractal designs are also presented.

Chapter 8 is a summary of the optimisation results, remarks and limitations of this thesis. Recommendations for future works are made in areas where this study had not been able to investigate.

1.4 References

[1] Boccaccio, A., Ballini, A., Pappalettere, C., Tullo, D., Cantore, S. & Desiate, A. 2011. Finite Element Method (FEM), Mechanobiology and Biomimetic Scaffolds in Bone Tissue Engineering. *International Journal of Biological Sciences,* 7**,** 112-132.

[2] Hart, D.A., Shrive, N.G. & Goulet, F. 2005. Tissue engineering of ACL replacements. *Sports Medicine and Arthroscopy Review,* 13**,** 170-176.

[3] de Isla, N., Huseltein, C., Jessel, N., Pinzano, A., Decot, V., Magdalou, J., Bensoussan, D. & Stoltz, J.F. 2010. Introduction to tissue engineering and application for cartilage engineering. *Bio-Medical Materials and Engineering,* 20**,** 127-133.

[4] Guilak, F., Butler, D.L., Goldstein, S.A. & Baaijens, F.P.T. 2014. Biomechanics and mechanobiology in functional tissue engineering. *Journal of Biomechanics,* 47**,** 1933-1940.

[5] Han, W.M., Heo, S.J., Driscoll, T.P., Boggs, M.E., Duncan, R.L., Mauck, R.L. & Elliott, D.M. 2014. Impact of cellular microenvironment and mechanical perturbation on calcium signalling in meniscus fibrochondrocytes. *European Cells & Materials,* 27**,** 321-331.

[6] Rose, F.R., Cyster, L.A., Grant, D.M., Scotchford, C.A., Howdle, S.M. & Shakesheff, K.M. 2004. In vitro assessment of cell penetration into porous hydroxyapatite scaffolds with a central aligned channel. *Biomaterials,* 25**,** 5507-14.

[7] Salerno, A., Guarnieri, D., Iannone, M., Zeppetelli, S., Di Maio, E., Iannace, S. & Netti, P.A. 2009. Engineered mu-bimodal poly(epsilon-caprolactone) porous scaffold for enhanced hMSC colonization and proliferation. *Acta Biomater,* 5**,** 1082-93.

[8] Malda, J., Woodfield, T.B., van der Vloodt, F., Kooy, F.K., Martens, D.E., Tramper, J., van Blitterswijk, C.A. & Riesle, J. 2004. The effect of PEGT/PBT scaffold architecture on oxygen gradients in tissue engineered cartilaginous constructs. *Biomaterials,* 25**,** 5773-80.

[9] Yu, P., Lee, T.S., Zeng, Y. & Low, H.T. 2009. Fluid dynamics and oxygen transport in a micro-bioreactor with a tissue engineering scaffold. *International Journal of Heat and Mass Transfer,* 52**,** 316-327.

[10] Ishaug, S.L., Crane, G.M., Miller, M.J., Yasko, A.W., Yaszemski, M.J. & Mikos, A.G. 1997. Bone formation by three-dimensional stromal osteoblast culture in biodegradable polymer scaffolds. *J Biomed Mater Res,* 36**,** 17-28.

[11] Papenburg, B.J., Liu, J., Higuera, G.A., Barradas, A.M., de Boer, J., van Blitterswijk, C.A., Wessling, M. & Stamatialis, D. 2009. Development and analysis of multi-layer scaffolds for tissue engineering. *Biomaterials,* 30**,** 6228-39.

[12] Kang, T.-Y., Kang, H.-W., Hwang, C.M., Lee, S.J., Park, J., Yoo, J.J. & Cho, D.-W. 2011. The realistic prediction of oxygen transport in a tissue-engineered scaffold by introducing time-varying effective diffusion coefficients. *Acta Biomaterialia,* 7**,** 3345-3353.

[13] Silva, M.M., Cyster, L.A., Barry, J.J., Yang, X.B., Oreffo, R.O., Grant, D.M., Scotchford, C.A., Howdle, S.M., Shakesheff, K.M. & Rose, F.R. 2006. The effect of anisotropic architecture on cell and tissue infiltration into tissue engineering scaffolds. *Biomaterials,* 27**,** 5909-17.

[14] Malda, J., Rouwkema, J., Martens, D.E., le Comte, E.P., Kooy, F.K., Tramper, J., van Blitterswijk, C.A. & Riesle, J. 2004. Oxygen gradients in tissue-engineered Pegt/Pbt cartilaginous constructs: Measurement and modeling. *Biotechnology and Bioengineering,* 86**,** 9-18.

[15] Radisic, M., Malda, J., Epping, E., Geng, W., Langer, R. & Vunjak-Novakovic, G. 2006. Oxygen gradients correlate with cell density and cell viability in engineered cardiac tissue. *Biotechnology and Bioengineering,* 93**,** 332-343.

[16] Koch, M.A., Vrij, E.J., Engel, E., Planell, J.A. & Lacroix, D. 2010. Perfusion cell seeding on large porous PLA/calcium phosphate composite scaffolds in a perfusion bioreactor system under varying perfusion parameters. *J Biomed Mater Res A,* 95**,** 1011-8.

[17] Radisic, M., Euloth, M., Yang, L., Langer, R., Freed, L.E. & Vunjak-Novakovic, G. 2003. High-density seeding of myocyte cells for cardiac tissue engineering. *Biotechnology and Bioengineering,* 82**,** 403-414.

[18] Bettahalli, N.M.S., Steg, H., Wessling, M. & Stamatialis, D. 2011. Development of poly(l-lactic acid) hollow fiber membranes for artificial vasculature in tissue engineering scaffolds. *Journal of Membrane Science,* 371**,** 117-126.

[19] Melchels, F.P.W., Barradas, A.M.C., van Blitterswijk, C.A., de Boer, J., Feijen, J. & Grijpma, D.W. 2010. Effects of the architecture of tissue engineering scaffolds on cell seeding and culturing. *Acta Biomaterialia,* 6**,** 4208-4217.

[20] Oh, S.H., Park, I.K., Kim, J.M. & Lee, J.H. 2007. In vitro and in vivo characteristics of PCL scaffolds with pore size gradient fabricated by a centrifugation method. *Biomaterials,* 28**,** 1664-71.

[21] Bai, F., Zhang, J.K., Wang, Z., Lu, J.X., Chang, J.A., Liu, J.A., Meng, G.L. & Dong, X. 2011. The effect of pore size on tissue ingrowth and neovascularization in porous bioceramics of controlled architecture in vivo. *Biomedical Materials,* 6.

[22] Adachi, T., Osako, Y., Tanaka, M., Hojo, M. & Hollister, S.J. 2006. Framework for optimal design of porous scaffold microstructure by computational simulation of bone regeneration. *Biomaterials,* 27**,** 3964-72.

[23] Chen, Y., Zhou, S. & Li, Q. 2011. Microstructure design of biodegradable scaffold and its effect on tissue regeneration. *Biomaterials,* 32**,** 5003-5014.

[24] Hollister, S.J. 2005. Porous scaffold design for tissue engineering. *Nat Mater,* 4**,** 518-24.

[25] Hollister, S.J. 2009. Scaffold design and manufacturing: from concept to clinic. *Adv Mater,* 21**,** 3330-42.

[26] Lebourg, M., Sabater Serra, R., Mas Estelles, J., Hernandez Sanchez, F., Gomez Ribelles, J.L. & Suay Anton, J. 2008. Biodegradable polycaprolactone scaffold with controlled porosity obtained by modified particle-leaching technique. *J Mater Sci Mater Med,* 19**,** 2047-53.

[27] Nge, T., Nogi, M., Yano, H. & Sugiyama, J. 2010. Microstructure and mechanical properties of bacterial cellulose/chitosan porous scaffold. *Cellulose,* 17**,** 349-363.

[28] Croll, T.I., Gentz, S., Mueller, K., Davidson, M., O'Connor, A.J., Stevens, G.W. & Cooper-White, J.J. 2005. Modelling oxygen diffusion and cell growth in a porous, vascularising scaffold for soft tissue engineering applications. *Chemical Engineering Science,* 60**,** 4924-4934.

[29] Hosseinkhani, H., Hosseinkhani, M., Tian, F., Kobayashi, H. & Tabata, Y. 2006. Ectopic bone formation in collagen sponge self-assembled peptide-amphiphile nanofibers hybrid scaffold in a perfusion culture bioreactor. *Biomaterials,* 27**,** 5089-98.

[30] Mekala, N.K., Baadhe, R.R. & Potumarthi, R. 2014. Mass transfer aspects of 3D cell cultures in tissue engineering. *Asia-Pacific Journal of Chemical Engineering,* 9**,** 318-329.

[31] Sun, W., Darling, A., Starly, B. & Nam, J. 2004. Computer-aided tissue engineering: overview, scope and challenges. *Biotechnol Appl Biochem,* 39**,** 29-47.

[32] Melchels, F.P.W., Tonnarelli, B., Olivares, A.L., Martin, I., Lacroix, D., Feijen, J., Wendt, D.J. & Grijpma, D.W. 2011. The influence of the scaffold design on the distribution of adhering cells after perfusion cell seeding. *Biomaterials,* 32**,** 2878-2884.

[33] Pierre, J., David, B., Petite, H. & Oddou, C. 2008. Mechanics of active porous media: Bone tissue engineering application. *Journal of Mechanics in Medicine and Biology,* 8**,** 281-292.

[34] Gardel, L.S., Serra, L.A., Reis, R.L. & Gomes, M.E. 2014. Use of Perfusion Bioreactors and Large Animal Models for Long Bone Tissue Engineering. *Tissue Engineering Part B-Reviews,* 20**,** 126-146.

[35] Li, Z.H. & Cui, Z.F. 2014. Three-dimensional perfused cell culture. *Biotechnology Advances,* 32**,** 243-254.

[36] Prendergast, P.J., Huiskes, R. & Søballe, K. 1997. Biophysical stimuli on cells during tissue differentiation at implant interfaces. *Journal of Biomechanics,* 30**,** 539-548.

[37] Sumanasinghe, R.D., Bernacki, S.H. & Loboa, E.G. 2006. Osteogenic differentiation of human mesenchymal stem cells in collagen matrices: effect of uniaxial cyclic tensile strain on bone morphogenetic protein (BMP-2) mRNA expression. *Tissue Eng,* 12**,** 3459-65.

[38] Reilly, G.C. & Engler, A.J. 2010. Intrinsic extracellular matrix properties regulate stem cell differentiation. *Journal of Biomechanics,* 43**,** 55-62.

[39] Sumanasinghe, R.D., Osborne, J.A. & Loboa, E.G. 2009. Mesenchymal stem cell-seeded collagen matrices for bone repair: Effects of cyclic tensile strain, cell density, and media conditions on matrix contraction in vitro. *Journal of Biomedical Materials Research Part A,* 88A**,** 778-786.

[40] Candiani, G., Raimondi, M.T., Aurora, R., Lagana, K. & Dubini, G. 2008. Chondrocyte response to high regimens of cyclic hydrostatic pressure in 3-dimensional engineered constructs. *International Journal of Artificial Organs,* 31**,** 490-499.

[41] Khayyeri, H., Checa, S., Tagil, M. & Prendergast, P.J. 2009. Corroboration of Mechanobiological Simulations of Tissue Differentiation in an In Vivo Bone Chamber Using a Lattice-Modeling Approach. *Journal of Orthopaedic Research,* 27**,** 1659-1666.

[42] Pioletti, D.P. 2011. Biomechanics and tissue engineering. *Osteoporosis International,* 22**,** 2027-2031.

[43] Xu, Y., Dong, S., Zhou, Q., Mo, X., Song, L., Hou, T., Wu, J., Li, S., Li, Y., Li, P., Gan, Y. & Xu, J. 2014. The effect of mechanical stimulation on the maturation of TDSCs-poly(L-lactide-co-e-caprolactone)/collagen scaffold constructs for tendon tissue engineering. *Biomaterials,* 35**,** 2760-2772.

[44] Murray, C.D. 1926. The Physiological Principle of Minimum Work: I. The Vascular System and the Cost of Blood Volume. *Proceedings of the National Academy of Sciences of the United States of America,* 12**,** 207-214.

2 Literature Review

Tissue scaffolding is an emerging technique that aims to facilitate the restoration of body defects [1]. While some tissues such as blood and liver can regenerate and recover from a significant mass loss, many other body tissues cannot be restored easily. More specifically, at the site of a critical-size wound or defect, natural recovery will not occur during the lifetime of an animal; non-functional scar tissue may fill the void at best. The prospect of scaffolding treatment is that it is possible to initiate and guide the wound healing process, and achieve a desirable outcome by tailoring tissue scaffold design. Recent Biomedical Engineering studies have helped us develop a better understanding of aided body recovery, yet much work is to be done to fully realise the potential of such applications.

Scaffolding and temporary tissue replacement is a complex process and involves material engineering, cells biology, grafting techniques, and working with biomechanical environment [2, 3]. To tackle the tissue restoration problem from an engineering design perspective, one must first understand the interaction between scaffold materials and cell-tissue development. Then some specific design objectives can be defined based on these biological requirements. Following this, appropriate engineering design processes are selected and applied to create an all-rounded solution.

2.1 Artificial scaffold

In tissue scaffold engineering, a scaffold (Figure 2-1) can be designed and tailored to address two major challenges: cell survival and development. It has been shown that the diffusion-advection mass transport determines the cell viability [4], and biomechanics and mechanobiology play the critical role in tissue development and regeneration [5, 6]. In

general, tissue scaffolds can be categorised by their topology (section 2.1.1), material properties (section 2.1.2), biomechanics/mechanobiology (section 2.1.3), nutrient supply model (section 2.1.4) and biology (section 2.1.5), and customised to address one or more design problems. This regeneration technique becomes increasingly challenging as researchers try to accommodate multidiscipline elements through technical-design measures.

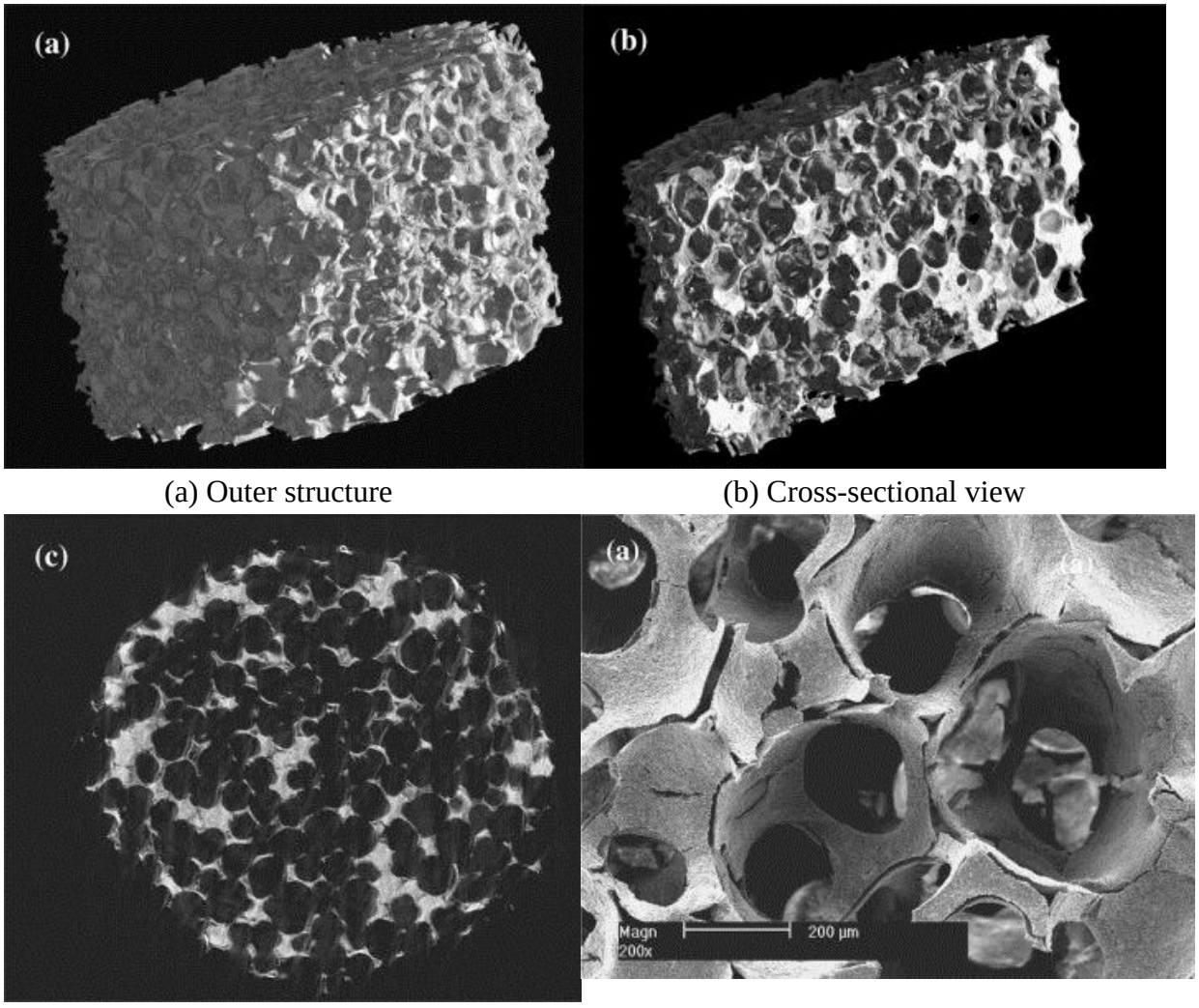

(a) Outer structure (b) Cross-sectional view

(c) Slice of a tissue scaffold (d) Microstructure

Figure 2-1. CT-images of a porous tissue scaffold [7].

First, as an ideal structural substitute, the scaffold should possess mechanical properties similar to its replaced counterpart to minimise physical disruption on the local tissues while maintaining its own structural integrity. Mechanical strength is crucial to load bearing applications. Secondly, the scaffold surface must allow new tissues to attach, regenerate and

integrate with the engineering material [8]. Thirdly, the design must ensure the cell vitality within the construct during and after the cell invasion. Lastly, the new cell mass must become self-sustainable and functional before the disintegration of scaffolds and the exhaustion of any artificial biochemical supplements. The new tissue-scaffold composite (non-biodegradable) or new tissue (with biodegradable scaffold) is expected to restore the lost biological functionalities to a satisfactory level. So far, vast researches have been conducted targeting multidiscipline factors and systemic cell-scaffold response [9]; yet a unified, comprehensive design solution has not been produced.

Nevertheless, it is known that structural design allows us to manipulate different scaffold properties to meet specific design requirements [10]. Structural design is therefore an area of exploration for a comprehensive solution. Time dependent design is also a topic of investigation [11]. When manipulating scaffold properties, a conflict between different competing design requirements may surface [12]. Such conflict can be minimised through fine-tuning the scaffold micro-architecture until a compromised solution is obtained [13].

Remarkable progress and promising results in scaffold treatment has been shown in small animal test subjects [14, 15], yet there is no report on upscaling this level of success to human subjects. Researchers have started looking into the response of human mesenchymal stem cells (hMSCs) in tissue scaffolds, however there is still much work to be done to gain a full understanding of cell-scaffold interaction (section 2.1.5). Many problems remain in terms of translating the success from animal studies to human clinical trials due to limitations of animal models, inadequate animal data and overestimation of treatment efficacy [16].

Given the scope of this design challenge, a literature review was conducted specifically in the area of scaffold architecture. This literature review firstly looks into the characterisation of the fundamental properties of scaffold (section 2.1.1), then the contemporary scaffold

fabrication techniques (section 2.1.2), followed by the discussion of major design obstacles and considerations (section 2.1.3 and onwards). Following this, the current progress and applications of topology optimisation in scaffolds design and engineering are reviewed (section 2.2).

2.1.1 Characterisation

Different topographical characteristics are known to prompt unique cell responses [17]. Material properties of substrate also affect cell morphology [18]. To take advantage of this knowledge in tissue scaffolds design, one should properly identify the structural characteristics that are beneficial to tissue regeneration and be able to recreate those conditions. However, the intricate relationship between biology and engineering mechanics presents a significant challenge to the control and the analysis of mechano-biological responses [19]. Quantifying the characteristics and standardising the design criteria is another challenge for those who attempt to recreate certain results.

Some structural characterisations are made possible by micro-CT technology. Micro-CT is an effective, accurate and non-destructive approach for the evaluation of a wide range of parameters and the visualisation of morphological characteristics [20]. Porosity and pore shapes, especially closed pores, can be captured, with the possibility to derive permeability [21, 22]. Micro-CT scanning reconstructs the topology with reasonable accuracy, but this application is restricted to its hardware/software capability. This section looks into the most prominent characteristics established from the past research using various characterisation techniques.

2.1.1.1 Porosity

Many fundamental scaffold properties are derived directly from pore characterisation, especially in bone tissue engineering [23]. They provide some crude information regarding

the viability of a particular construct since mechanical strength, fluid conductivity and biological response can often be related to pore topology. In non-gel scaffolds, interconnecting pores are essential for cell colonisation and ingrowth to take place. High porosity is generally required for three-dimensional tissue proliferation and vascularisation. Pore size should be sufficiently large to allow the migration of cells and the infiltration of blood vessels. The void volume must be well connected, allowing cell and fluid access and movement. Well-structured pore connection is expected to guide the cells growth through the construct and to facilitate cell proliferation. Without doubt, the optimisation of pore topology and fabrication techniques is the centre of tissue engineering. A number of desirable pore characteristics as well as design constraints have already been quantified for design purposes. For example, a pore size requirement can be established based on vascularisation [24]. However, the ideal pore structure remains an unknown.

As a topic of solid mechanics, the conflict between porosity and compressive strength is well-recognized [25-29]. Increasing porosity implies reducing the volume of solid materials, which can in turn affect structural shape and continuity. So far, material science and manufacturing has been the most common approach to solving this porosity-versus-strength dilemma. For example, Nge et al. [26] found in their bacterial cellulose/chitosan scaffolds (BC/CTS) prepared by freeze-lyophilisation technique, scaffolds produced at low freezing temperature had larger pore size but lower mechanical strength. However, increasing bacterial cellulose weight percentage resulted in not only larger mean pore diameter but also higher compressive strength. This is attributed to the closer packing of bacterial cellulose nanofibrils network with increasing micro-fibrillated bacterial cellulose content and degree of crosslink integration with chitosan matrix.

The pore size of scaffold can influence cell attachment [29]. Oh et al. [29] made the following observation in their scaffolds specifically prepared to create porosity gradient: Fibroblasts exhibited the highest cell growth in the region with pores ranging from 186 to 200 microns. Meanwhile, chondrocytes and osteoblasts preferred larger pores, typically around 380 to 405 microns, which allow higher mass transportation rate. In their rabbit testing subjects, faster bone formation was observed in pores of 290-310 microns in size. Some bone formation was also seen in the regions with relatively large pore size; on the other hand, limited regrowth was observed in the regions with small pore sizes. Cell growth shows preference toward macro-porosity which is likely a result of better diffusion condition. Small pore size might hinder the ability of cells to migrate and colonise porous space [28].

2.1.1.2 Interconnectivity

Pore interconnectivity is a derived scaffold property that predicts ease or difficulty in mass transport. Normally high pore interconnectivity is required for nutrient transport across all regions of scaffold, in addition to the cell migration. Voids can be intentionally introduced to scaffold constructs during the manufacturing process in order to create space and pathway. However, without the interconnectivity, the voids may simply compromise structural integrity without improving the mass transport efficiency.

Use of large channels in scaffolds has a clear fluid dynamics advantage by allowing forced mass transport [30]. Artificial channels can be introduced for the same reason [31]. Rose et al. [30] found in their needle-channelled HA scaffolds that channel dimensions (varying from 170 to 421 microns) could be directly correlated to both percentage and total cell coverage area. Based a linear mathematical extrapolation, they predicted that the minimal channel diameter required for cell infiltration is 82 microns, or around 80 microns. The outer and medium sections of the scaffold showed statistical significance in the increasing average cell

coverage (area or percentage) with respect to the increasing channel size. Also, the introduction of the channels actually improved the scaffolds strength probably due to the formation of strut around the channel upon needle insertion.

Studies have shown that the surface of macro-channels appears to attract cell migration more than microscopic pores [32]. Silva et al. [32] developed an anisotropic macro-architecture through stainless needle insertion which left large channels in the constructs after sintering. In their study, osmium tetroxides straining revealed cell proliferation throughout the channels. The incorporation of channels allowed the cells to infiltrate deeper into the scaffold by migration along such artificial cavities. In contrast, the scaffolds without channels showed more intense cell growth only in the shallow surface regions. In summary, better cell growth can be achieved through artificial channel creation, which does not compromise the mechanical properties of the scaffolds.

2.1.1.3 Morphology and Biomimeticity

Recovery of defect is more than a process of elevating cell count in scaffold, more importantly cells have to differentiate to become functional tissues. It is hypothesised that that cells are aware of the physical characteristics of their surroundings, and can respond accordingly in terms of specific biological expressions [17]. Such cell-scaffold interaction can be utilised in guiding cell and tissue development. Based on this concept, morphological research aims to create special biomimetic environments, which cells can recognise and respond in a desirable or controlled manner. The influence of cell micro-patterning on tissue growth has drawn a fair amount of attention recently with the prospect of influencing biological expression through introducing topological cues.

A typical example of this biomimeticity concept is the gas-foamed scaffolds, which is well-known for the strut architecture that resembles trabecular bones [33]. Thus gas foaming and

sintering of ceramics materials [34] has dominated this research field in bone tissue engineering. Although foaming can also be applied to polymer, hydroxyapatite [35] and Bioglass [36] are often chosen because of their biocompatibility and chemical similarity to bone. Foamed Titania trabecular scaffolds have also been manufactured [37]. Clear trabecular-bone-like structure is observed in these studies.

Cell alignment is believed to be an indicator of cell communication. The importance of cell alignment is emphasised particularly in the regeneration of highly organised tissues such as vascular wall and body organs [38-40]. Some studies attempted to create microscopic artefacts to not only guide the regeneration, but manipulate cell alignment in order to achieve desired outcome [39, 41, 42]. Sarkar et al. [38] showed in their study that cells seeded in such scaffolds with grooved micro-pattern were elongated and aligned (based on cell angle) compared to those cells in irregular microstructure in unmodified scaffolds. Micro-grooves improved cell alignment even if the cell aggregates outgrew the size of the artefacts, good cell alignment was reasonably maintained [39]. Furthermore, Sarkar et al. [38] suggested that fabrication techniques such as leaching, phase separation and freeze drying produce pore sizes greater than the critical size on a cellular scale, thus they cannot facilitate the alignment process. Pore shape also affects the cell aggregation pattern [43]. It is worth noting that cells can lose their preferential alignment in shape memory materials after the shape of the materials returns to their original state [44].

Inverted colloidal scaffolds (inverted volume of hexagonal-close-packing) have been fabricated with well-connected spherical pore network [45]. These constructs find applications in the liver scaffolding where liver spheroid cell clusters colonise and proliferated within the tailored pore space [46].

Scaffolds with non-uniform material properties are another area of research. Scaffolds with functionally-graded material have been proposed, which takes into account the changing material properties along tissue interfaces [47]. Additionally, it has been demonstrated that microelasticity gradient can also influence cell migration and induce mechanotaxis [48].

2.1.1.4 Surface properties

Surface properties of scaffolds can affect cell adhesion and differentiation [35]. The geometric organisation on a molecular scale for example can influence cell adhesion [49]. There exist various treatment methods to enhance surface cell attachment through mechanical or chemical means. In one study, Verma et al. [50] successfully applied P-15 modified PLGA microsphere to PLGA scaffolds to increase the surface roughness; in addition, P-15 is a synthetic analogue of cell-binding domain of specific collagen. This combined strategy helped improved the cell attachment.

Ragetly et al. [51] conducted a comparison test on sponge and fibre chitosan scaffolds and demonstrated the advantage of fibrous constructs in cell differentiation. The experiment shows better mesenchymal stem cell selective differentiation in the fibre scaffolds through improved cell-cell, cell-matrix interaction.

Bettahalli et al. [52] developed some biodegradable PLLA hollow fibres with high clean water and low protein retention at high medium fluxes. In static culturing, cells attached and proliferated well on the surface, showing high affinity to the material. However, under dynamic culturing condition, the cell attachment rate dropped significantly. This is considered advantageous as protein/cell adhesion can be strategically discouraged and flow pathway blockage can be prevented.

2.1.2 Materials and fabrication techniques

Material Science is a classic research field in tissue scaffold engineering. It aims to provide better design solutions with advanced materials and fabrication techniques. Compression moulding [53-55], particulate-leaching [55-58], foaming [35, 37] and phase separation [28, 43, 52, 57, 59] are commonly used techniques in the preparation of porous scaffolds. Casting [55, 56], fibre sintering [57] and deposition approaches [15] have also been developed to grant better control of the architectural details of tissue scaffolds. Techniques based on electrospun polymer fibres are also popular due to the products' high porosity and low stiffness [60, 61]. Materials exhibiting shape-memory characteristic have also generated interest in tissue scaffold applications [62-64].

These popular fabrication techniques also come with disadvantages. In terms of scaffold topology, compression moulding and particulate-leaching tend to create random porous network, therefore desirable structural characteristics can be difficult to attain. The ceramic scaffolds by gas foaming-sintering are general known for their biomimetic features but also poor mechanical strength, likely to be a result of microscopic cracks in solid struts [37]. Attempts have been made to overcome such difficulty by introducing a polymeric coating to the ceramic trabecular scaffolds: Novak et al. [37] shows that (1) poly(D,L)lactide coating significantly improves compressive strength by filling the micro-cracks and increasing the strut thickness. Rates of poly(D,L)lactide coating degradation and cell growth have direct effect on the mechanical properties over time. (2) The improvement in strength is predominantly a result of increasing strut thickness. They advise there is a need to increase the strut thickness to produce more robust ceramic products, without a significant impact on scaffold porosity or pore connectivity.

Freeze-dry, or phase separation, is a favourable fabrication option in some studies because of the superior pore interconnectivity of the final products. The major interest in this technique is the ability to regulate pore formation process by altering freezing regime. Zmora et al. [43] demonstrated that freezing regime has a decisive effect on the final pore structure. They found that the resultant pore sizes as well as pore shape vary across the scaffold cooled in oil bath; more complex pore shapes were observed in the scaffolds cooled by liquid nitrogen. Only the scaffolds cooled by freezer displayed uniform, round, isotropic pore throughout the construct.

Solid freeform fabrication is gaining popularity because of its potential in topological design, precision and versatility [65]. Combining computer-aided design, models with variable and tailored porosity can be produced [66]. Solid freeform fabrication however has its technological limitation: the amount of detail that can be produced is limited to its printing resolution. Unwanted topological artefacts and textured surface may form if the original models have low resolution [67]. Miot et al. [53] compared three-dimensional fibre deposition (3DF) scaffolds to those produced from compression moulding and showed that 3DF scaffolds have lower surface area per volume ratio but also lower tortuosity (degree of twisting).

Overall, solid freeform fabrication has the advantage over conventional techniques for being able to produce well-defined topological details on a macro/mesoscopic scale and has been applied in intervertebral disc research [68]. Besides direct scaffold printing, solid freeform fabrication can be used to produce sacrificial moulds that define the void space of scaffolds. The most significant implication of this application is that the scaffold material is no long exclusive to polymers, but any material mixture such as ceramic slurry that fills the void space can be used [67]. Mould replication technique has been done with foam [69].

Zhang et al. [27] developed an in-situ cement injection technique with calcium phosphate. This technique eliminates the need of machining and directly fills the void space of any shape. Use of porogen (mannitol in the study) gives the ability to control the scaffold porosity. Increasing porogen mannitol content also leads to increasing conversion rate of calcium phosphate cement to hydroxyapatite. The addition of chitosan improves mechanical properties.

Two-photon polymerisation is also developed to fabricate suspended web structures and to tune Poisson's ratio [70] or guide cell alignment [42].

2.1.2.1 Materials

The choice of materials usually depends on the site of implant and the desired material properties. For this reason, polymeric engineering materials are a popular choice and have been widely tested in tissue engineering due to their versatility [71] (Table 2-1). Notably, polycaprolactone (PCL) has recently attracted much attention because of its toughness and ease to process [54]. Metallic scaffolds such as porous titanium for bone tissue scaffolds have also been studied to some extend [72].

Researchers have also extensively studied ceramic biomaterials such as hydroxyapatite [35, 67] and chitosan [25-27, 51]. The idea is to utilise natural materials' biocompatibility, bioactivity, osteoconductivity and structural similarities to natural body tissues, with the anticipation that the implant will be recognised by the body as own structure and a seamless integration can be achieved. Osteoconductivity of bone scaffolds are induced by using calcium phosphate-based constructs (typically hydroxyapatite), which are chemically similar to the natural mineral phase of human bone. This mechanism is explained by Chai et al. [73], showing how calcium and phosphate ions initiate cell proliferation by pushing cell cycle into S-synthesis and M-mitotic phases. Past researches have successfully produced highly porous

trabecular hydroxyapatite scaffolds with permeability similar to natural trabecular bones [35]. In vivo, hydroxyapatite scaffolds demonstrate outstanding cell adhesion and osteoconductivity [15].

Biomaterials are not without their drawbacks: poor mechanical strength and rapid degradation in vivo are two common constraints in loading bearing application [37, 69]. Chitosan for example, a deacetylated derivative of chitin, is a relatively new biodegradable material whose application is hindered by its mechanical properties and rapid degradation rate [74]. Bi et al. [25] showed that high degree of crosslink lowered degradation rate initially; higher temperature also adds to lowering degradation rate.

Table 2-1. Engineering materials used in recent tissue scaffold studies

Alumina [69]	ECM [75, 76]	Polystyrene mould[46]
bFGF [14]	Glass beads [45]	PDLLA [37]
Bioglass [36, 37]	HA [15, 27, 30, 32, 35, 67, 69]	Salt/sugar [57]
Calcium phosphate [15, 69, 73, 81]	Hydrogel [45, 46]	Silica [45]
Cartilage [80]	Nylon [14]PBT/PEGT [53]	TG [28]
Chitosan [25-27, 51]	PCL [28, 38, 54, 77-79]	TGF [15]
Collagen [83, 84]	PLA [32, 56]	TiO2 [37]
Collagen sponge/peptide-amphiphile (PA) hybrid [83]	PLLA [39, 40, 52, 57]	VEGF [85]
Coral [82]	PLGA [50, 55, 58]	Wax [56, 79]
	PLGA mould [38]	

2.1.2.2 Bimodal/Multimodal designs

Bimodal and multimodal scaffolds are the more elaborated versions of scaffold design that incorporate different topologies into one. They typically consist of two types of porous structures, namely the macroscopic pores for mass movement such as cell migration [30, 32] and the microscopic pores for improved permeability [81] and diffusivity [39]. A number of studies have successfully combined different scaffold preparation techniques and produced structures with mixed but distinguishable characteristics, found in the scaffolds prepared from

the individual processes [28, 59]. Their hybrid designs showcase well-defined macro- to microscopic features, which work together to facilitate cellular activities on all scales. Such individual "modes" can also be added and created independently of each other to address different needs. For example, adding micro-porosity enhances transport condition [15, 57] while creating macro-channels improves mass transport [28, 59], and printing micro-patterns influences cell alignment [39].

Casting, moulding and solid freeform fabrication have been used to build the major (macroscopic) pore network for effective mass transport and mesoscopic artefacts [56, 78]. An obvious advantage of this is the improved guidance for cell colonisation across the scaffold. Experiments show that macroporosity in bimodal/multimodal models helps guide cell invasion through the porous network, thus more uniform cell distribution can be achieved [59, 86]. More conventional techniques such as porogen-leaching are incorporated to produce the microscopic structures for cell colonisation [56, 78]. Fibre sintering and fibre deposition are also used to create highly porous and interconnected network, nano-fibre deposition for example defines the nanoscopic structural characteristics [57].

2.1.3 Solid mechanics

Scaffold solid mechanics is of strong interest in bone tissue [87] and cartilage [88] engineering, particularly in bone remodelling. Mechanobiology in particular plays an influential role in regulating cell development in tissue scaffolds [19]. To design from a mechanical perspective, one should examine the well-established links between mechanical properties and the biological response of cells, and formulate design processes with appropriate objectives and constraints. Therefore in this section, recent studies are surveyed

in terms of elastic modulus, compressive strength and strain pattern, and their roles in the indirect regulation of tissue restoration.

2.1.3.1 Stiffness and Compressive strength

Mechanical properties including stiffness (or elastic modulus), impact strength and flexural strength are often compromised by the need for porosity. Bi et al. [25] shows that higher temperature and higher genipin concentration in their chitosan scaffolds results in larger pore size and lower compressive strength. Zhang et al. [27] also reported the relationship between increasing porosity and decreasing flexural strength, stiffness and fracture toughness in an in situ scaffold with porogen-induced porosity. Other studies show decreasing elastic modulus in relation to increasing porosity [54, 77]. Pore shape is also shown to play a role as spherical pores resist compression better than the elongated pores [28]. The failure of porous construct is found to be initiated by the collapse of the pore network [59]. Furthermore, stiffness can affect skeletal myoblasts differentiation [89] and adhesion [90], thus it must be properly controlled during manufacturing.

Strengthening of certain biomaterials can be achieved by means of chemical crosslinking. Bi et al. [25] developed a genipin-based crosslinking technique to improve chitosan scaffolds' compressive strength. Bi et al. showed that an optimal strength was attained at a specific genipin concentration/temperature condition (1.0%, 20°C). Other strengthening techniques such as fibre reinforcement has also been applied (collagen scaffolds [83]).

2.1.3.2 Strain stimulation

Mechanical strain in bone tissue is a known stimulus as well as a regulator of cell differentiation [91-96], tissue formation [97, 98] and mineralisation [99]. Mechanical stress stimulates the differentiation of mesenchymal cells to ligament cells [100] and induces chondrogenesis [101]. Sumanasinghe et al. [92] have demonstrated that human mesenchymal

cells can be cultured in collagen matrices under mechanical load, which initiates the osteogenesis process; mechanical strain alone is proven sufficient to increase the expression of bone morphogenetic protein 2 (an indicator of growth) in the absence of chemical agents.

Mechanical compression affects cellular activities in general [102, 103]. Cyclic hydraulic pressure has a similar effect [104]. However, scaffold strain does not always translate proportionally to cellular deformation [60]. This has fundamental implications in strategizing strain-stimulated growth.

Computational simulation of cell differentiation is a useful tool for establishing the followings: (1) the timeline of tissue regeneration and cell type composition; (2) the transient mechanical properties in relation to specific mechanical input [105]. This information can help predict the minimum initial mechanical strength required to maintain scaffold integrity. An optimal combination of scaffold dissolution rate (medium), material elastic modulus, and initial porosity could also be determined. Byrne et al. [105] utilised random walk algorithms in their work to simulate in-scaffold tissue growth from mesenchymal stem cells (MSC) differentiation and established the follows: (1) the simulation results predicted that osteoblasts-dominated growth concentrated at the central region of the scaffold while soft tissue proliferated around periphery as a consequence of stress concentration. The initial stiffness was dictated by the porosity. Increasing initial porosity promoted bone tissue and cartilage generation. (2) The total volume of solid materials decreased initially at a steady rate as a result of scaffold dissolution (assuming constant degradation) but later increased rapidly as a result of accelerated bone formation. The change in stiffness directly reflected the change in solid volume. (3) The rate of bone formation depended on the availability of growth space. Although high dissolution rate is beneficial for cell growth, the scaffold might

collapse before the new-grown bone tissue can garner enough mechanical strength to take over the loading bearing function.

Using a computational model similar to the one developed by Byrne et al. [105], Checa et al. [80] simulated in-scaffold bone differentiation process and found that: (1) with a uniform seeding density of 1% MSCs, dense capillary network formed at the periphery of the scaffolds, while very little blood vessel invasion was found at the central region. (2) With 5% uniform seeding density, blood vessels were able to fully penetrate the constructs after 1 week. By the time MSC differentiation took place, capillaries had reached the deeper region, and were able to support bone growth. (3) Cartilage was only presented in the periphery due to high fluid flow. Peripheral seeding also promoted bone formation at the centre, where capillary network became well-developed before MSCs arrived at the sites. (4) Under a 1MPa loading, cell formation was predominately cartilage regardless of initial cell seeding conditions. The high mechanical environment led to a decrease of vascularisation initially. The empty space however allowed for the growth of vascular network after 6 weeks. In their conclusion, low mechanical load favours bone cell differentiation; high loading inhibits bone formation, but stimulates cartilage generation. It is also found in another experimental study that excessive loading of tendon is detrimental [106].

It has been demonstrated that the mechanical environment can override the influence specific substrates have on the long-term MSC development [107]. In short, the prominence of mechanical stimulation in cell biology is very well established.

2.1.4 Fluid dynamics

Fluid dynamics plays another fundamental role in bone tissue engineering [23], where the primary function of flow is nutrient transport. Perfusion system is already in common use in many tissue engineering researches to facilitate nutrient transport [16, 108]. The introduction

of fluid flow however brings up a unique design challenge, manifesting in form of complex hydrodynamic-microstructural interaction. To analyse this interaction, computational fluid dynamics (CFD) simulation can be utilise to study the fluid behaviour on a microscopic scale, and to help elucidate the interaction among myriad of design variables.

As a nutrient transport problem, maintaining an adequate supply of oxygen and glucose, as well as effective removal of metabolic waste becomes a major challenge as cell density increases [109, 110]. Uniform cell seeding is typical of experimental studies, yet some computational studies have predicted poor cell vitality in uniformly seeded scaffolds, and questioned the practicality of such exercise [111, 112]. Poor viability is normally a result of high oxygen consumption at periphery of scaffold and the subsequent exhaustion of oxygen [109, 113]. The result is a brewing hypoxic condition in the core region, where cell death becomes inevitable. Normally, cells growth starts and is concentrated on the outermost region of scaffold, in contact with the culturing medium [114]. This implies that the uniformity of cell density is naturally difficult to maintain.

It can be concluded from these observations that nutrient transport is another critical scaffold design criterion. The fluid dynamic properties of scaffolds are the decisive factors of nutrient transport. The basic mechanical properties of scaffolds may have to be sacrificed in order to create a more efficient fluid dynamic environment that allows mass transport deep in the constructs.

2.1.4.1 Wound healing

The transportation of oxygen is one of the most critical factors that determine the outcome of tissue scaffolding. The availability of oxygen impacts every aspect of wound healing whether as a source of energy, a chemical agent, or as a building block in molecule synthesis [115]. In cellular metabolism, oxygen is consumed in electron transfer system during synthesis of

adenosine-tri-phosphate and as mixed function oxidase. In an event of oxygen starvation, anaerobic reaction occurs by converting glucose to pyruvic acid and lactic acid with significantly lower amount of adenosine-tri-phosphate being synthesised while consuming the same amount of glucose molecules. Without an adequate oxygen and glucose supply, un-vascularised tissue will struggle to stay viable when the wound healing process competes for oxygen, which is used for inflammatory response, fibrin formation and tissue regeneration.

Considering that implantation site is also a wounded site, the implant is automatically subject to natural immune response and chemical reactions that would normally take place in a wound. These events are highly oxygen-dependent. The inflammatory response involving polymorphonuclear cells (PMN) requires high level of oxidants for the production of superoxide, hydrogen oxide, hydrogen peroxide and nitric oxide. Therefore oxygen tension has a direct impact on the execution of oxidative bacterial killing, affecting the efficiency of infection-fighting function. Synthesis of collagen provides materials for temporary matrix during early stages of wound healing. Substantial amount of oxygen is required for hydroxylation, a fundamental step in collagen maturation. Formation of collagen is impossible without an adequate supply of oxygen in addition to proline and lysine. High oxygen concentration also increases the enzyme activity. Hence, oxygen concentration is an fundamental element in tissue scaffolds design and application.

2.1.4.2 Permeability, diffusivity and conductivity

Permeability is a measure of ease of advection transport and is directly related to the pore size and interconnection [21, 79]. However, porosity and interconnectivity is a poor indicator of cancellous bone permeability [116]. A series of events starting from increasing number of cells, obstruction of flow path, to lowered permeability all contribute to the steep oxygen gradient [112, 113, 117], and porosity alone is not predictive of any of these events. The

relationship between porous topology and flow behaviour is somehow difficult to analyse experimentally. On the other hand, computational tools provide an alternative approach to investigate the hydrodynamic system in tissue scaffolds. Computational diffusion modelling is in fact now a popular topic of study in the design analysis of scaffold architecture, more specifically, in the performance analysis of perfusion systems [111, 117-119]. Computational studies of diffusion in porous network are typically Fick-law based [120], but Monte-Carlo method or random-walk algorithm may be utilised to simulate particle movement [121, 122].

Experimental studies typically adds extra porosity features to improve nutrient diffusion [39]. Papenburg et al. [39] developed sheet scaffolds with micro-pattern and micropores, and confirmed the critical role of these microscopic features in mass transport. The rate of increase of nutrient concentration was found to be significantly higher in the presence of micro-porosity. The initial increase in nutrient concentration (in the first 24 hours) was nearly linear; subsequently, the rate of rising concentration dropped as the concentration gradient decreased.

While computational design has created a new avenue in tissue scaffold engineering, the characterisation of diffusivity and permeability requires advanced modelling of the pore network [123]. Zhou et al. [124] studied the stochastic particle movement in randomised pore network, and made the following observations in their computational structural analysis: (1) Both increasing pore size and increasing pore density lead to increasing degree of pore overlaps, that is, improved interconnections. (2) The changing dimension of apertures at overlaps has a significant influence on the resultant diffusivity especially if the apertures are relatively small (compared to the pore diameter); such effect diminishes at high porosity. This is true for both amorphous and structured architectures. (3) Smaller particles size also leads to

higher diffusion rate. The effectively diffusivity is inversely related to the increasing particle size.

Besides nutrient transport, permeability also has a decisive effect on biological activities, for example, chondrogenesis and osteogenesis. It was found that high cartilaginous matrix is correlated to high permeability design [79]. Increasing collagen fibrillar density (a major component of bone extracellular matrix) is correlated to decreasing permeability and the inhibiting effect on MSC-induced matrix contraction [125].

2.1.4.3 Wall shear stress

High flow rate improves viability [119], induces cell migration [126], and upregulates chondrogenic expression [127]. However, the resultant high wall shear stress threatens cell attachment [40, 52]. Such dilemma is found in perfusion system where mass transport is advection-driven. Thus, wall shear stress level is a critical limiting factor in perfused systems.

Experimental results show that perfusion is beneficial but only within certain range of perfusion rate: shear stress below 10 MPa promotes formation of extracellular matrix [128]; osteoblast-like cells grew extensively under 30 MPa [129]; rising flow easily elevates the oxygen and glucose levels to support local cell proliferation, yet the flowing medium can also wash cells away from the solid surfaces [52]. Beyond this range, the detrimental effect outweighs the benefit of elevated oxygen and glucose level, and consequently lowers the culturing efficiency [130]. There exist some optimal flow rates for transport of different nutrients [110]. Flow perfusion adversely affects chondrogenesis [131].

A minimum wall shear stress design gives rise to another dilemma: high surface-to-volume ratio implies high resistance and high wall shear stress, which leads to high energy loss and subsequently lower permeability. On the other hand, area-to-volume ratio is believed to be an important parameter for cell attachment – this is based on the observation that the cell

regrowth relies on the availability of attachment site provided by the scaffold [58]. In spite of this, some studies proposed the use of minimal surface constructs in favour of the fluid dynamic system [66, 132]. These designs are typically based on the triply periodic minimal surfaces including Schwarz's primitive surface and Schwann's gyroid surface, manufacturable by solid freeform fabrication. From a solid mechanics perspective, Rajagopalan et al. [133] showed that these surfaces are free of sharp corner, turns, and steep angle; the solid partitions have higher modulus and lower stress concentration compared to other constructs; the stress distribution is ideal. Scaling of the strut size led to a nonlinear decrease in the modulus. The force-displacement relationship was almost linear in their fabricated scaffolds.

Melchels et al. [134] observed that given the same porosity and mean pore size distribution, gyroid scaffolds have clear advantages over salt-leached scaffolds in fluid dynamics environment: (1) the interconnectivity of gyroid scaffolds prepared from stereolithography is far superior; (2) the permeability is one order of magnitude higher. (3) Cell seeding is easily done in those gyroid scaffolds whilst salt-leached scaffolds find cells entrapped in the outer region of scaffolds. (4) Poor cell retention is the major drawback for the minimal-surface construct.

Fluid shear stress is strongly micro-architecture-dependent [72, 135]. Even on a microscopic scale, architectural difference [136] and perfusion condition [83] can influence the shear stress pattern on the solid surface, leading to dissimilar cell growth.

2.1.4.4 Other fluid dynamics observations

Solving the perfusion system as a CFD model, Yu [137] showed that Reynolds number was predictive of fluid behaviour inside and outside scaffold constructs. In their study, fluid flow approaching the scaffold became more perpendicular at a high Reynolds number; vortex

breakdown bubble appeared at Reynolds number above 1200. (2) With perfusion, the oxygen concentration in scaffold was around 40% lower than that of culture medium; high at the flow front (approaching) and lower on the opposite side (flow exiting). In contrast, in a diffusion-only model, oxygen concentration was only 10% of that at the scaffold surface and nearly zero at the centre of the scaffold. In summary, the minimum oxygen concentration as well as the concentration pattern is associated with Reynolds number. The general flow direction also affects concentration pattern.

The interstitial fluid velocity and tissue shear strain are another key mechanical stimuli for skeletal tissue differentiation [138]. It has also been suggested that fluid shear stress may be a more potent stimulus than mechanical compressive strain in inducing bone formation [139].

2.1.5 Cell biology

Tissue regeneration can be initiated in vitro and enhanced using bioreactors. Common techniques such as programmed stimuli (as discussed in Section 2.1.3.2) are employed to simulate in vivo mechanical environment, which is thought to regulate cell development. New bioreactors are being developed to allow imposing simultaneous mechanical and hydrodynamic stimuli on cells [140-142].

It has been reported in many studies that under a static culturing condition, where oxygen transport is diffusion-driven, the depth of cell invasion is limited to approximately 200 microns from the outermost scaffold surface [58]. Such short infiltration distance undermines the idea of scaffold-aided healing on any practical scale. Another research conducted by Papenburg et al. [40] reaffirmed the 200 μm diffusion limit using stacked sheet scaffolds. In that study, the resultant cell density peaked at the outermost layer, and declined to zero over several layers. Glucose content in the culturing medium dropped over time while lactate level increased steadily, which is an evident of inadequate diffusion transport.

2.1.5.1 Cell culturing techniques

Growing autologous tissue in scaffolds prior to implantation is a typical treatment strategy, believed to be beneficial to the overall tissue restoration process [143]. It is expected that living tissue can generate, mature to a functional level, and colonise the cavity in vitro. From a treatment perspective, the principle of such tissue scaffolds is to pre-fill a wound or a defect with specific living tissue rather than an empty scaffold. This in vitro cell cultivation is also known as seeding.

Current in vitro tissue culturing research focuses on effective cell seeding. Experimental results have shown that cell seeding density affects hMSC proliferation [94]. Ishaug et al. [58] concluded from their study on osteoblast proliferation in vitro that: (1) Seeding density affects both cell attachment and proliferation rate, but not cell function; high density seeding results in a higher cell count than the ones tested at a lower seeding density. Goldstein et al. [55] also suggested that higher seeding density might improve cell-cell communication, which would give raise to better cell growth. (2) The available surface area might be a limiting factor of cell density. (3) Scaffolds with low initial cell seeding density exhibited rapid initial growth rate. The total cell count in low seeding density scaffolds reached that of high seeding-density scaffolds after a period of time. (4) Pore size did not affect the expression of ALPase activity of osteoblasts at any given period. (5) Neither pore size nor seeding density was found to have a significant effect on the degradation rate of the biodegradable constructs. In other words, pore size did not significantly affect osteoblast proliferation or function in vitro.

The utilisation of perfusion has a fundamental impact on cell morphology and on scaffold structure [118]. Preparation of live tissue scaffolds with higher cell density [55, 83, 144], more developed external cellular matrix [145], and homogeneity [134, 146] has been

achieved with perfusion. The type of perfusion system (constant flow, rotary vessel, and spinner flask) does not have a significant effect on cell density [55]. Though thickness perfusion was found more effective than surface perfusion [119].

Koch et al. [146] suggested that a minimum fluid flow velocity and spin cycle number were required to attain uniform cell distribution and high cell density in perfusion culture. Their study demonstrated that increasing number of perfusion cycle increases cell density and distribution in culture; an increase in flow velocity improves the distribution throughout the scaffold but had little influence on the cell number in scaffolds or on the overall seeding efficiency. Very high velocity resulted in high cell detachment due to high shear stress [40, 130]. Low flow velocity of perfusion culture favours the differentiation of MSC to osteoblast [83]. Increasing perfusion rate (rpm) increased the number of cells seeded but decreased the cell viability; a speed of 100 rpm was considered optimal for cell seeding [30]. According to Bancroft et al. [145], the rate of cellular matrix mineralisation also increases as the flow increases, but there exists an upper mineralisation limit. However at medium to high flow rate, overproduction of cell matrix seemed to obstruct the porous network and this might have attributed to the non-linear increase of the mineralised matrix production, as well as an increase in wall shear stress. These studies have also demonstrated that osteoblast culturing does not require high media flow rates [55, 145].

Croll et al. [111] argued that homogeneous cell seeding in scaffold of any practical dimension will invariably fail because of the inability to maintain adequate oxygen supply in vivo without blood vessel network. This claim is supported by their animal test results ran in parallel with the experiment. This study suggested that future seeding strategy should pay more attention to the early-stage rapid vascularisation at the periphery of scaffold to secure a sustained oxygen support.

Architectural anisotropy also play a role in the seeding outcome [147]. Malda et al. [113] conducted a comparison study between compression-moulded/particle-leached sponge (CM) and 3D-deposited fibre (3DF) and concluded the superiority of 3DF fabrication in terms of effective nutrient transport and cell ingrowth. In both designs, cell density appeared to be much lower in the inner region compared to the peripheral region. The 3DF scaffolds achieved a lower cell count in the peripheral region but a higher cell count in the central region – thus a smaller cell density gradient. The study suggests the community effect might have been responsible for the lower cell count at the periphery of 3DF scaffolds. Cell proliferation might have been prohibited by signalling agents released by activated cells. In addition, a less pronounced fibrous tissue was observed encapsulating the construct. Overall, the cell distribution in 3DF scaffolds appeared more homogeneous and cartilage-like.

As an alternative to cell farming for transplantation, culturing can be used for the production of cell matrix to transform the biologically inert material surfaces of scaffolds to a more biologically-friendly environment. In this culturing technique, the vitality of the seeded cells is only maintained during the period of cell matrix formation. Some researchers proposed using cultured cells to lay an osteoinductive matrix on scaffold surface [55]. The cell matrix will facilitate healing even if the cells die as a result of hypoxia before scaffold implantation. An in vitro study has demonstrated the potential of differentiated bone marrow stromal cells and developed matrices in bone formation by providing an osteoconductive environment during the repair of critical size bone defects in rats [148].

2.1.5.2 Growth factors

Use of growth factors is a supplementary technique. It has two applications in tissue engineering: one is to accelerate tissue growth and maturation rate and the other is to control differentiation of mesenchymal stem cells. In contrast to cell culturing technique discussed

earlier that focuses on increasing cell mass, growth factors emphasise the regulation of cell growth cycle.

While growth factor stimulated recovery appears to be a promising approach, it comes with a number of issues: growth factors are short-lived, lacking long term stability, tissue-specific and dose-dependent, and a single dose of growth factor may not be sufficient for a sustained recovery process [14, 100]. Growth factor carriers are designed to deliver and regulate dose release. Growth factors may be coated, mixed or encapsulated within the scaffold constructs. Carriers can also be incorporated into the biodegradable scaffolds construct, allowing the drug release rate to match the tissue regeneration rate. As a biodegradable material, the carriers should be biocompatible, non-toxic and can disintegrate through natural biological enzymic activities.

Recent studies have demonstrated the effect of growth factors on bone regeneration and neovascularisation (angiogenesis) in rat models [14, 15]. Typical growth factors for this application include (1) transforming, (2) insulin-like, (3) fibroblast, and (4) vascular endothelial growth factor; and bone morphogenetic protein and platelet-derived growth factor for cartilage [100].

Vascular endothelial growth factor (VEGF) is a vasculature mediator. VEGF stimulates cell proliferation and endothelial cell migration. The key function of VEGF in tissue engineering is to initial angiogenesis, a process of sprouting of new blood vessel from existing network in the scaffold surrounding, which lays the foundation for the later cell invasion. To improve the long-term effectiveness of growth factor, Chen et al. [85] developed a technique utilising chemical crosslinking to increase the VEGF carrying capacity of demineralised bone matrix. In their study, the scaffold material was demineralised bone matrix, a biocompatible derivative from native bone tissues; heparin was added to the surface of scaffolds by

adsorption and crosslinking. This surface had the ability to bind more VEGF compared to untreated scaffold surfaces. The VEGF release rate over time was found to be higher in those heparin-treated demineralised bone matrix scaffolds compared to the untreated ones. In vivo, the VEGF treated scaffolds exhibited better biological activity as well as higher degree of angiogenesis, reflected by the higher blood vessel density.

2.1.5.3 Vascularisation

Regardless of types of tissue scaffold, blood eventually has to take over the mass transport function to resolve any nutrient-related problems. Regeneration of blood vessels is obviously the ideal solution to sustained cell viability in vivo. In the absence of blood vessel network, cell necrosis is inevitable and this leads to an uneven live cell distribution [32]. It is expected at the end of the differentiation process that cells have correct genotype composition with an overall functionality matching the original tissues with proper blood vessel network.

Early wound healing process normally involves angiogenesis. Angiogenesis is the growth of new blood vessel from existing network, characterised by the invasion of the new blood vessels into fibrin matrix, which is the biological scaffold. Angiogenesis is triggered by oxygen starvation, which stimulates the release of various growth factors such as transforming growth factor- beta 1 (TGF-β1) [149], platelet-derived growth factor (PDGF) [150] and vascular endothelial growth factor (VEGF) [151]. These growth factors are also found in tissues suffering hypoxia. Methods have been developed by adding growth hormones to the scaffold solid to stimulate the growth of new blood network at the site of wound [115], or incorporating oxygen carrier such as calcium peroxide to elevate oxygen concentration [152]. The development of oxygen releasing materials also presents a possible avenue to address this challenging cell viability issue [153].

2.2 Design optimisation

Computer-aided design (CAD) and simulation is a growing field in the characterisation, design and analysis of tissue scaffolds [154]. Computer models are also increasingly used and combined with manufacturing systems [155]. Computational studies have been done to investigate the regeneration of bone tissue after scaffold implantation [156]. Computational scaffold design has shown tremendous potential in this field, and would benefit from increasing computational power and development of more accurate biological and genetic algorithms [157].

2.2.1 Characterisation of material properties

It has been shown that elastic and plastic mechanical behaviour in scaffolds can be computationally modelled with reasonable accuracy [158]. However, for the topological optimisation of scaffolds, full-scale modelling is normally impractical considering the complexity of porous network. To simplify the problem, effective scaffold properties are commonly derived through the analysis of a much small but representative block known as the representative volume element [159].

An alternative mathematical approach to determine properties of a material that has a complex composition is through homogenisation, usually based on asymptotic expansion. The word homogenisation here is referred to as a mathematical technique that predicts the macroscopic material behaviour of porous or composite materials by analysing a microscopic representative volume element (RVE) in a controlled condition. The homogenisation principle can be applied to engineering tissue scaffolds and scaffold structure can be designed on both macroscopic and microscopic scales [160]. The Homogenisation Design Method was firstly established by Bendsoe and Kikuchi [161] which shapes the foundation for some optimisation techniques as well as design of composite [162] and porous materials [163].

This method institutes the characterisation and up-scaling procedures for composites and multi-scale models, thus allowing design optimisation to be performed on porous or non-uniform structures. The Homogenisation Design Method is later expanded to form the so-called inverse homogenisation method for microstructure design and optimisation [164], which seeks optimal microscopic structures that can be used as the building block of macroscopic models. The homogenisation of effective permeability established by Sanchez-Palencia et al. [165] has laid the groundwork for the characterisation of porosity medium in fluid flow systems. Hybrid lattice Boltzmann based approach is another approach to solving diffusion equation in CFD problems [166, 167].

2.2.2 Topology optimisation of tissue scaffolds

The advanced computational design of tissue scaffolds was carried out utilising topology optimisation techniques, and studies had looked into the manipulation of microstructure based on multiple design criteria [13, 132, 164, 168]. Multi-objective topological optimisation helps address a multitude of design considerations, conflicts and constraints simultaneously [12, 169]. Optimisation algorithms such as bi-directional evolutionary structural optimisation (B/ESO), level-set [170, 171], and inverse homogenisation [164] have been applied and all-rounded design solutions have been obtained. However, a design method for time-dependent criteria has yet been established. Nevertheless, it has been suggested using a dynamically evolving culturing condition to match tissue maturity and maximise the efficiency of tissue regeneration process [172].

To evaluate and select the most suitable methods for scaffold design, various topology optimisation methods and results obtained from past researches were analysed. In this section, the merits and issues associated with computational techniques are discussed in the

context of structural modelling, along with their potential and limitations in tackling the key challenges in tissue engineering.

2.2.2.1 Modelling and optimisation methods

There exist a number of fully-developed topology optimisation methods, such as the Evolutionary Structural Optimisation and the Bi-directional variant, the Solid Isotropic Material Penalisation method, and the Level Set method. These techniques provide the design capability essential to generate and manipulate complex structural.

Evolutionary Structural Optimisation (ESO) technique and its improved version, Bi-directional Evolutionary Structural Optimisation (BESO), are two well-established finite element methods for topological design [173-175]. They are based on the idea of gradual structural evolution by eliminating less contributing elements and reinforcing the more critical ones (only in BESO) in a fixed finite element domain. The end result is a design with the highest average criteria across all individual constituent elements, hence the maximisation of design objective such as stiffness. The BESO approach allows the addition of efficient material, or the restoration of erroneously removed elements and provides a more flexible evolution path to the global optimum [176]. Recently studies have also demonstrated the capability of BESO of generating complex micro- and macro-structures [177-179]. While these methods enjoy computation robustness and versatility, the fact that they are using fixed, often square and cubic, mesh makes them strongly resolution dependent.

The Solid Isotropic Material with Penalisation (SIMP) approach is a density or volume fraction based representation originally used in topological optimisation of macrostructures [175, 180] but later implemented in the design of porous materials [162]. Often combined with the method of moving asymptote [181], it uses partially solid elements with penalised material properties. The concept of ersatz material, i.e. conceptual material that only exists in

computational environment, is closely associated with SIMP only with an ultra-low density to mimic void. The implementation of sensitivity filtering is critical to the rigorousness of this density approach through the elimination of numerical artefacts [182]. Ersatz material and sensitivity filtering are also applied to numerical methods other than BESO when tackling similar issues. A major drawback is that volume fraction representation results in a grey scale model with a blurred boundary that is difficult to track. This approach makes better sense in solid evolution than fluidic design.

It has been well known that conventional topology optimisation methods frequently encounter two issues: (1) one being the ambiguous, blurred boundary as a result of voxelisation or filtering, and dependence on resolution; (2) the common use of smeared Heaviside and δ functions that is responsible for level set function deterioration [183]. To tackle the second issue, numerous re-initialisation algorithms have been developed and implemented, but more than often the process is accompanied by adverse numerical side effects and inconsistency [184]. Meanwhile, the advances in unstructured mesh generation [185-189] and the development of new level-set based adaptive meshing methods [190] makes unstructured mesh a promising alternative to voxelised models and offers a possible optimisation pathway to a more accurate solution [171, 191].

To solve dynamic fluid boundary problems, the level set method stands out as a more favourable approach because of its surface tracking capability. Level set provides an implicit means for defining a stationary or dynamic boundary evolving in space, and is particularly useful for interface tracking. Level set method is well-established and has been incorporated into many numerical techniques such as image segmentation [192], fluid dynamics [170, 193, 194], and shape optimisation [183, 190, 191] due to its versatility in tracking boundaries of random or complex bodies. A fictitious energy technique has been recently introduced to

allow formation of holes and the capability of topological optimisation [195]. The level set based topology optimisation was first developed by Sethian [196] and a more standard method was established by Osher et al. [197], Wang et al. [198], and Allaire et al. [183]. This technique clearly defines boundaries that divide a design domain into separate regions. For general solid design, the concept of ersatz material has also been incorporated into the level-set method to improve computational robustness [199, 200].

Many researches on the topic of level-set optimisation emphasize building more robust model with relatively low computational expense by avoiding re-meshing, but fail to take full advantage of such prospective boundary tracking technique. One of the most common approaches involves combining signed distance function and smeared Heaviside function when defining a fixed-grid level-set function and evaluate sensitivity as an evolution criterion [198]. However, this method suffers from a number of issues: it experiences certain degree of numerical diffusion which is a necessary process in sensitivity filtering; the simulation is not performed on the same design boundary (voxelised) drawn by the level-set function; also, the boundary sharpness is strictly limited by grid resolution used in finite element analysis. Implementing the re-meshing step is becoming inevitable in level-set based optimisation if a better boundary definition beyond the current tracking capacity is to be found. Recently, there are developments on level-set optimisation with implementation of unstructured grid [171, 191] and new adaptive meshing technique found on level-set function [190]. These studies are making steps toward a possible breakthrough of a highly versatile mesh generation suitable for implicit modelling in an evolution purpose. In computational fluid dynamics (CFD), meshing is critical to the capture of topological effect, thus it holds the key to the accurate optimal solution in flow optimisation problems. Phase-field method is similar to level-set method but will not be discussed in this study [201].

In summary, existing optimisation methods have the potential but not the full capacity to define the optimal structure of tissue scaffolds. Some modifications must be made to their surface tracking technique to resolve the modelling issues.

2.2.2.2 Topology optimisation

Topology optimisation has recently found applications in the field of scaffold tissue engineering. The key benefit of such application is that the structural design process can be carried out away from laboratories, thus it helps reduce experimental cost. Additionally, topology optimisation can help assess and verify the optimality of different structural characteristics, and create a clearer picture of the ideal tissue scaffolds.

Past studies have shown support to the hypothesis that bone tissue regeneration in porous scaffold responds to local mechanical strain [202] or mechanical stimuli such as pulsatile pressure [203]. This implies that the basic properties of tissue scaffolds will affect tissue regeneration. For this reason, properties such as stiffness and bulk modulus can be subject to design optimisation to indirectly influence cell development. A number of studies has applied topology optimisation on microstructure using the effective stiffness [164, 204, 205] and bulk modulus [10, 206, 207] as a design criterion.

Fluid flow behaviour in a porous tissue scaffold is a complex mechanical problem and is difficult to analyse on a microscopic level. Fortunately, computational fluid dynamics (CFD) and the homogenisation technique together make it possible to study the fluid-structure interaction. Topology optimisation of tissue scaffolds based on conductivity/diffusivity criterion has already been looked into [10, 12]. Results of permeability optimisation are seen as a potential solution to general issues associated with in-scaffold cell activity [84, 134]. Recent modelling studies have also investigated fluid transport phenomena in tissue scaffolds and suggested that optimised fluid domains somewhat resemble the Schwarz's Primitive

surface, which led to the speculation that Schwarz's Primitive surface construct is optimised for permeability and conductivity [170, 208, 209]. There is also a growing interest in characterising various triply minimal surfaces' fluid-dynamics properties [66, 133, 134, 209, 210]. Examples of triply minimal surfaces are Schwarz's Primitive surface and Schwann's Gyroid surface. However, apart from crude resemblance, researchers have yet provided rigorous proof that the optimised surface is exactly the same as the Schwarz's Primitive surface, or counter-proof that the Schwarz's Primitive construct can be improved further.

2.2.3 Biological response

Computer models have been used to analyse tissue regeneration and to predict biological response to different mechanical environments [211, 212]. It is known that on a cellular level, cells are capable of sensing and gathering mechanical information and interacting with scaffold materials correspondingly [213]. With this knowledge, cell movement (mechanotaxis) becomes predictable. On a macroscopic level, growth is directly related to the scaffold structural properties. Sanz-Herrera et al. showed in a computational study that increasing scaffold stiffness and mean pore size led to increasing rate of bone regeneration [214]. Zahedmanesh et .al demonstrated that low scaffold compliance compared to host arteries leads to increased luminal ingrowth and development [203].

Improving analytical and discretised algorithms is a research area by itself in tissue regeneration modelling. Reina-Romo et al. developed a discrete-continuum formulation, allowing more realistic approach of the cell migration and proliferation process [122]. Second gradient hyperelastic theory was developed to describe volumetric growth and mass transport phenomena in a continuum model [215].

Biodegradable material is another emerging field of research that considers the complex scaffold-cell interaction in tissue regeneration process. Computational modelling can be

utilised to deal with such complex design scenario, and help the researchers track the constantly changing biomechanical environment [206]. Another point of interest with biodegradable materials is their structural integrity. It has been found that scaffold can collapse if biomaterial resorption rate is high [214]. This warrants the transient analysis in topology optimisation if maintaining structural integrity is a critical design requirement.

In summary, a comprehensive computational investigation would not only improve scaffold design, but also help predict cell response and explicate biological mechanisms that lead to the success or the failure of tissue regeneration in scaffolds. Computational analysis may also provide an insight into natural optimisation and feedback system. With a better understanding of the dynamic behaviour of tissues, biological requirements can be more effectively translated to engineering design criteria.

2.3 References

[1] Boccaccio, A., Ballini, A., Pappalettere, C., Tullo, D., Cantore, S. & Desiate, A. 2011. Finite Element Method (FEM), Mechanobiology and Biomimetic Scaffolds in Bone Tissue Engineering. *International Journal of Biological Sciences,* 7**,** 112-132.

[2] Hart, D.A., Shrive, N.G. & Goulet, F. 2005. Tissue engineering of ACL replacements. *Sports Medicine and Arthroscopy Review,* 13**,** 170-176.

[3] de Isla, N., Huseltein, C., Jessel, N., Pinzano, A., Decot, V., Magdalou, J., Bensoussan, D. & Stoltz, J.F. 2010. Introduction to tissue engineering and application for cartilage engineering. *Bio-Medical Materials and Engineering,* 20**,** 127-133.

[4] Mekala, N.K., Baadhe, R.R. & Potumarthi, R. 2014. Mass transfer aspects of 3D cell cultures in tissue engineering. *Asia-Pacific Journal of Chemical Engineering*, 9**,** 318-329.

[5] Guilak, F., Butler, D.L., Goldstein, S.A. & Baaijens, F.P.T. 2014. Biomechanics and mechanobiology in functional tissue engineering. *Journal of Biomechanics,* 47**,** 1933-1940.

[6] Han, W.M., Heo, S.J., Driscoll, T.P., Boggs, M.E., Duncan, R.L., Mauck, R.L. & Elliott, D.M. 2014. Impact of cellular microenvironment and mechanical perturbation on calcium signalling in meniscus fibrochondrocytes. *European Cells & Materials,* 27**,** 321-331.

[7] Wu, C., Ramaswamy, Y. & Zreiqat, H. 2010. Porous diopside (CaMgSi2O6) scaffold: A promising bioactive material for bone tissue engineering. *Acta Biomaterialia,* 6**,** 2237-2245.

[8] Williams, G.M., Chan, E.F., Temple-Wong, M.M., Bae, W.C., Masuda, K., Bugbee, W.D. & Sah, R.L. 2010. Shape, loading, and motion in the bioengineering design, fabrication, and testing of personalized synovial joints. *Journal of Biomechanics,* 43**,** 156-165.

[9] Wang, J.W., Lu, D.Y., Mao, D.B. & Long, M. 2014. Mechanomics: an emerging field between biology and biomechanics. *Protein & Cell,* 5**,** 518-531.

[10] de Kruijf, N., Zhou, S., Li, Q. & Mai, Y.-W. 2007. Topological design of structures and composite materials with multiobjectives. *International Journal of Solids and Structures,* 44**,** 7092-7109.

[11] Bai, Y., Lee, P.-F., Humphrey, J.D. & Yeh, A.T. 2014. Sequential Multimodal Microscopic Imaging and Biaxial Mechanical Testing of Living Multicomponent Tissue Constructs. *Annals of Biomedical Engineering,* 42**,** 1791-1805.

[12] Chen, Y., Zhou, S. & Li, Q. 2010. Multiobjective topology optimization for finite periodic structures. *Computers & Structures,* 88**,** 806-811.

[13] Chen, Y.H., Zhou, S.W. & Li, Q. 2009. Computational design for multifunctional microstructural composites. *International Journal of Modern Physics B,* 23**,** 1345-1351.

[14] Qu, D., Li, J., Li, Y., Gao, Y., Zuo, Y., Hsu, Y. & Hu, J. 2011. Angiogenesis and osteogenesis enhanced by bFGF ex vivo gene therapy for bone tissue engineering in reconstruction of calvarial defects. *J Biomed Mater Res A,* 96**,** 543-51.

[15] Lan Levengood, S.K., Polak, S.J., Poellmann, M.J., Hoelzle, D.J., Maki, A.J., Clark, S.G., Wheeler, M.B. & Wagoner Johnson, A.J. 2010. The effect of BMP-2 on micro- and macroscale osteointegration of biphasic calcium phosphate scaffolds with multiscale porosity. *Acta Biomater,* 6**,** 3283-91.

[16] Gardel, L.S., Serra, L.A., Reis, R.L. & Gomes, M.E. 2014. Use of Perfusion Bioreactors and Large Animal Models for Long Bone Tissue Engineering. *Tissue Engineering Part B-Reviews,* 20**,** 126-146.

[17] Sheets, K., Wang, J., Meehan, S., Sharma, P., Ng, C., Khan, M., Koons, B., Behkam, B. & Nain, A.S. 2013. Cell-Fiber Interactions on Aligned and Suspended Nanofiber Scaffolds. *Journal of Biomaterials and Tissue Engineering,* 3**,** 355-368.

[18] Raimondi, M.T., Balconi, G., Boschetti, F., Di Metri, A., Mohammed, S.A.A., Quaglini, V., Araneo, L., Galvez, B.G., Lupi, M., Latini, R. & Remuzzi, A. 2013. An opto-structural method to estimate the stress-strain field induced by cell contraction on substrates of controlled stiffness in vitro. *Journal of Applied Biomaterials & Functional Materials,* 11**,** 143-150.

[19] Thompson, M.S., Epari, D.R., Bieler, F. & Duda, G.N. 2010. In vitro models for bone mechanobiology: applications in bone regeneration and tissue engineering. *Proceedings of the Institution of Mechanical Engineers Part H-Journal of Engineering in Medicine,* 224**,** 1533-1541.

[20] Ho, S.T. & Hutmacher, D.W. 2006. A comparison of micro CT with other techniques used in the characterization of scaffolds. *Biomaterials,* 27**,** 1362-1376.

[21] Zeng, Y., Yao, X.-H. & Liu, X.-H. 2014. Numerical simulation of the effect of permeability on the hydrodynamics in a parallel-plate coculture flow chamber. *Computer Methods in Biomechanics and Biomedical Engineering,* 17**,** 875-887.

[22] Boutin, C. & Geindreau, C. 2010. Periodic homogenization and consistent estimates of transport parameters through sphere and polyhedron packings in the whole porosity range. *Physical Review E,* 82**,** 036313.

[23] Pierre, J., David, B., Petite, H. & Oddou, C. 2008. Mechanics of active porous media: Bone tissue engineering application. *Journal of Mechanics in Medicine and Biology,* 8**,** 281-292.

[24] Bai, F., Zhang, J.K., Wang, Z., Lu, J.X., Chang, J.A., Liu, J.A., Meng, G.L. & Dong, X. 2011. The effect of pore size on tissue ingrowth and neovascularization in porous bioceramics of controlled architecture in vivo. *Biomedical Materials,* 6.

[25] Bi, L., Cao, Z., Hu, Y., Song, Y., Yu, L., Yang, B., Mu, J., Huang, Z. & Han, Y. 2011. Effects of different cross-linking conditions on the properties of genipin-cross-linked chitosan/collagen scaffolds for cartilage tissue engineering. *J Mater Sci Mater Med,* 22**,** 51-62.

[26] Nge, T., Nogi, M., Yano, H. & Sugiyama, J. 2010. Microstructure and mechanical properties of bacterial cellulose/chitosan porous scaffold. *Cellulose,* 17**,** 349-363.

[27] Zhang, Y., Xu, H.H., Takagi, S. & Chow, L.C. 2006. In-situ hardening hydroxyapatite-based scaffold for bone repair. *J Mater Sci Mater Med,* 17**,** 437-45.

[28] Salerno, A., Di Maio, E., Iannace, S. & Netti, P. 2011. Tailoring the pore structure of PCL scaffolds for tissue engineering prepared via gas foaming of multi-phase blends. *Journal of Porous Materials***,** 1-8.

[29] Oh, S.H., Park, I.K., Kim, J.M. & Lee, J.H. 2007. In vitro and in vivo characteristics of PCL scaffolds with pore size gradient fabricated by a centrifugation method. *Biomaterials,* 28**,** 1664-71.

[30] Rose, F.R., Cyster, L.A., Grant, D.M., Scotchford, C.A., Howdle, S.M. & Shakesheff, K.M. 2004. In vitro assessment of cell penetration into porous hydroxyapatite scaffolds with a central aligned channel. *Biomaterials,* 25**,** 5507-14.

[31] Mesallati, T., Buckley, C.T., Nagel, T. & Kelly, D.J. 2011. Introducing Microchannels into Chondrocyte-Seeded Agarose Hydrogels Influences Matrix Accumulation in Response to Dynamic Compression and TGF-beta 3 Stimulation. *In:* ELHAJ, A. & BADER, D. (eds.) *8th International Conference on Cell & Stem Cell Engineering.*

[32] Silva, M.M., Cyster, L.A., Barry, J.J., Yang, X.B., Oreffo, R.O., Grant, D.M., Scotchford, C.A., Howdle, S.M., Shakesheff, K.M. & Rose, F.R. 2006. The effect of anisotropic architecture on cell and tissue infiltration into tissue engineering scaffolds. *Biomaterials,* 27**,** 5909-17.

[33] Shimko, D.A., Shimko, V.F., Sander, E.A., Dickson, K.F. & Nauman, E.A. 2005. Effect of porosity on the fluid flow characteristics and mechanical properties of tantalum scaffolds. *J Biomed Mater Res B Appl Biomater,* 73**,** 315-24.

[34] Haugen, H., Will, J., Köhler, A., Hopfner, U., Aigner, J. & Wintermantel, E. 2004. Ceramic TiO2-foams: characterisation of a potential scaffold. *Journal of the European Ceramic Society,* 24**,** 661-668.

[35] Teixeira, S., Ferraz, M.P. & Monteiro, F.J. 2008. Biocompatibility of highly macroporous ceramic scaffolds: cell adhesion and morphology studies. *J Mater Sci Mater Med,* 19**,** 855-9.

[36] Ochoa, I., Sanz-Herrera, J.A., Garcia-Aznar, J.M., Doblare, M., Yunos, D.M. & Boccaccini, A.R. 2009. Permeability evaluation of 45S5 Bioglass-based scaffolds for bone tissue engineering. *J Biomech,* 42**,** 257-60.

[37] Novak, S., Druce, J., Chen, Q.-Z. & Boccaccini, A. 2009. TiO2 foams with poly-(D,L-lactic acid) (PDLLA) and PDLLA/Bioglass®coatings for bone tissue engineering scaffolds. *Journal of Materials Science,* 44**,** 1442-1448.

[38] Sarkar, S., Lee, G.Y., Wong, J.Y. & Desai, T.A. 2006. Development and characterization of a porous micro-patterned scaffold for vascular tissue engineering applications. *Biomaterials,* 27**,** 4775-82.

[39] Papenburg, B.J., Vogelaar, L., Bolhuis-Versteeg, L.A., Lammertink, R.G., Stamatialis, D. & Wessling, M. 2007. One-step fabrication of porous micropatterned scaffolds to control cell behavior. *Biomaterials,* 28**,** 1998-2009.

[40] Papenburg, B.J., Liu, J., Higuera, G.A., Barradas, A.M., de Boer, J., van Blitterswijk, C.A., Wessling, M. & Stamatialis, D. 2009. Development and analysis of multi-layer scaffolds for tissue engineering. *Biomaterials,* 30**,** 6228-39.

[41] Heo, S.-J., Nerurkar, N.L., Baker, B.M., Shin, J.-W., Elliott, D.M. & Mauck, R.L. 2011. Fiber Stretch and Reorientation Modulates Mesenchymal Stem Cell Morphology and Fibrous Gene Expression on Oriented Nanofibrous Microenvironments. *Annals of Biomedical Engineering,* 39**,** 2780-2790.

[42] Marino, A., Ciofani, G., Filippeschi, C., Pellegrino, M., Pellegrini, M., Orsini, P., Pasqualetti, M., Mattoli, V. & Mazzolai, B. 2013. Two-Photon Polymerization of Sub-micrometric Patterned Surfaces: Investigation of Cell-Substrate Interactions and Improved Differentiation of Neuron-like Cells. *Acs Applied Materials & Interfaces,* 5**,** 13012-13021.

[43] Zmora, S., Glicklis, R. & Cohen, S. 2002. Tailoring the pore architecture in 3-D alginate scaffolds by controlling the freezing regime during fabrication. *Biomaterials,* 23**,** 4087-94.

[44] Tseng, L.-F., Mather, P.T. & Henderson, J.H. 2013. Shape-memory-actuated change in scaffold fiber alignment directs stem cell morphology. *Acta Biomaterialia,* 9**,** 8790-8801.

[45] Lee, J., Cuddihy, M.J., Cater, G.M. & Kotov, N.A. 2009. Engineering liver tissue spheroids with inverted colloidal crystal scaffolds. *Biomaterials,* 30**,** 4687-94.

[46] Nichols, J.E., Cortiella, J., Lee, J., Niles, J.A., Cuddihy, M., Wang, S., Bielitzki, J., Cantu, A., Mlcak, R., Valdivia, E., Yancy, R., McClure, M.L. & Kotov, N.A. 2009. In vitro analog of human bone marrow from 3D scaffolds with biomimetic inverted colloidal crystal geometry. *Biomaterials,* 30**,** 1071-9.

[47] Lu, H.H. & Thomopoulos, S. 2013. Functional Attachment of Soft Tissues to Bone: Development, Healing, and Tissue Engineering. *Annual Review of Biomedical Engineering, Vol 15,* 15**,** 201-226.

[48] Kawano, T. & Kidoaki, S. 2011. Elasticity boundary conditions required for cell mechanotaxis on microelastically-patterned gels. *Biomaterials,* 32**,** 2725-2733.

[49] Schvartzman, M., Palma, M., Sable, J., Abramson, J., Hu, X., Sheetz, M.P. & Wind, S.J. 2011. Nanolithographic Control of the Spatial Organization of Cellular Adhesion Receptors at the Single-Molecule Level. *Nano Letters,* 11**,** 1306-1312.

[50] Verma, S. & Kumar, N. 2010. Effect of biomimetic 3D environment of an injectable polymeric scaffold on MG-63 osteoblastic-cell response. *Materials Science and Engineering: C,* 30**,** 1118-1128.

[51] Ragetly, G.R., Griffon, D.J., Lee, H.B., Fredericks, L.P., Gordon-Evans, W. & Chung, Y.S. 2010. Effect of chitosan scaffold microstructure on mesenchymal stem cell chondrogenesis. *Acta Biomater,* 6**,** 1430-6.

[52] Bettahalli, N.M.S., Steg, H., Wessling, M. & Stamatialis, D. 2011. Development of poly(l-lactic acid) hollow fiber membranes for artificial vasculature in tissue engineering scaffolds. *Journal of Membrane Science,* 371**,** 117-126.

[53] Miot, S., Woodfield, T., Daniels, A.U., Suetterlin, R., Peterschmitt, I., Heberer, M., van Blitterswijk, C.A., Riesle, J. & Martin, I. 2005. Effects of scaffold composition and architecture on human nasal chondrocyte redifferentiation and cartilaginous matrix deposition. *Biomaterials,* 26**,** 2479-89.

[54] Yao, D., Smith, A., Nagarajan, P., Vasquez, A., Dang, L. & Chaudhry, G.R. 2006. Fabrication of polycaprolactone scaffolds using a sacrificial compression-molding process. *J Biomed Mater Res B Appl Biomater,* 77**,** 287-95.

[55] Goldstein, A.S., Juarez, T.M., Helmke, C.D., Gustin, M.C. & Mikos, A.G. 2001. Effect of convection on osteoblastic cell growth and function in biodegradable polymer foam scaffolds. *Biomaterials,* 22**,** 1279-88.

[56] Taboas, J.M., Maddox, R.D., Krebsbach, P.H. & Hollister, S.J. 2003. Indirect solid free form fabrication of local and global porous, biomimetic and composite 3D polymer-ceramic scaffolds. *Biomaterials,* 24**,** 181-94.

[57] Zhang, R. & Ma, P.X. 2000. Synthetic nano-fibrillar extracellular matrices with predesigned macroporous architectures. *J Biomed Mater Res,* 52**,** 430-8.

[58] Ishaug, S.L., Crane, G.M., Miller, M.J., Yasko, A.W., Yaszemski, M.J. & Mikos, A.G. 1997. Bone formation by three-dimensional stromal osteoblast culture in biodegradable polymer scaffolds. *J Biomed Mater Res,* 36**,** 17-28.

[59] Salerno, A., Guarnieri, D., Iannone, M., Zeppetelli, S., Di Maio, E., Iannace, S. & Netti, P.A. 2009. Engineered mu-bimodal poly(epsilon-caprolactone) porous scaffold for enhanced hMSC colonization and proliferation. *Acta Biomater,* 5**,** 1082-93.

[60] Stella, J.A., Liao, J., Hong, Y., Merryman, W.D., Wagner, W.R. & Sacks, M.S. 2008. Tissue-to-cellular level deformation coupling in cell micro-integrated elastomeric scaffolds. *Biomaterials,* 29**,** 3228-3236.

[61] Chao, P.-h.G., Hsu, H.-Y. & Tseng, H.-Y. 2014. Electrospun microcrimped fibers with nonlinear mechanical properties enhance ligament fibroblast phenotype. *Biofabrication,* 6.

[62] Tseng, L.-F., Mather, P.T., Henderson, J.H. & Ieee 2012. *A Programmable Shape-Changing Scaffold for Regenerative Medicine*.

[63] Xu, X., Davis, K.A., Yang, P., Gu, X., Henderson, J.H. & Mather, P.T. 2011. Shape Memory RGD-Containing Networks: Synthesis, Characterization, and Application in Cell Culture. *Advanced Polymers in Medicine,* 309-310**,** 162-172.

[64] Baker, R.M., Henderson, J.H. & Mather, P.T. 2013. Shape memory poly(epsilon-caprolactone)-co-poly(ethylene glycol) foams with body temperature triggering and two-way actuation. *Journal of Materials Chemistry B,* 1**,** 4916-4920.

[65] Tran, V. & Wen, X. 2014. Rapid prototyping technologies for tissue regeneration. *In:* NARAYAN, R. (ed.) *Rapid Prototyping of Biomaterials: Principles and Applications.* Woodhead Publ Ltd, Abington Hall Abington, Cambridge Cb1 6ah, Cambs, Uk.

[66] Melchels, F.P.W., Tonnarelli, B., Olivares, A.L., Martin, I., Lacroix, D., Feijen, J., Wendt, D.J. & Grijpma, D.W. 2011. The influence of the scaffold design on the distribution of adhering cells after perfusion cell seeding. *Biomaterials,* 32**,** 2878-2884.

[67] Wilson, C.E., de Bruijn, J.D., van Blitterswijk, C.A., Verbout, A.J. & Dhert, W.J. 2004. Design and fabrication of standardized hydroxyapatite scaffolds with a defined macro-architecture by rapid prototyping for bone-tissue-engineering research. *J Biomed Mater Res A,* 68**,** 123-32.

[68] Hsieh, A.H. & Twomey, J.D. 2010. Cellular mechanobiology of the intervertebral disc: New directions and approaches. *Journal of Biomechanics,* 43**,** 137-145.

[69] Costa, H., Mansur, A., Barbosa-Stancioli, E., Pereira, M. & Mansur, H. 2008. Morphological, mechanical, and biocompatibility characterization of macroporous alumina scaffolds coated with calcium phosphate/PVA. *Journal of Materials Science,* 43**,** 510-524.

[70] Zhang, W., Soman, P., Meggs, K., Qu, X. & Chen, S. 2013. Tuning the Poisson's Ratio of Biomaterials for Investigating Cellular Response. *Advanced Functional Materials,* 23**,** 3226-3232.

[71] Boffito, M., Sartori, S. & Ciardelli, G. 2014. Polymeric scaffolds for cardiac tissue engineering: requirements and fabrication technologies. *Polymer International,* 63**,** 2-11.

[72] Maes, F., Van Ransbeeck, P., Van Oosterwyck, H. & Verdonck, P. 2009. Modeling Fluid Flow Through Irregular Scaffolds for Perfusion Bioreactors. *Biotechnology and Bioengineering,* 103**,** 621-630.

[73] Chai, Y.C., Roberts, S.J., Schrooten, J. & Luyten, F.P. 2011. Probing the osteoinductive effect of calcium phosphate by using an in vitro biomimetic model. *Tissue Eng Part A,* 17**,** 1083-97.

[74] She, Z., Zhang, B., Jin, C., Feng, Q. & Xu, Y. 2008. Preparation and in vitro degradation of porous three-dimensional silk fibroin/chitosan scaffold. *Polymer Degradation and Stability,* 93**,** 1316-1322.

[75] Li, S., De Wijn, J.R., Li, J., Layrolle, P. & De Groot, K. 2003. Macroporous biphasic calcium phosphate scaffold with high permeability/porosity ratio. *Tissue Eng,* 9**,** 535-48.

[76] Checa, S. & Prendergast, P.J. 2010. Effect of cell seeding and mechanical loading on vascularization and tissue formation inside a scaffold: a mechano-biological model using a lattice approach to simulate cell activity. *J Biomech,* 43**,** 961-8.

[77] Hosseinkhani, H., Hosseinkhani, M., Tian, F., Kobayashi, H. & Tabata, Y. 2006. Ectopic bone formation in collagen sponge self-assembled peptide-amphiphile

nanofibers hybrid scaffold in a perfusion culture bioreactor. *Biomaterials,* 27**,** 5089-98.

[78] Sundararaghavan, H.G., Monteiro, G.A., Lapin, N.A., Chabal, Y.J., Miksan, J.R. & Shreiber, D.I. 2008. Genipin-induced changes in collagen gels: Correlation of mechanical properties to fluorescence. *Journal of Biomedical Materials Research Part A,* 87A**,** 308-320.

[79] Tran, C.T., Gargiulo, C., Thao, H.D., Tuan, H.M., Filgueira, L. & Michael Strong, D. 2010. Culture and differentiation of osteoblasts on coral scaffold from human bone marrow mesenchymal stem cells. *Cell Tissue Bank.*

[80] Ulrich, T.A., Jain, A., Tanner, K., MacKay, J.L. & Kumar, S. 2010. Probing cellular mechanobiology in three-dimensional culture with collagen-agarose matrices. *Biomaterials,* 31**,** 1875-1884.

[81] Kumar, S. 2009. Cell-matrix mechanobiology: applications to brain tumors and design of tissue engineering scaffolds. *Conference proceedings : ... Annual International Conference of the IEEE Engineering in Medicine and Biology Society. IEEE Engineering in Medicine and Biology Society. Annual Conference,* 2009**,** 3350-2.

[82] Lebourg, M., Sabater Serra, R., Mas Estelles, J., Hernandez Sanchez, F., Gomez Ribelles, J.L. & Suay Anton, J. 2008. Biodegradable polycaprolactone scaffold with controlled porosity obtained by modified particle-leaching technique. *J Mater Sci Mater Med,* 19**,** 2047-53.

[83] Kang, H.-W., Rhie, J.-W. & Cho, D.-W. 2009. Development of a bi-pore scaffold using indirect solid freeform fabrication based on microstereolithography technology. *Microelectronic Engineering,* 86**,** 941-944.

[84] Kemppainen, J.M. & Hollister, S.J. 2010. Differential effects of designed scaffold permeability on chondrogenesis by chondrocytes and bone marrow stromal cells. *Biomaterials,* 31**,** 279-87.

[85] Chen, L., He, Z., Chen, B., Yang, M., Zhao, Y., Sun, W., Xiao, Z., Zhang, J. & Dai, J. 2010. Loading of VEGF to the heparin cross-linked demineralized bone matrix improves vascularization of the scaffold. *J Mater Sci Mater Med,* 21**,** 309-17.

[86] Radisic, M., Malda, J., Epping, E., Geng, W., Langer, R. & Vunjak-Novakovic, G. 2006. Oxygen gradients correlate with cell density and cell viability in engineered cardiac tissue. *Biotechnology and Bioengineering,* 93**,** 332-343.

[87] Soucacos, P.N., Johnson, E.O. & Babis, G. 2008. An update on recent advances in bone regeneration. *Injury-International Journal of the Care of the Injured,* 39**,** S1-S4.

[88] McMahon, L.A., O'Brien, F.J. & Prendergast, P.J. 2008. Biomechanics and mechanobiology in osteochondral tissues. *Regenerative Medicine,* 3**,** 743-759.

[89] Romanazzo, S., Forte, G., Ebara, M., Uto, K., Pagliari, S., Aoyagi, T., Traversa, E. & Taniguchi, A. 2012. Substrate stiffness affects skeletal myoblast differentiation in vitro. *Science and Technology of Advanced Materials,* 13.

[90] Van Tam, J.K., Uto, K., Ebara, M., Pagliari, S., Forte, G. & Aoyagi, T. 2012. Mesenchymal stem cell adhesion but not plasticity is affected by high substrate stiffness. *Science and Technology of Advanced Materials,* 13.

[91] Prendergast, P.J., Huiskes, R. & Søballe, K. 1997. Biophysical stimuli on cells during tissue differentiation at implant interfaces. *Journal of Biomechanics,* 30**,** 539-548.

[92] Sumanasinghe, R.D., Bernacki, S.H. & Loboa, E.G. 2006. Osteogenic differentiation of human mesenchymal stem cells in collagen matrices: effect of uniaxial cyclic tensile strain on bone morphogenetic protein (BMP-2) mRNA expression. *Tissue Eng,* 12**,** 3459-65.

[93] Reilly, G.C. & Engler, A.J. 2010. Intrinsic extracellular matrix properties regulate stem cell differentiation. *Journal of Biomechanics,* 43**,** 55-62.

[94] Sumanasinghe, R.D., Osborne, J.A. & Loboa, E.G. 2009. Mesenchymal stem cell-seeded collagen matrices for bone repair: Effects of cyclic tensile strain, cell density, and media conditions on matrix contraction in vitro. *Journal of Biomedical Materials Research Part A,* 88A**,** 778-786.

[95] Candiani, G., Raimondi, M.T., Aurora, R., Lagana, K. & Dubini, G. 2008. Chondrocyte response to high regimens of cyclic hydrostatic pressure in 3-dimensional engineered constructs. *International Journal of Artificial Organs,* 31**,** 490-499.

[96] Khayyeri, H., Checa, S., Tagil, M. & Prendergast, P.J. 2009. Corroboration of Mechanobiological Simulations of Tissue Differentiation in an In Vivo Bone Chamber Using a Lattice-Modeling Approach. *Journal of Orthopaedic Research,* 27**,** 1659-1666.

[97] Pioletti, D.P. 2011. Biomechanics and tissue engineering. *Osteoporosis International,* 22**,** 2027-2031.

[98] Xu, Y., Dong, S., Zhou, Q., Mo, X., Song, L., Hou, T., Wu, J., Li, S., Li, Y., Li, P., Gan, Y. & Xu, J. 2014. The effect of mechanical stimulation on the maturation of TDSCs-poly(L-lactide-co-e-caprolactone)/collagen scaffold constructs for tendon tissue engineering. *Biomaterials,* 35**,** 2760-2772.

[99] Sittichockechaiwut, A., Scutt, A.M., Ryan, A.J., Bonewald, L.F. & Reilly, G.C. 2009. Use of rapidly mineralising osteoblasts and short periods of mechanical loading to accelerate matrix maturation in 3D scaffolds. *Bone,* 44**,** 822-829.

[100] Lee, S.H. & Shin, H. 2007. Matrices and scaffolds for delivery of bioactive molecules in bone and cartilage tissue engineering. *Adv Drug Deliv Rev,* 59**,** 339-59.

[101] Schumann, D., Kujat, R., Nerlich, M. & Angele, P. 2006. Mechanobiological conditioning of stem cells for cartilage tissue engineering. *Bio-Medical Materials and Engineering,* 16**,** S37-S52.

[102] Demarteau, O., Wendt, D., Braccini, A., Jakob, M., Schafer, D., Heberer, M. & Martin, I. 2003. Dynamic compression of cartilage constructs engineered from expanded human articular chondrocytes. *Biochemical and Biophysical Research Communications,* 310**,** 580-588.

[103] Angele, P., Schumann, D., Angele, M., Kinner, B., Englert, C., Hente, R., Fuchtmeier, B., Nerlich, M., Neumann, C. & Kujat, R. 2004. Cyclic, mechanical compression enhances chondrogenesis of mesenchymal progenitor cells in tissue engineering scaffolds. *Biorheology,* 41**,** 335-346.

[104] Puetzer, J., Williams, J., Gillies, A., Bernacki, S. & Loboa, E.G. 2013. The Effects of Cyclic Hydrostatic Pressure on Chondrogenesis and Viability of Human Adipose- and

Bone Marrow-Derived Mesenchymal Stem Cells in Three-Dimensional Agarose Constructs. *Tissue Engineering Part A,* 19**,** 299-306.

[105] Byrne, D.P., Lacroix, D., Planell, J.A., Kelly, D.J. & Prendergast, P.J. 2007. Simulation of tissue differentiation in a scaffold as a function of porosity, Young's modulus and dissolution rate: application of mechanobiological models in tissue engineering. *Biomaterials,* 28**,** 5544-54.

[106] Wang, J.H.C., Guo, Q. & Li, B. 2012. Tendon Biomechanics and Mechanobiology-A Minireview of Basic Concepts and Recent Advancements. *Journal of Hand Therapy,* 25**,** 133-140.

[107] Thorpe, S.D., Buckley, C.T., Steward, A.J. & Kelly, D.J. 2012. European Society of Biomechanics SM Perren Award 2012: The external mechanical environment can override the influence of local substrate in determining stem cell fate. *Journal of Biomechanics,* 45**,** 2483-2492.

[108] Li, Z.H. & Cui, Z.F. 2014. Three-dimensional perfused cell culture. *Biotechnology Advances,* 32**,** 243-254.

[109] Yu, P., Zeng, Y., Lee, T.S. & Low, H.T. 2009. A numerical analysis of cell density effect on oxygen transport in a micro-bioreactor with a tissue engineering scaffold. *International Communications in Heat and Mass Transfer,* 36**,** 569-573.

[110] Provin, C., Takano, K., Sakai, Y., Fujii, T. & Shirakashi, R. 2008. A method for the design of 3D scaffolds for high-density cell attachment and determination of optimum perfusion culture conditions. *Journal of Biomechanics,* 41**,** 1436-1449.

[111] Croll, T.I., Gentz, S., Mueller, K., Davidson, M., O'Connor, A.J., Stevens, G.W. & Cooper-White, J.J. 2005. Modelling oxygen diffusion and cell growth in a porous, vascularising scaffold for soft tissue engineering applications. *Chemical Engineering Science,* 60**,** 4924-4934.

[112] Sumaru, K. & Kanamori, T. 2004. Optimal design of bio-hybrid systems with a hollow fiber scaffold: model analysis of oxygen diffusion/consumption. *Biochemical Engineering Journal,* 20**,** 127-136.

[113] Malda, J., Rouwkema, J., Martens, D.E., le Comte, E.P., Kooy, F.K., Tramper, J., van Blitterswijk, C.A. & Riesle, J. 2004. Oxygen gradients in tissue-engineered Pegt/Pbt cartilaginous constructs: Measurement and modeling. *Biotechnology and Bioengineering,* 86**,** 9-18.

[114] Ng, S.S., Su, K., Li, C., Chan-Park, M.B., Wang, D.-A. & Chan, V. 2012. Biomechanical study of the edge outgrowth phenomenon of encapsulated chondrocytic isogenous groups in the surface layer of hydrogel scaffolds for cartilage tissue engineering. *Acta Biomaterialia,* 8**,** 244-252.

[115] Tandara, A.A. & Mustoe, T.A. 2004. Oxygen in wound healing--more than a nutrient. *World J Surg,* 28**,** 294-300.

[116] Teo, J.C.M. & Teoh, S.H. 2012. Permeability study of vertebral cancellous bone using micro-computational fluid dynamics. *Computer Methods in Biomechanics and Biomedical Engineering,* 15**,** 417-423.

[117] Yu, P., Lee, T.S., Zeng, Y. & Low, H.T. 2009. Fluid dynamics and oxygen transport in a micro-bioreactor with a tissue engineering scaffold. *International Journal of Heat and Mass Transfer,* 52**,** 316-327.

[118] Raimondi, M.T., Boschetti, F., Falcone, L., Fiore, G.B., Remuzzi, A., Marinoni, E., Marazzi, M. & Pietrabissa, R. 2002. Mechanobiology of engineered cartilage cultured under a quantified fluid-dynamic environment. *Biomechanics and Modeling in Mechanobiology,* 1**,** 69-82.

[119] Raimondi, M.T., Boschetti, F., Falcone, L., Migliavacca, F., Remuzzi, A. & Dubini, G. 2004. The effect of media perfusion on three-dimensional cultures of human chondrocytes: Integration of experimental and computational approaches. *Biorheology,* 41**,** 401-410.

[120] Wu, R., Zhu, X., Liao, Q., Wang, H., Ding, Y.-d., Li, J. & Ye, D.-d. 2010. Determination of oxygen effective diffusivity in porous gas diffusion layer using a three-dimensional pore network model. *Electrochimica Acta,* 55**,** 7394-7403.

[121] Shanbhag, S., Woo Lee, J. & Kotov, N. 2005. Diffusion in three-dimensionally ordered scaffolds with inverted colloidal crystal geometry. *Biomaterials,* 26**,** 5581-5585.

[122] Reina-Romo, E., Gomez-Benito, M.J., Dominguez, J. & Garcia-Aznar, J.M. 2012. A lattice-based approach to model distraction osteogenesis. *Journal of Biomechanics,* 45**,** 2736-2742.

[123] White, J.A., Borja, R.I. & Fredrich, J.T. 2006. Calculating the effective permeability of sandstone with multiscale lattice Boltzmann/finite element simulations. *Acta Geotechnica,* 1**,** 195-209.

[124] Zhou, H., Chen, S.B., Peng, J. & Wang, C.-H. 2010. A study of effective diffusivity in porous scaffold by Brownian dynamics simulation. *Journal of Colloid and Interface Science,* 342**,** 620-628.

[125] Serpooshan, V., Julien, M., Nguyen, O., Wang, H., Li, A., Muja, N., Henderson, J.E. & Nazhat, S.N. 2010. Reduced hydraulic permeability of three-dimensional collagen scaffolds attenuates gel contraction and promotes the growth and differentiation of mesenchymal stem cells. *Acta Biomater,* 6**,** 3978-87.

[126] Polacheck, W.J., Charest, J.L. & Kamm, R.D. 2011. Interstitial flow influences direction of tumor cell migration through competing mechanisms. *Proceedings of the National Academy of Sciences of the United States of America,* 108**,** 11115-11120.

[127] Abdel-Sayed, P., Darwiche, S.E., Kettenberger, U. & Pioletti, D.P. 2014. The role of energy dissipation of polymeric scaffolds in the mechanobiological modulation of chondrogenic expression. *Biomaterials,* 35**,** 1890-1897.

[128] Raimondi, M.T., Candiani, G., Cabras, M., Cioffi, M., Lagana, K., Moretti, M. & Pietrabissa, R. 2008. Engineered cartilage constructs subject to very low regimens of interstitial perfusion. *Biorheology,* 45**,** 471-478.

[129] Botchwey, E.A., Pollack, S.R., El-Amin, S., Levine, E.M., Tuan, R.S. & Laurencin, C.T. 2003. Human osteoblast-like cells in three-dimensional culture with fluid flow. *Biorheology,* 40**,** 299-306.

[130] Cartmell, S.H., Porter, B.D., Garcia, A.J. & Guldberg, R.E. 2003. Effects of medium perfusion rate on cell-seeded three-dimensional bone constructs in vitro. *Tissue Eng,* 9**,** 1197-203.

[131] Kock, L.M., Malda, J., Dhert, W.J.A., Ito, K. & Gawlitta, D. 2014. Flow-perfusion interferes with chondrogenic and hypertrophic matrix production by mesenchymal stem cells. *Journal of Biomechanics,* 47**,** 2122-2129.

[132] Chen, Y., Zhou, S., Cadman, J. & Li, Q. 2010. Design of cellular porous biomaterials for wall shear stress criterion. *Biotechnology and Bioengineering,* 107**,** 737-746.

[133] Rajagopalan, S. & Robb, R.A. 2006. Schwarz meets Schwann: Design and fabrication of biomorphic and durataxic tissue engineering scaffolds. *Medical Image Analysis,* 10**,** 693-712.

[134] Melchels, F.P.W., Barradas, A.M.C., van Blitterswijk, C.A., de Boer, J., Feijen, J. & Grijpma, D.W. 2010. Effects of the architecture of tissue engineering scaffolds on cell seeding and culturing. *Acta Biomaterialia,* 6**,** 4208-4217.

[135] Hendrikson, W.J., van Blitterswijk, C.A., Verdonschot, N., Moroni, L. & Rouwkema, J. 2014. Modeling Mechanical Signals on the Surface of mu CT and CAD Based Rapid Prototype Scaffold Models to Predict (Early Stage) Tissue Development. *Biotechnology and Bioengineering,* 111**,** 1864-1875.

[136] Porter, B., Zauel, R., Stockman, H., Guldberg, R. & Fyhrie, D. 2005. 3-D computational modeling of media flow through scaffolds in a perfusion bioreactor. *Journal of Biomechanics,* 38**,** 543-549.

[137] Yu, P. Numerical simulation on oxygen transfer in a porous scaffold for animal cell culture. *International Journal of Heat and Mass Transfer*.

[138] Hayward, L.N.M. & Morgan, E.F. 2009. Assessment of a mechano-regulation theory of skeletal tissue differentiation in an in vivo model of mechanically induced cartilage formation. *Biomechanics and Modeling in Mechanobiology,* 8**,** 447-455.

[139] Kim, B.G., Kwag, J.H., Kim, H.S., Kim, K.H. & Kim, C.H. 2009. Bone Cell Response to Fluid Shear Stress and Cyclic Compressive Strain in 3D Trabecular Bone. *Tissue Engineering and Regenerative Medicine,* 6**,** 540-548.

[140] Demarteau, O., Jakob, M., Schafer, D., Heberer, M. & Martin, I. 2003. Development and validation of a bioreactor for physical stimulation of engineered cartilage. *Biorheology,* 40**,** 331-336.

[141] Lagana, K., Moretti, M., Dubini, G. & Raimondi, M.T. 2008. A new bioreactor for the controlled application of complex mechanical stimuli for cartilage tissue engineering. *Proceedings of the Institution of Mechanical Engineers Part H-Journal of Engineering in Medicine,* 222**,** 705-715.

[142] Neidlinger-Wilke, C., Wurtz, K., Liedert, A., Schmidt, C., Borm, W., Ignatius, A., Wilke, H.J. & Claes, L. 2005. A three-dimensional collagen matrix as a suitable culture system for the comparison of cyclic strain and hydrostatic pressure effects on intervertebral disc cells. *Journal of Neurosurgery-Spine,* 2**,** 457-465.

[143] Tran, N., Li, Y., Bertrand, S., Bangratz, S., Carteaux, J.P., Stoltz, J.F. & Villemot, J.P. 2003. Autologous cell transplantation and cardiac tissue engineering: Potential applications in heart failure. *Biorheology,* 40**,** 411-415.

[144] Radisic, M., Euloth, M., Yang, L., Langer, R., Freed, L.E. & Vunjak-Novakovic, G. 2003. High-density seeding of myocyte cells for cardiac tissue engineering. *Biotechnology and Bioengineering,* 82**,** 403-414.

[145] Bancroft, G.N., Sikavitsas, V.I., van den Dolder, J., Sheffield, T.L., Ambrose, C.G., Jansen, J.A. & Mikos, A.G. 2002. Fluid flow increases mineralized matrix deposition in 3D perfusion culture of marrow stromal osteoblasts in a dose-dependent manner. *Proc Natl Acad Sci U S A,* 99**,** 12600-5.

[146] Koch, M.A., Vrij, E.J., Engel, E., Planell, J.A. & Lacroix, D. 2010. Perfusion cell seeding on large porous PLA/calcium phosphate composite scaffolds in a perfusion bioreactor system under varying perfusion parameters. *J Biomed Mater Res A,* 95**,** 1011-8.

[147] Sanz-Herrera, J.A., Doblare, M. & Garcia-Aznar, J.M. 2010. Scaffold microarchitecture determines internal bone directional growth structure: A numerical study. *Journal of Biomechanics,* 43**,** 2480-2486.

[148] Jiang, X., Zhao, J., Wang, S., Sun, X., Zhang, X., Chen, J., Kaplan, D.L. & Zhang, Z. 2009. Mandibular repair in rats with premineralized silk scaffolds and BMP-2-modified bMSCs. *Biomaterials,* 30**,** 4522-4532.

[149] Santilli, S.M., Fiegel, V.D., Aldridge, D.E. & Knighton, D.R. 1991. Rabbit Aortic Endothelial Cell Hypoxia Induces Secretion of Transforming Growth Factor Beta and Augments Macrophage Adhesion In Vitro. *Annals of Vascular Surgery,* 5**,** 429-438.

[150] Tahara, A., Yasuda, M., Itagane, H., Toda, I., Teragaki, M., Akioka, K., Oku, H., Takeuchi, K., Takeda, T., Bannai, S., Takanashi, N. & Tsukada, H. 1991. Plasma levels of platelet-derived growth factor in normal subjects and patients with ischemic heart disease. *American Heart Journal,* 122**,** 986-992.

[151] Stavri, G.T., Hong, Y., Zachary, I.C., Breier, G., Baskerville, P.A., Ylä-Herttuala, S., Risau, W., Martin, J.F. & Erusalimsky, J.D. 1995. Hypoxia and platelet-derived growth factor-BB synergistically upregulate the expression of vascular endothelial growth factor in vascular smooth muscle cells. *FEBS Letters,* 358**,** 311-315.

[152] Oh, S.H., Ward, C.L., Atala, A., Yoo, J.J. & Harrison, B.S. 2009. Oxygen generating scaffolds for enhancing engineered tissue survival. *Biomaterials,* 30**,** 757-762.

[153] Camci-Unal, G., Alemdar, N., Annabi, N. & Khademhosseini, A. 2013. Oxygen-releasing biomaterials for tissue engineering. *Polymer International,* 62**,** 843-848.

[154] Wettergreen, M., Bucklen, B., Sun, W., Liebschner, M.A.K. & Asme 2005. *Computer-aided tissue engineering in whole bone replacement treatment*.

[155] Song, M.J., Dean, D. & Tate, M.L.K. 2013. Mechanical modulation of nascent stem cell lineage commitment in tissue engineering scaffolds. *Biomaterials,* 34**,** 5766-5775.

[156] Checa, S., Byrne, D.P. & Prendergast, P.J. 2010. *Predictive Modelling in Mechanobiology: Combining Algorithms for Cell Activities in Response to Physical Stimuli Using a Lattice-Modelling Approach*.

[157] Lacroix, D., Planell, J.A. & Prendergast, P.J. 2009. Computer-aided design and finite-element modelling of biomaterial scaffolds for bone tissue engineering. *Philosophical Transactions of the Royal Society a-Mathematical Physical and Engineering Sciences,* 367**,** 1993-2009.

[158] Almeida, H.A. & Bartolo, P.J. 2013. Numerical simulations of bioextruded polymer scaffolds for tissue engineering applications. *Polymer International,* 62**,** 1544-1552.

[159] Xia, Z., Zhang, Y. & Ellyin, F. 2003. A unified periodical boundary conditions for representative volume elements of composites and applications. *International Journal of Solids and Structures,* 40**,** 1907-1921.

[160] Smit, R.J.M., Brekelmans, W.A.M. & Meijer, H.E.H. 1998. Prediction of the mechanical behavior of nonlinear heterogeneous systems by multi-level finite element modeling. *Computer Methods in Applied Mechanics and Engineering,* 155**,** 181-192.

[161] Bendsøe, M.P. & Kikuchi, N. 1988. Generating optimal topologies in structural design using a homogenization method. *Computer Methods in Applied Mechanics and Engineering,* 71**,** 197-224.

[162] Guedes, J. & Kikuchi, N. 1990. Preprocessing and postprocessing for materials based on the homogenization method with adaptive finite element methods. *Computer Methods in Applied Mechanics and Engineering,* 83**,** 143-198.

[163] Hollister, S.J.K., Noboru 1992. A comparison of homogenization and standard mechanics analyses for periodic porous composites. *Computational Mechanics,* 10**,** 73-95.

[164] Guest, J.K. & Prévost, J.H. 2006. Optimizing multifunctional materials: Design of microstructures for maximized stiffness and fluid permeability. *International Journal of Solids and Structures,* 43**,** 7028-7047.

[165] Sanchez-Palencia, E. 1983. Asymptotic Analysis II — Homogenization method for the study of composite media *In:* VERHULST, F. (ed.). Springer Berlin / Heidelberg.

[166] Pilotti, M., Succi, S. & Menduni, G. 2002. Energy dissipation and permeability in porous media. *EPL (Europhysics Letters),* 60**,** 72.

[167] Sun, W. & Andrade, J.E. 2010. Capturing the effective permeability of field compaction band using hybrid lattice Boltzmann/Finite element simulations. *IOP Conference Series: Materials Science and Engineering,* 10**,** 012077.

[168] Torquato, S., Hyun, S. & Donev, A. 2002. Multifunctional composites: optimizing microstructures for simultaneous transport of heat and electricity. *Phys Rev Lett,* 89**,** 266601.

[169] Li, N., Zhang, H. & Ouyang, H. 2009. Shape optimization of coronary artery stent based on a parametric model. *Finite Elements in Analysis and Design,* 45**,** 468-475.

[170] Zhou, S. & Li, Q. 2008. A variational level set method for the topology optimization of steady-state Navier–Stokes flow. *Journal of Computational Physics,* 227**,** 10178-10195.

[171] Zhou, S., Li, W. & Li, Q. 2010. Level-set based topology optimization for electromagnetic dipole antenna design. *Journal of Computational Physics,* 229**,** 6915-6930.

[172] Couet, F., Meghezi, S. & Mantovani, D. 2012. Fetal development, mechanobiology and optimal control processes can improve vascular tissue regeneration in bioreactors: An integrative review. *Medical Engineering & Physics,* 34**,** 269-278.

[173] Huang, X. & Xie, M. 2010. *Evolutionary Topology Optimization of Continuum Structures: Methods and Applications,* Wiley.

[174] Xie, Y.M. & Steven, G.P. 1997. *Evolutionary structural optimization,* Springer.

[175] Bendsøe, M.P.S., Ole 2003. *Topology optimization: theory, methods, and applications,* New York, Springer.

[176] Yang, X. 1999. *Bi-directional evolutionary method for stiffness and displacement optimisation.* Research Master thesis thesis, Victoria University of Technology.
[177] Huang, X., Radman, A. & Xie, Y.M. 2011. Topological design of microstructures of cellular materials for maximum bulk or shear modulus. *Computational Materials Science,* 50**,** 1861-1870.
[178] Radman, A., Huang, X. & Xie, Y.M. 2012. Topological optimization for the design of microstructures of isotropic cellular materials. *Engineering Optimization,* 45**,** 1331-1348.
[179] Huang, X., Zhou, S.W., Xie, Y.M. & Li, Q. 2013. Topology optimization of microstructures of cellular materials and composites for macrostructures. *Computational Materials Science,* 67**,** 397-407.
[180] Allaire, G. 2002. *Shape Optimization by the Homogenization Method,* Springer.
[181] Svanberg, K. 1987. The method of moving asymptotes—a new method for structural optimization. *International Journal for Numerical Methods in Engineering,* 24**,** 359-373.
[182] Li, Q., Steven, G.P. & Xie, Y.M. 2001. A simple checkerboard suppression algorithm for evolutionary structural optimization. *Structural and Multidisciplinary Optimization,* 22**,** 230-239.
[183] Allaire, G., Jouve, F. & Toader, A.-M. 2004. Structural optimization using sensitivity analysis and a level-set method. *Journal of Computational Physics,* 194**,** 363-393.
[184] Gomes, J. & Faugeras, O. 2000. Reconciling Distance Functions and Level Sets. *Journal of Visual Communication and Image Representation,* 11**,** 209-223.
[185] Edelsbrunner, H. & Shah, N.R. 1996. Incremental Topological Flipping Works for Regular Triangulations. *Algorithmica,* 15**,** 223-241.
[186] Si, H. & Gaertner, K. Meshing Piecewise Linear Complexes by Constrained Delaunay Tetrahedralizations. 14th International Meshing Roundtable, September 2005 2005. 147-163.
[187] Si, H. On Refinement of Constrained Delaunay Tetrahedralizations. 15th International Meshing Roundtable, September 2006 2006.
[188] Fang, Q. & Boas, D. Tetrahedral mesh generation from volumetric binary and gray-scale images. IEEE International Symposium on Biomedical Imaging 2009, 2009. 1142-1145.
[189] Victoria, M., Querin, O.M. & Martí, P. 2011. Topology design of three-dimensional continuum structures using isosurfaces. *Advances in Engineering Software,* 42**,** 671-679.
[190] Allaire, G., Dapogny, C. & Frey, P. 2011. Shape optimization of elastic structures using a level-set based mesh evolution method. *Fifth International Conference on Advanced Computational Methods in Engineering.* Li`ege, Belgium.
[191] Ha, S.-H. & Cho, S. 2008. Level set based topological shape optimization of geometrically nonlinear structures using unstructured mesh. *Computers & Structures,* 86**,** 1447-1455.
[192] Sumengen, B. 2004. *Variational Image Segmentation and Curve Evolution on Natural Images.* University of California.

[193] Borrvall, T. & Petersson, J. 2003. Topology optimization of fluids in Stokes flow. *International Journal for Numerical Methods in Fluids,* 41**,** 77-107.

[194] Challis, V.J. & Guest, J.K. 2009. Level set topology optimization of fluids in Stokes flow. *International Journal for Numerical Methods in Engineering,* 79**,** 1284-1308.

[195] Yamada, T., Izui, K., Nishiwaki, S. & Takezawa, A. 2010. A topology optimization method based on the level set method incorporating a fictitious interface energy. *Computer Methods in Applied Mechanics and Engineering,* 199**,** 2876-2891.

[196] Sethian, J.A. 1999. *Level Set Methods and Fast Marching Methods: Evolving Interfaces in Computational Geometry, Fluid Mechanics, Computer Vision and Materials Science,* Cambridge: Cambridge University Press.

[197] Osher, S. & Fedkiw, R.P. 2001. Level Set Methods: An Overview and Some Recent Results. *Journal of Computational Physics,* 169**,** 463-502.

[198] Wang, M.Y., Wang, X. & Guo, D. 2003. A level set method for structural topology optimization. *Computer Methods in Applied Mechanics and Engineering,* 192**,** 227-246.

[199] Liu, Z., Korvink, J.G. & Huang, R. 2005. Structure topology optimization: fully coupled level set method via FEMLAB. *Structural and Multidisciplinary Optimization,* 29**,** 407-417.

[200] Challis, V. 2010. A discrete level-set topology optimization code written in Matlab. *Structural and Multidisciplinary Optimization,* 41**,** 453-464.

[201] Takezawa, A., Nishiwaki, S. & Kitamura, M. 2010. Shape and topology optimization based on the phase field method and sensitivity analysis. *J. Comput. Phys.,* 229**,** 2697-2718.

[202] Baas, E., Kuiper, J.H., Yang, Y., Wood, M.A. & El Haj, A.J. 2010. In vitro bone growth responds to local mechanical strain in three-dimensional polymer scaffolds. *Journal of Biomechanics,* 43**,** 733-739.

[203] Zahedmanesh, H. & Lally, C. 2012. A multiscale mechanobiological modelling framework using agent-based models and finite element analysis: application to vascular tissue engineering. *Biomechanics and Modeling in Mechanobiology,* 11**,** 363-377.

[204] Sturm, S., Zhou, S., Mai, Y.W. & Li, Q. 2010. On stiffness of scaffolds for bone tissue engineering-a numerical study. *J Biomech,* 43**,** 1738-44.

[205] Lin, C.Y., Kikuchi, N. & Hollister, S.J. 2004. A novel method for biomaterial scaffold internal architecture design to match bone elastic properties with desired porosity. *Journal of Biomechanics,* 37**,** 623-636.

[206] Chen, Y., Zhou, S. & Li, Q. 2011. Microstructure design of biodegradable scaffold and its effect on tissue regeneration. *Biomaterials,* 32**,** 5003-5014.

[207] Kang, H., Lin, C.-Y. & Hollister, S. 2010. Topology optimization of three dimensional tissue engineering scaffold architectures for prescribed bulk modulus and diffusivity. *Structural and Multidisciplinary Optimization,* 42**,** 633-644.

[208] Guest, J.K. & Prévost, J.H. 2007. Design of maximum permeability material structures. *Computer Methods in Applied Mechanics and Engineering,* 196**,** 1006-1017.

[209] Jung, Y., Chu, K.T. & Torquato, S. 2007. A variational level set approach for surface area minimization of triply-periodic surfaces. *Journal of Computational Physics,* 223**,** 711-730.

[210] Kapfer, S.C., Hyde, S.T., Mecke, K., Arns, C.H. & Schröder-Turk, G.E. 2011. Minimal surface scaffold designs for tissue engineering. *Biomaterials,* 32**,** 6875-6882.

[211] Lacroix, D. & Prendergast, P.J. 2002. A mechano-regulation model for tissue differentiation during fracture healing: analysis of gap size and loading. *Journal of Biomechanics,* 35**,** 1163-1171.

[212] Kelly, D.J. & Prendergast, P.J. 2005. Mechano-regulation of stem cell differentiation and tissue regeneration in osteochondral defects. *Journal of Biomechanics,* 38**,** 1413-1422.

[213] Garcia-Aznar, J.M., Sanz-Herrera, J.A. & Moreo, P. 2011. Cell-Material Communication: Mechanosensing Modelling for Design in Tissue Engineering. *In:* GEFEN, A. (ed.) *Cellular and Biomolecular Mechancis and Mechanobiology.*

[214] Sanz-Herrera, J.A., Garcia-Aznar, J.M. & Doblare, M. 2009. On scaffold designing for bone regeneration: A computational multiscale approach. *Acta Biomaterialia,* 5**,** 219-229.

[215] Ciarletta, P., Ambrosi, D. & Maugin, G.A. 2012. Mass transport in morphogenetic processes: A second gradient theory for volumetric growth and material remodeling. Journal of the Mechanics and Physics of Solids, 60, 432-450.

3 Isosurface Modelling

Image segmentation techniques are well-established and widely used in medical imaging and engineering modelling, particularly for the creation of high quality visualisation and computational model. Modelling porous tissue scaffolds typically requires Computerized Axial Tomography scan (CT scan) and image segmentation. However, image segmentation processes are mostly manually performed, and are time-consuming and difficult to execute correctly in an iterative process. Therefore these techniques are rarely used in transient and iterative simulations due to high computational cost. Topology optimisation methods are typically iterative, thus they have benefited little from the rapid development of image segmentation techniques. Topology modelling is normally restricted to voxelised models.

To overcome this technical limitation, an isosurface modelling technique was developed to bridge the gap between topology optimisation, finite element modelling and the generation of smooth material boundary. This new technique treats optimisation models as level set functions, from which closed-isosurfaces are rapidly extracted using the Marching Cubes methods. This technique involves a rigorous mesh-smoothing operation that improves the quality of isosurface meshes and the definition of 3D domains and boundaries, which in turn provide a suitable foundation for finite element analysis. Its robustness, flexibility and suitability for applications in medical imaging and topology optimisation are demonstrated in some numerical examples in this work.

3.1 Introduction

Converting an image with complex geometrical features to a smooth Finite Element Analysis (FEA) model normally requires manual image segmentation. The manual image segmentation procedure is highly time-consuming and is likely carried out only if it is a one-

off event. Constructing smooth models is deemed impractical if the models change dynamically over time or over iterations, since repeating the segmentation process can increase the computational cost considerably. For that reason, topology optimisation methods, which are typically iterative, often opt for voxelised models to minimise computational cost. This modelling choice comes at a cost to numerical accuracy.

Isosurface-based high quality modelling and meshing has been well-developed and are available on both commercial and open-source platforms [1-3]. With the ever-increasing hardware power, these programs have the potential to conduct and automate iterative modelling processes at an acceptable computational cost. It has come to a point that the full-automation of isosurface and body mesh generation directly from image input is possible [4], only the robustness of the algorithms and computation speed are the limitations. One study has demonstrated the possibility of incorporating smooth mesh generation into two-dimensional topology optimisation [5]. Hence, isosurface modelling appears to be an ideal candidate for 3D model creation in a fully automatic iterative process.

Marching cubes is one of the well-known methods for isosurface generation, originally developed for the 3D modelling of binary images [6]. Most isosurface generators are developed based on the Marching Cubes method with additional numerical processing. Nowadays, high quality isosurface can be easily created from grey-scale images. However, typical isosurface modelling software is not developed with FEA applications in mind, thus the resultant mesh quality is usually unfit for body mesh generation for FEA. During meshing generation, postprocessing and modification of the isosurface are required to remedy the ill-shaped mesh grid by relocating nodes of isosurface mesh [7]. Various vertex locating techniques have also been developed to allow the construction of isosurface and body mesh with guaranteed mesh quality [7, 8].

Having realised what smooth isosurface modelling could offer, a customised program was developed. The first part of this topology optimisation study aimed to develop an isosurface modelling technique suitable for iterative simulation. The development of this technique enabled the automatic translation of grey-scale images to isosurfaces and 3D mesh with sound quality.

3.2 Isosurface generation

An isosurface model is a reasonably smooth representation of a 3D image, and it is expected that using a smoother FEA model can improve numerical accuracy as opposed to using voxelised format provided by the 3D image itself.

Computationally, an isosurface is defined by a set of points with a constant value (Figure 3-1). In a design space, any point carrying that value is part of the boundary. Such definition is exactly the same as contour line in 2D space (Figure 3-1a). In 3D space, this set of points forms a continuous surface (Figure 3-1b).

Isosurface is commonly used as a visualisation tool. It can also be used to represent or to track numerical boundaries in systems of any dimension. The focus of this study is on the generation of high quality isosurface model in a computational environment. A four-step isosurface generation method is thereby proposed: surface triangulation, surface point merging, mesh clean-up and mesh smoothing.

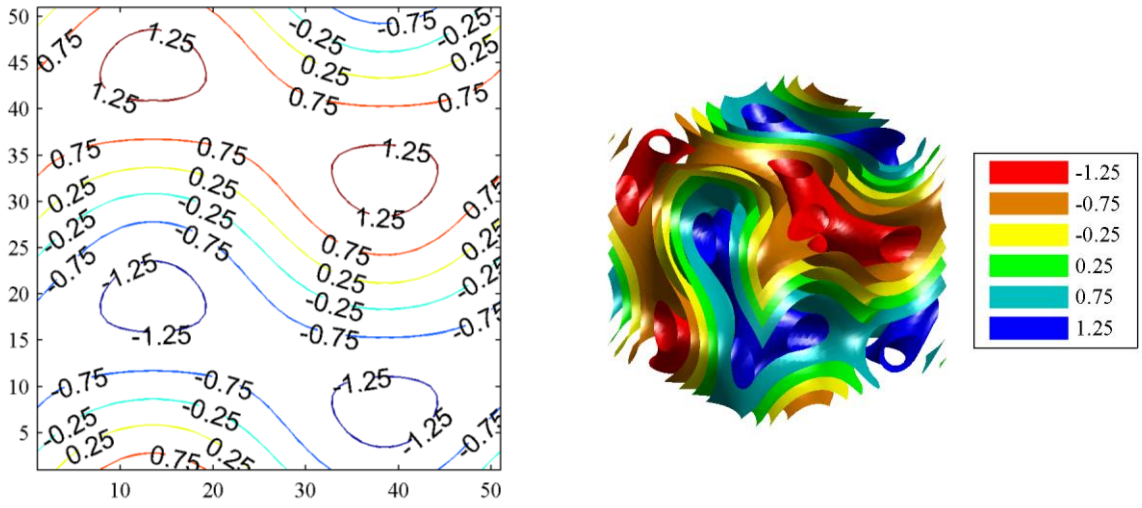

(a) 2D (b) 3D

Figure 3-1. Examples of isosurface. Isosurfaces in 2D space are equivalent to contour lines. Each line and each surface is a collection of a set of points of a certain value (set_1 = -1.25, set_2 = -0.75, set_3 = -0.25, etc.).

3.2.1 Surface triangulation

An isosurface represents a set of points in a 3D numerical array. The location and connection of such set of points is found by using the Marching Cubes algorithm, which goes through the 3D array 8 points at a time (8 vertices per cubic array), and identifies any point of a certain value. Once all points are identified, the triangulation of the points is carried out to configure their interconnection. The result of this is the creation of one or more triangulated surfaces, which divide the 3D space into at least two separated domains.

To properly define individual domains in a two-phase system, the isosurfaces have to be closed by extending and wrapping them around the modelling space. As seen in Figure 3-b, none of the individual domains is closed. To create wrapped surfaces and closed domains, a modelling procedure has been developed as illustrated in Figure 3-2.

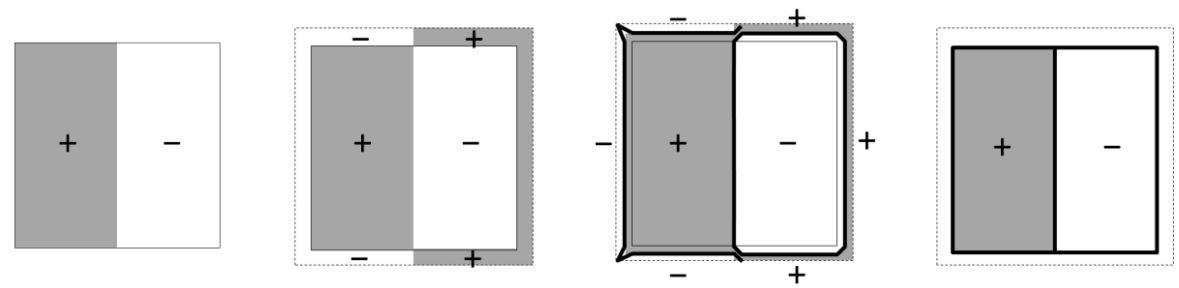

(a) Original array (b) Pad one layer (c) Extract isosurface (d) Collapse boundary

Figure 3-2. Demonstration of the process of creating closed isosurface. The solid grey lines are the original modelling boundary, the dashed grey lines are the temporary modelling boundary, and the thick solid lines are the outlines of isosurfaces.

Basically, the original image is padded with one layer of elements, in which the values have opposite signs to the domains they are wrapping (Figure 3-2a-b). Isosurfaces are extracted in the extended modelling space (Figure 3-2c), collapsed, and then snapped to the original modelling boundary (Figure 3-2d). Boundary surfaces for different phases can be created at the same time to generate isosurface junctions (Figure 3-2d).

3.2.2 Merge isosurface points

Isosurface smoothing can be achieved by merging isosurface points that are very close to each other (Figure 3-3). From a computational perspective, an isosurface is smoothed by the identification and deletion of poor shaped triangles based on a length criterion. This process involves going through the vertex-face data of isosurface, determining if any edges of any triangle is too short (in other words, vertices are too close), and deleting them. When a short edge is identified (Figure 3-3a-c, red edges), two triangles that share this edge are deleted from the vertex-face data (F1 and F2 in Figure 3-3a; F1 and F4 in Figure 3-3b; F1, F2, F9 and F10 in Figure 3-3c), and the neighbouring triangles are reshaped to fill the gap (F3 in Figure 3-3a; F3 in Figure 3-3b; F3-8 in Figure 3-3c). When two vertices are merged, one of the vertices is kept while the other is permanently deleted. Any triangle that uses the deleted vertex will use the remained one instead.

All slender triangles (with 1 short edge) and small triangles (with 2 or 3 short edges) are subjected to deletion unless their shapes can be improved. The order of their removal is based on the edge lengths in the ascending order. The edge lengths of all removal candidate are computed again just before the deletion in case that the length has changed during the process.

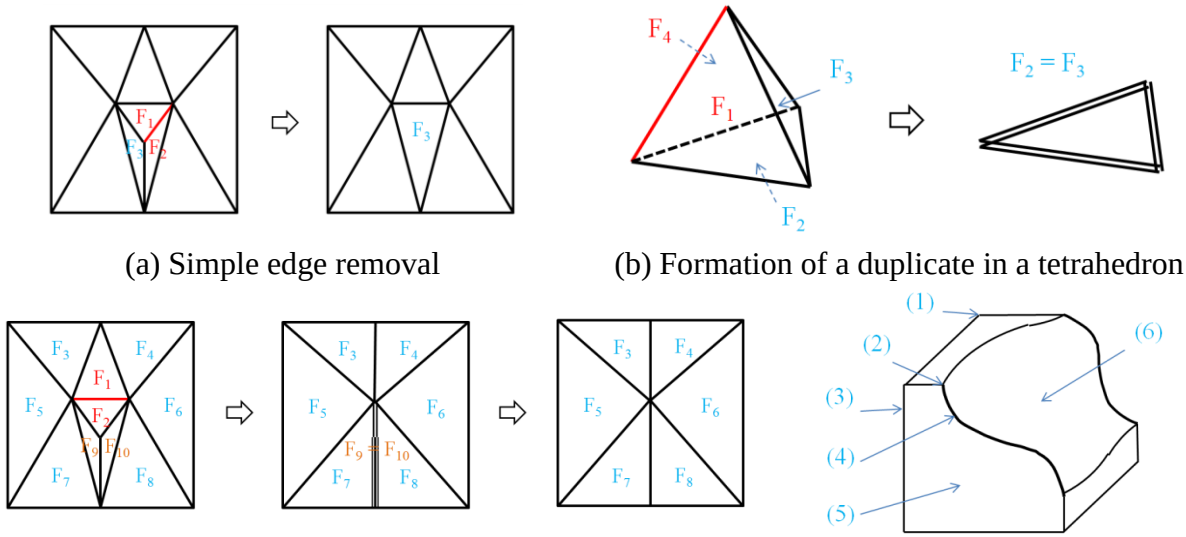

(a) Simple edge removal (b) Formation of a duplicate in a tetrahedron

(c) Duplicate formation and deletion (d) The order of importance

Figure 3-3. Schematic of the isosurface point-merging process.

To preserve critical geometric features in this process, the decision regarding which point to be deleted and if the remained point should be re-located is made according to the position of the individual point (Figure 3-3d). Intuitively, the less critical vertex on an edge should be deleted. The importance of a point depends on a number of factors. The order from the most critical to the least critical is: (1) corners of modelling boundary; (2) isosurface intersection at the edges of modelling boundary; (3) edges of modelling boundary; (4) isosurface intersection at the surfaces of modelling boundary; (5) surfaces of modelling boundary; (6) inner modelling space. If both vertices are equally critical, they will be merged into one at the midpoint. Vertex removal based on local mean curvature can also be considered as means to help preserve sharp features [8]. By following this deletion order, a gap-free surface model is guaranteed. Sharp edges and corners on modelling boundaries are also preserved.

3.2.3 Post-merging clean-up operation

The removal of vertices usually results in the formation of geometric defects and redundancy (Figure 3-4). Three common types of defect and redundancy are duplicated faces, degenerated faces and unused vertices. To rectify these issues, a number of clean-up operations are required and must be carried out in a strict order to avoid the deformation of isosurface models. In this modelling procedure, face duplicates are firstly removed (F1 in Figure 3-4). Then, all unused vertices are deleted (V2 in Figure 3-4). Unused vertices can be found by counting the number of times each vertex is used. If a vertex is used only once and is not sitting on the modelling boundary (V1 in Figure 3-4), itself and the associated triangle (F2 in Figure 3-4) will also be deleted. Finally, all tetrahedrons (Figure 3-3b) and large-size triangles that contain exactly 3 smaller triangles (Figure 3-3a) are identified and replaced with a single triangle. The reason for this is they are often physically and graphically redundant.

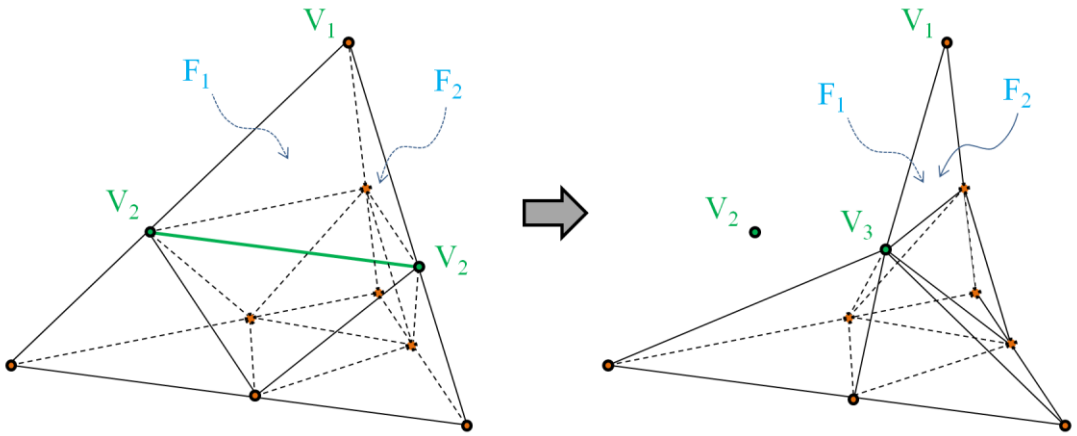

Figure 3-4. Schematic of the formation of vertex-face redundancy (F1, F2, V1 and V2).

3.2.4 Additional smoothing operation

On the modelling boundary, further mesh quality enhancement can be achieved by relocating all vertices in-plane simultaneously so they are evenly spaced. A direct approach for vertex relocation is to treat every edge of triangles as a spring that can exert a force directly proportional to its length. Long edges exert stronger force than the short edges and move the

vertices closer to themselves. At the state of equilibrium, the vertices rearrange themselves and become more evenly distributed as a result. An edge-swapping technique is further applied to fix pairs of slender triangles as well as re-orientate force direction of individual springs (section 3.3.2.3).

3.3 Computational implementation

Isosurface and mesh generation can be built as a program or a function. The purpose of this modelling function is to translate mathematical models to finite element models, in the element-node format for finite element analysis. This requires a level set function as the input and produces 3D FEA mesh as the output. This isosurface-based model generation is a two-step process (Figure 3-5). Firstly, the 3D level set function is translated to a 3D surface model in the face-node format. This format is subsequently used as the input of the element-node generating function. The third-party applications *iso2mesh* and *tetgen* are employed to construct 3D unstructured mesh (element-node) from the isosurface model (face-node). The FEA model has two typical components, nodes and 3D elements, which are labelled with material number so they can be later identified as solid, fluid or other constitutes. Triangular elements can also be exported if required.

3.3.1 Isosurface generation

The isosurface generator aims to create a model in a format the same or similar to the stereolithography format, which is readable by most FEA mesh generators and programs. The output must have fully enclosed bodies so that every material phase in the model is clearly defined. The framework of isosurface generator is illustrated in Figure 3-6.

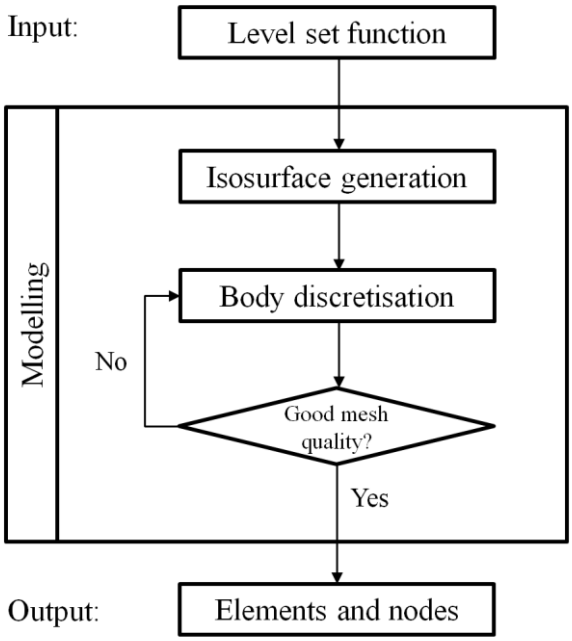

Figure 3-5. Isosurface-based modelling and meshing process.

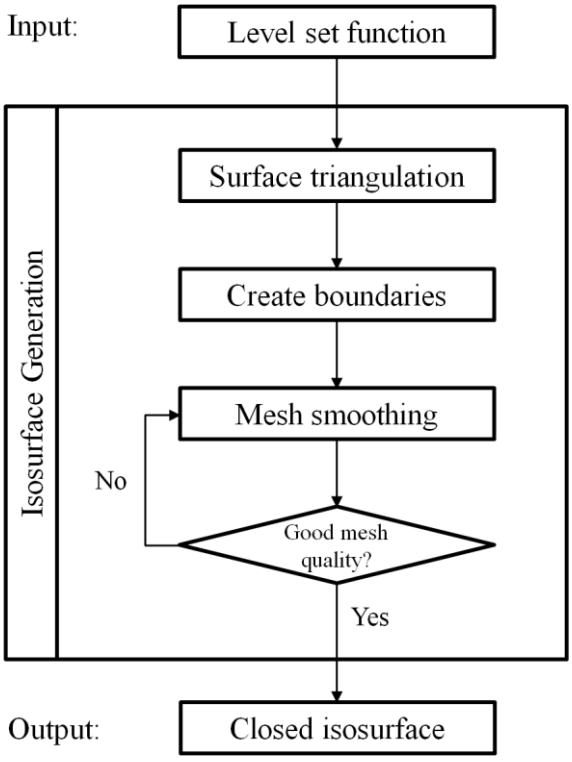

Figure 3-6. Isosurface generation process.

The most basic isosurface requires two inputs, a level set function as a 3D matrix and a level set constant as a scalar value. The actual construction is a rather standardised process that

interpolates level set points and creates a triangulated isosurface. This output also has two components, one being a list of node defined by their coordinates:

$$\begin{matrix} (\text{Node } 1) & x_1 & y_1 & z_1 \\ (\text{Node } 2) & x_2 & y_2 & z_2 \\ (\text{Node } i) & x_i & y_i & z_i \end{matrix}$$

and the other being a list of face consisting of three nodal numbers ($n_{face\#,node\#\ of\ face}$)

$$\begin{matrix} (\text{Face } 1) & n_{1,1} & n_{1,2} & n_{1,3} \\ (\text{Face } 2) & n_{2,1} & n_{2,2} & n_{2,3} \\ (\text{Face } i) & n_{i,1} & n_{i,2} & n_{i,3} \end{matrix}$$

For example shown in Figure 3-7, to draw a square surface from four level set points (0,0,0), (1,0,0), (1,1,0) and (0,1,0) requires two triangular faces:

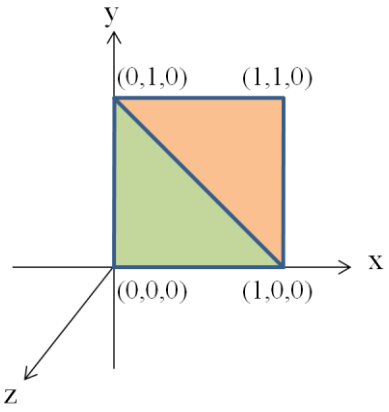

Figure 3-7. Triangular discretisation of a square.

In the matrix format, the nodal list is written as:

$$\begin{matrix} 0 & 0 & 0 \\ 1 & 0 & 0 \\ 1 & 1 & 0 \\ 0 & 1 & 0 \end{matrix}$$

The nodal number is assigned based on the row number, i.e. (0,0,0) is node #1 (first row) and (0,1,0) is node #4 (fourth row). The face list is then generated as:

$$\begin{matrix} 1 & 2 & 4 \\ 2 & 3 & 4 \end{matrix}$$

where the first face consists of node #1, #2 and #4 and the second face consists of node #2, #3 and #4. Some finite element mesh generators require that the faces to be oriented (the direction the surface normal is pointing) based on the right-hand rule, and point away from

the body they are wrapping. In the example above, both faces are pointing in the positive z-direction (out of the page). [2,1,4] and [3,2,4] would otherwise face the negative z-direction (into the page).

To ensure that the isosurface has fully enclosed a body, the boundary has to be drawn along with the boundary of modelling space as illustrated in Figure 3-8.

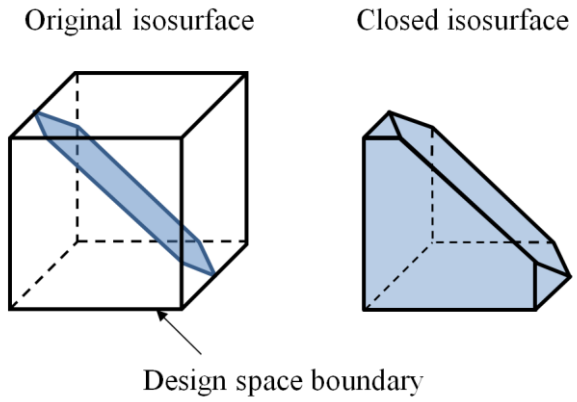

Figure 3-8. Demonstration of a non-closed and a closed isosurfaces.

In a two-phase problem, the entire modelling space boundary is drawn, rather than the single-phase boundary shown above. Computationally, the creation of those additional boundary surfaces is executed in three steps (here it is assumed that the level set constant is 0):

1. The original input matrix is padded with one layer of numbers around its borders (see Figure 3-2a-b). Below is a numerical example:

$$\begin{matrix} -10 & -10 & -10 & 10 & 10 & 10 \\ -10 & 1 & 1 & -1 & -1 & 10 \\ -10 & 1 & 1 & -1 & -1 & 10 \\ -10 & 1 & 1 & -1 & -1 & 10 \\ -10 & 1 & 1 & -1 & -1 & 10 \\ -10 & -10 & -10 & 10 & 10 & 10 \end{matrix}$$

The padded numbers are given the opposite signs of values along the border, i.e. if the value at the border is positive, the padded value will be negative; if the value at the border is negative, the padded value will be positive. The padded value is significantly greater (10) in magnitude than the values along the border (1).

2. Because of the opposite signs, a surface is created around the border when isosurface is generated (Figure 3-2c).

3. The boundary isosurface is shrink-wrapped around the original border and joined to form a continuous surface (Figure 3-2d).

Shrink-wrapping means that any node created outside the original modelling space (the solid grey line in Figure 3-2) is relocated to the modelling boundary surfaces. This shrink-wrapping technique allows the creation of an intersecting isosurface, which is critical for two-phase and multi-phase problems due to the ability to create multiple connected bodies at the same time. Connecting two isosurfaces requires removing some of the redundant nodes along the joined boundary. However, to distinguish the original isosurface from the added boundaries during the mesh smoothing process, shrink-wrapping is only carried out after the smoothing operation.

3.3.2 Mesh smoothing

The goal of mesh smoothing function is to remove or modify any triangular faces that are either redundant or severely skewed in the isosurface model. The end result of this operation is an isosurface model with evenly spaced nodes, and a more concise nodal-face set. Consequently, the FEA will be more accurate because of the improved element quality. Computational time can also be reduced due to the reduced number of element. Three different mesh smoothing techniques are used in this study: (1) point-merging, (2) finite element spacing and (3) long edge split. Point-merging is the most important mechanism and is applied to the entire isosurface mode. The other two techniques are only performed on the shrink-wrapped boundary surfaces.

3.3.2.1 Merging isosurface nodes

In this study, mesh smoothing is carried out as an iteration process that removes faces and nodes, or vertices in non-FEA context (Figure 3-3 and Figure 3-9). The decision of removal is made according to a simple edge length criterion: any triangle that contains an edge shorter than a specified value will be deleted (red edges in Figure 3-9). This length value is user-defined according to their modelling requirements. As face deletion will result in a hole on the isosurface, it must be patched by reshaping the neighbouring triangles. Node-merging also results in face degeneration (F9 and F10 in Figure 3-3c). These degenerated faces are also removed. Computationally, the node-merging process is carried out in the following sequence:

1. The edge lengths of all triangles are calculated and sorted in the ascending order. Triangles with shorter edge(s) are deleted first.
2. The location of all nodes is checked for order of importance (Figure 3-3d). Less critical nodes are deleted first.
3. When a merging decision is made, one of the two nodes becomes redundant and is moved outside the modelling space and later deleted (Figure 3-9).

Each node is given a importance value between 0 and 3.5 points. Basically, 1 point is given to a node if it is on the x-surfaces of the modelling boundary, 1 point if on the y-surfaces, 1 point if on the z-surfaces, and an additional 0.5 points if the node is part of the boundary of the original isosurface. If two nodes are equally critical, they are merged at the midpoint, and one of them is randomly picked for deletion.

Figure 3-9 (also Figure 3-3a) is also a special case, demonstrating the merging of three triangles into one. Tetrahedron as shown in Figure 3-3b is another special case where a face duplicate is created through face deletion and must be dealt with separately. To do this, once a tetrahedron is identified, two of the triangles containing the shortest edge are determined

and deleted (F1 and F4 in Figure 3-3b), and then one of the duplicated faces can be removed (F2 and F3 in Figure 3-3b).

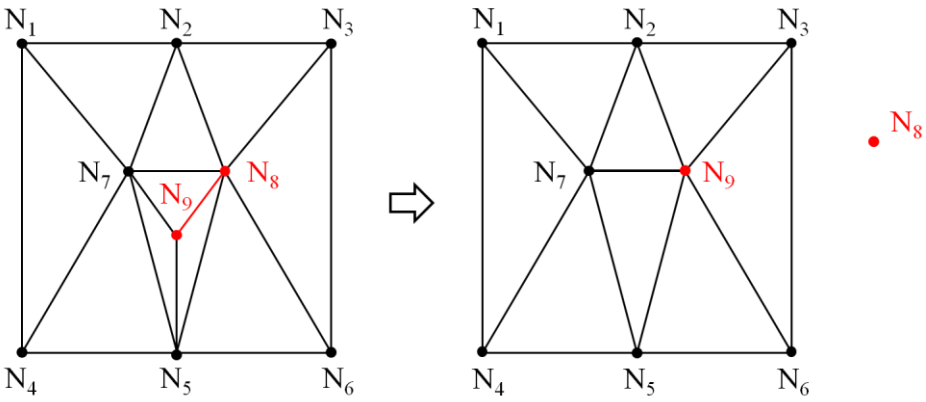

Figure 3-9. Schematic of the node-merging and face-patching process.

Tetrahedrons can be identified in the node-face set by counting how many times each node has appeared in the nodal list. Those that appear exactly 4 times and share exactly 4 triangular faces are part of a tetrahedron. Sometimes the entire tetrahedron can be deleted if it is not connected with the rest of isosurface model.

3.3.2.2 Condensing the face-node lists

The mesh smoothing process inevitably creates a large number of redundant nodes and face duplicates. Maintaining correct nodal and face lists is therefore an essential task in this isosurface smoothing process. A small function is warranted to maintain a concise face-node set. However, caution must be taken as removing any node from the list will result in a change in the nodal number, thus the face list must be updated concurrently.

To save computational time, the actual node and face deletion from the vertex-face set takes place after the node-merging process is completed for the entire model, rather than every time two nodes. Using Figure 3-9 as an example, when nodes N_8 and N_9 are merged, it is apparent that:

1. Face 1 N_7-N_8-N_9 becomes N_7-N_9-N_9.

2. Face 2 N_9-N_8-N_5 becomes N_9-N_9-N_5.

3. Face 3 N_5-N_7-N_9 remains the same.

4. Node 8 N_8 is moved out of the modelling space.

Assuming this is the end of the operation, the mesh integrity is then examined.

1. Face 1 N_7-N_9-N_9 is no longer a face. This entity is deleted.

2. Face 2 N_9-N_9-N_5 is no longer a face. This entity is deleted.

3. Node 8 N_8 is not used by any face. This node is deleted.

4. Node 9 N_9 moves up the list and becomes the new N_8.

5. Face 3 N_5-N_7-N_9 is re-numbered as N_5-N_7-N_8.

Node 9 could have been removed instead of Node 8 in the first place since they are equally critical as both have 0 point. If the nodes N_2 and N_9 were to be removed, Node 9 (0 point) would be moved out of the modelling space since Node 2 was more critical (1 point for being on the modelling boundary).

3.3.2.3 Boundary mesh smoothing through finite element method

An alternative approach to improve the mesh quality is node spacing through finite element method, where all edges are treated as a tension spring that pulls its neighbouring nodes toward each other. Let this "tensile force" of every edge be directly proportional to its length, long edges would exert more force on their neighbouring nodes than short edges. Consequently, the mesh will re-arrange itself to counter-balance all forces by moving nodes to some intermediate positions. In other words, the goal of this technique is to relocate nodes in a way that the mesh quality can be enhanced. This process is combined with node-merging and is repeated a number of times until no further improvement is possible. This process is executed at most six runs per iteration as there are six boundaries in a 3D modelling space. Each run is conducted on its own 2D plane and in a 2D FEA context.

As an FEA problem, a global stiffness matrix representing the spring tension is created. The elemental stiffness matrix of one spring element, AB, is

$$\begin{bmatrix} 1 & 0 & -1 & 0 \\ 0 & 1 & 0 & -1 \\ -1 & 0 & 1 & 0 \\ 0 & -1 & 0 & 1 \end{bmatrix} \begin{Bmatrix} x_A \\ y_A \\ x_B \\ y_B \end{Bmatrix} = \begin{Bmatrix} F_{A,x} \\ F_{A,y} \\ F_{B,x} \\ F_{B,y} \end{Bmatrix}$$

where the x's are the current coordinates of nodes. The global stiffness matrix is assembled from elemental matrices. The *x*/*y*/*z* coordinates of all nodes that are on the edges, on the corners of the modelling boundary, or on the boundary of the original isosurface are fixed, hence they are unaffected by this operation.

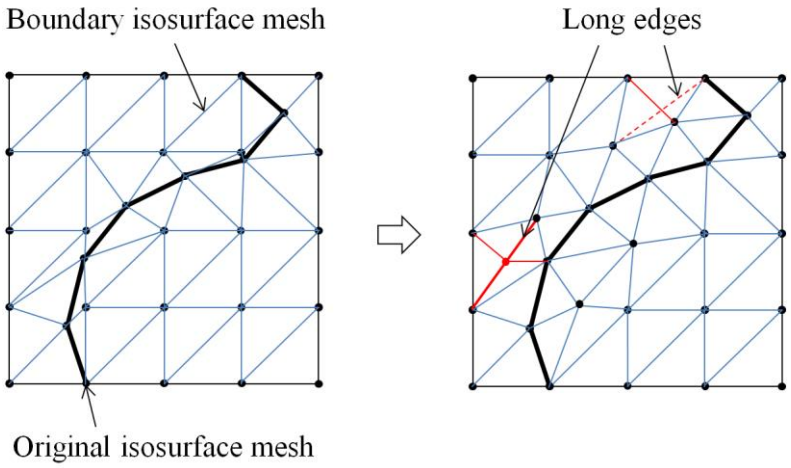

Figure 3-10. Reconstruction and splitting of triangles on the isosurface boundary.

Triangles with long edges can be dealt with in two different ways through reconstruction or splitting based on the length criterion (Figure 3-10). Either that a new pair of triangles can be defined with different nodal compositions (Figure 3-10, right, dashed red line), or the original triangles can be split into four (Figure 3-10, right, thick red line). Both techniques directly remove long edges, and indirectly affect the subsequent mesh-smoothing operation that rearranges the "forces field" of the current spring system (Figure 3-11, red edges).

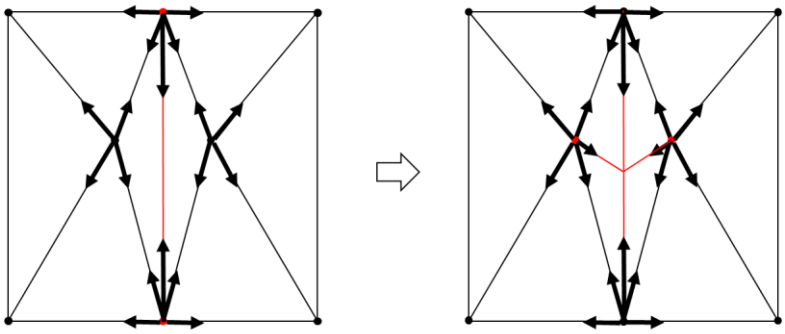

Figure 3-11. Edge splitting adds force vectors to the existing spring system.

For every long edge removed, two triangles are split or reconstructed. The surface normal of the new faces are oriented in the same direction as the original faces according to the right hand rule. Edge-splitting is performed separately in a fashion similar to the short edge removal process. However it adds new nodes and faces to the existing set. Edge-splitting is executed based on a list of faces that contain long edges, and rectify the issues one by one. A long edge will not be split if it happens to be part of the original 3D isosurface (Figure 3-3d, surface 6), or it is part of the modelling boundary edges (Figure 3-3d, point 1, point 2 and edge 3). Also, if either new edges being created is too short according to the short edge removal criterion, the process is skipped. Node relocation by finite element method and edge modification is repeated alternately for a number of times to ensure that both sets of smoothing criteria are satisfied.

3.3.3 Body generation

The body mesh generating function takes the isosurface model as an input, discretises the enclosed body, and produces unstructured tetrahedral mesh as the output (Figure 3-12). Parameters such as model size, mesh size, and the original LSF are also used to augment this discretisation process.

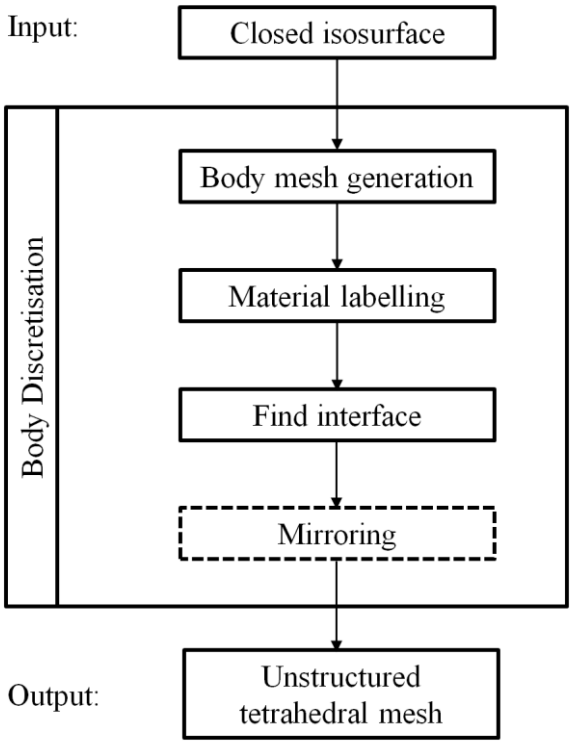

Figure 3-12. Generation of unstructured 3D mesh from isosurface.

The first task of this function is identifying and labelling the enclosed bodies. In this thesis, the negative LSF domain represents fluid or void, and the positive LSF domain represents solid. There can be more than one solid body and more than one fluid body in a FE model at the same time. The identification of individual bodies is done using the flood-fill technique as illustrated in Figure 3-13.

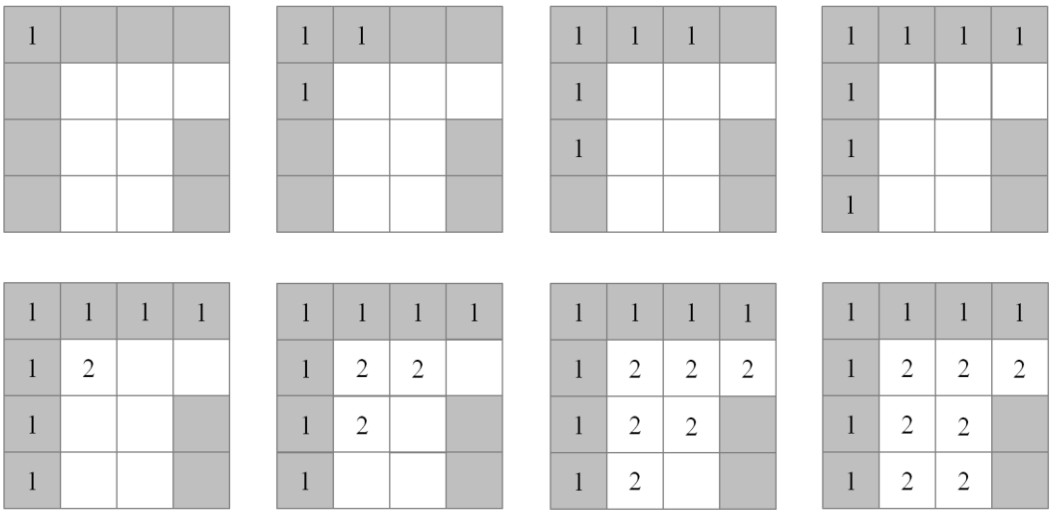

Figure 3-13. Schematic demonstration of the flood-fill process.

The flood-fill is carried out on a matrix the same size as the LSF, each matrix entry will be given a number as a material label, which is referred to as a set of material properties. Using Figure 3-13 as an example and starting with an empty matrix, the first empty entry is given a material number "1" (the top-left grey-coloured square). This material number is replicated and written into all its neighbouring entries that are empty and are in the same material domain (grey colour). In this LSF structure, nodes are connected orthogonally in six directions (x+, x-, y+, y-, z+ and z-). This step is repeated until no more squares can be filled (four subplots on the top), and then a new material number ("2") is created for the next flood-fill process (bottom left) and seeded in the first unoccupied matrix entry. New material numbers are created until the entire matrix is filled. When the body mesh generation is completed by the third-party programs, every solid and fluid body is marked by a material number. It is crucial to match all solid and fluid domains correctly by feeding the mesh generator the material information. The material labels, known as "material points" by some FEA software, are created for every zone/body to indicate what material and where each body is. These material points can be spatially back-tracked to its original level-set function and verified.

If the FE model is symmetric, only one eighth of the isosurface and 3D FEA model has to be built. To reconstruct the entire model from the 1/8th model, the resultant 3D mesh is mirrored and duplicated three times in x, y and z directions (Figure 3-14). Following this, elements on the mirroring planes are connected by merging nodes at the interface (N_3 and N_{12} for example in Figure 3-14). Similar to the isosurface node deletion process, the element definition have to be updated simultaneously to use the new nodal number. This produces the final element-node set of the FE model.

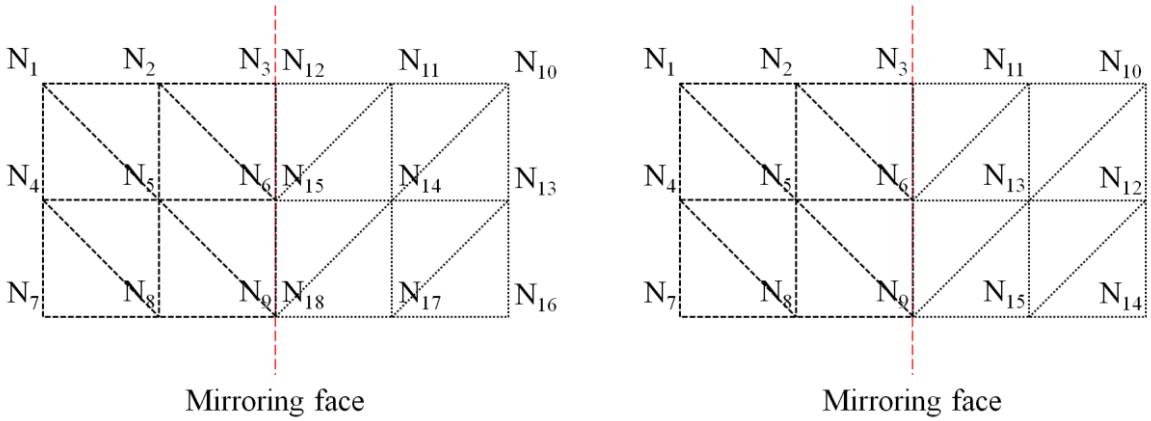

(a) Node and element mirroring (b) Node deletion and element re-numbering

Figure 3-14. Schematic demonstration of mesh reconstruction through mirroring.

In a computational fluid dynamics simulation, nodes at material interface have to be specifically marked. These nodes can be easily identified by going through the element lists. Nodes that appear on both solid element and fluid element lists are marked as such.

3.4 Results and discussion

Since the publication of the Marching Cubes algorithm in the 1980s, isosurface construction has become a well-established technique and a common procedure in 3D modelling. While high quality model and mesh are desirable in finite element analysis, they are rarely used in iterative processes such as transient analysis and topology optimisation due to high implementation cost and complexity. Therefore a custom isosurface and mesh generation program was built, designated for automated modelling in topology optimisation.

A smooth isosurface modelling technique has been developed based on the Marching Cubes method and a number of numerical operations. In this part of study, this technique was used to generate enclosed triangulated surfaces for a human brain, a CT-scan cuttlebone image, a multi-objective design optimisation model and the Clebsch model (Figure 3-15a, b-c, d-f and Figure 3-16, respectively) to test its modelling capability. The isosurfaces generated have captured the characteristic geometry of the structure of brain [4], the micro-structure of cuttlebone [9], and tracked the evolving shape of the topology optimisation model. The vertex or node-merging procedure and the mesh smoothing operations had eliminated all poorly-shaped triangles and condensed the overall isosurface model size. The final mesh sizes were larger than their pre-processed counterparts as fine meshes were merged to form coarser meshes. For the high resolution CT-scan image such as the cuttlebone, the deletion criteria are set at a value much greater than the pixel size of the input image to produce a significantly coarsened model. When combined with a robust body mesh generator such as tetgen [3], this isosurface modelling technique makes automatic re-meshing feasible and time-efficient.

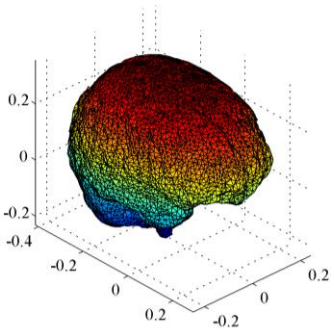

(a) Human brain

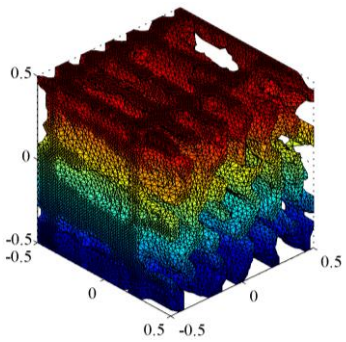

(b) Cuttlebone - solid phase

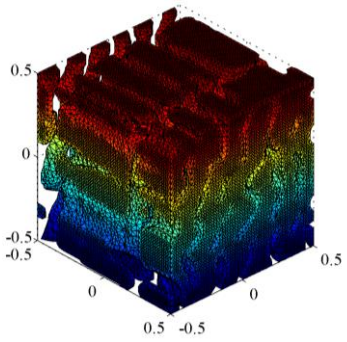

(c) Cuttlebone - void phase

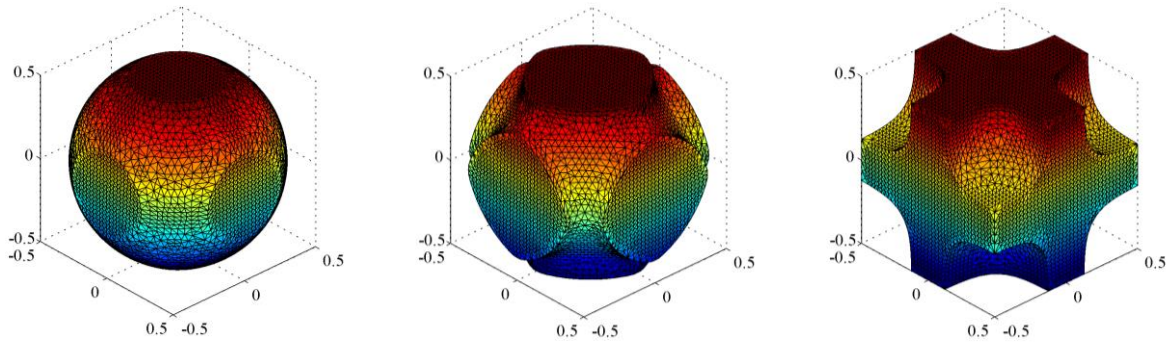

(d) Initial model (e) 50th iteration (f) Optimal model

Figure 3-15. Smoothed isosurface examples in practical modelling (a)-(c) and topology optimisation (d)-(f).

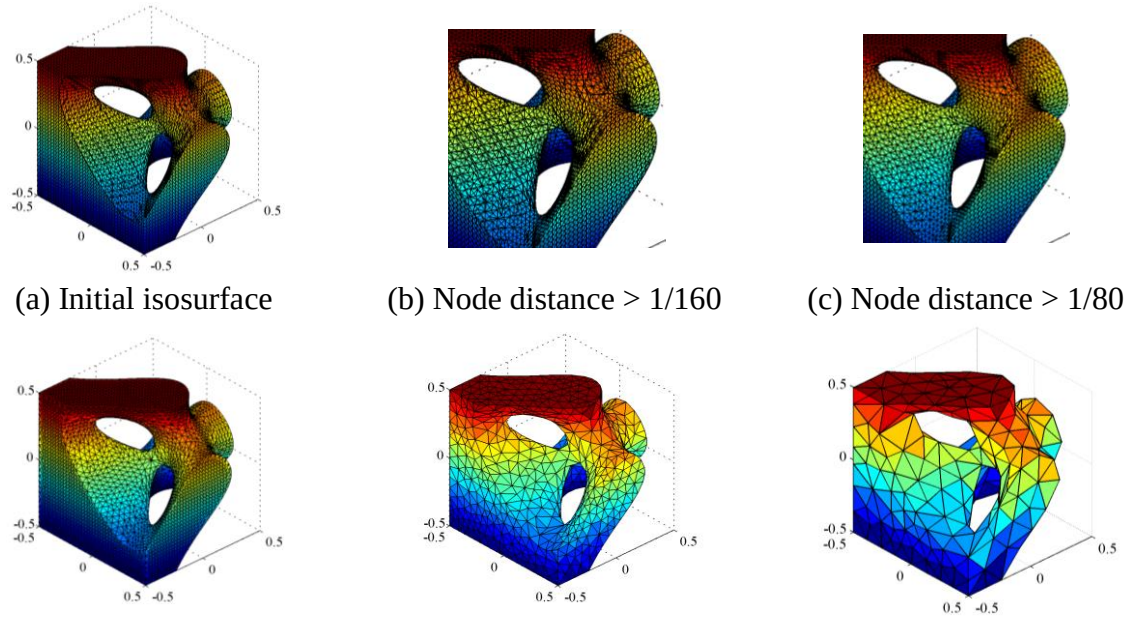

(a) Initial isosurface (b) Node distance > 1/160 (c) Node distance > 1/80

(d) Node distance > 1/40 (e) Node distance > 1/20 (f) Node distance > 1/10

Figure 3-16. The resultant Clebsch isosurfaces with different minimum node distances (as a fraction of the model size). The input data has a resolution of 41^3 and 1/40 spacing.

The deletion order has helped preserve the boundary features at the isosurface intersection in both the cuttlebone and the design optimisation models. Smoothing technique by numerical filtering was not being used in the cuttlebone case to avoid moving those feature-defining points. Unless all boundary vertices are properly constrained in one or more appropriate directions, moving an isosurface-boundary intersection or any boundary point would directly result in the degeneration of the model.

Body meshes have been automatically generated by the program, *tetgen*, to fill these isosurface models (Figure 3-17). As shown in Figure 3-17, the inner domain is filled with unstructured tetrahedral mesh. Mesh generation in the outer domain could be done simultaneously to fill the entire modelling space. A topology optimisation was also successfully carried out over 200 iterations to confirm the robustness of the program.

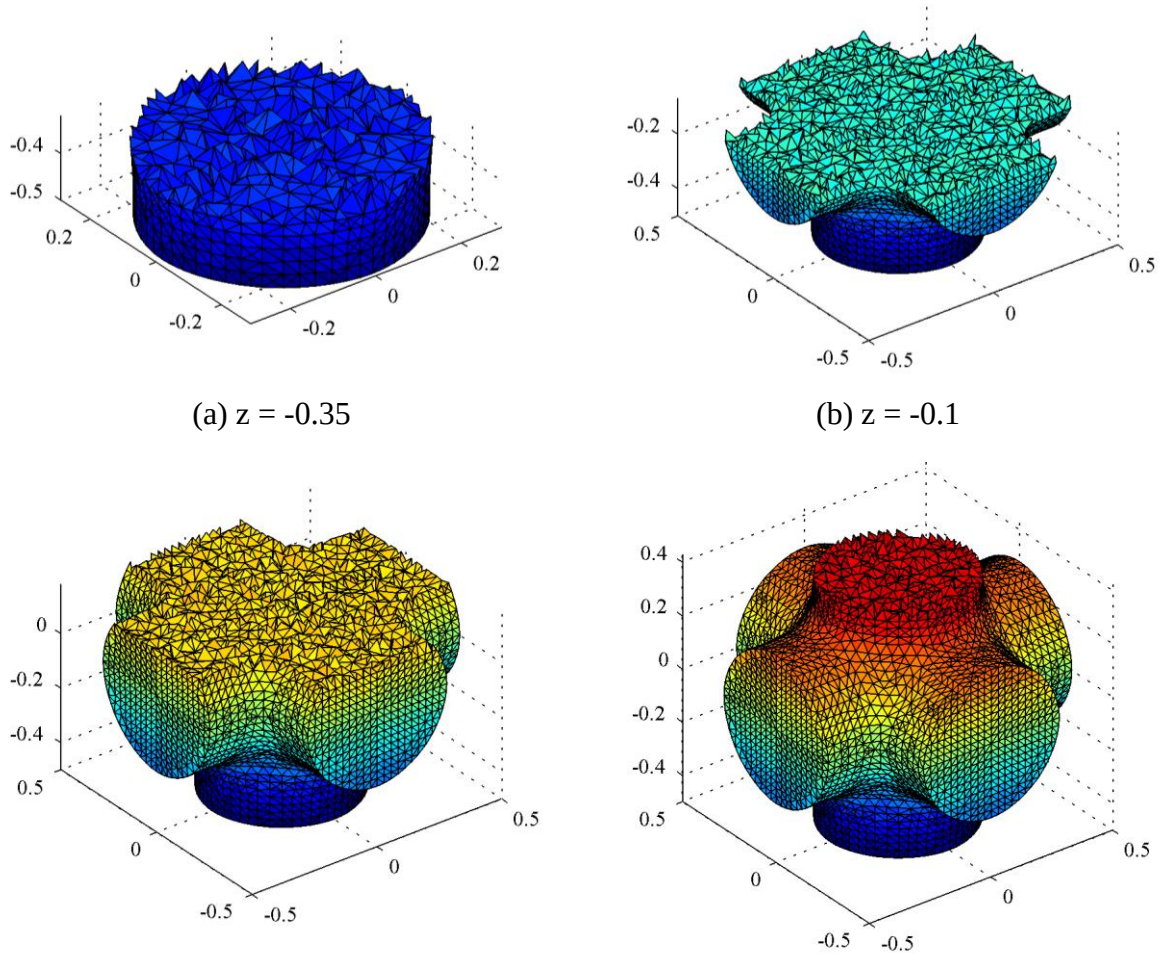

(a) z = -0.35 (b) z = -0.1

(c) z = 0.15 (d) z = 0.4

Figure 3-17. Cross-sectional views of a body mesh of a topology optimisation model. Z indicates the position of the cross-section in the Cartesian coordinate system.

Following the deletion order, the node-merging criterion is flexible and has no upper limit. This allows a virtually unlimited vertex-face condensation until the entire structure fully degenerates, as demonstrated in the Clebsch model (Figure 3-16). In the meantime, geometric features degenerate at a much slower rate. These results also show that the proposed

modelling program has outperformed similar functions provided in the Iso2Mesh toolbox (mesh resampling) in term of feature preservation, but at a higher computational cost. However, additional tests show that extracting a very coarse isosurface from a very high resolution image (100*100*100 and higher) can be impractical although possible by using a large distance value in node deletion. It is more efficient to reduce the input image resolution beforehand than repeating the node deletion.

Breaking down one deletion process into multiple runs, with each subsequent run using a larger deletion distance, improves the stability and helps obtain more accurate results. For example, if the desired merging distance is 0.8 units, the function can be called twice with the first run merging nodes within 0.4 units, and the second run merging those within 0.8 units. It should be noted that the distance between nodes may change during the deletion process as a result of node re-location. Furthermore, constantly re-computing the nodal distance is inefficient, so the distance calculation is performed only once per deletion run. Consequently, deletion does not occur in a strictly ascending order. Some nodes distances that are close to the tolerance value can change their state from too short to satisfactory, therefore the distance should be double-checked just before deletion. Running the deletion process in multiple small steps allows it to be carried out in mostly ascending order.

Merging nodes at their midpoint preserves the overall shape of the 3D models. However, some fine geometric details such as sharp edges and spikes can still be lost if the node-merging process is extensive. All models shown in Figure 3-15 and Figure 3-16 were obtained with vertex relocation to the midpoints of the deleted edges. It can be seen in Figure 3-16 that the final Clebsch models manage to retain most of its initial characteristics. Nevertheless, this midpoint relocation led to geometrical deviation every time an isosurface vertex is moved. In terms of volumetric deviation and numerical errors, such error can

accumulate over iteration. Alternatively, surface curvature-based relocation tactic can be used to ensure the new nodal locations stay on the original isosurface, but at a higher computational cost.

Overall, the proposed technique guarantees high surface quality. Together with the octree mesh-generating method, a robust body mesh can be built. Mesh-generating methods such as Delaunay triangulation and advancing front are not recommended here as they may not always succeed in filling the body of a model. The development of more vigorous and comprehensive tetrahedral mesh generation will further improve the practical value of this isosurface modeller and strengthen its integration in iteration processes.

3.5 Programming considerations

In the isosurface-based topology optimisation (starting from the next chapter), modelling is the largest and most complicated programming components. The correct transformation of an implicit input to an unstructured mesh is the greatest challenge.

When tetrahedral mesh is generated, some material zones (LSF subdomains) have been found to be very small and difficult to distinguish. They become a potential problem when assigning material properties to elements if the location of the elements cannot be clearly identified, in other words, it is unclear to which LSF zone the elements belong. There are two solutions to this problem, one is to analyse more or all elements from the zone until there is a general agreement; another solution is to merge the entire material group into its neighbouring group. In many structural design scenarios, discontinuity is forbidden and any isolated zone is automatically dissolved into its surrounding material zone.

The nodal definition of an element has to conform to the FEA program standard. Normally, a tetrahedral element contains four unique nodes and is written as a row vector:

$$N_1 \quad N_2 \quad N_3 \quad N_4.$$

The numbering order must follow the right-hand rule where the surface normal of triangle N_1-N_2-N_3 points toward N_4 (Figure 3-18).

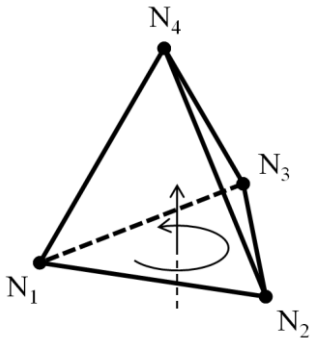

Figure 3-18. Node numbering of a tetrahedral element based on the right-hand rule.

In the ANSYS environment however, the element has to be expressed in the 8-node hexahedral element format with repeated nodal numbers:

$$N_1 \quad N_2 \quad N_3 \quad N_3 \quad N_4 \quad N_4 \quad N_4 \quad N_4.$$

3.6 Concluding remarks

The implementation and automation of smooth isosurface generation in an iterative process requires a robust modelling system. The rapid surface model construction using the Marching Cubes method and the proposed edge clean-up technique together provide the robustness and allow the conversion of structured volumetric data to a two-phase surface model. This procedure guarantees the smoothness of final results as well as flexible control of mesh size and density. Its suitability for 3D medical and topological modelling has been demonstrated in this part of study.

3.7 References

[1] Edelsbrunner, H. & Shah, N.R. 1996. Incremental Topological Flipping Works for Regular Triangulations. *Algorithmica*, 15**,** 223-241.

[2] Si, H. & Gaertner, K. Meshing Piecewise Linear Complexes by Constrained Delaunay Tetrahedralizations. 14th International Meshing Roundtable, September 2005 2005. 147-163.

[3] Si, H. On Refinement of Constrained Delaunay Tetrahedralizations. 15th International Meshing Roundtable, September 2006 2006.

[4] Fang, Q. & Boas, D. Tetrahedral mesh generation from volumetric binary and gray-scale images. IEEE International Symposium on Biomedical Imaging 2009, 2009. 1142-1145.

[5] Zhou, S., Li, W. & Li, Q. 2010. Level-set based topology optimization for electromagnetic dipole antenna design. *Journal of Computational Physics,* 229**,** 6915-6930.

[6] Lorensen, W.E. & Cline, H.E. 1987. Marching cubes: A high resolution 3D surface construction algorithm. *SIGGRAPH Comput. Graph.,* 21**,** 163-169.

[7] Labelle, F. & Shewchuk, J.R. 2007. Isosurface stuffing: fast tetrahedral meshes with good dihedral angles. *ACM SIGGRAPH 2007 papers.* San Diego, California: ACM.

[8] Wang, J. & Yu, Z. 2012. Feature-sensitive tetrahedral mesh generation with guaranteed quality. *Computer-Aided Design,* 44**,** 400-412.

[9] Cadman, J., Chang, C.C., Chen, J., Chen, Y., Zhou, S., Li, W. & Li, Q. 2013. Bioinspired lightweight cellular materials--understanding effects of natural variation on mechanical properties. *Mater Sci Eng C Mater Biol Appl,* 33**,** 3146-52.

4 Topology Optimisation of Tissue scaffolds

Topology optimisation methods commonly employ fixed mesh and density-based model. Although such approach minimises the complexity of finite element modelling, it comes at the cost of the accuracy of finite element analysis (FEA). To improve accuracy and to validate the claims made by past studies aforementioned in the Chapter 2 Literature Review, the isosurface and level set function (LSF) co-modelling technique has been utilised in the design and optimisation of tissue scaffolds. This new method is based on the established level set optimisation method, with the addition of isosurface construction, unstructured tetrahedral meshing, and an isosurface-based topology update system that replaces the level-set based sensitivity analysis. The optimisation results were compared to those obtained from Bi-directional Evolutionary Structural Optimisation (BESO), Solid Isotropic Material Penalisation (SIMP) and the conventional level-set method (LSM).

There were three design objectives in this part of tissue scaffold design: maximisation of (1) effective bulk modulus, (2) effective diffusivity and (3) effective permeability. The optimal microstructures of tissue scaffold would be generated using the isosurface modelling method (Chapter 3) to create smooth and unambiguous material boundaries.

4.1 Introduction

Architectures of porous tissue scaffolds have been shown to have a major impact on tissue proliferation [1-3]. Past studies have attempted to tackle various mechanical and biological issues as structural design problems, in which the design criteria primarily focused on the properties of tissue scaffold such as pore connectivity [4], stiffness [5], diffusivity [6, 7] and

fluid flow interaction [8, 9]. Effective material properties such as bulk modulus, diffusivity and permeability have been used as objectives of topology optimisation [5, 10, 11]. In these studies, the design and characterisation of microstructure was typically carried out on a microscopic representative volume element (RVE), where the scaffold is assumed to be constructed by self-repeated unit cells in which the material distribution uniquely determines the effective properties in terms of homogenisation theory.

Past computational studies have successfully applied topology optimisation to microstructure design to maximise effective stiffness [5], bulk modulus [12], conductivity [12, 13], and permeability [5, 14-17]. Some studies have also recommended using special mathematical models as the scaffold microstructure [2, 3]. However the optimisation results contain numerical artefacts such as voxelised surface (ESO, BESO and SIMP) [18], blurred boundary (level set method) [19] and diffused interface (phase field method) [20]. Such physical ambiguity can become a problem in the actual fabrication of tissue scaffolds by solid freeform fabrication (SFF) [2, 21].

To overcome this design and modelling limitation, an optimisation method has been selected and modified for the fabrication purpose. From the topology design point of view, a non-parametric method is preferred and there are two possible options: density method (ESO, BESO and SIMP) and surface tracking (level set method and phase field method). While the density method are more versatile as they allow the formation of holes in both 2D and 3D spaces, it has been demonstrated that surface tracking can achieve the same in 3D space [22, 23]. Level set function (LSF) is commonly used to track surface or boundary over time in computer simulations [24-26] before being utilised in topology optimisation [16, 27, 28]. The LSF method approximates the location of material boundary in a fixed mesh and has a voxelised, density-based band of boundary [19].

What appears to be a possible solution to improving the boundary modelling is the explicit counterpart of level set, known as the isosurface. Isosurface is a well-developed visualisation and finite element modelling technique [29] but it is not well-known in topology optimisation. Nevertheless, a 2D isosurface-based topology optimisation method had been developed, which successfully produced smooth boundary models and eliminated the need of approximation or density modelling [30]. The implication is that the implicit level-set method can be combined with the explicit isosurface modelling to allow surface tracking and accurate finite element modelling at the same time.

The implementation of isosurface modelling in a modified level set optimisation framework is hereby proposed. The goal of this study is to develop a smooth topology optimisation technique designated for tissue scaffold design and fabrication. This new method will determine the optimal microstructures for structural stiffness, diffusion transport and perfusion. The design criteria are homogenized bulk modulus, effective diffusivity and effective permeability. The proposed method will also be benchmarked in terms of the highest achievable material properties against a range of optimisation methods that utilise fix-mesh.

4.2 Single-objective topology optimisation

4.2.1 Topology optimisation

This part of study introduces an isosurface-based topology optimisation technique. Building on the established level-set optimisation framework [31], this technique replaces the conventional fixed-mesh density model with a smooth, non-density-based unstructured mesh. The design objective is to maximise the effective bulk modulus, diffusivity and permeability, which are calculated according to the homogenisation theory [32, 33].

4.2.1.1 The level set method

A level set is a surface that consists of points of a prescribed value. Together these points form one or multiple continuous boundaries between points with greater values and points with lower values (Figure 4-1). In an explicit model, the movement of a boundary is typically initiated by relocating the set of boundary points to the desired position. In an implicit model however, all points are stationary; a moving boundary is tracked by adjusting the value of the entire function so that only points at the new boundary position have the prescribed value (Figure 4-1b). Boundary tracking by level set method is an implicit technique that tracks the location of boundaries by adjusting the level set function value.

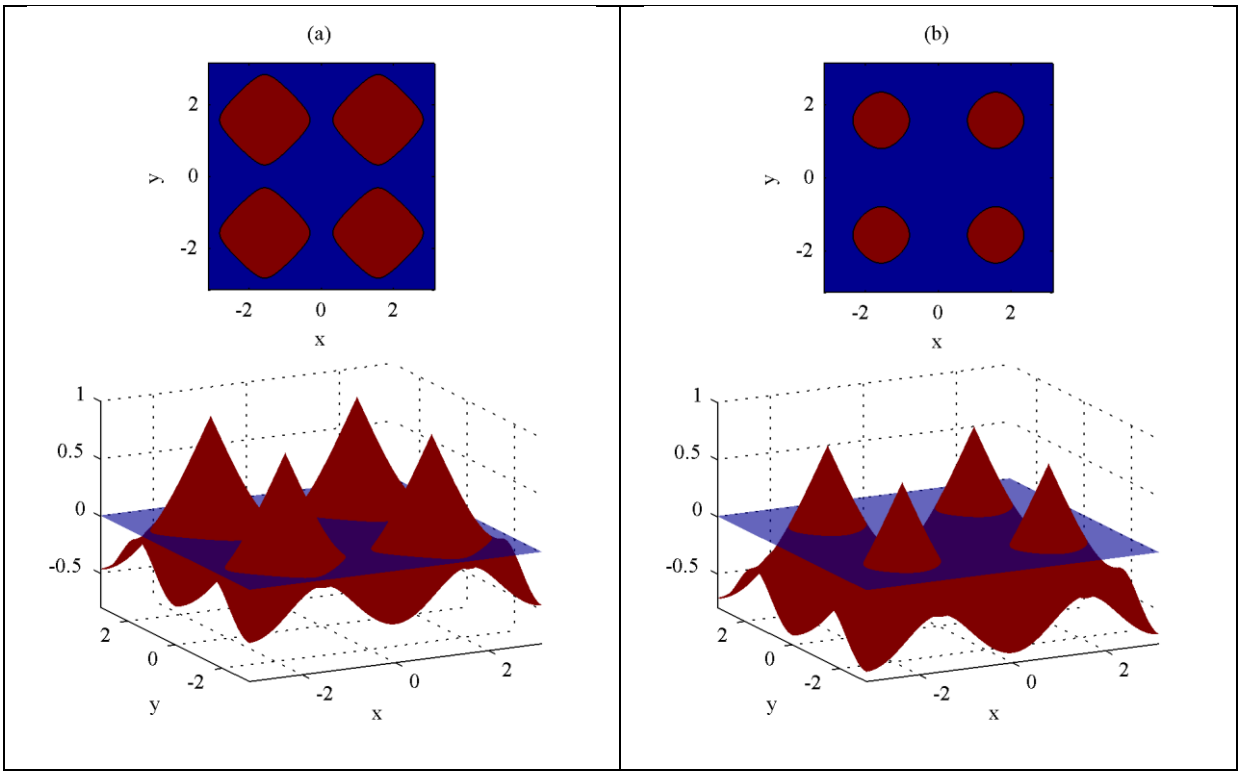

Figure 4-1. Exemplar level set functions (bottom) and their respective level set boundaries (top) of an evolving system: (a) the original state, and (b) the new state.

Mathematically, a level set (Γ) is defined as a set of points with a common value:

$$\Gamma: \phi(x_1, x_2, \dots) = k. \tag{4-1}$$

where ϕ is the level set function. For example in Figure 4-1, $\phi = z(x, y)$ and the level set value k is zero. If the level set function (ϕ) is continuous, a level set forms a continuous

surface that divides the entire space into two domains. Isosurface shares exactly the same mathematical definition, but the location of boundary points are explicitly determined and listed.

In the design of porous tissue scaffolds, there are two material phases, namely solid (scaffold material) and void (pores). The part of LSF space with values smaller than *k* represents the void phase ($\Omega_v: \phi(x) < k$) whereas the part of LSF space with values greater than *k* represents the solid phase ($\Omega_s: \phi(x) > k$). The constant *k* is typically zero in a two-phase problem. By this definition, the isosurface represents the phase boundary.

Topology change is initiated through the manipulation of the LSF. If $k = 0$, a change in the sign of the LSF value will result in a change in phase, and consequently a change in the boundary position. Mathematically, this rate of change is expressed as a velocity function of the phase boundary. The actually change in LSF (ϕ) can be found mathematically by solving a Hamilton-Jacobi equation when the velocity function is given:

$$\frac{\partial \phi}{\partial \tau} + v_n |\nabla \phi| = 0 \tag{4-2}$$

where $\partial\tau$ is the pseudo-time, v_n is the velocity function, and $\nabla\phi$ is the gradient field of LSF. A boundary with a positive velocity moves toward the solid side (the void phase expands) while a boundary with negative velocity moves to the void side (the solid phase expands). The actual displacement over time is controlled by a time step, $\partial\tau$. Multiplying the velocity function by level set gradient and the time step yields the change in LSF, $\partial\phi$:

$$\partial \phi = -\partial \tau \times v_n |\nabla \phi|. \tag{4-3}$$

To determine the rate of change of the LSF, the objective function is firstly defined as:

$$\begin{aligned} &\text{maximise: } J(\phi) = \tfrac{1}{|\Omega|} \textstyle\int_{\Omega} H(\phi)\alpha(\phi, u)d\Omega \\ &\text{subject to: } \int_{\Omega} H(\phi)d\Omega = \Omega_S \end{aligned} \tag{4-4}$$

where $|\Omega|$ is the total volume of design space, $H(\phi)$ is the Heaviside function, $\alpha(\phi, u)$ is the nominal local effective material property, and Ω_S is the total allowable volume of solid material. Multiplying $\alpha(\phi, u)$ by $H(\phi)$ yields the local effective property. The integral yields the total effective property. The time derivative of this objective function is [19]:

$$\frac{\partial J(u,\phi)}{\partial \tau} = \int_{\Omega} \delta(\phi)\beta(u,\phi)v_n|\nabla\phi|d\Omega \tag{4-5}$$

where $\delta(\phi)$ is the delta function, $\beta(u, \phi)$ is the nominal local sensitivity. This equation can be broken down by chain rule into two components:

$$\frac{\partial J(u,\phi)}{\partial \phi} = \int_{\Omega} \delta(\phi)\beta(u,\phi)d\Omega \tag{4-6}$$

$$\frac{\partial \phi}{\partial \tau} = v_n|\nabla\phi| \tag{4-7}$$

where $\frac{\partial J(u,\phi)}{\partial \phi}$ is the shape derivative of the objective function. For effective bulk modulus and effective conductivity optimisation problems, Wang et al. had derived the shape sensitivity as [34]:

$$\frac{\partial J(u,\phi)}{\partial \phi} = -\frac{1}{|\Omega|}\int_{\Omega} \delta(\phi)\left(I - \frac{\partial u}{\partial x}\right)^T D(\phi)\left(I - \frac{\partial u}{\partial x}\right)d\Omega \tag{4-8}$$

where *u* is the degree of freedom, and *D* is the stiffness or conductivity of scaffold material.

The same derivation can be applied to the effective permeability optimisation problem and this yields:

$$\frac{\partial J(u,\phi)}{\partial \phi} = -\frac{1}{|\Omega|}\int_{\Omega} \delta(\phi)\left(\frac{\partial u}{\partial x}\right)^T K(\phi)\left(\frac{\partial u}{\partial x}\right)d\Omega \tag{4-9}$$

where *K* is the fluid viscosity. Matching Eq. (4-6) with Eq. (4-8) and (4-9) reveals that:

$$\beta(u,\phi) = -\tfrac{1}{|\Omega|}\left(1 - \tfrac{\partial u}{\partial x}\right)^T D(\phi)\left(1 - \tfrac{\partial u}{\partial x}\right), \tag{4-10}$$

$$\beta(u,\phi) = -\tfrac{1}{|\Omega|}\left(\tfrac{\partial u}{\partial x}\right)^T K(\phi)\left(\tfrac{\partial u}{\partial x}\right). \tag{4-11}$$

As all effective material properties must be positive, $\beta(u, \phi) \leq 0$. Hence $\alpha(\phi, u) = -\beta(u, \phi) \times |\Omega|$, and

$$\frac{\partial J(u,\phi)}{\partial \tau} = -\frac{1}{|\Omega|}\int_{\Omega} \delta(\varphi)\alpha(\phi,u)v_n|\nabla\phi|d\Omega, \tag{4-12}$$

$\alpha(\phi,u) \geq 0$. If $v_n = -\alpha(\phi,u) \leq 0$, $\frac{\partial J(u,\phi)}{\partial \tau} \geq 0$. However, to meet the volume constraint, the net change in volume must be zero, i.e. $\int_{\Gamma} v_n d\Gamma = 0$, where $d\Gamma$ is the local boundary area and $v_n d\Gamma$ yields change in local solid volume. Choosing $v_n = -(\alpha(\phi,u) + \lambda)$ yields [19]:

$$\begin{gathered} -\int_{\Gamma} (\alpha(\phi,u) + \lambda)\mathrm{d}\Gamma = 0, \\ \lambda = -\frac{\int_{\Gamma} \alpha(\phi,u)d\Gamma}{\int_{\Gamma} d\Gamma}, \end{gathered} \tag{4-13}$$

where λ is the Lagrange multiplier, or namely the velocity adjustment term. Substituting $\alpha(\phi,u) = -v_n - \lambda$ back into Eq. (4-12), the following equation is obtained:

$$\frac{\partial J(u,\phi)}{\partial \tau} = \frac{1}{V_{RVE}}\int_{\Omega} \delta(\phi)v_n^2|\nabla\phi|dV + \frac{\lambda}{V_{RVE}}\int_{\Omega} \delta(\phi)v_n|\nabla\phi|d\Omega. \tag{4-14}$$

If ϕ is a signed distance function, $|\nabla\phi| = 1$ everywhere, and $\int_{\Omega} \delta(\phi)v_n|\nabla\phi|d\Omega = 0$, the volume constraint is therefore satisfied. Also, $\int_{\Omega} \delta(\phi)v_n^2|\nabla\phi|dV$ is equal to or greater than zero, therefore $\frac{\partial J(u,\phi)}{\partial \tau} \geq 0$ is guaranteed.

4.2.1.2 Maximising effective permeability

The primary goal of this topology optimisation is to maximise the effective material properties, specifically the effective permeability. The effective permeability is the measure of ease of fluid to travel through a presumably homogeneous porous medium under a pressure. Permeability is therefore crucial in the nutrient transport in tissue scaffold. The objective function is thereby formulated as a permeability maximisation problem:

$$\text{Maximise: } J_K(w) = K^H = \int_{\Omega_{\text{void}}} \left(\frac{\partial w}{\partial x}\right)^T \boldsymbol{K}(\phi)\left(\frac{\partial w}{\partial x}\right) d\Omega \tag{4-15}$$

$$\text{Subject to: } \int_{\Omega_{\text{void}}} \mathrm{d}\Omega = \Omega_0 \tag{4-16}$$

where w is the characteristic fluid velocity, K^H is the effective permeability, $\boldsymbol{K}(\phi)$ is the nominal fluid viscosity, and Ω_0 is the void volume constraint. K^H in a matrix form has the same size as $\boldsymbol{K}(\phi)$. If isotropy of model is enforced, K^H can be expressed as a scalar value and used as the objective number. Otherwise, the objective number is obtained by summing up the diagonal values in the objective matrix. In Eq. (4-12), $\alpha = \frac{1}{3}\sum_{i=1}^{3}\left(\frac{\partial w}{\partial x}_{ii}\right)^T \boldsymbol{K}(\phi)\left(\frac{\partial w}{\partial x}_{ii}\right)$. The summation is done outside the integral.

The characteristic fluid velocity w is obtained by solving the homogenized Stokes equation:

$$\nabla^2 w - \nabla\pi = -\mathrm{I} \quad \forall x \in \Omega_1(x) \tag{4-17}$$

$$\nabla \cdot w = 0 \quad \forall x \in \Omega_1(x) \tag{4-18}$$

$$w = 0 \quad \text{on } \Gamma(x) \tag{4-19}$$

where π is the characteristic pressure field, and I is an identity tensor applied as a body force. For an n-D model, the equations need to be solved n times to build the full homogenisation matrix.

4.2.1.3 Maximising effective bulk modulus

The effective bulk modulus is indicative of the mechanical property of the tissue scaffold. The objective function can be expressed as:

$$\begin{gathered}\text{Maximise: } J_B(u) = B^H = \frac{1}{9}\sum_{i=1}^{3}\sum_{j=1}^{3}\boldsymbol{E}_{ij}^H \\ \boldsymbol{E}^H = \int_{\Omega_{\text{solid}}}\left(1-\frac{\partial u}{\partial x}\right)^T \boldsymbol{E}(\phi)\left(1-\frac{\partial u}{\partial x}\right)d\Omega\end{gathered} \tag{4-20}$$

$$\text{Subject to: } \int_{\Omega_{\text{solid}}} d\Omega = 1 - \Omega_0 \tag{4-21}$$

where u is the characteristic displacement, B^H is the effective bulk modulus, $\boldsymbol{E}^H$ is the effective stiffness, and $\boldsymbol{E}(\phi)$ is the nominal stiffness matrix of the scaffold material. In Eq.

(4-12), $\alpha = \frac{1}{9}\sum_{i=1}^{3}\sum_{j=1}^{3}\left(1-\frac{\partial u}{\partial x_{ij}}\right)^{T}\boldsymbol{E}(\phi)\left(1-\frac{\partial u}{\partial x_{ij}}\right)$. The summation is done outside the integral.

The characteristic displacement is obtained by solving the homogenisation stiffness response equation:

$$\frac{\partial}{\partial x}\boldsymbol{E}(\phi)\left(I-\frac{\partial u}{\partial x}\right)=0 \tag{4-22}$$

where I is the unit-strain field, which is computationally an identity tensor. In 3D space, Eq. (4-20) is solved three times in three normal directions to produce a partial effective stiffness matrix $\boldsymbol{E}^{H}$ (recreating the full matrix requires six sets of characteristic displacement solutions, three normal and three shear cases).

4.2.1.4 Maximising effective diffusivity

The effective diffusivity plays an important role in the nutrient transport in the tissue scaffolds. The objective function can be written as the following:

$$\begin{gathered}\text{Maximise: } J_D(q)=D^H=\frac{1}{3}\sum_{i=1}^{3}\boldsymbol{D}_{ii}^{H}\\ \boldsymbol{D}^H=\int_{\Omega_{\text{void}}}\left(1-\frac{\partial q}{\partial x}\right)^{T}\boldsymbol{D}(\phi)\left(1-\frac{\partial q}{\partial x}\right)d\Omega\end{gathered} \tag{4-23}$$

$$\text{Subject to: }\int_{\Omega_{\text{void}}}d\Omega=\Omega_0 \tag{4-24}$$

where q is the characteristic concentration filed, D^H is the scalar effective diffusivity, $\boldsymbol{D}^H$ is the effective stiffness in a matrix form, and $\boldsymbol{D}(\phi)$ is the local diffusivity matrix of the fluid. In Eq. (4-12), $\alpha = \frac{1}{3}\sum_{i=1}^{3}\left(1-\frac{\partial q}{\partial x_{ii}}\right)^{T}\boldsymbol{D}(\phi)\left(1-\frac{\partial q}{\partial x_{ii}}\right)$. The summation is done outside the integral.

The characteristic concentration filed is found by solving the homogenized thermal equation:

$$\frac{\partial}{\partial x}\boldsymbol{D}(\phi)\left(I-\frac{\partial q}{\partial x}\right)=0 \tag{4-25}$$

where I is the unit-gradient or the identity tensor. In 3D space, Eq. (4-23) is also solved three times to create the full effective diffusivity matrix $\boldsymbol{D}^H$, whose diagonal values are then summed to produce a scalar value.

4.2.1.5 Boundary conditions

The homogenisation equations are solved using the standard finite element method. A combination of periodicity and symmetry boundary condition is applied as shown in Figure 4-2. Under periodic boundary condition, the degree of freedom on one boundary of design domain (e.g. T_1) must be the same as the opposite boundary (i.e. T_2). Under symmetry boundary condition, the normal component of boundary flux or displacement at boundaries of design domain must be zero (e.g. v_y=0 and u_y=0 on y-plane).

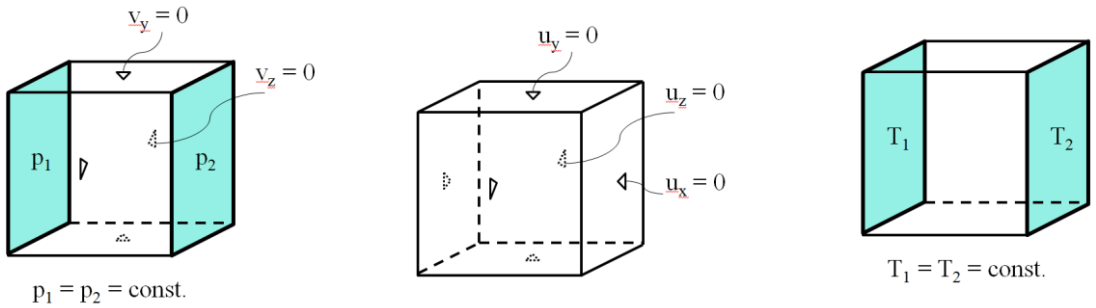

(a) Pressure, p, and velocity, v (b) Displacement, u (c) Temperature, T

Figure 4-2. Boundary conditions for the homogenisation of effective (a) permeability (x component), (b) bulk modulus and (c) conductivity (x component).

4.2.2 Isosurface modelling

4.2.2.1 Isosurface extraction

The generation of isosurface-based model involves three separate steps: (1) direct interpolation of isosurface vertices from the LSF, (2) isosurface triangulation and mesh smoothing, and (3) generation of finite elements. The position of isosurface vertices is found through interpolation of fixed-grid level set function (Figure 4-3a) to locate any points with

$\phi = 0$ (dark dots in Figure 4-3b, Eq. (4-2)). The points are then patched to form a triangulated surface (Figure 4-3c). Such operation is performed at each iteration step to explicitly track the motion of boundary. As the isosurfaces generated in such a direct manner often contains slender or highly skewed triangles that can affect the accuracy of finite element analysis, a mesh-smoothing operation is required to remove those low quality elements (Figure 4-3d).

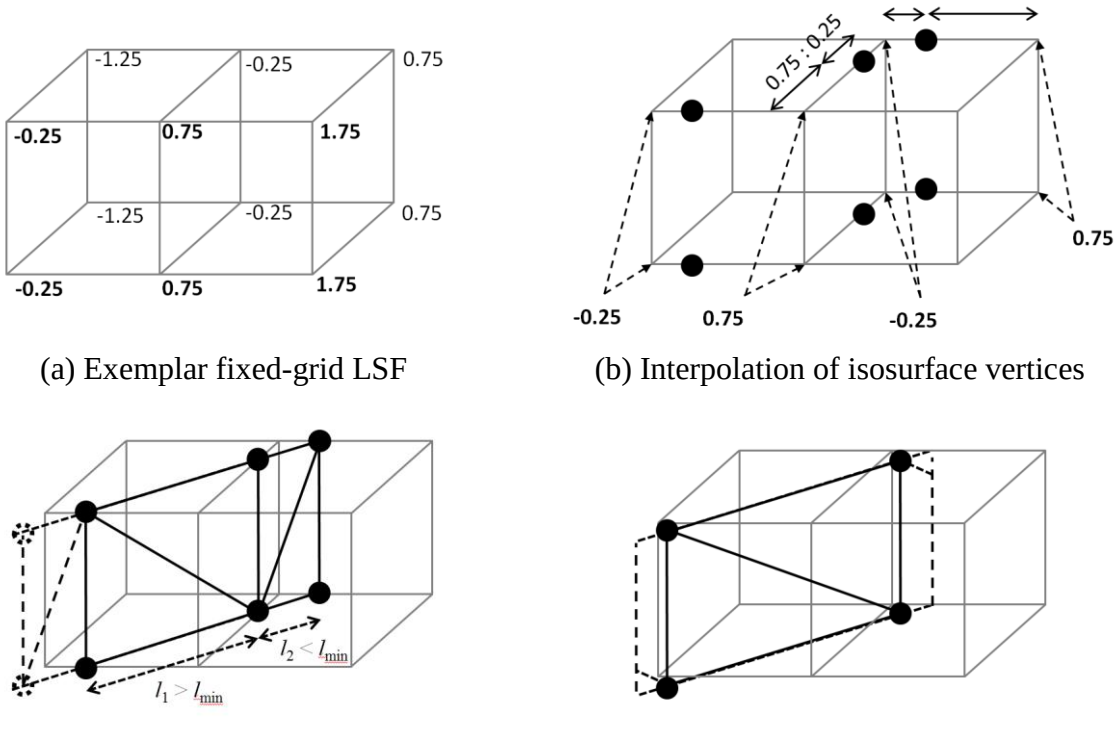

(a) Exemplar fixed-grid LSF (b) Interpolation of isosurface vertices

(c) Face patching with triangular faces (d) Face deletion

Figure 4-3. Schematic of the extraction process of an isosurface from a level set function.

An iterative mesh-smoothing algorithm is implemented to remove slender and small triangular faces from the isosurface model. This basically involves identifying and then deleting all elements that contains one or more edges whose length fall short of a given tolerance (Figure 4-3 c-d), as described in detail in Chapter 3.

This smoothed isosurface mesh is subsequently used as the foundation of tetrahedral mesh generation using *tetgen* [35-37] from the "iso2mech" Matlab toolbox [38] to produce

conforming meshes for both solid and void phases. Additional points may be added to the original isosurface mesh by the program to further improve mesh quality.

4.2.2.2 Sensitivity interpolation

After the FEA and homogenisation, the effective material properties and the sensitivity information stored in the unstructured FE model have to be passed on to the structured level-set optimisation system. In this part of study, this information relay occurred in two steps. Firstly, the nodal objective and sensitivity are interpolated from the elemental values and secondly, the sensitivity at the structured LS grid points is interpolated from the nodal values. An inverse distance weight method was employed to determine the nodal sensitivity, J_n,

$$J_n = \frac{\sum \frac{1}{d_e} J_e}{\sum \frac{1}{d_e}} \tag{4-26}$$

where the subscripts n and e denote nodal and elemental properties respectively, and d_e is the distance from each node to element centroid. The step basically weighs and averages the sensitivity values from all neighbouring nodes. Since only the surface sensitivity is of interest in the level set method, the interpolation is only performed at nodes that are within a certain distance to the isosurface. The second step relays the nodal values to the surrounding LSF grid also by means of weighted interpolation:

$$J_g = \frac{\sum \frac{1}{(d_n + 0.1h)^2} J_n}{\sum \frac{1}{(d_n + 0.1h)^2}} \tag{4-27}$$

where the subscript g denotes the LSF grid, and d_n is the distance between node and the LSF grid point. All nodal values within $3 \times h$ distance to the point are taken into account. Adding $0.1h$ (one tenth of the grid spacing) to the distance is to avoid zero division. It is worth noting that this two-step interpolation process can induce some degree of numerical diffusion so that

an additional numerical filtering is not required. Taking the squared weight in the second step reduces numerical diffusion.

The level set function is adjusted to maintain periodicity and isotropy at the boundaries of design domain. This is done by taking average of the level set function and the velocity function in the *x*-*x*, *y*-*y* and *z*-*z* directions (e.g. $\phi(x,y,z) = \phi(-x,y,z) = \frac{1}{2}[\phi(x,y,z) + \phi(-x,y,z)]$); swapping *x*-*y* axes ($\phi(x,y,z) = \phi(y,x,z) = \frac{1}{2}[\phi(x,y,z) + \phi(y,x,z)]$); and then rotating all three axes, i.e. $\phi(x,y,z) = \phi(y,z,x) = \frac{1}{2}[\phi(x,y,z) + \phi(y,z,x)]$. The second and the third operations work in conjunction to produce isotropy.

4.2.2.3 Topology optimisation in the discretised domain

Lagrange multiplier λ in Eq. (4-13) serves as a velocity adjustment term. Computationally, $\alpha(\phi,u)$ can be regarded as the relative velocity of the level set boundary, and λ as the velocity correction. When the integral of the velocity function, $-\alpha(\phi,u) + \lambda$, over the level set boundary (Γ) equals zero ($\Delta V = \int_\Gamma v_n dS = 0$), the volume constraint is satisfied. The value of the Lagrange multiplier can be explicitly estimated by calculating the average movement of the isosurface. This computation is done over the discretised isosurface model as follows:

$$\lambda = -\frac{\sum_{f=1}^{n} A_f \frac{\left(v_{f_1} + v_{f_2} + v_{f_3}\right)}{3}}{\sum_{f=1}^{n} A_f} \tag{4-28}$$

where subscript f denotes triangular face of the isosurface, A_f is the area of f^{th} triangle, and v_{f_1} , v_{f_2} and v_{f_3} are three nodal velocities at three vertices.

The gradient field of the LSF, namely $\nabla\phi$, is computed using the first order upwind scheme:

$$\nabla_{x+}\phi = \frac{\phi_{i+1,j,k} - \phi_{i,j,k}}{h}, \tag{4-29}$$

$$\nabla_{x-}\phi = \frac{\phi_{i,j,k} - \phi_{i-1,j,k}}{h}.$$

A total of six gradients in six orthogonal directions (x^+, y^-, x^+, y^-, z^+, z^-) are required to derive the local absolute gradient field, $|\nabla\phi|$:

$$\begin{aligned} |\nabla\phi|^+ = sqrt(&\max(\nabla_{x-}\phi, 0)^2 + \min(\nabla_{x+}\phi, 0)^2 + \\ &\max\left(\nabla_{y-}\phi, 0\right)^2 + \min\left(\nabla_{y+}\phi, 0\right)^2 + \\ &\max(\nabla_{z-}\phi, 0)^2 + \min(\nabla_{z+}\phi, 0)^2) \\ |\nabla\phi|^+ = sqrt(&\min(\nabla_{x-}\phi, 0)^2 + \max(\nabla_{x+}\phi, 0)^2 + \\ &\min\left(\nabla_{y-}\phi, 0\right)^2 + \max\left(\nabla_{y+}\phi, 0\right)^2 + \\ &\min(\nabla_{z-}\phi, 0)^2 + \max(\nabla_{z+}\phi, 0)^2) \end{aligned} \tag{4-30}$$

Using these two set of gradients, the LSF is updated as follows:

$$\phi^{k+1} = \phi^k - \partial\tau^k \left(\frac{\partial x^+}{\partial\tau}|\nabla\phi|^+ - \frac{\partial x^-}{\partial\tau}|\nabla\phi|^-\right). \tag{4-31}$$

where $\partial\tau^k$ is the time step and

$$\begin{cases} \dfrac{\partial x^+}{\partial\tau} = 0, \dfrac{\partial x^-}{\partial\tau} = v_n & \text{if } v_n > 0 \\ \dfrac{\partial x^+}{\partial\tau} = v_n, \dfrac{\partial x^-}{\partial\tau} = 0 & \text{if } v_n < 0 \end{cases}$$

To obtain a stable shape evolution, the maximal boundary motion ∂x should be less than one grid space per time step. The time step size is adjusted accordingly to maintain stability:

$$\partial\tau^k = \frac{h_0}{\max(\mathrm{abs}(v_n + \lambda))} \tag{4-32}$$

where $h_0 < h$; h is the length of LSF grid-space $\left(h = \frac{1}{\mathrm{size(LSF)}}\right)$.

Isosurface discretisation error can also affect the resultant solid and void volume. To correct this error, the solid and void volume are adjusted every iteration by moving the level set boundary uniformly toward one side or the other. Numerically, this can be achieved by adding a secondary volume correction term, θ, defined as:

$$\theta = \text{sign}(\Omega_0 - \int_S vdS) \times \min\left(\left|\frac{\Omega_0 - \int_S vdS}{\int_S dS}\right|, h_0\right) \tag{4-33}$$

where Ω_0 is the target volume fraction. The corrector θ has the same magnitude as the maximum allowable distance of movement (h_0) or the volume error divided by the isosurface area, whichever is smaller. The desirable movement of the level set function can then be expressed as

$$\partial x = \partial\tau(v + \lambda) + \theta. \tag{4-34}$$

The final change in LSF at the current time step can then be calculated from:

$$\partial\phi = -[\partial\tau(v + \lambda) + \theta]|\nabla\phi|. \tag{4-35}$$

4.2.2.4 Computation of full velocity function and re-initialisation

A simple flood-fill mechanism is introduced by this study to augment the isosurface-based topology optimisation. Following the interpolation process as described in Eq. (4-26)-(4-27), the velocity function is only non-zero in the vicinity of the level set boundary. Such narrow-band function will result in the deterioration of the smooth gradient field over the course of structural evolution. Therefore the rest of velocity function where the value is zero or missing is reconstructed using a rapid iterative filling technique as illustrated in Figure 4-4a.

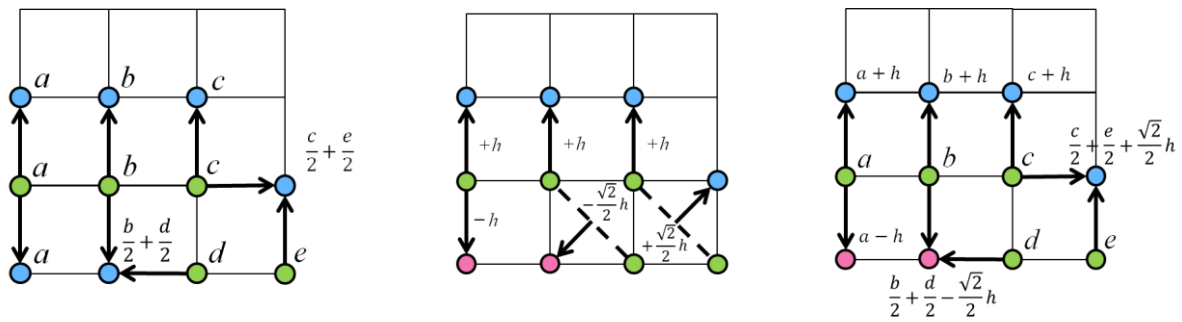

(a) Flood-fill the velocity function

(b) Approximate the SDF

(c) Flood-fill the SDF

Figure 4-4. Schematic of the flood-filling operation: (a) the velocity function (green dots represent filled points, blue dots represent points being filled in the current iteration); (b) the signed-distance function, SDF (green dots represent filled points, blue and red points

represent points being filled in the current iteration; blue points are closer to the solid phase and red points are closer to the void phase).

To maintain the smoothness of level set function and its gradient, a re-initialisation process is performed regularly to reconstruct the level set function as a signed-distance function (SDF). The signed distance function represents the shortest distance of any given point in design space from the level set boundary. In this study, the computation of SDF is carried out through both direct computation and indirect approximation, which is illustrated in Figure 4-4b-c:

1. In the direct computation, SDF is the shortest distance from a point to the isosurface model, where the location of the boundary is explicitly defined.
2. In the indirect approximation, SDF is the accumulative distance covered by the flood-filling operation. For example, if it takes the flood front three time-steps to reach a point, one unit-distance per time-step, then the point is three unit-distances away from the flood front.

4.2.2.5 Conventional level set method, BESO and SIMP

Topology optimisation methods that make use of fixed mesh, including (1) the level set method, (2) BESO, and (3) SIMP method with the MMA solver [39] can be run with the same design criteria to benchmark the performance of the proposed isosurface-based technique. The major difference is that in the BESO method, each element is cubic and is either solid ($x = 1$) or void ($x \approx 0$). SIMP method uses elements in intermediate states, i.e. partially solid and partially void ($0 \leq x \leq 1$), which however tend to converge toward either nearly-solid or nearly-void state through the topological evolution. In the level set method, most elements are either solid or void, except that the elements on material boundaries can be partially solid. The maximised effective material properties obtained from these methods are to be compared.

4.3 Computational implementation

The programming of topology optimisation can be broken down into a few critical components: modeller, FEA, sensitivity analysis and structural evolution. In a programming environment, each component is built as a function with own input and output. These functions are compiled in a looped sequence and executed in an iterative manner. The programming workflow is illustrated in Figure 4-5.

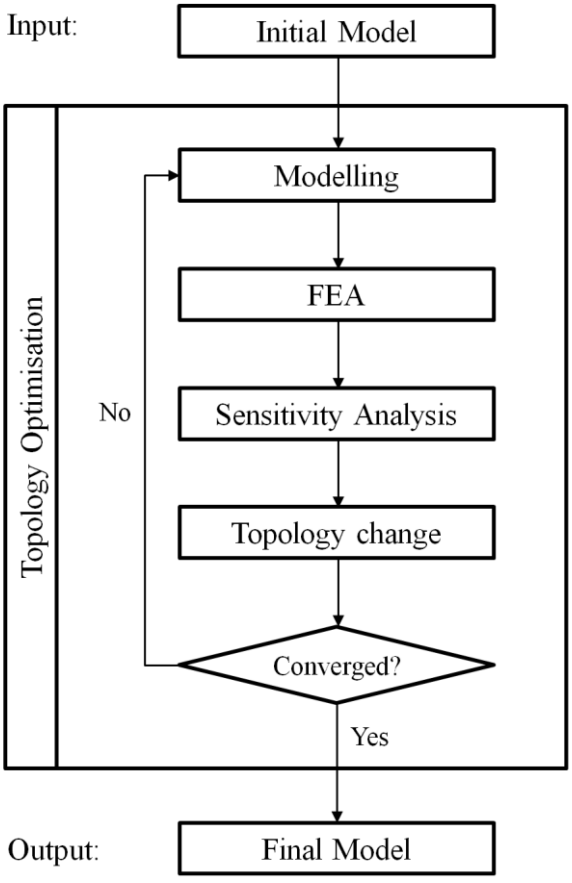

Figure 4-5. Topology optimisation framework. The primary inputs are the initial model and parameters required for initialising individual functions.

Initial model. This optimisation program begins by defining a range of modelling and optimisation parameters and initialising variables. Key parameters and variables are listed in Table 4-1.

Table 4-1. Primary parameters

Optimisation parameters:	Modelling parameters:	
Number of iterations	Model dimensions	Level set constant
Volume constraint	Model resolution	Initial model (user defined)
LSF re-initialisation (yes/no)	FE mesh size	Orthotropic / isotropic
Time step size	RVE (yes/no)	Symmetric model (yes/no)
Step size scaling	Solid B.C.s	Solid material properties
Weights of objectives	Fluid B.C.s	Fluid material properties

Modelling. The first set of functions in topology optimisation is the *modelling* functions that translate a LSF to a FE model. An initial arbitrary LSF is firstly generated in a fixed modelling domain. The model is known as the representative volume element (RVE). This LSF is then used as an input variable to create an isosurface model. If symmetry and isotropy (Figure 4-6) is assumed, only one eighth of the RVE model is required as an input. Like all optimisation models, this initial model must meet the volume constraint. Therefore as soon as the initial isosurface model is created, the volume is examined. If the volume constraint is not satisfied, the LSF is adjusted and a new FE model is regenerated. Volume adjustment is repeated until all volume constraints are satisfied, by then finite element analysis is ready to be performed to determine the performance of the current design.

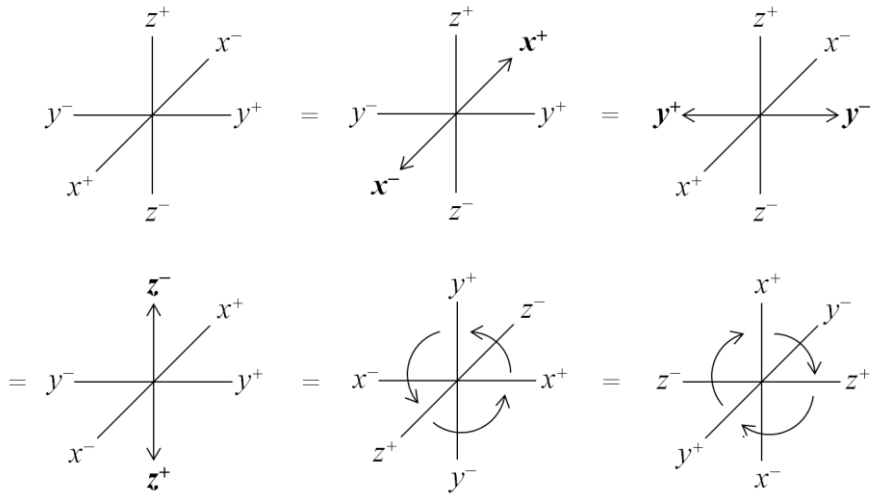

Figure 4-6. Conditions of symmetry and isotropy.

FEA. The material properties of design model is assessed and characterised based on the theory of homogenisation. These material properties can be quantified according to the objective function to produce an objective number, which is an indicator of optimality of the model in this topology optimisation process. In a multiobjective design scenario, multiple objective numbers are gathered through separate FEA simulations (e.g. static elastic, thermal, and fluid flow analyses), then each objective is weighted and summed to yield a meta (upper level) objective number. In the meantime, the sensitivity is calculated to predict the change in the object number in response to changing element density (x).

Topological change. The structural evolution involved two operations: topology update and re-initialisation of LSF. As part of the level set optimisation routine, some Lagrange multiplier and adjustment parameters are computed to determine how much the topology is altered per iteration. Once the model is updated, a re-initialisation function is executed to smooth the LSF. The execution is on-demand only, depending on the degree of LSF deterioration. This initialisation function regenerates a LSF with a smooth gradient field but keeps approximately the same level set boundary.

All essential programming syntax is presented in this section in equation form, with vectors and matrices as variables. Some examples of data manipulation are also provided and written in the programming language of Matlab. Additional instructions are given to demonstrate how mathematical equations can be translated to syntax.

4.3.1 Finite element analysis

The finite element analysis (FEA) functions can be carried out by some third party applications such as ANSYS outside the main program. In this case, modelling and simulation information is passed on to the third party applications, where finite element models are solved. A typical FEA process involves modelling, defining the boundary

conditions, solving, and some postprocessing to derive additional information from the degree-of-freedom results as illustrated in the flow chart, Figure 4-7.

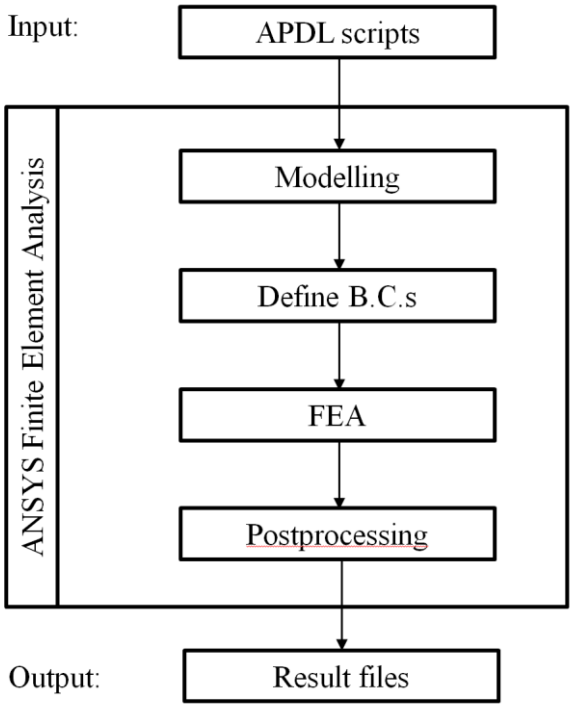

Figure 4-7. Process of finite element analysis using ANSYS as a solver.

To automate this FEA solution process using ANSYS as a solver, ANSYS Parametric Design Language (APDL) scripts are required. The script file contains commands to instruct the program what to do. In addition to this file, modelling information such as node and element lists are also written to file and exported to ANSYS.

The creation of APDL script files is automated to allow streamlined computational process. In principle, these script-generating functions read the modelling conditions in forms of input variables and write all essential commands to conduct FEA in ANSYS. The complete script (command) file is an executable file that calls the target program, guides every aspect of the FEA solution process, and quits the program with some readable result files. Once the program is called, node and element files created earlier (see flow chart in Figure 3-5) are firstly loaded, then boundary conditions are defined, followed by the FE solution process, and

finally the exportation of data (Figure 4-8). Unlike other functions, output variables such as degree of freedom are not directly available to the main program. The results obtained from the third-party finite element solver have to be retrieved using separated commands after the successful execution of these functions.

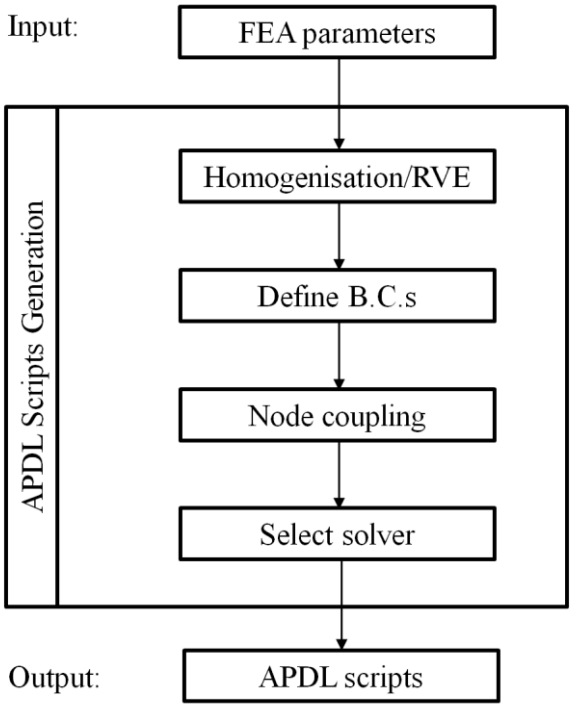

Figure 4-8. Generation of APDL scripts file. This file is used as the input of the FEA program shown in Figure 4-7.

The APDL script generating functions take various inputs, including the loads, boundary conditions (BCs) and material properties. Whether the node-element information should be loaded or not depends on the nature of the simulation and the BCs. In case the periodic boundary is used, the position of nodes in the Cartesian coordinate system has to be loaded in order to determine periodic nodal pairs; otherwise, the modelling information is normally not required here to produce APDL scripts. The homogenisation BCs is often imposed on the nodes on the boundaries of modelling domain. If the BCs are non-linear, they can be written in function or tabular form. Imposing a functional or tabular load/force requires a more organised input format that can be easily translated to a readable format for the solver

program to understand. The final output of this generator includes one APDL command file, one element file, one node file, up to six homogenisation force files, up to seven node-coupling files, and one material label file.

4.3.1.1 Homogenisation and force

A dedicated function is programmed to create the nodal force required to run homogenisation analysis. This function requires the node and element information of the FE model, and material properties of the all elements or all material phases in the modelling space. The output is the nodal force vectors, which are written to files and to be read by ANSYS. The number of force vectors created depends on the simulation condition. Normally 6 vectors are required for stiffness homogenisation (x-x, y-y, z-z, x-y, y-z and z-x) and 3 vectors for conductivity or permeability homogenisation (x-x, y-y and z-z). If only the normal stress-strain response or the bulk modulus of the solid material is required, only 3 vectors are computed (x-x, y-y and z-z). If the RVE model is structurally isotropic, only 1 vector is necessary to determine the scalar value of conductivity or permeability (x-x or y-y or z-z). Diffusivity shares the same governing equations with thermal conductivity problem, therefore the same script generator can be used. Throughout this study, both terms diffusivity and conductivity are used interchangeably.

In this program, each mathematical or programming variable is written in a matrix form. The homogenisation force vector field, F from the governing equation $K\boldsymbol{u} = F$, is defined mathematically as:

$$F = \int \frac{\partial}{\partial x_i} E_{ij} I_{\varepsilon_j} dV$$

where $\frac{\partial}{\partial x_i}$ is the partial differentiation matrix, E_{ij} is the material property matrix, I_{ε_j} is the unit strain, i and j are directional indices (1 for x, 2 for y and 3 for z), and dV is the elemental volume. In a structural problem, E_{ij} is the stiffness matrix defined by Hooke's law:

$$E = \frac{E_0}{(1+v)(1-2v)}\begin{bmatrix} 1-v & v & v & \ddots & & \\ v & 1-v & v & & 0 & \\ v & v & 1-v & & & \ddots \\ & & & \frac{1-2v}{2} & 0 & 0 \\ & \ddots & & & \frac{1-2v}{2} & \\ & 0 & & 0 & & 0 \\ & & \ddots & & & \\ & & & 0 & 0 & \frac{1-2v}{2} \end{bmatrix}$$

where E_0 is the Young's modulus, and v is the Poisson's ratio. In a thermal or conductivity problem, E_{ij} is the conductivity matrix:

$$E = D_0\begin{bmatrix} 1 & 0 & 0 \\ 0 & 1 & 0 \\ 0 & 0 & 1 \end{bmatrix}$$

where D_0 is the conductivity coefficient, assuming the material is isotropic. Each unique material has its own stiffness matrix.

The partial differentiation matrix has a size of 12-by-3 or 12-by-6, depending on the size of E_{ij}. The number 12 comes from the number of degrees of freedom (3) times the number of nodes per tetrahedral element (4). The unit strain is an identity matrix and has the same size as the stiffness (6-by-6) or conductivity matrix (3-by-3).

4.3.1.1.1 Structural hexahedral element

A complete FEA programming instruction is provided in this section, specifically to explain how homogenisation is performed. The following sections demonstrate how the homogenisation force vectors are assembled in a programming environment and how effective material properties are computed. Some fundamental FEA information is also provided here so that the functional output can be easily reproduced by any potential learners if they follow the instructions.

Firstly, the differentiation matrix, $\frac{\partial}{\partial x_i}$, from $\int \frac{\partial}{\partial x_i} E_{ij} I_{\varepsilon_j} dV$ is computed on the elemental level in the natural coordinate system S_1-S_2-S_3. Note that the notation x_i represents the Cartesian coordinate system, where $x_1 = x$, $x_2 = y$ and $x_3 = z$. $\frac{\partial}{\partial x_i}$ is calculated from the chain rule:

$$\frac{\partial}{\partial x_i} = \sum_{k=1}^{8} \frac{\partial \mathcal{N}_k}{\partial S_l} \frac{\partial S_l}{\partial x_i}.$$

While $\frac{\partial \mathcal{N}_k}{\partial S_l}$ can be calculated directly, the $\frac{\partial S_l}{\partial x_i}$ derivative has to be derived from the equation, $\frac{\partial}{\partial S_l} = \sum_{i=1}^{3} \frac{\partial x_i}{\partial S_l} \times \frac{\partial}{\partial x_i}$:

$$\begin{bmatrix} \frac{\partial}{\partial S_1} \\ \frac{\partial}{\partial S_2} \\ \frac{\partial}{\partial S_3} \end{bmatrix} = \begin{bmatrix} \frac{\partial x}{\partial S_1} & \frac{\partial y}{\partial S_1} & \frac{\partial z}{\partial S_1} \\ \frac{\partial x}{\partial S_2} & \frac{\partial y}{\partial S_2} & \frac{\partial z}{\partial S_2} \\ \frac{\partial x}{\partial S_3} & \frac{\partial y}{\partial S_3} & \frac{\partial z}{\partial S_3} \end{bmatrix} \begin{bmatrix} \frac{\partial}{\partial x} \\ \frac{\partial}{\partial y} \\ \frac{\partial}{\partial z} \end{bmatrix}.$$

The 3-by-3 matrix of $\left[\frac{\partial x_i}{\partial S_l}\right]$ here is known as the Jacobian matrix, $[J]$. Individual entries of the Jacobian matrix can be calculated directly. By multiplying both sides of the equation by the inverse of the Jacobian matrix, $[J]^{-1}$, $\frac{\partial}{\partial x_i}$ is found:

$$\begin{bmatrix} \frac{\partial}{\partial x} \\ \frac{\partial}{\partial y} \\ \frac{\partial}{\partial z} \end{bmatrix} = \begin{bmatrix} \frac{\partial x}{\partial S_1} & \frac{\partial y}{\partial S_1} & \frac{\partial z}{\partial S_1} \\ \frac{\partial x}{\partial S_2} & \frac{\partial y}{\partial S_2} & \frac{\partial z}{\partial S_2} \\ \frac{\partial x}{\partial S_3} & \frac{\partial y}{\partial S_3} & \frac{\partial z}{\partial S_3} \end{bmatrix}^{-1} \begin{bmatrix} \frac{\partial}{\partial S_1} \\ \frac{\partial}{\partial S_2} \\ \frac{\partial}{\partial S_3} \end{bmatrix}.$$

To compute $\frac{\partial \mathcal{N}_k}{\partial S_l}$ (the first component of chain rule equation) in a matrix form, the shape functions of an 8-node hexahedral element are firstly defined as illustrated in the following figure (Figure 4-9):

$$\mathcal{N}_1 = (1-S_1)(1-S_2)(1-S_3)$$
$$\mathcal{N}_2 = (1+S_1)(1-S_2)(1-S_3)$$
$$\mathcal{N}_3 = (1+S_1)(1+S_2)(1-S_3)$$
$$\mathcal{N}_4 = (1-S_1)(1+S_2)(1-S_3)$$
$$\mathcal{N}_5 = (1-S_1)(1-S_2)(1+S_3)$$
$$\mathcal{N}_6 = (1+S_1)(1-S_2)(1+S_3)$$
$$\mathcal{N}_7 = (1+S_1)(1+S_2)(1+S_3)$$
$$\mathcal{N}_8 = (1-S_1)(1+S_2)(1+S_3)$$

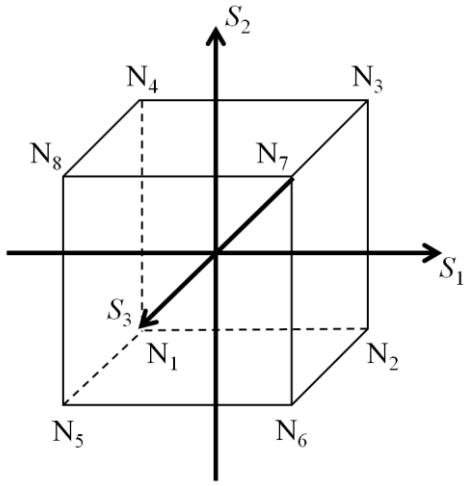

Figure 4-9. Shape functions, $\mathcal{N}$, in a Natural coordinate system.

where $\mathcal{N}_1 - \mathcal{N}_8$ are eight shape functions in a natural coordinate system, and $S_1 - S_3$ are three natural coordinates. The numbering of nodes obeys the right-hand rule, i.e. N_1-N_2-N_3-N_4 points toward N_5-N_6-N_7-N_8. The partial derivatives of these shape functions, $\frac{\partial \mathcal{N}}{\partial S}$, with respect to each natural coordinate can be written in a table:

	dNk/dS1								dNk/dS2								dNk/dS3								
	N1	N2	N3	N4	N5	N6	N7	N8	N1	N2	N3	N4	N5	N6	N7	N8	N1	N2	N3	N4	N5	N6	N7	N8	
[1]	-1	1	1	-1	-1	1	1	-1	-1	-1	1	1	-1	-1	1	1	-1	-1	-1	-1	1	1	1	1	
[S1]	0	0	0	0	0	0	0	0	1	-1	1	-1	1	-1	1	-1	1	-1	-1	1	-1	1	1	-1	
[S2]	1	-1	1	-1	1	-1	1	-1	0	0	0	0	0	0	0	0	1	1	-1	-1	-1	-1	1	1	
[S3]	1	-1	-1	1	-1	1	1	-1	1	1	-1	-1	-1	-1	1	1	0	0	0	0	0	0	0	0	/8
[S1S2]	0	0	0	0	0	0	0	0	0	0	0	0	0	0	0	0	-1	1	-1	1	1	-1	1	-1	
[S1S3]	0	0	0	0	0	0	0	0	-1	1	-1	1	1	-1	1	-1	0	0	0	0	0	0	0	0	
[S2S3]	-1	1	-1	1	1	-1	1	-1	0	0	0	0	0	0	0	0	0	0	0	0	0	0	0	0	

where the 1st column represents $\frac{\partial \mathcal{N}_1}{\partial S_1} = -1 + S_2 + S_3 - S_2S_3$, the 2nd column is $\frac{\partial \mathcal{N}_2}{\partial S_1} = 1 - S_2 - S_3 + S_2S_3$, the 9th column is $\frac{\partial \mathcal{N}_1}{\partial S_2}$, the 10th column is $\frac{\partial \mathcal{N}_2}{\partial S_2}$, and so on. The 1st row is the coefficient of term "1", the 2nd row is the coefficient of term "S_1", and so on. For example, the first column says

$$\frac{\partial \mathcal{N}_1}{\partial S_1} = -1(1) + 0(S_1) + 1(S_2) + 1(S_3) + 0(S_1S_2) + 0(S_1S_3) - 1(S_2S_3).$$

An elemental matrix $\left[\frac{\partial \mathcal{N}_k}{\partial S_l}\right]_E$ can then be created as shown below in terms of S_1, S_2 and S_3, where (k,l) denotes $\frac{\partial \mathcal{N}_k}{\partial S_l}$:

```
(1,1) 0 0 (2,1) 0 0 (3,1) 0 0 (4,1) 0 0 (5,1) 0 0 (6,1) 0 0 (7,1) 0 0 (8,1) 0 0
0 (1,2) 0 0 (2,2) 0 0 (3,2) 0 0 (4,2) 0 0 (5,2) 0 0 (6,2) 0 0 (7,2) 0 0 (8,2) 0
0 0 (1,3) 0 0 (2,3) 0 0 (3,3) 0 0 (4,3) 0 0 (5,3) 0 0 (6,3) 0 0 (7,3) 0 0 (8,3)
(1,1) 0 0 (2,1) 0 0 (3,1) 0 0 (4,1) 0 0 (5,1) 0 0 (6,1) 0 0 (7,1) 0 0 (8,1) 0 0
0 (1,2) 0 0 (2,2) 0 0 (3,2) 0 0 (4,2) 0 0 (5,2) 0 0 (6,2) 0 0 (7,2) 0 0 (8,2) 0
0 0 (1,3) 0 0 (2,3) 0 0 (3,3) 0 0 (4,3) 0 0 (5,3) 0 0 (6,3) 0 0 (7,3) 0 0 (8,3)
(1,1) 0 0 (2,1) 0 0 (3,1) 0 0 (4,1) 0 0 (5,1) 0 0 (6,1) 0 0 (7,1) 0 0 (8,1) 0 0
0 (1,2) 0 0 (2,2) 0 0 (3,2) 0 0 (4,2) 0 0 (5,2) 0 0 (6,2) 0 0 (7,2) 0 0 (8,2) 0
0 0 (1,3) 0 0 (2,3) 0 0 (3,3) 0 0 (4,3) 0 0 (5,3) 0 0 (6,3) 0 0 (7,3) 0 0 (8,3)
```

It is obvious that multiplying $\left[\frac{\partial \mathcal{N}_k}{\partial S_l}\right]_E$ by the elemental displacement $[\boldsymbol{u}]_E$ = $[u_{x,1}\ u_{y,1}\ u_{z,1}\ u_{x,2}\ u_{y,2}\ u_{z,2}\ \ldots\ u_{z,8}]^{\mathrm{T}}$ produces the elemental strain $\left[\frac{\partial \boldsymbol{u}}{\partial S_l}\right]_E$ = $[\frac{\partial u_x}{\partial S_1}\ \frac{\partial u_y}{\partial S_1}\ \frac{\partial u_z}{\partial S_1}\ \frac{\partial u_x}{\partial S_2}\ \frac{\partial u_y}{\partial S_2}\ \frac{\partial u_z}{\partial S_2}\ \frac{\partial u_x}{\partial S_3}\ \frac{\partial u_y}{\partial S_3}\ \frac{\partial u_z}{\partial S_3}]^{\mathrm{T}}$. T denotes transpose matrix.

The Jacobian matrix, as part of the chain rule, is computed from

$$J_{l,i} = \frac{\partial \mathrm{x}_i}{\partial \mathrm{S}_\mathrm{l}} = \sum_{k=1}^{8} \frac{\partial \mathcal{N}_k}{\partial S_l} x_{i,k}$$

for i = [1, 2, 3] and l = [1, 2, 3]. The summation is over 8 hexahedral nodes. This 3-by-3 matrix is inversed to create the inverse Jacobian matrix:

$$J^{-1} = \frac{\partial S_l}{\partial x_i} = \begin{bmatrix} J_{1,1}^{-1} & J_{1,2}^{-1} & J_{1,3}^{-1} \\ J_{2,1}^{-1} & J_{2,2}^{-1} & J_{2,3}^{-1} \\ J_{3,1}^{-1} & J_{3,2}^{-1} & J_{3,3}^{-1} \end{bmatrix}.$$

Also, the determinant of the Jacobian matrix is the volume of the element, i.e.:

$$|J| = dV.$$

To find six strain components, the inverse Jacobian matrix is rearranged and $\left[\frac{\partial S_l}{\partial x_i}\right]_E$ is defined as:

$$\begin{bmatrix} J_{1,1}^{-1} & J_{1,2}^{-1} & J_{1,3}^{-1} & 0 & 0 & 0 & 0 & 0 & 0 \\ 0 & 0 & 0 & J_{2,1}^{-1} & J_{2,2}^{-1} & J_{2,3}^{-1} & 0 & 0 & 0 \\ 0 & 0 & 0 & 0 & 0 & 0 & J_{3,1}^{-1} & J_{3,2}^{-1} & J_{3,3}^{-1} \\ 0 & 0 & 0 & J_{2,1}^{-1} & J_{2,2}^{-1} & J_{2,3}^{-1} & J_{1,1}^{-1} & J_{1,2}^{-1} & J_{1,3}^{-1} \\ J_{2,1}^{-1} & J_{2,2}^{-1} & J_{2,3}^{-1} & 0 & 0 & 0 & J_{3,1}^{-1} & J_{3,2}^{-1} & J_{3,3}^{-1} \\ J_{1,1}^{-1} & J_{1,2}^{-1} & J_{1,3}^{-1} & J_{3,1}^{-1} & J_{3,2}^{-1} & J_{3,3}^{-1} & 0 & 0 & 0 \end{bmatrix}$$

so that

$$\left[\frac{\partial S_l}{\partial x_i}\right]_E \times \left[\frac{\partial \mathcal{N}_k}{\partial S_l}\right]_E = \left[\frac{\partial}{\partial x_i}\right]_E$$

[6×9] × [9×24] = [6×24].

The order of row 4, 5 and 6 has to match the stiffness matrix E_{ij} in the function. Note that any matrix operation of $\left[\frac{\partial \mathcal{N}_k}{\partial S_l}\right]_E$ will invoke the summation of shape functions, $\mathcal{N}_k$, for k = 1 to 8 due to the way it is defined. Therefore there is no shape function $\mathcal{N}_k$ on the right hand side of the equation. It is apparent now that the strain matrix can be calculated in this form:

$$\left[\frac{\partial S_l}{\partial x_i}\right]_E \times \left[\frac{\partial \mathcal{N}_k}{\partial S_l}\right]_E \times [\boldsymbol{u}]_E = \left[\frac{\partial \boldsymbol{u}}{\partial x_i}\right]_E$$

[6×9] × [9×24] × [24×1] = [6×1],

where $\left[\frac{\partial \boldsymbol{u}}{\partial x_i}\right]_E = \left[\frac{\partial u}{\partial x} \;\; \frac{\partial v}{\partial y} \;\; \frac{\partial w}{\partial z} \;\; \left(\frac{\partial v}{\partial z} + \frac{\partial w}{\partial y}\right) \;\; \left(\frac{\partial u}{\partial z} + \frac{\partial w}{\partial x}\right) \;\; \left(\frac{\partial u}{\partial y} + \frac{\partial v}{\partial x}\right)\right]$, in which u, v and w are three displacement components.

The finite element integration involves summing values at eight Gaussian points (denoted by G for Gaussian). Substituting S values into the equations above yields a matrix at a Gaussian point (see table below). The substitution of S has to be performed 8 times for eight Gaussian points, and summed to create the elemental matrix (E). For example:

$$\left[\frac{\partial \mathcal{N}_k}{\partial S_l}\right]_E = \sum_{G=1}^{8} \left[\frac{\partial \mathcal{N}_k}{\partial S_l}\right]_G$$

$$\left[\frac{\partial S_l}{\partial x_i}\right]_E \times \left[\frac{\partial \mathcal{N}_k}{\partial S_l}\right]_E = \sum_{G=1}^{8} \left(\left[\frac{\partial S_l}{\partial x_i}\right]_G \times \left[\frac{\partial \mathcal{N}_k}{\partial S_l}\right]_G\right)$$

Table 4-2. Location of eight Gaussian points in a hexahedral elements.

(G)	S_1	S_2	S_3
1^{st}	$-\frac{1}{\sqrt{3}}$	$-\frac{1}{\sqrt{3}}$	$-\frac{1}{\sqrt{3}}$
2^{nd}	$\frac{1}{\sqrt{3}}$	$-\frac{1}{\sqrt{3}}$	$-\frac{1}{\sqrt{3}}$
3^{rd}	$\frac{1}{\sqrt{3}}$	$\frac{1}{\sqrt{3}}$	$-\frac{1}{\sqrt{3}}$
4^{th}	$-\frac{1}{\sqrt{3}}$	$\frac{1}{\sqrt{3}}$	$-\frac{1}{\sqrt{3}}$
5^{th}	$-\frac{1}{\sqrt{3}}$	$-\frac{1}{\sqrt{3}}$	$\frac{1}{\sqrt{3}}$
6^{th}	$\frac{1}{\sqrt{3}}$	$-\frac{1}{\sqrt{3}}$	$\frac{1}{\sqrt{3}}$
7^{th}	$\frac{1}{\sqrt{3}}$	$\frac{1}{\sqrt{3}}$	$\frac{1}{\sqrt{3}}$
8^{th}	$-\frac{1}{\sqrt{3}}$	$\frac{1}{\sqrt{3}}$	$\frac{1}{\sqrt{3}}$

Here, the difference between $\left[\frac{\partial \mathcal{N}_k}{\partial S_l}\right]_G$ and $\left[\frac{\partial \mathcal{N}_k}{\partial S_l}\right]_E$ is that $\left[\frac{\partial \mathcal{N}_k}{\partial S_l}\right]_G$ contains $S_{1,2,3}$ in symbolic terms, while $\left[\frac{\partial \mathcal{N}_k}{\partial S_l}\right]_E$ contains only numbers and no symbol. $\left[\frac{\partial S_l}{\partial x_i}\right]_G$ and $\left[\frac{\partial S_l}{\partial x_i}\right]_E$ go with the same notation. This substitution of $S_{1,2,3}$ is done before any matrix multiplication.

Following this, the elemental force vector can be computed through matrix operation:

$$F_E = \int \frac{\partial}{\partial x_i} E_{ij} I_{\varepsilon_j} dV = \sum_{G=1}^{8} \left(\left[\frac{\partial \mathcal{N}_k}{\partial S_l}\right]_G^T \times \left[\frac{\partial S_l}{\partial x_i}\right]_G^T \times E_{ij} \times I_{\varepsilon_j} \times |J| \right).$$

The summation on the right hand side is over eight Gaussian points. Similarly, the elemental stiffness matrix K is a 24-by-24 matrix, computed from the matrix operation:

$$K = \sum_{G=1}^{8} \left(\left[\frac{\partial \mathcal{N}_k}{\partial S_l}\right]_G^T \times \left[\frac{\partial S_l}{\partial x_i}\right]_G^T \times E_{ij} \times \left[\frac{\partial S_l}{\partial x_i}\right]_G \times \left[\frac{\partial \mathcal{N}_k}{\partial S_l}\right]_G \times |J| \right).$$

4.3.1.1.2 Structural tetrahedral element

The matrix operation can be largely simplified if tetrahedral elements are used. In a 4-node tetrahedral element, the shape function is defined as the tetrahedral volume ratio as shown in the figure below (Figure 4-10).

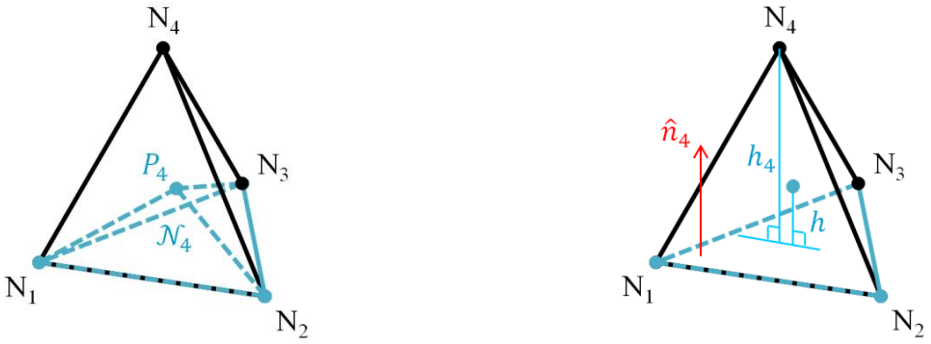

Figure 4-10. Shape functions, $\mathcal{N}$, in a tetrahedral Natural coordinate system.

A shape function is defined as the volume ratio:

$$\begin{aligned}\mathcal{N}_4 &= \frac{V_{\mathrm{N_1N_2N_3P_4}}}{V_{\mathrm{N_1N_2N_3N_4}}} \\ &= \frac{h \cdot A_{\mathrm{N_1N_2N_3}}/3}{V_{\mathrm{N_1N_2N_3N_4}}} \\ &= \frac{(P_4 - N_k) \cdot \hat{n}_4 \cdot A_{\mathrm{N_1N_2N_3}}/3}{V_{\mathrm{N_1N_2N_3N_4}}}\end{aligned}$$

where V is the volume, P_4 represents the coordinates of an arbitrary point in the tetrahedral element, N_k represents the coordinates of the point $\mathrm{N_k}$ (k can be 1, 2 or 3 but not 4 in this example), and $A_{\mathrm{N_1N_2N_3}}$ denotes the area of triangle $\mathrm{N_1}$-$\mathrm{N_2}$-$\mathrm{N_3}$. The dot product, $(P_4 - N_k) \cdot \hat{n}_4 = h$, yields the height of the small tetrahedron $\mathrm{N_1}$-$\mathrm{N_2}$-$\mathrm{N_3}$-$\mathrm{P_4}$. Let $\mathrm{P_4} = \boldsymbol{x}_i = [x\ y\ z]$,

$$\frac{\partial \mathcal{N}_4}{\partial \boldsymbol{x}_i} = \frac{1 \cdot \hat{n}_4 \cdot A_{\mathrm{N_1N_2N_3}}/3}{V_{\mathrm{N_1N_2N_3N_4}}}$$

that is true for i = 1, 2 and 3. As the volume of the element is a constant, i.e. $dV = V_{\mathrm{N_1N_2N_3N_4}}$,

$$\left(\sum_{k=1}^{4} \frac{\partial \mathcal{N}_k}{\partial x_i}\right) dV = \sum_{k=1}^{4} \left(\frac{\partial \mathcal{N}_k}{\partial x_i} dV\right)$$

$$= \sum_{k=1}^{4} \left(\frac{\hat{n}_4 \cdot A_k/3}{dV} \times dV \right)$$

$$= \sum_{k=1}^{4} (\hat{n}_4 \cdot A_k/3)$$

As the area $A_k = \frac{1}{2} \left| \overrightarrow{\mathrm{N}_{\sim \mathrm{k},1}\mathrm{N}_{\sim \mathrm{k},2}} \times \overrightarrow{\mathrm{N}_{\sim \mathrm{k},2}\mathrm{N}_{\sim \mathrm{k},3}} \right|$, where $\sim k,l$ denotes 3 nodes constituting the triangle, which excludes the k^{th} node, the following equation is obtained:

$$\left(\sum_{k=1}^{4} \frac{\partial \mathcal{N}_k}{\partial x_i} \right) dV = \sum_{k=1}^{4} \left(\hat{n}_k \cdot \left| \overrightarrow{\mathrm{N}_{\sim \mathrm{k},1}\mathrm{N}_{\sim \mathrm{k},2}} \times \overrightarrow{\mathrm{N}_{\sim \mathrm{k},2}\mathrm{N}_{\sim \mathrm{k},3}} \right| /6 \right)$$

$$= \sum_{k=1}^{4} \left(\overrightarrow{\mathrm{N}_{\sim \mathrm{k},1}\mathrm{N}_{\sim \mathrm{k},2}} \times \overrightarrow{\mathrm{N}_{\sim \mathrm{k},2}\mathrm{N}_{\sim \mathrm{k},3}} /6 \right)$$

Since this result contains neither the natural coordinates nor the Cartesian coordinates, in other words the strain is non-variable, the derivative $\sum_{k=1}^{4} \frac{\partial \mathcal{N}_k}{\partial x_i}$ can be computed directly without using the chain rule and Gaussian integration. Therefore, the $\frac{\partial}{\partial x}$ matrix of a tetrahedral element (N_1-N_2-N_3-N_4) is:

$$\begin{bmatrix} \frac{\partial}{\partial x_1} & \frac{\partial}{\partial y_1} & \frac{\partial}{\partial z_1} \\ \frac{\partial}{\partial x_2} & \frac{\partial}{\partial y_2} & \frac{\partial}{\partial z_2} \\ \frac{\partial}{\partial x_3} & \frac{\partial}{\partial y_3} & \frac{\partial}{\partial z_3} \\ \frac{\partial}{\partial x_4} & \frac{\partial}{\partial y_4} & \frac{\partial}{\partial z_4} \end{bmatrix} = \frac{1}{6} \times \begin{bmatrix} \overrightarrow{\mathrm{N}_2\mathrm{N}_4} \times \overrightarrow{\mathrm{N}_4\mathrm{N}_3} \\ \overrightarrow{\mathrm{N}_1\mathrm{N}_3} \times \overrightarrow{\mathrm{N}_3\mathrm{N}_4} \\ \overrightarrow{\mathrm{N}_1\mathrm{N}_4} \times \overrightarrow{\mathrm{N}_4\mathrm{N}_2} \\ \overrightarrow{\mathrm{N}_1\mathrm{N}_2} \times \overrightarrow{\mathrm{N}_2\mathrm{N}_3} \end{bmatrix}$$

where the right-hand side is four cross products. The 6-by-12 elemental matrix $\left[\frac{\partial \mathcal{N}_k}{\partial \mathrm{x_i}} \right]_E$ is defined as:

$$\begin{matrix}
\frac{\partial}{\partial x_1} & 0 & 0 & \frac{\partial}{\partial x_2} & 0 & 0 & \frac{\partial}{\partial x_3} & 0 & 0 & \frac{\partial}{\partial x_4} & 0 & 0 \\
0 & \frac{\partial}{\partial y_1} & 0 & 0 & \frac{\partial}{\partial y_2} & 0 & 0 & \frac{\partial}{\partial y_3} & 0 & 0 & \frac{\partial}{\partial y_4} & 0 \\
0 & 0 & \frac{\partial}{\partial z_1} & 0 & 0 & \frac{\partial}{\partial z_2} & 0 & 0 & \frac{\partial}{\partial z_3} & 0 & 0 & \frac{\partial}{\partial z_4} \\
0 & \frac{\partial}{\partial z_1} & \frac{\partial}{\partial y_1} & 0 & \frac{\partial}{\partial z_2} & \frac{\partial}{\partial y_2} & 0 & \frac{\partial}{\partial z_3} & \frac{\partial}{\partial y_3} & 0 & \frac{\partial}{\partial z_4} & \frac{\partial}{\partial y_4} \\
\frac{\partial}{\partial z_1} & 0 & \frac{\partial}{\partial x_1} & \frac{\partial}{\partial z_2} & 0 & \frac{\partial}{\partial x_2} & \frac{\partial}{\partial z_3} & 0 & \frac{\partial}{\partial x_3} & \frac{\partial}{\partial z_4} & 0 & \frac{\partial}{\partial x_4} \\
\frac{\partial}{\partial y_1} & \frac{\partial}{\partial x_1} & 0 & \frac{\partial}{\partial y_2} & \frac{\partial}{\partial x_2} & 0 & \frac{\partial}{\partial y_3} & \frac{\partial}{\partial x_3} & 0 & \frac{\partial}{\partial y_4} & \frac{\partial}{\partial x_4} & 0
\end{matrix} \quad / 4$$

which corresponds to 12 elemental displacements $[\boldsymbol{u}]_E = [u_{x,1}\ u_{y,1}\ u_{z,1}\ u_{x,2}\ u_{y,2}\ u_{z,2}\ \dots\ u_{z,4}]^{\mathrm{T}}$. Consequently, the elemental force vector can be compute from the following matrix operation:

$$F_E = \int \frac{\partial}{\partial x_i} E_{ij} I_{\varepsilon_j} dV = \left[\frac{\partial \mathcal{N}_k}{\partial \mathrm{x_i}}\right]_E^T \times E_{ij} \times I_{\varepsilon_j}.$$

Note that the term $\left[\frac{\partial \mathcal{N}_k}{\partial \mathrm{x_i}}\right]_E^T$ includes both $\frac{\partial}{\partial x_i}$ and dV. Any matrix operation of $\left[\frac{\partial \mathcal{N}_k}{\partial \mathrm{x_i}}\right]_E^T$ also involves the summation of 4 shape functions.

4.3.1.1.3 Thermal hexahedral element

For thermal and diffusion analysis, there is only one degree of freedom and the strain has no shear components. Continuing from the derivation of 8-node stiffness element, the elemental matrix $\left[\frac{\partial \mathcal{N}_k}{\partial S_l}\right]_E$ of thermal element can be defined as shown below, where (*k*,*l*) indicates $\frac{\partial \mathcal{N}_k}{\partial S_l}$:

```
(1,1) (2,1) (3,1) (4,1) (5,1) (6,1) (7,1) (8,1)
(1,2) (2,2) (3,2) (4,2) (5,2) (6,2) (7,2) (8,2)
(1,3) (2,3) (3,3) (4,3) (5,3) (6,3) (7,3) (8,3).
```

The elemental matrix of $\left[\frac{\partial \mathrm{S_l}}{\partial \mathrm{x_i}}\right]_E$ is simply the inverse of the Jacobian matrix without rearrangement:

$$\left[\frac{\partial \mathrm{S_l}}{\partial \mathrm{x_i}}\right]_E = [J]^{-1} = \begin{bmatrix} J_{1,1}^{-1} & J_{1,2}^{-1} & J_{1,3}^{-1} \\ J_{2,1}^{-1} & J_{2,2}^{-1} & J_{2,3}^{-1} \\ J_{3,1}^{-1} & J_{3,2}^{-1} & J_{3,3}^{-1} \end{bmatrix}$$

$$\left[\frac{\partial}{\partial \mathrm{x_i}}\right]_E = \left[\frac{\partial \mathrm{S_l}}{\partial \mathrm{x_i}}\right]_E \times \left[\frac{\partial \mathcal{N}_k}{\partial S_l}\right]_E$$

[3×8] = [3×3] × [3×8]

In the Matlab programming environment, instead of multiplying $\left[\frac{\partial \mathcal{N}_k}{\partial S_l}\right]_E$ by the inverse Jacobian, the elemental derivative matrix $\left[\frac{\partial}{\partial \mathrm{x_i}}\right]_E$ can be found by issuing the backward division command, i.e.

$$\left[\frac{\partial}{\partial \mathrm{x_i}}\right]_E = [J] \setminus \left[\frac{\partial \mathcal{N}_k}{\partial S_l}\right]_E$$

d_dx = Jacobian \ dN_dS;

$$\left[\frac{\partial u}{\partial \mathrm{x_i}}\right]_E = \begin{bmatrix} \frac{\partial u}{\partial \mathrm{x}} \\ \frac{\partial u}{\partial \mathrm{y}} \\ \frac{\partial u}{\partial \mathrm{z}} \end{bmatrix} = \left[\frac{\partial \mathrm{S_l}}{\partial \mathrm{x_i}}\right]_E \times \left[\frac{\partial \mathcal{N}_k}{\partial S_l}\right]_E \times [\boldsymbol{u}]_E$$

[3×1] = [3×3] × [3×8] × [8×1].

The final elemental homogenisation force vector can then be constructed as:

$$F_E = \int \frac{\partial}{\partial x_i} E_{ij} I_{\varepsilon_j} dV = \sum_{G=1}^{8} \left(\left[\frac{\partial}{\partial \mathrm{x_i}}\right]_G^T \times E_{ij} \times I_{\varepsilon_j} \times |J| \right)$$

where the summation is over eight Gaussian points.

4.3.1.1.4 Thermal tetrahedral element

Continuing from Section 4.3.1.1.2, there are only 4 degrees of freedom per element in a thermal tetrahedral element. The 3-by-4 elemental matrix $\left[\frac{\partial \mathcal{N}_k}{\partial \mathrm{x_i}}\right]_E$ is thus defined as

$$\left[\frac{\partial \mathcal{N}_k}{\partial \mathrm{x_i}}\right]_E = \begin{bmatrix} \frac{\partial}{\partial x_1} & \frac{\partial}{\partial x_2} & \frac{\partial}{\partial x_3} & \frac{\partial}{\partial x_4} \\ \frac{\partial}{\partial y_1} & \frac{\partial}{\partial y_2} & \frac{\partial}{\partial y_3} & \frac{\partial}{\partial y_4} \\ \frac{\partial}{\partial z_1} & \frac{\partial}{\partial z_2} & \frac{\partial}{\partial z_3} & \frac{\partial}{\partial z_4} \end{bmatrix} = \frac{1}{6} \times \begin{bmatrix} \overrightarrow{N_2N_4} \times \overrightarrow{N_4N_3} \\ \overrightarrow{N_1N_3} \times \overrightarrow{N_3N_4} \\ \overrightarrow{N_1N_4} \times \overrightarrow{N_4N_2} \\ \overrightarrow{N_1N_2} \times \overrightarrow{N_2N_3} \end{bmatrix}^T.$$

The tetrahedral element force vector is formulated the same way as the hexahedral element:

$$F_E = \left[\frac{\partial \mathcal{N}_k}{\partial \mathrm{x_i}}\right]_E^T \times E_{ij} \times I_{\varepsilon_j} = \frac{1}{6} \times \begin{bmatrix} \overrightarrow{N_2N_4} \times \overrightarrow{N_4N_3} \\ \overrightarrow{N_1N_3} \times \overrightarrow{N_3N_4} \\ \overrightarrow{N_1N_4} \times \overrightarrow{N_4N_2} \\ \overrightarrow{N_1N_2} \times \overrightarrow{N_2N_3} \end{bmatrix} \times E_{ij} \times I_{\varepsilon_j}.$$

4.3.1.2 Boundary conditions

A separated and dedicated variable is used to specify the boundary conditions (BCs) for FEA. A range of BC writers are included in this scripting function and the one to be used in the actual FEA is chosen by this variable. This selection variable has two major components: loading condition and degree-of-freedom BC (Figure 4-11). In the homogenisation of permeability, two possible loading types are body force (gravitational) and uniform pressure load; two possible BCs are periodicity and symmetry. All nodes on the material boundary have to be exclusively defined in order to impose the no-slip fluid dynamics BC. In the homogenisation of stiffness, two possible BCs are periodicity and full symmetry. In the homogenisation of diffusivity and analysis of biological environment, four possible loading types are homogenisation force, wall flux, body force and tabular conditions; three possible BCs are periodicity, uniform gradient, and uniform gradient combined with periodicity.

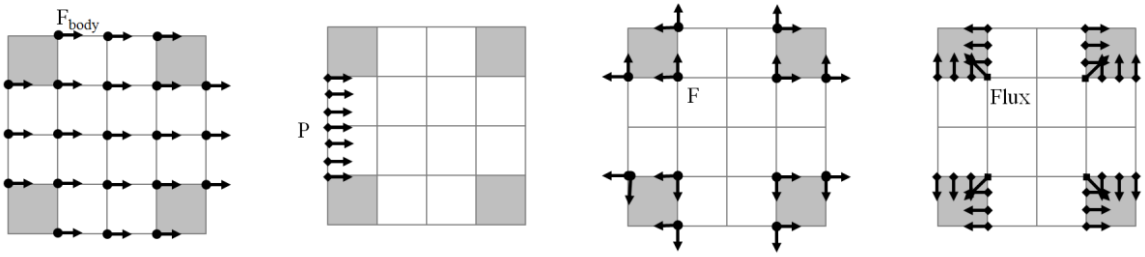

(a) Body force (b) Uniform pressure (c) Homogenisation (d) Wall flux

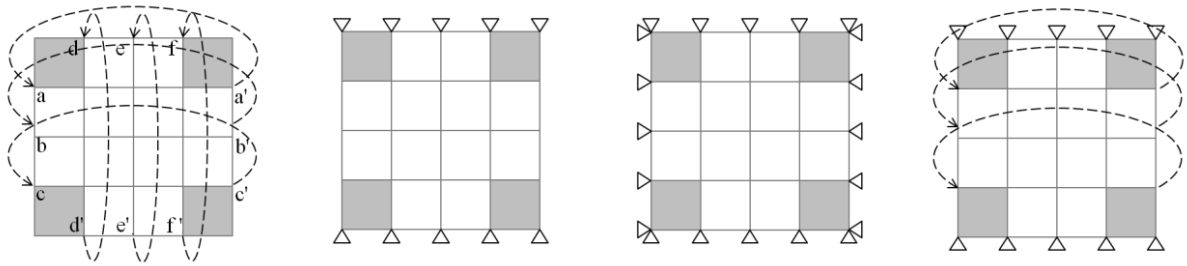

(e) Periodic (f) Partial symmetry (g) Full symmetry (h) Combined

Figure 4-11. Schematic sketches of different types of loading conditions (a)-(d) and boundary conditions (e)-(h) used in homogenisation. The grey and white areas represent two different materials.

4.3.1.3 Node coupling

The imposition of periodicity BC on a FE model is done by means of node coupling. Principally, two nodes at the same position but on the opposite side of the modelling boundaries are linked (Figure 4-12), thus the word coupling. A node can belong to many different couples, and the result is that multiple nodes are linked to one another. The DOFs of all linked node are equal.

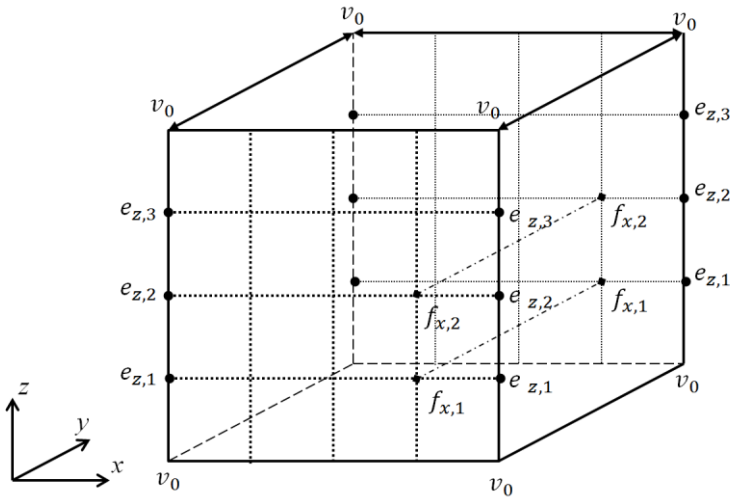

Figure 4-12. Schematic sketch of node coupling. $f_{x,1}$ is a face node couple and contains 2 nodes. $e_{z,1}$ is an edge node group but contains 4 nodes. v_0 is a vertex node group containing 8 nodes.

List of nodal couples or groups is generated through the following steps:

1. Each node is assigned a nodal number as a form of identification. Each node is defined by four pieces of numerical information: Nodal number (#), and x, y and z coordinates.

2. Identify all nodes that sit on the faces but not on the edges of the boundary of modelling space (Figure 4-12, points $f_{x,i}$). A temporary list of these nodes is compiled in this format:

$$\begin{array}{cccc} \#1 & x_1 & y_1 & z_1 \\ \#2 & x_2 & y_2 & z_2 \\ \#3 & x_3 & y_3 & z_3 \\ \#\# & \dots & \dots & \dots \end{array}$$

Assume that the modelling boundaries are [x/y/z = ±d] planes in the Cartesian coordinate system. To couple nodes in a 3D domain, 3 separate lists are required:

$$\text{x-face couples: } |x| = d \;\&\; |y| \neq d \;\&\; |z| \neq d$$
$$\text{y-face couples: } |x| \neq d \;\&\; |y| = d \;\&\; |z| \neq d$$
$$\text{z-face couples: } |x| \neq d \;\&\; |y| \neq d \;\&\; |z| = d$$

Each of the three lists is sorted in the ascending order according to the value of x/y/z. In case (a), nodes with the same y/z values but with opposite x signs, i.e.

$$\begin{array}{cccc} \#i & d & y_i & z_i \\ \#j & -d & y_j = y_i & z_j = z_i \end{array}$$

are identified. nodes $\#i$ and $\#j$ are said to be coupled. The process is repeated to create two other lists, i.e.

$$\begin{array}{cccc} \#i & x_i & d & z_i \\ \#j & x_j = x_i & -d & z_j = z_i \end{array}$$

and

$$\begin{array}{cccc} \#i & x_i & y_i & d \\ \#j & x_j = x_i & y_j = y_i & -d \end{array}$$

In Matlab, organizing and rearranging each list requires five commands:

```
[~,~,couple] = unique(node(:,3:4),'rows');   %ID each couple

    nnum = node(:,1);  % nodal number #i, #j, etc
```

```
[~,couple]   = sort(couple);   %Sort the nodes based on the ID
couple = reshape(couple,[2, length(couple)/2]);   %Create a table
couple = nnum( couple );   %Create the final list
```

where node is a list compiled at step (2), and couple is a 2-column list of couples in this format:

$$\begin{matrix} \#i & \#j \\ \#k & \#l \\ \dots & \dots \end{matrix}$$

3. Three more lists are compiled for nodes sitting on the edges but not at the corner of the boundary (Figure 4-12, points $e_{z,i}$):

$$|x| \neq d \;\&\; |y| = d \;\&\; |z| = d,$$
$$|x| = d \;\&\; |y| \neq d \;\&\; |z| = d,$$
$$|x| = d \;\&\; |y| = d \;\&\; |z| \neq d.$$

Each of the three lists above is again sorted in the ascending order according to the value of x/y/z. In case (a), nodes with the same x coordinate but with different y/z signs, i.e.

$$\begin{matrix} \#i & x_i & d & d \\ \#j & x_j = x_i & d & -d \\ \#k & x_k = x_i & -d & d \\ \#l & x_l = x_i & -d & -d \end{matrix}$$

are identified. These nodes, $\#i$, $\#j$, $\#k$ and $\#l$ are coupled. In Matlab, the list generation also requires five commands:

```
[~,~,couple] = unique(node(:,2),'rows');   %ID each group
    nnum = node(:,1);  % nodal number #i, #j, #k, etc
[~,couple]   = sort(couple);   %Sort the nodes based on the ID
couple = reshape(couple,[4, length(couple)/4]);   %Create a table
couple = nnum( couple );   %Create the final list
```

where node is a list compiled at step (2), and couple is a 4-column list of couples:

$$\begin{matrix} \#i & \#j & \#k & \#l \\ \#m & \#n & \#o & \dots \end{matrix}$$

This process is repeated for the other two lists.

Finally, all nodes at the corners of the boundary of design domain are linked:

$$\begin{array}{cccc} \#i & d & d & d \\ \#j & d & d & -d \\ \#k & d & -d & d \\ \#l & d & -d & -d \\ \#m & -d & d & d \\ \#n & -d & d & -d \\ \#o & -d & -d & d \\ \#p & -d & -d & -d \end{array}$$

4. Up to 8 nodes can be grouped in the cubic modelling domain (Figure 4-12, points v_0).

All seven lists (3 faces, 3 edges and 1 corner) are written to external files in a format readable by the external FEA program.

4.3.2 Postprocessing function and sensitivity analysis

The FEA results obtained from ANSYS are post-processed to determine the objective number and the sensitivity (Figure 4-32). The FE model, the FEA results and design constraints are required as an input variable for postprocessing. Sensitivity of the level set model is computed and exported as the output variable.

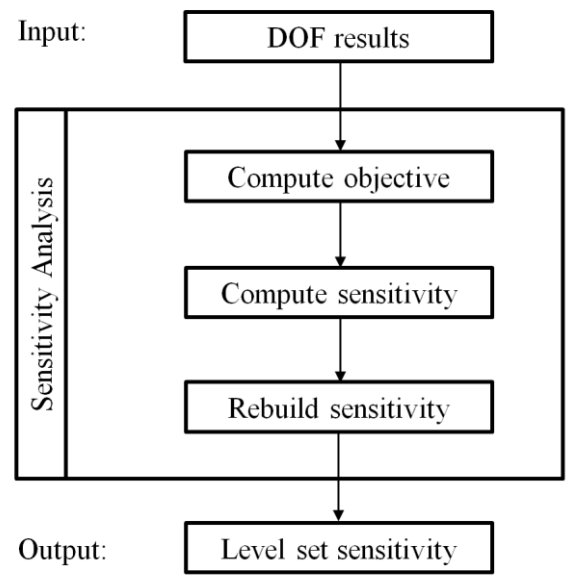

Figure 4-13. Sensitivity analysis process.

The calculation of the objective number (homogenised material property) follows a procedure similar to the one presented in the previous calculation of the homogenisation force in terms of matrix operation and assembly. Using the notations from Section 4.3.1.1, the homogenised stiffness, conductivity/diffusivity and permeability can be computed from the following formula, respectively, if the mesh is hexahedron-based:

$$E_{ij}^{H} = \sum_{e=1}^{n}\sum_{G=1}^{8}\left[\left(I - [\boldsymbol{u}]_E^T \times \left[\frac{\partial \mathcal{N}_k}{\partial S_l}\right]_G^T \times \left[\frac{\partial S_l}{\partial x_i}\right]_G^T\right) \times E_{ij} \times \left(I - \left[\frac{\partial S_l}{\partial x_i}\right]_G \times \left[\frac{\partial \mathcal{N}_k}{\partial S_l}\right]_G \times [\boldsymbol{u}]_E\right) \times |J|\right],$$

$$E_{ij}^{H} = \sum_{e=1}^{n}\sum_{G=1}^{8}\left[E_{ij} \times \left(I - \left[\frac{\partial S_l}{\partial x_i}\right]_G \times \left[\frac{\partial \mathcal{N}_k}{\partial S_l}\right]_G \times [\boldsymbol{u}]_E\right) \times |J|\right], \text{ and}$$

$$E_{ij}^{H} = \sum_{e=1}^{n}\sum_{G=1}^{8}\left[[\boldsymbol{u}]_E^T \times \left[\frac{\partial \mathcal{N}_k}{\partial S_l}\right]_G^T \times \left[\frac{\partial S_l}{\partial x_i}\right]_G^T \times E_{ij} \times \left[\frac{\partial S_l}{\partial x_i}\right]_G \times \left[\frac{\partial \mathcal{N}_k}{\partial S_l}\right]_G \times [\boldsymbol{u}]_E \times |J|\right],$$

where the capital H denotes homogenised property, e is the element index, n is the number of elements, and I is the identity matrix representing the unit-strain field. Different elements can have different differentiation matrices if the mesh consists of non-brick element (cubic). If tetrahedral elements are used, the homogenised stiffness, conductivity/diffusivity and permeability can be computed from the formula below, respectively:

$$E_{ij}^{H} = \sum_{e=1}^{n}\left[\left(I - [\boldsymbol{u}]_E^T \times \left[\frac{\partial}{\partial \mathrm{x_i}}\right]_E^T\right) \times E_{ij} \times \left(I - \left[\frac{\partial}{\partial \mathrm{x_i}}\right]_E \times [\boldsymbol{u}]_E\right) \times dV\right]_e,$$

$$E_{ij}^{H} = \sum_{e=1}^{n}\left[E_{ij} \times \left(I - \left[\frac{\partial}{\partial \mathrm{x_i}}\right]_E \times [\boldsymbol{u}]_E\right) \times dV\right]_e, \text{ and}$$

$$E_{ij}^{H} = \sum_{e=1}^{n}\left[[\boldsymbol{u}]_E^T \times \left[\frac{\partial}{\partial \mathrm{x_i}}\right]_E^T \times E_{ij} \times \left[\frac{\partial}{\partial \mathrm{x_i}}\right]_E \times [\boldsymbol{u}]_E \times dV\right]_e.$$

The end result of E_{ij}^{H} should be a 6-by-6 stiffness matrix with normal and shear components; a 3-by-3 stiffness matrix with only normal components; a 3-by-3 conductivity, diffusivity or permeability matrix; or a 1-by-1 isotropic conductivity, diffusivity or permeability matrix. This matrices are used to derive the final objective number, Obj, which is a scalar. For bulk modulus,

$$Obj = \frac{1}{9}\sum_{j=1}^{3}\left(\sum_{i=1}^{3} E_{ij}^{H}\right).$$

If a set of desirable material properties E_{ij}^{*} is given, then the objective is minimising the difference:

$$Obj = \sum_{j=1}^{3}\left[\sum_{i=1}^{3} w_{ij}\left(E_{ij}^{*} - E_{ij}^{H}\right)^{2}\right],$$

where w_{ij} is a weight factor for each matrix entry. This objective is used in the next chapter.

In the isosurface-based topology optimisation method, the sensitivity of an element is directly proportional to its elemental objective value (mathematical derivation is provided in section 4.2.1.1, where $\delta(\phi)$ is a constant on the level set boundary). On the other hand, the sensitivity number ($Sens$) in a SIMP-based optimisation has to be calculated using the following formula:

$$Sens_E = p\sum_{G=1}^{8}\left[\frac{1}{\rho}\times\left(I - [\boldsymbol{u}]_E^T \times \left[\frac{\partial \mathcal{N}_k}{\partial S_l}\right]_G^T\right)\times\left[\frac{\partial \mathrm{S_l}}{\partial \mathrm{x_i}}\right]_G^T \times E_{ij} \times \left[\frac{\partial \mathrm{S_l}}{\partial \mathrm{x_i}}\right]_G \times \left(I - \left[\frac{\partial \mathcal{N}_k}{\partial S_l}\right]_G \times [\boldsymbol{u}]_E\right)\times |J|\right]$$

where p is the penalisation factor, and ρ is the "density" or "porosity" of the element. The sensitivity value in every element is unique and needs not to be summed over the design space.

The nodal sensitivity is interpolated from the elemental sensitivity using a distance-weighted method as illustrated in Figure 4-14. The weight of each element is defined as the inverse value of the distance between its elemental centroid to the node of interest. Assuming an idealistic level set model, only nodes on the material boundary (the isosurface) has non-zero sensitivity. In that sense, the interpolation only has to be performed on the boundary nodes. Theoretically all non-boundary nodes have zero sensitivity, so the interpolation at non-boundary nodes is unnecessary.

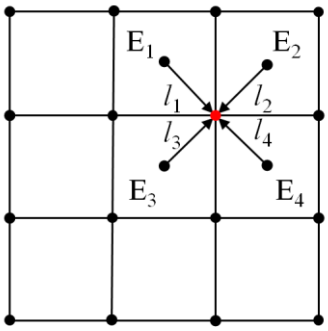

$$Sens_N = \frac{\sum_{i=1}^{4} Sens_{E_i}/l_i}{\sum_{i=1}^{4} 1/l_i} = \frac{\sum_{i=1}^{4} Sens_{E_i}}{4}$$

(a) Interpolation in a structured mesh

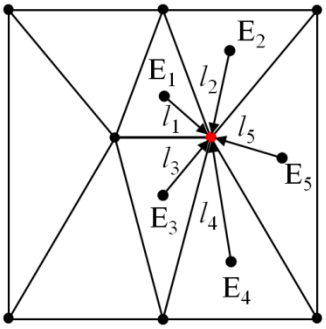

$$Sens_N = \frac{\sum_{i=1}^{5} Sens_{E_i}/l_i}{\sum_{i=1}^{5} 1/l_i}$$

(b) Interpolation in an unstructured mesh

Figure 4-14. Schematic elemental-to-node sensitivity interpolation in structured and unstructured FE models.

The sensitivity of individual LSF points (LSF grid sensitivity) is subsequently interpolated from the nodal sensitivity, again using the weighted-distance interpolation (Figure 4-15). The weight is the distance between a node and a grid point this time.

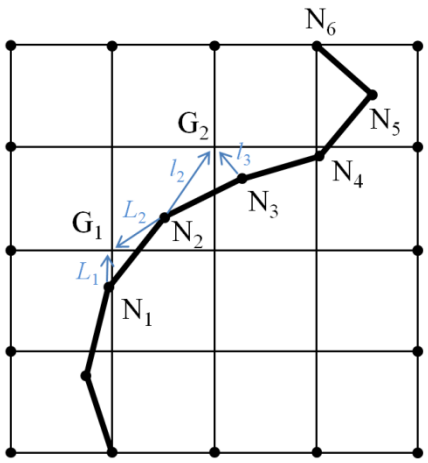

$$Sens_{G_1} = \frac{\sum_{i=1,2}\left(\frac{Sens_{N_i}}{L_i + k}\right)}{\sum_{i=1,2}\left(\frac{1}{L_i + k}\right)}$$

$$Sens_{G_2} = \frac{\sum_{i=2,3}\left(\frac{Sens_{N_i}}{l_i + k}\right)}{\sum_{i=2,3}\left(\frac{1}{l_i + k}\right)}$$

Figure 4-15. Schematic node-to-grid interpolation process in an isosurface model.

During the node-to-grid interpolation, a constant value *k* is added to the weight. This addition prevents the division by zero if the original weight is zero, which happens when the node is at the same location as the grid point. This two-step interpolation process is repeated for every objective-sensitivity function. The resultant sensitivity numbers are weighted and summed per design optimisation condition to produce a single sensitivity value per element.

In the programming environment, the nodal sensitivity ($Sens_N$ in Figure 4-14) is saved in a vector format, with the same length as the number of nodes. The grid sensitivity ($Sens_{G_1}$ and $Sens_{G_2}$ in Figure 4-15) is saved in a matrix format with the same size as the original LSF matrix. In addition to this sensitivity matrix, a companion matrix is used to record whether a sensitivity matrix entry is empty or filled. In the node-to-grid interpolation technique, empty entries can be given a default value of zero, whereas filled entries can have a zero or a non-zero value. Therefore there is a need to label any point that has been filled during this operation. This additional matrix represents the approximated location of the isosurface boundary.

4.3.3 Topology change and update

In this level-set-isosurface method, the topology change is induced by the numerical manipulation of the LSF (Figure 4-16). The topology update function takes the current LSF and its sensitivity as the inputs and produces a new LSF as the output. The new tissue scaffold design should outperform the predecessor model. The numerical change required to produce the desired topology change is calculated based on the Hamilton-Jacobi like equation derived in section 4.2.1.1. The magnitude of change in topology is decided by two factors: sensitivity and volume constraint.

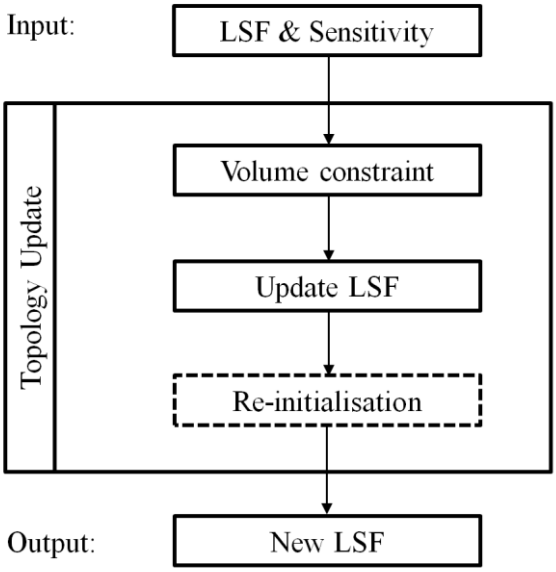

Figure 4-16. The process of topology update.

In this LSF update function, the volume information that is essential to enforce the volume constraint is processed. As shown in Figure 4-17a, here V_0 is defined as the volume constraint ($\int_\Omega \ dV \leq V_0$), V_m as the total solid volume of the current FE model ($V_m = \int_\Omega \ dV$), V_Δ as the difference between these two values ($V_\Delta = V_0 - V_m$), and A_m as the total surface area of the current FE model ($A_m = \int_\Gamma \ dS$). In a discretised model, $A_m = \sum_{j=1}^{n} A_{m,j}$ where $A_{m,j}$ is the individual surface area of triangle j (Figure 4-17b). V_Δ is used to calculate the secondary volume correction factor, θ, mentioned in section 4.2.2.3:

$$\theta = \frac{\mathrm{V}_\Delta}{|\mathrm{V}_\Delta|} \times \min\left(\left|\frac{\mathrm{V}_\Delta}{A_m}\right|, \mathrm{h}_0\right)$$

where h_0 is the desirable change in topology. The term $\frac{\mathrm{V}_\Delta}{|\mathrm{V}_\Delta|}$ returns the sign of V_Δ. Taking the minimum value of $\left|\frac{\mathrm{V}_\Delta}{A_m}\right|$ and h_0 limits the magnitude of volume correction and prevent excessive topology change. If $\left|\frac{\mathrm{V}_\Delta}{A_m}\right|$ and h_0 are reasonably small in term of magnitude, the change in volume is roughly equal to the distance of change times the total isosurface area ($V_m{}' \approx h \times A_m$, Figure 4-17a).

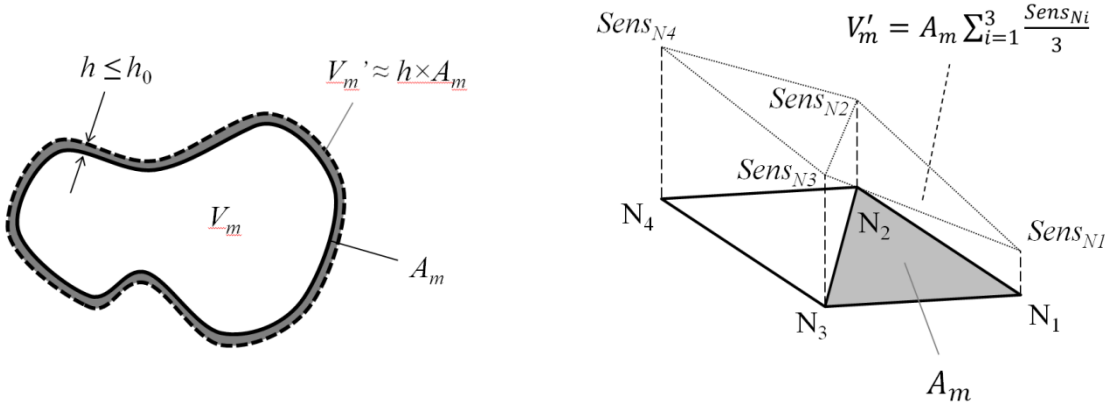

(a) Modelling volume correction (b) Sensitivity volume correction

Figure 4-17. Schematic illustration of volume correction of the isosurface model.

The primary volume correction factor, namely the Lagrange multiplier λ, is calculated based on the nodal sensitivity values and integrated across the discretised isosurface (Figure 4-17b):

$$\lambda = -\frac{\sum_{j=1}^{n} V_m'}{A_m} = -\frac{\sum_{j=1}^{n} \left(A_{m,j} \sum_{i=1}^{3} \frac{Sens_{N,i}}{3} \right)}{\sum_{j=1}^{n} A_{m,j}}$$

where n is the number of triangular faces of the isosurface, j is the face index, and i is the vertex index of each triangular face (1st, 2nd and 3rd vertices). Only the part of isosurface that forms the material boundary is considered, whereas the isosurface on the modelling boundary is not used in this part of the calculation. The Lagrange multiplier is then added directly to the sensitivity function that is also the relative velocity function.

The sensitivity function is the relative "speed" or "velocity" function in the LSF update. Recall that the sensitivity matrix obtained previously is only partially filled. A full sensitivity matrix must be reconstructed, which is done using the flood-fill mechanism introduced in Section 3.3.3 (Figure 4-18, also see Figure 3-13).

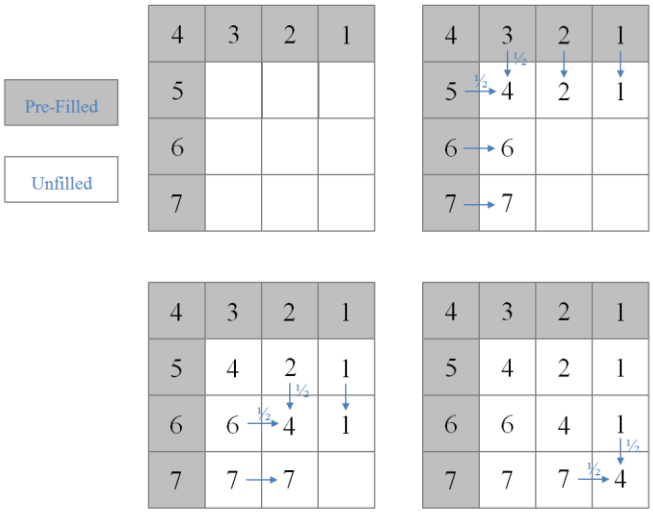

Figure 4-18. Schematic demonstration of matrix reconstruction by flood-filling.

Unlike the modelling process, the goal of this flood-fill operation is to actually fill the blank entries in the sensitivity matrix rather than finding neighbours. This operation inserts values in empty entries in both solid and void/fluid domain by simply copying and taking average of filled entries to those blank ones as demonstrated in the figure.

The time step ($d\tau$) size determines the distance of movement of the level-set-isosurface boundary. The $d\tau$ value is found by dividing the desirable magnitude of topology change by the maximum "speed," which is the maximum value of the sensitivity matrix. Note that only the sensitivity along with its Lagrange multiplier is factored into the finding of $d\tau$. The secondary volume correction factor, θ, is independent of $d\tau$ as its goal is to rectify any numerical error that could not have been predicted and corrected during the sensitivity derivation.

The gradient field of the LSF can be calculated in a number of ways with first order or third order accuracy. In this study, the gradient field is calculated with the first order accuracy.

4.3.4 Re-initialisation

The re-initialisation process aims to reconstruct the LSF as a signed-distance function of the isosurface (Figure 4-19). The value of this function represents the shortest distance between each LSF grid point and the triangulated isosurface (Figure 4-19a). Each value also comes with a sign, which indicates what material phase the domain is in (Figure 4-19b, positive value for solid and negative value for void/fluid). The original LSF is used as the main input variable, along with the model size and distance limit as optional inputs. This re-initialisation is a two-part calculation process: the first part determines the actual shortest distance and the second part approximates the shortest distance. A special distance parameter (l_0) is used in this study to decide which LSF grid points undergo the first part of calculation, based on how far they are from the current isosurface. The rest of LSF is reconstructed through a distance approximation technique that will be explained later on.

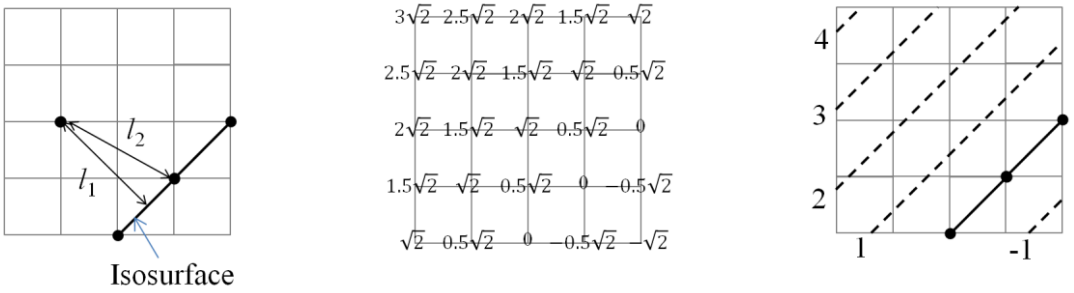

(a) l_1 is the shortest distance (b) The shortest-distance in matrix form (3) The idealistic signed distance function

Figure 4-19. Exemplar construction of signed distance function and its matrix form.

The signed distance function (SDF) has two components, the sign and the magnitude. The magnitude is determined first, then signs are assigned. The SDF calculation checks one isosurface triangle at a time, and calculates the shortest distance (l_1) between the triangle and all of its surrounding LSF grid points. The distance value is only recorded if $l_1 \leq l_0$. The shortest distance between a grid point and all isosurface triangles is not known until all triangles are checked. Each point of the output SDF has the same sign as its input LSF.

4.3.4.1 *Calculate the shortest distance: actual*

In this study, only grid points that are within 3 grid-spaces away will be considered in the actual calculation of the actual shortest distance ($l_0 = 3$). This program starts by assigning a very large value to every SDF matrix entry (Figure 4-20, left). As the program processes the isosurface model triangle by triangle, each iteration produces new distance values for all surrounding grid points (Figure 4-20, middle). If smaller values are found, the SDF values are updated. The initial value must be sufficiently large, at least be as large as the length of two furthest points in the model, so that SDF update takes place correctly. The SDF function is finalised when all discrete isosurface components are considered (Figure 4-20, right).

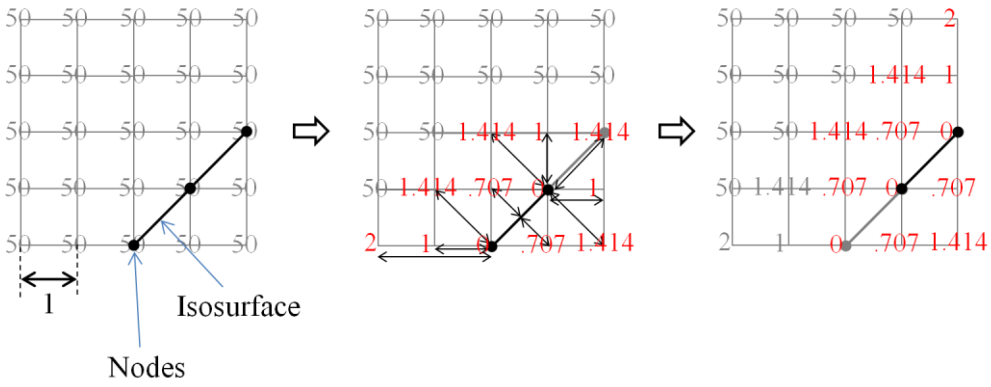

Figure 4-20. Exemplar construction of the actual SDF. Red values indicate updated entries and grey values indicated ignored entries.

To calculate the shortest distance between a point and a triangular plate in a 3D space, the relative normal position of the point to the triangle is firstly determined. There are seven possible positions as shown in the following figure (Figure 4-21):

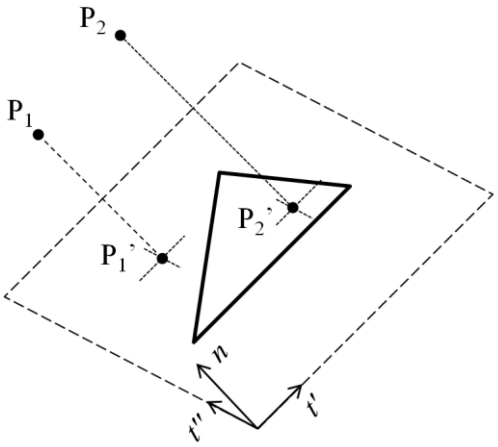

Projection of a point on the n-t'-t'' plane where the triangle resides

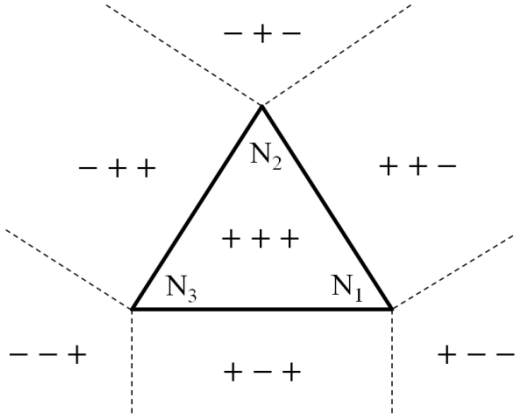

Seven possible relative positions on the n-t'-t'' plane

Figure 4-21. Relative position of a point to a triangle in 3D space.

When point P is projected perpendicularly onto the 3D plane where the triangular surface resides, this point can be either in the triangle (+++), or in one of the "edge zones" (−++, +−+ and ++−), or in one of the "vertex zones" (+−−, −+−, and −−+). The shortest distance is its perpendicular distance to the face (P_2), to one of the edges (P_1) or to one of the vertices (P_3), respectively, as illustrated in the next figure (Figure 4-22):

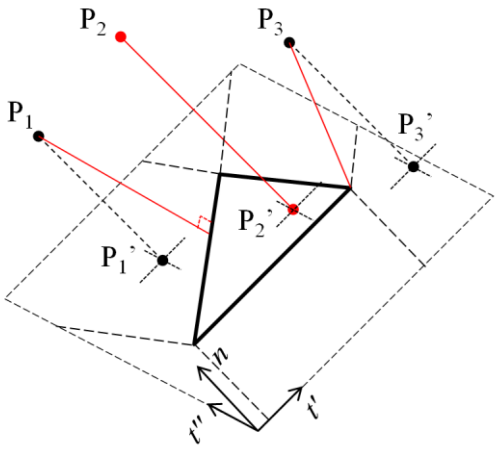

Figure 4-22. The shortest distance between point P and the triangle. The red lines are the shortest paths between individual points and the triangle in 3D space.

4.3.4.1.1 Face zone (+++)

The projection of a point (P_2) in a triangle can be defined in relation to the three vertices of the triangle. As shown the following figure, an imaginary plane (Plane AB) containing the line AB and being perpendicular to the triangle ABC is created (Figure 4-23):

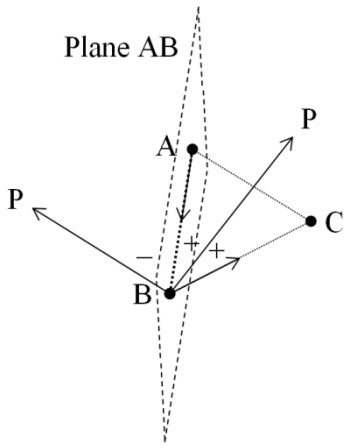

Figure 4-23. Relative position of a point to edges of a triangle.

If points P and C are on the same side of the plane (right-hand side), then the following condition must have been satisfied:

$$\left(\overrightarrow{AB} \times \overrightarrow{BC}\right) \cdot \left(\overrightarrow{AB} \times \overrightarrow{BP}\right) \geq 0$$

In other words, the surface normals of the triangles ABC and ABP' (P' is the projection of P) must be pointing in the same direction. Otherwise, if $\left(\overrightarrow{AB} \times \overrightarrow{BC}\right) \cdot \left(\overrightarrow{AB} \times \overrightarrow{BP}\right) < 0$, points P and C must be on the opposite sides of the plane. If the dot product is zero, the point P must be directly above or below the edge AB. Similarly, if

$$\left(\overrightarrow{BC} \times \overrightarrow{CA}\right) \cdot \left(\overrightarrow{BC} \times \overrightarrow{CP}\right) \geq 0$$
$$\left(\overrightarrow{CA} \times \overrightarrow{AB}\right) \cdot \left(\overrightarrow{CA} \times \overrightarrow{AP}\right) \geq 0$$

then points P and A are on the same side of the BC plane, and points P and B are on the same side of the CA plane, respectively. Satisfying all three conditions means that point P is directly above or below the triangle ABC, thus its projection is within the triangle ABC. The shortest distance, d_P, can then be found using the following formula:

$$d_P = \left| \overrightarrow{AP} \cdot \frac{\overrightarrow{AB} \times \overrightarrow{BC}}{\left| \overrightarrow{AB} \times \overrightarrow{BC} \right|} \right| = \left| \overrightarrow{AP} \cdot \widehat{n_{ABC}} \right|$$

where $\widehat{n_{ABC}}$ is the surface normal of the triangle ABC. $\widehat{n_{ABC}}$ is a unit vector.

4.3.4.1.2 Edge zones (−++, +−+ and ++−)

Consider three projections, P_1, P_2 and P_3, in the following figure (Figure 4-24):

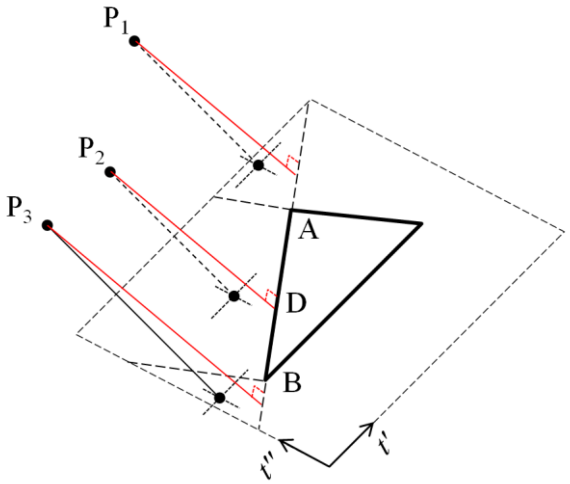

Figure 4-24. Relative position of a point to vertices of a triangle.

Only the projection of P_2 is in the zone of edge-AB. Mathematically, a point P in the edge zone AB must satisfy the following condition:

$$0 \leq \overrightarrow{AP} \cdot \widehat{n_{AB}} \leq \left| \overrightarrow{AB} \right|$$

where $\widehat{n_{AB}}$ is the unit vector of edge AB. The shortest distance is calculated from the formula:

$$d_P = \overline{P_2 D} = \left| \overrightarrow{AP} \times \widehat{n_{AB}} \right|.$$

If the point P is not in the zone edge of $\overrightarrow{AB}$, this process is repeated to check if P falls into the edge zones of $\overrightarrow{BP}$ or $\overrightarrow{CP}$. In those cases, $d_P = \left| \overrightarrow{BP} \times \widehat{n_{BC}} \right|$ and $d_P = \left| \overrightarrow{CP} \times \widehat{n_{CA}} \right|$, respectively.

4.3.4.1.3 Vertex zones (+−−, −+−, and −−+)

If the point P fails to satisfy any of the above conditions, then its closest point to the triangle must be one of the vertices, A, B or C:

$$d_P = \min(|\overrightarrow{AP}|, |\overrightarrow{BP}|, |\overrightarrow{CP}|).$$

4.3.4.2 Calculate the shortest distance: estimated

Once the calculation of actual shortest distance is completed, the rest of the SDF matrix is flood-filled with the estimated shortest distance. The SDF entries found earlier are used as the starting point of an iterative flood-filling process. To mimic the characteristic of a distance function, the values have to increase or decrease gradually according to their relative distance to the isosurface, as illustrated below (Figure 4-25).

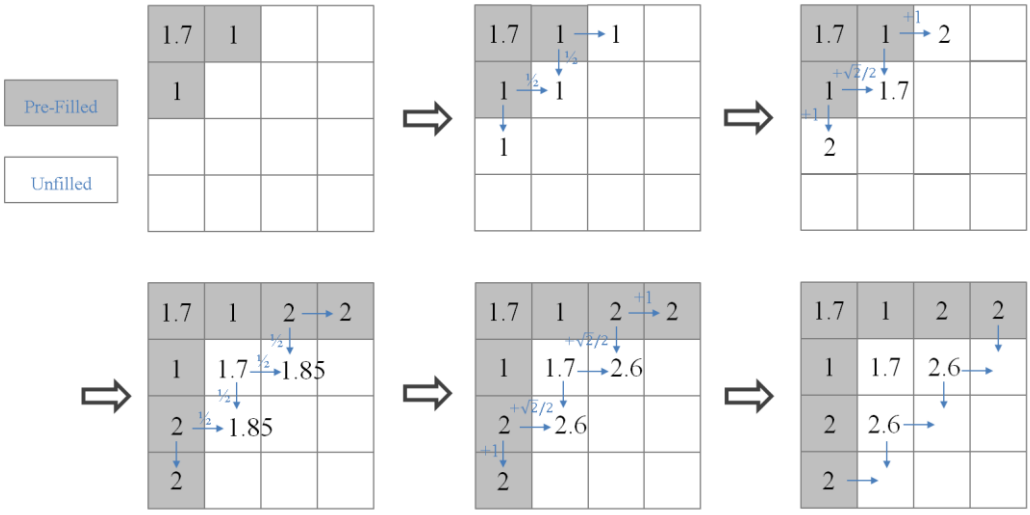

Figure 4-25. Approximation of the shortest distance by flood-fill.

In this process, the SDF matrix is filled layer by layer, where each layer is the von Neumann neighbourhood of the filled SDF. In each step one layer of empty matrix entries is produced by taking average of its neighbouring entries (grey blocks), and a "distance value," Δd (blue values in the figure) is added to every entry. Δd may have three different values depending on the existence and positions of its pre-filled neighbours. Some graphical examples of the distance value, Δd, are shown below (Figure 4-26):

Having a pre-filled neighbour in the cell(s) …			$\Delta d =$
"North" or "South"	"East" or "West"	"Top" or "Bottom"	
Yes	No	No	1
No	**Yes**	No	1
No	No	**Yes**	1
Yes	**Yes**	No	$1/\sqrt{2}$
Yes	No	**Yes**	$1/\sqrt{2}$
No	**Yes**	**Yes**	$1/\sqrt{2}$
Yes	Yes	Yes	$1/\sqrt{3}$

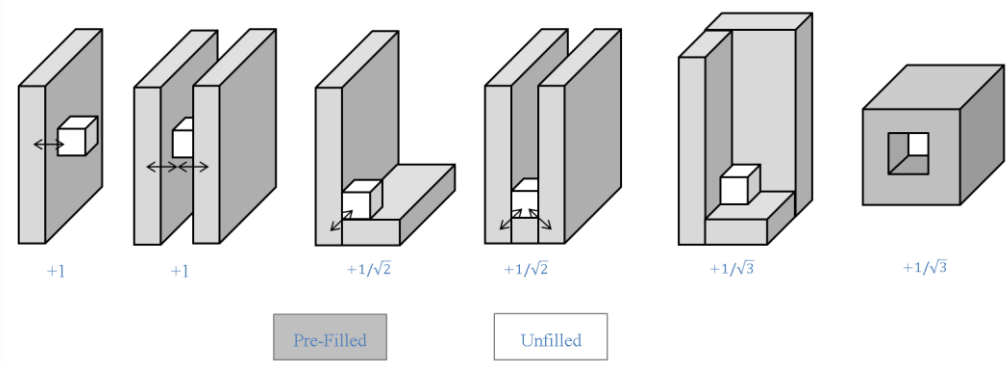

Figure 4-26. Graphical illustration of the determination of "distance value," Δd.

4.4 Results and discussion

The structure and pore connectivity of tissue scaffolds are the key determinants of their elastic properties and nutrient transportation efficiency. These material properties subsequently affect cell survival and proliferation. To improve the environment for cell survival and proliferation, topology optimisation of the microstructure of tissue scaffolds was performed. This part of study aimed to configure the micro-architecture of tissue scaffolds based on various design criteria, and to determine the best possible living conditions for cells in topological terms. The level set method and isosurface modelling technique were chosen for this task.

4.4.1 Isosurface modelling of RVE

The proposed technique combining LSF tracking and isosurface modelling has been successfully implemented in the design optimisation for permeability, effective bulk modulus

and diffusivity of unit-cell structure, or the representative volume element (RVE). The LSF provides the means for dynamic modelling while the isosurface model enables more accurate FEA and simulation. The integration was streamlined to allow modelling information to be passed between the structured optimisation LSF system and the unstructured isosurface model. Simulations were conducted on the smooth tetrahedral mesh. Three effective material properties, namely the bulk modulus, diffusivity and permeability were computed based on the theory of homogenisation. Following the FEA and the homogenisation process, various numerical operations were carried out to construct and transform the objective and sensitivity functions from the initially unstructured form to a structured array, then the LSF was updated. The symmetry and periodic boundary conditions were enforced to improve stability of structural evolution. In addition to the typical optimisation routine, the flood-fill technique has been introduced to approximate the velocity function and to accelerate the LSF re-initialisation. The signed-distance-function re-initialisation was performed every fourth iteration to maintain the smoothness of the LSF. The final optimisation results were unambiguous, smooth, and explicitly defined.

The default modelling space of all models was cubic, 1 unit in length, with a LSF resolution of 37×37×37 and a grid space of 1/36th unit. The initial void space consisted of three square channels intersecting at the cubic centre. Schwarz's primitive surface ($\phi = \cos(x) + \cos(y) + \cos(z) = 0$) was used as an alternative initial model if the original model experienced severe convergence issue. A 50% solid volume (constraint) was to be maintained throughout the optimisation process. Symmetry, periodicity and isotropy modelling conditions were applied and enforced. In the isosurface tetrahedral mesh, the maximum elemental volume is 6.33×10^{-6} cubic units.

The isosurface modelling technique translated the implicit LSF matrix to finite element models through linear interpolation, surface triangulation and mesh smoothing. The mesh smoothing step removed and merged any triangles with one or more short edges (0.75 × level set grid length was used in the study as shown in Figure 4-27a). The resultant triangulated surfaces had more evenly sized and spaced mesh (Figure 4-27b-c). Figure 4-27d is demonstration of isosurface construction of gyroid surface. The mesh generator Iso2Mesh [38] and *tetgen* [35-37] slightly modified the isosurface mesh by inserting additional nodes and triangle, which improved the quality of FE body mesh.

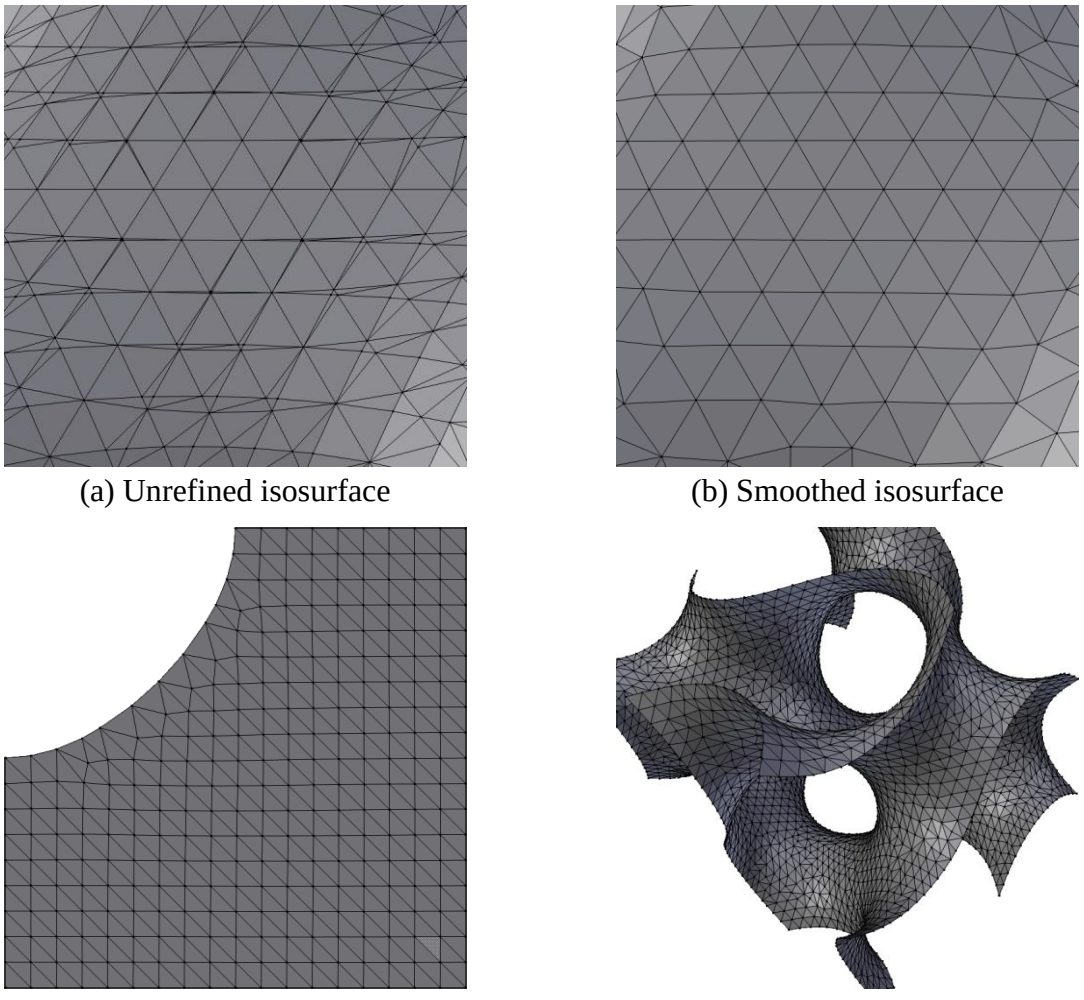

(a) Unrefined isosurface (b) Smoothed isosurface

(c) Isosurface on the modelling boundary (d) Smoothed gyroid surface model

Figure 4-27. Examples of smoothed 3D isosurfaces: (a-c) the Schwarz's primitive surface model and (d) the gyroid surface model.

4.4.2 Topology optimisation

Three optimal level-set-isosurface models have been obtained at a matrix resolution of 37×37×37. The resultant effective permeability is 0.003551. The maximum effective diffusivity is 0.4 (unit length^2 / s) at the porosity of 50%, which is close to the theoretical maximum value predicted by the Hashin-Shtrikman upper bound. The maximum effective bulk modulus is 0.2316 (Pascal, Poisson's ratio = 0.3, and elastic modulus E = 1 unit). The topology optimisation was considered successful in the all isosurface- (Figure 4-28 a-c) and SIMP-based (Figure 4-28 j-k) models, but un-converged in all voxelised, non-density-based models (Figure 4-28 g-i, l and m). Introducing intermediate-density element to the conventional level set method had resulted in some success in the bulk modulus and diffusivity optimisation scenarios (Figure 4-28 e-f), and a less optimal permeability model (Figure 4-28 d). A recent study [40] used an improved version of BESO and the optimised structure had a maximum effective bulk modulus of 0.218, which is lower than the isosurface model presented here.

Permeability (unit length^2)	Bulk modulus (Pa)	Diffusivity (unit length^2 / s)
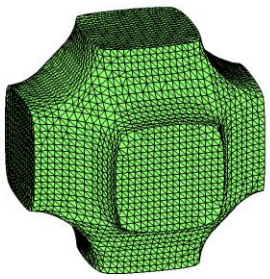	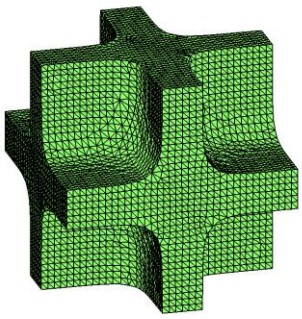	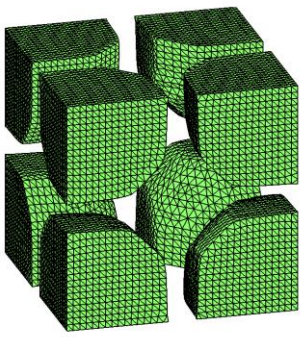
(a) 0.003551	(b) 0.2317	(c) 0.3965

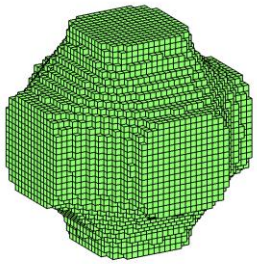	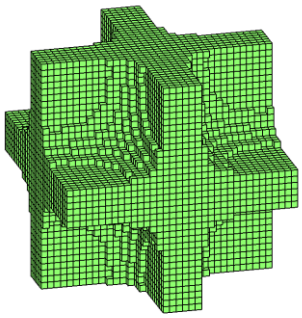	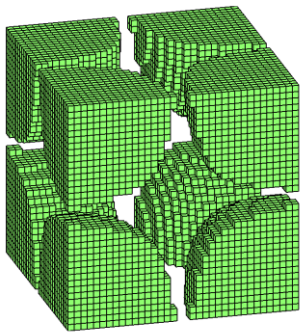
(d) 0.0032505	(e) 0.2288	(f) 0.3929
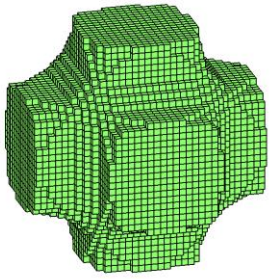	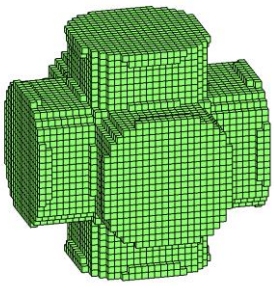	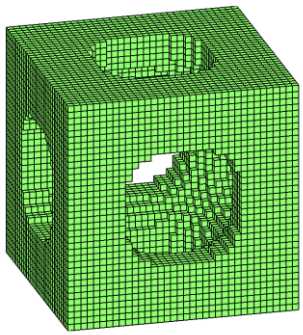
(g) 0.003178	(h) 0.1535	(i) 0.3306
	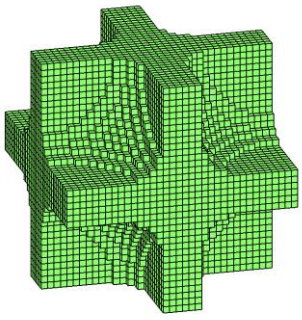	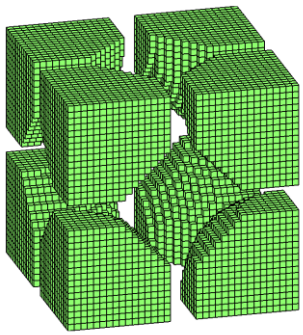
	(j) 0.2287	(k) 0.3889
	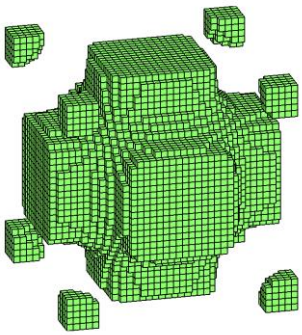	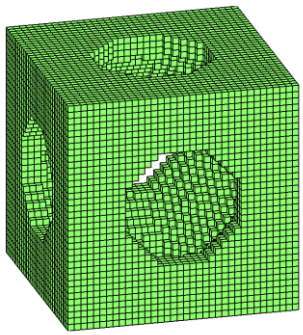
	(l) 0.1441	(m) 0.3305

Figure 4-28. The optimised tissue scaffold models using the isosurface method (a-c), the conventional level set method with intermediate materials (d-f) and without (g-i), SIMP with MMA solver (j-k), and BESO without intermediate materials (l-m).

The averaging operations of the LSF and the velocity function (section 4.2.2.2) ensured that the topology change took place symmetrically. These operations had also helped dampen the numerical error originated from the unstructured mesh. The topology could therefore converge smoothly with limited fluctuation in the objective number, which was mostly affected by the size of time step (Figure 4-30, level set method).

It has been suggested that for 50% porosity, the Schwarz's primitive structure has the highest permeability [5] and the even wall shear stress [11]. This study attempted to verify these claims by building and testing isosurface model of the Schwarz's primitive structure, and characterizing the fluid dynamics behaviour. The result of this study reveals that the Schwarz's primitive structure has a lower permeability and higher wall shear stress than the model optimized for permeability.

Topologically, the Schwarz's primitive structure shows resemblance but is not the exact shape of the optimized model (Figure 4-29). More specifically, the cross-sectional shape of channels in the optimized model is close to perfect circle (Figure 4-29a), whereas the Schwarz's primitive structure has more diamond-shaped channels, which account for the less uniform wall shear stress distribution (Figure 4-29b). The channel necks in the optimized model are also wider and straighter than those in the Schwarz's primitive structure. Wider channels imply lower flow resistance, thus higher permeability.

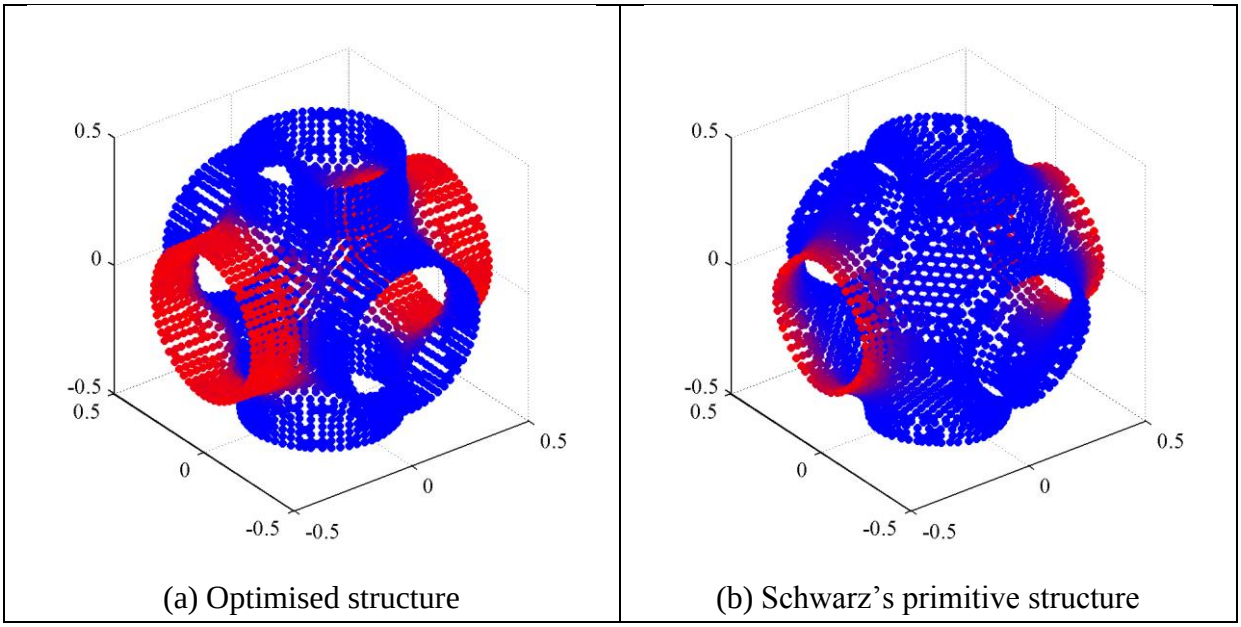

(a) Optimised structure (b) Schwarz's primitive structure

Figure 4-29. Normalized wall shear stress distribution on the isosurface wall in the permeability models. The wall shear stress is more concentrated in the Schwarz's primitive structure.

4.4.3 Optimisation comparison

Overall, the isosurface models have the highest objective numbers and the most stable convergence history, albeit slower structural evolution than the SIMP models (Figure 4-30). It was found that both BESO (Figure 4-28 h and i) and conventional level set method without banded material boundary (Figure 4-28 l and m) experienced difficulty in initiating drastic topology transition. The initial channelled structure (Figure 4-28h in particular) failed to transform and develop cellular-lattice structure like those found using other methods (Figure 4-28b, c, e, f, j and k). As a result, the effective material properties stopped increasing after a small number of iterations (Figure 4-30 b-c, solid/void level set models). Changing the initial model from three orthogonal square channels to the Schwarz's primitive surface model helped improve the optimisation result but only to a small extent (Figure 4-30a, Level set (2) and (1), respectively). Using density-based element enabled the models to break the transformation barrier and increase the objective value (Figure 4-30 b-c, density-based level set models).

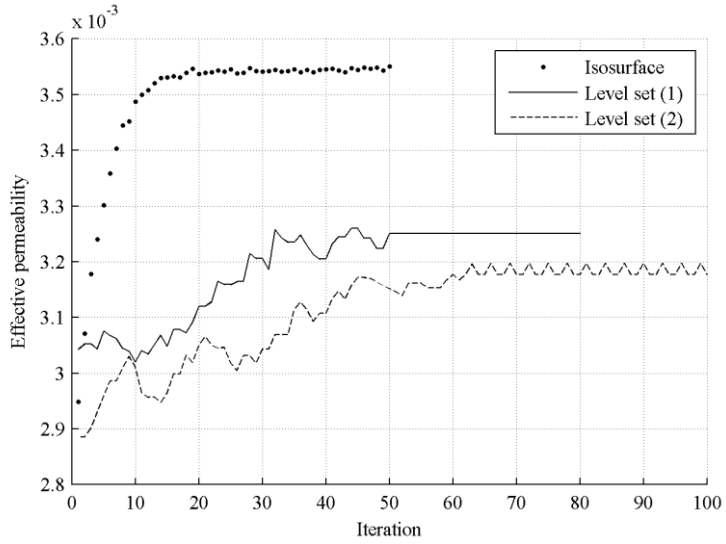

(a) Effective permeability. All models are non-density-based.

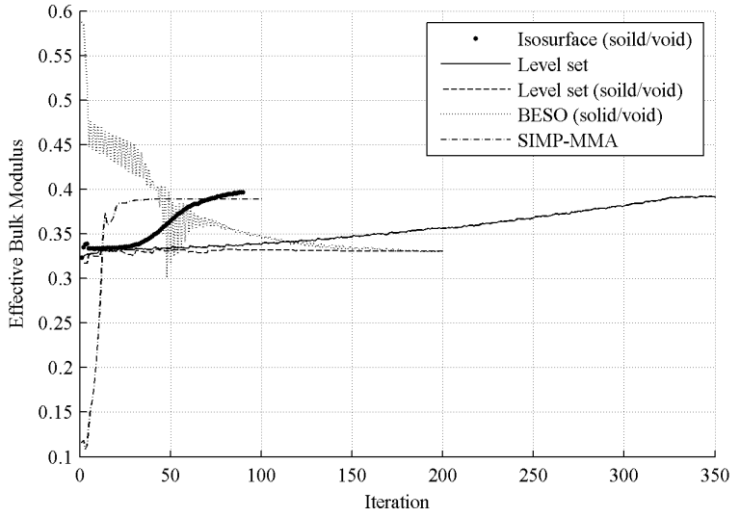

(b) Effective bulk modulus

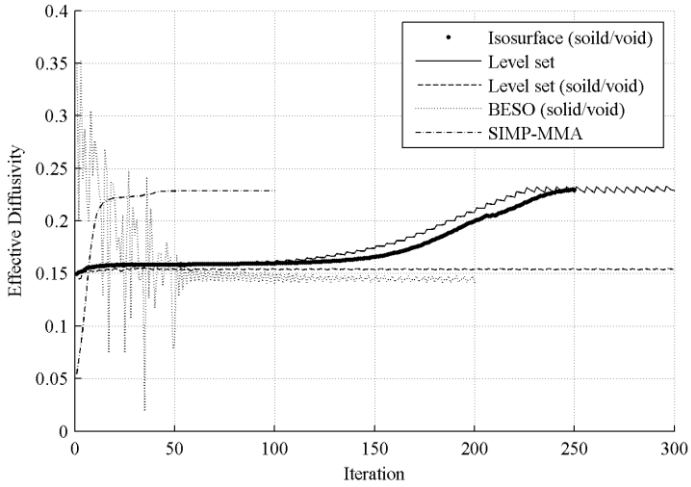

(c) Effective diffusivity

Figure 4-30. The convergence of objective functions. The solid/void label denotes non-density-based models.

Density-based models were considered non-ideal for computational fluid dynamics simulation as there was no obvious boundary at which non-slip boundary condition could be applied. Furthermore, the Navier-Stokes equation only describes flow behaviour in purely fluidic space, therefore homogenisation of permeability could not be carried out on a SIMP-based model. A past study done by Guest et al. attempted to work around this modelling limitation by combining Stokes Equation and Darcy's equation to describe the fluid behaviour in the partially solid element [5]. The resultant effective permeability found in their study (0.0032) is lower than the finding from isosurface modelling.

The SIMP method had improved the effective bulk modulus and diffusivity values, which matched the values found using the isosurface method (Figure 4-30 b-c). However, at the same modelling resolution, the optimised isosurface models attained a slightly higher diffusivity value when the models converged (Figure 4-28c versus k). Improved modelling accuracy and flexibility was likely the reason why the isosurface method outperformed the fixed-mesh methods. Such advantage becomes more obvious at low modelling resolution,

where the possible isosurface shape and configuration remains unlimited (Figure 4-31) whereas voxelised models have limited possible configurations (Figure 4-31c).

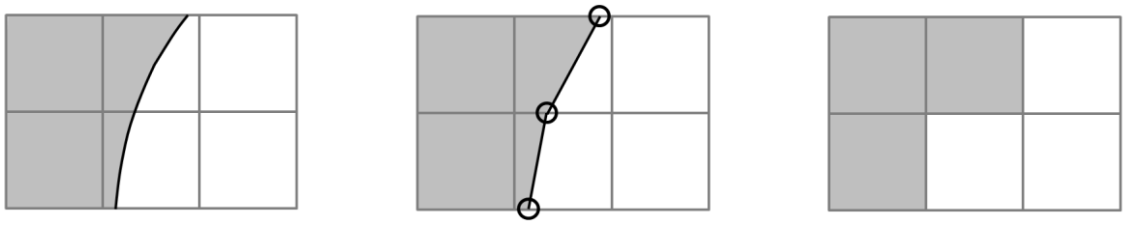

(a) (b) (c)

Figure 4-31. Schematics of boundary configuration: (a) original boundary; (b) isosurface interpretation; (c) voxelised interpretation.

A drawback of the isosurface method is that it requires extra computational time due to additional modelling operations and slower convergence. The preparation and postprocessing of isosurface model and other related operations accounted for approximately 5% of the total computation time; the re-initialisation added another 6-7% per iteration to the process but it was only performed every fourth iteration. For the level-set based optimisation, the periodic boundary condition was applied, which took longer to solve than the symmetry boundary condition. For the non-level-set-based bulk modulus and diffusivity optimisations, one eighth of the RVE model was used and symmetry boundary condition was applied to reduce computational cost.

Overall, the isosurface implementation has improved the modelling accuracy of topology optimisation. It can be seen in the convergence history that voxelised models have less smooth convergence history (Figure 4-30c). Furthermore, this technique helped avoid reversing the topology evolution progress during re-initialisation, which could happen to voxelised level-set models [40]. This study had presented the isosurface-based re-initialisation as a practical alternative to the existing re-initialisation technique. The model quality was improved without increasing the resolution of level set function, which directly influenced the computational cost. It was also found that the cost to extract and discretize

isosurface was small when compared to other parts of optimisation algorithm, accounting for a 5% to 10% increase in the total computational time.

A flood-fill strategy had been implemented to quickly construct the full velocity function and the signed-distance function in regions far away from the isosurface. The result was a smoother velocity function (Figure 4-32). This reconstructed velocity function allowed the non-boundary region of the level set model to be appropriately adjusted. Such extended model adjustment was effective in minimising the deterioration of gradient field by allowing the entire level set model to move at the same speed as the closest boundary. Additionally, it reduces the need of re-initialisation.

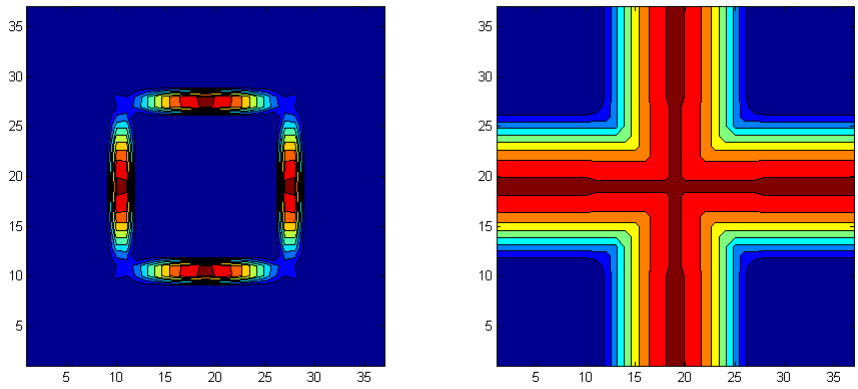

Figure 4-32. Cross-sectional contour plots of velocity function before (left) and after (right) flood-fill after the first time step.

The unstructured FE mesh and the LSF update had been identified as two major sources of numerical error. This error accumulated over iterations and caused the model volume to deviate from the target value. With the isosurface modelling implementation, the volume fraction of the solid and void domains was calculated by summing up the volume of the tetrahedral elements; whereas in the voxelised models, the volume would be the sum of the hexahedral element volumes. The change in volume in the discretised model had been more difficult to predict due to the added modelling complexity. This became a problem especially during the isosurface smoothing process in which nodes could shift slightly away from the

initial isosurface every time they were moved or deleted. Such error accumulated over extensive node moving-deletion process. Another contributor to the volume error was the LSF update, where the change in LSF depends on the gradient field. As the smoothness of the gradient field deteriorated, the accuracy suffered.

The original level set method rectified the volumetric discretisation error by adding additional correction term on top of the Lagrange multiplier (θ from Eq. (4-34)) [31]. This study has applied the same strategy. However, it was found that large optimisation step size could occasionally result in significant numerical errors that clearly violated the volume constraint. Furthermore, using large time step led to the severe fluctuation in the resultant solid volume as well as the objective number. To resolve this issue, the volume correction was carried out repeatedly until the volume constraint was satisfied or the error (residual) was reduced to an acceptable level. Computationally, these purely correctional iterations could be executed by skipping the optimisation process whenever the volume constraint was not satisfied.

Conventional level set optimisation method makes use of smeared Heaviside function, H(x), and $\delta(x)$ function to compute sensitivity (Eqs. (4-8) and (4-9)). This formulation creates a grey sensitivity zone around the level set boundary (Figure 4-33 a-b). The sensitivity of an element is adjusted depending on the distance between the element and the implicit level set boundary. The fact that Heaviside function is user-defined makes the sensitivity function dependent on the programmer's choice of interpretation. The isosurface modelling technique resolves such dependency by defining a material boundary explicitly (Figure 4-33 c-d). Based on the explicit formulation, the sensitivity function is only non-zero on the isosurface $\phi = 0$, so that every node is either 100% sensitive or 0% sensitive.

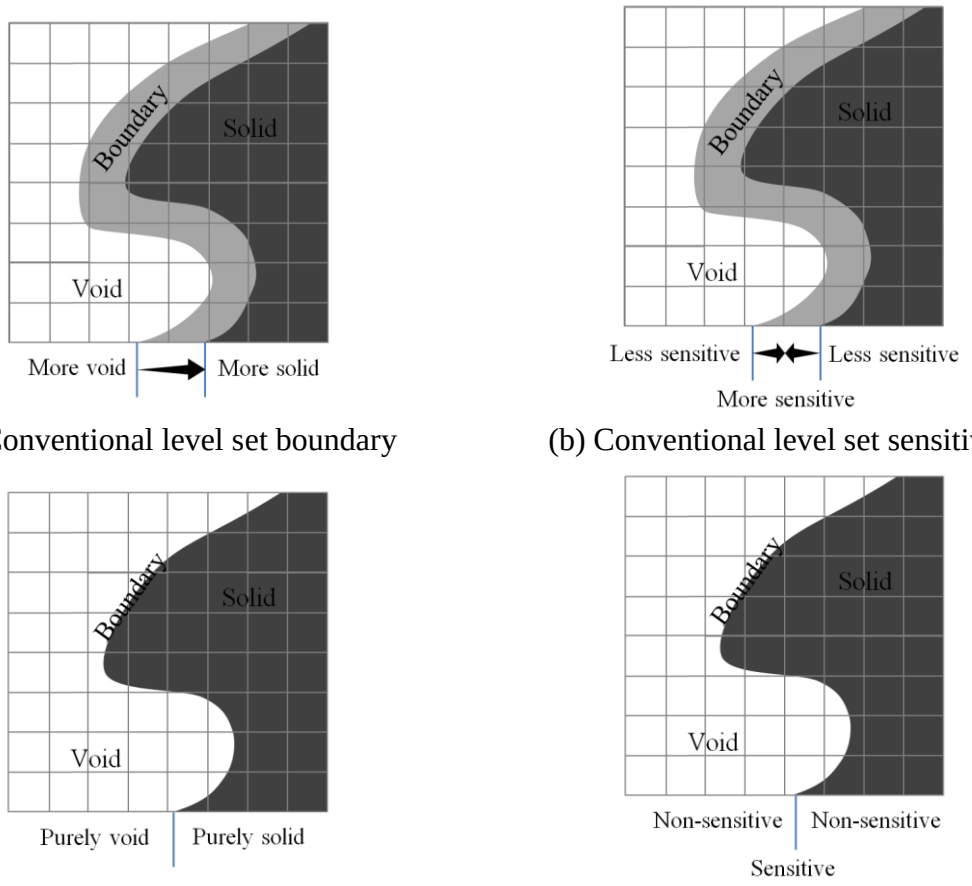

(a) Conventional level set boundary (b) Conventional level set sensitivity

(c) Isosurface boundary (d) Isosurface sensitivity

Figure 4-33. Comparison between conventional method and isosurface formulation.

Maintaining signed distance function is the most common re-initialisation strategy and has been a crucial part of level set based optimisation process. It maintains the smoothness of the LSF and allows topological change to take place in a correct manner. Without proper and timely re-initialisation, the degrading gradient field of LSF can undermine solution convergence [31]. The reason that the gradient field can deteriorate can be seen in Figure 4-33b. Conventionally, the velocity function is only non-zero within the grey boundary zone, which implies that the LSF change would only occur in this region. Changing the LSF in the far regions has no effect on the topology. This restricted LSF movement inevitably steepens the gradient field on one side and flatten the other. Hence it necessitates the re-initialisation. In contrast, the flood-filled velocity function devised by this study extended the LSF movement to the entire 3D domain. The far regions move alongside the level set boundary at

the same speed. Such numerical advection minimises the undesirable squeezing (steepening) or stretching (flattening) of the LSF and its gradient field, thus it minimises the distortion and the deterioration. Furthermore, the flood-fill re-initialisation strategy used in this study lowered the computational cost in reconstructing the less sensitive part of LSF.

The Courant–Friedrichs–Lewy stability condition requires the level set function to be updated at a rate no faster than one grid space per iteration. However, additional tests performed in this study showed that a maximum step size greater than one grid-space had no significant effect on model evolution. This was likely a result of the improved LSF update and re-initialisation, which was performed every fourth iteration and largely dampened the numerical instability. The convergence pattern was stable as long as the re-initialisation dampened the instability faster than it could accumulate. Note that the time step size capped the maximum boundary movement (Eq. (4-35)), therefore only part of the isosurface advanced at a rate faster than one grid space per iteration.

The implementation of dynamic and adaptive FE mesh generation has been one of the greatest technical barriers to conducting topology optimisation with smooth models. The underlining issue of the conventional level set tracking method is the lack of defined boundary outline for smooth surface for body meshing processes. This issue was resolved in this study by means of isosurface extraction, which provided a rigorous foundation for FE surface mesh. However, the program had been relying on *tetgen* to produce body mesh, as it was the only open-source mesh generator found suitable at the time this study was undertaken. Another technical limitation has been the programmability of external software. The ability to prescribe mesh parameters such as mesh density function would improve the accuracy, especially in CFD simulation with high Reynolds number. Discretising highly tortuous geometrical features and creating holes in the model would also require more robust

program. Both concepts are beyond the scope of this study. Despite all these technical challenges, the isosurface modelling technique is proven to be a viable approach to the design and optimisation of microstructure of tissue scaffolds.

4.5 Programming considerations

Compiling a topology optimisation program from individual, independent functions allows more flexibility when coding. The proposed programming framework permits individual functions and solvers to be changed and re-run with minimal effort. In multiobjective topology optimisation, such programming flexibility is especially important since drawing the Pareto front requires a large number of simulations, each with a slightly different objective function. In Chapter 5 for example, the relative weights of individual objective values and sensitivity formulation could be adjusted effortlessly. This framework is also useful in debugging the program and in assessing the effect of optimisation parameters such as mesh size and sensitivity filter. Troubleshooting can therefore be less time consuming since syntax errors can be easily isolated and detected.

The major reason for using the external FEA solver (ANSYS) is that commercial sparse matrix solvers tend to be more efficient and optimised, speed-wise and resource-wise. Writing an FEA solver using a high level language such as Matlab is usually easy if the FEM model has a fixed and structured mesh, i.e. all elements are cubic and have the same volume. However, it takes significantly more time to run the simulations. The introduction of the isosurface modelling method has increased the programming complexity as well as the hardware requirement, which made a Matlab solver a less practical choice.

To obtain the homogenised material properties in 3D space, a model has to be solved multiple times, each time with a different set of load and boundary conditions. To save time and computational resources, individual solution processes can be cascaded so that one occurs after another without quitting the external solver. In the simulations presented here, the DOF results were written directly to external files and then erased at the end of each matrix-solving process. A new set of BCs were applied, and the next solution process began. This workflow helped save time by eliminating overhead cost, i.e. loading the program, loading finite element mesh, and building the global stiffness matrix. The cascaded process could be terminated early without losing the results as they were written to files independently and immediately before the next solution process began.

The most complex component of these script generators is the boundary condition writer, which has the ability to write different types of boundary conditions. The reason for including many BC options is that obtaining solution convergence usually requires trial and error; it is often unclear at the beginning which type of boundary condition would generate the best result. Although the compilation of the BC options is time consuming, once done, this allows quick switch from one combination of loading and DOF conditions to another by simply changing the value of the input parameters in the main script file.

Commercial FEA programs that are currently available have very limited topology optimisation capability. The homogenised stiffness matrix E_{ij}^{H} is commonly known as the strain energy or the energy dissipation by the FEA programs (Eq. ((4-15), ((4-20) and ((4-23)). However in ANSYS, the elemental volume cannot be explicitly obtained or exported. As a result, the mathematical integration of E_{ij}^{H} could not be done within the program. Also the calculation of the off-diagonal matrix entries of E_{ij}^{H}, i.e. $i \neq j$, involves matrix multiplication. The programming complexity of carrying out a matrix multiplication in

ANSYS is no less than writing a stand-alone program. For this reason, all numerical operations were performed outside ANSYS using Matlab functions.

To save computational time in the node-to-grid interpolation, instead of finding the sensitivity at each grid point one by one, i.e. starting from j = 1, then j = 2 and so on:

$$Obj_{G_j} = \frac{\Sigma_{\mathrm{i}}\left(\frac{Obj_{\mathrm{N_i}}}{L_i+k}\right)}{\Sigma_{\mathrm{i}}\left(\frac{1}{L_i+k}\right)},$$

this can be done more efficiently by going through the nodal list (i = 1, 2, …) and update all Obj_{G_j} values systemically. More importantly, most grid points do not have a boundary node in the neighbourhood and the processing time is essentially a waste. Going through all the nodes j times translates to (n× j) times of processing. To eliminate such time wastage, the program can go through the node list instead and only add the nodal values ($Obj_{\mathrm{N_i}}$) to those grid points (Obj_{G_j}) that are in the vicinity, so that the grid points that have no neighbouring boundary node will never be considered in the first place. Using the schematic example of Figure 4-15 and starting with N_1, its distance-weight to all neighbouring grid points is calculated and the respective $\frac{Obj_{\mathrm{N_1}}}{L_i+k}$ and $\frac{1}{L_i+k}$ is added directly to the nominator and denominator of $Obj_{\mathrm{G_j}}$, N_2 and so on are then processed. The final values of $Obj_{\mathrm{G_j}}$ remain known until all i nodes are processed.

The location of a node determines which and how many grid points are involved in the computation. As illustrated in Figure 4-34, N_1 at the centre of the cube has eight neighbouring grid points ($\mathrm{G}_{1,2\ldots,8}$); N_2 on a face has four neighbouring grid points ($\mathrm{G}_{1,4,5,8}$); N_3 on a grid-line has two neighbouring grid points ($\mathrm{G}_{6,7}$); and N_4 which is at the same location as G_2 has only one neighbour, which is obviously G_2.

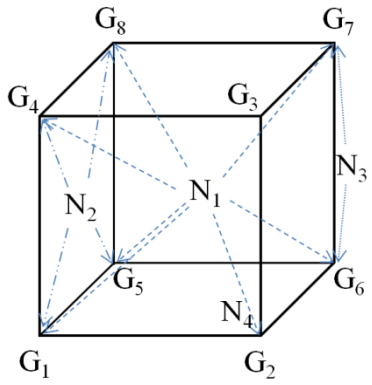

Figure 4-34. A schematic sketch depicting the relationship between nodal position and the number of neighbouring grid points.

The LSF update mechanism used in this function is significantly different from the established level set method. These operations focus on the discrete unstructured isosurface model. Some concepts of the level set method are not strictly followed, including the derivation of sensitivity function and volume correction. The flood-filled part of velocity function in particular has no mathematical or topological significance, because it theoretically has no effect on the final modelling outcome. However in the modelling context, they can still affect the gradient field. This indirectly affects the modelling accuracy whenever the LSF is updated, given that LSF change is a function of its gradient (see section 4.2.2.3).

4.6 Concluding remarks

The incorporation of isosurface modelling into the level set optimisation algorithm has improved various aspects of the topology optimisation, including the model definition, numerical accuracy, and convergence. The explicit boundary modelling and dynamic re-meshing have been successful implemented in this study through the computation of unstructured isosurface from the structured level set function matrix. The effective materials properties obtained from isosurface modelling are the closest to the theoretical maximum values for any design objective compared to the other optimisation methods. On the other

hand, fixed-mesh methods such as BESO, SIMP and LSM had only been able to obtain the optimal structures by using density-based modelling.

The isosurface modelling capacity have been tested in topology optimisation with effective permeability, bulk modulus and diffusivity criteria. At a reasonably low computational expense, this new technique has produced better optimisation results than those found using the conventional level set method and BESO. This is also suitable for computational fluid dynamics simulation where SIMP method may not be applicable. The optimisation of permeability structure in particular shows the importance of smooth boundary modelling that could only be achieved using the proposed method. Overall, the isosurface-based topology optimisation technique is more suitable for the design of porous tissue scaffolds.

4.7 References

[1] Malda, J., Woodfield, T.B., van der Vloodt, F., Kooy, F.K., Martens, D.E., Tramper, J., van Blitterswijk, C.A. & Riesle, J. 2004. The effect of PEGT/PBT scaffold architecture on oxygen gradients in tissue engineered cartilaginous constructs. *Biomaterials,* 25**,** 5773-80.

[2] Melchels, F.P.W., Barradas, A.M.C., van Blitterswijk, C.A., de Boer, J., Feijen, J. & Grijpma, D.W. 2010. Effects of the architecture of tissue engineering scaffolds on cell seeding and culturing. *Acta Biomaterialia,* 6**,** 4208-4217.

[3] Melchels, F.P.W., Tonnarelli, B., Olivares, A.L., Martin, I., Lacroix, D., Feijen, J., Wendt, D.J. & Grijpma, D.W. 2011. The influence of the scaffold design on the distribution of adhering cells after perfusion cell seeding. *Biomaterials,* 32**,** 2878-2884.

[4] Silva, M.M., Cyster, L.A., Barry, J.J., Yang, X.B., Oreffo, R.O., Grant, D.M., Scotchford, C.A., Howdle, S.M., Shakesheff, K.M. & Rose, F.R. 2006. The effect of anisotropic architecture on cell and tissue infiltration into tissue engineering scaffolds. *Biomaterials,* 27**,** 5909-17.

[5] Guest, J.K. & Prévost, J.H. 2006. Optimizing multifunctional materials: Design of microstructures for maximized stiffness and fluid permeability. *International Journal of Solids and Structures,* 43**,** 7028-7047.

[6] Rose, F.R., Cyster, L.A., Grant, D.M., Scotchford, C.A., Howdle, S.M. & Shakesheff, K.M. 2004. In vitro assessment of cell penetration into porous hydroxyapatite scaffolds with a central aligned channel. *Biomaterials,* 25**,** 5507-14.

[7] Croll, T.I., Gentz, S., Mueller, K., Davidson, M., O'Connor, A.J., Stevens, G.W. & Cooper-White, J.J. 2005. Modelling oxygen diffusion and cell growth in a porous, vascularising scaffold for soft tissue engineering applications. *Chemical Engineering Science,* 60**,** 4924-4934.

[8] Hosseinkhani, H., Hosseinkhani, M., Tian, F., Kobayashi, H. & Tabata, Y. 2006. Ectopic bone formation in collagen sponge self-assembled peptide-amphiphile nanofibers hybrid scaffold in a perfusion culture bioreactor. *Biomaterials,* 27**,** 5089-98.

[9] Bettahalli, N.M.S., Steg, H., Wessling, M. & Stamatialis, D. 2011. Development of poly(l-lactic acid) hollow fiber membranes for artificial vasculature in tissue engineering scaffolds. *Journal of Membrane Science,* 371**,** 117-126.

[10] Chen, Y.H., Zhou, S.W. & Li, Q. 2009. Computational design for multifunctional microstructural composites. *International Journal of Modern Physics B,* 23**,** 1345-1351.

[11] Chen, Y., Zhou, S., Cadman, J. & Li, Q. 2010. Design of cellular porous biomaterials for wall shear stress criterion. *Biotechnology and Bioengineering,* 107**,** 737-746.

[12] de Kruijf, N., Zhou, S., Li, Q. & Mai, Y.-W. 2007. Topological design of structures and composite materials with multiobjectives. *International Journal of Solids and Structures,* 44**,** 7092-7109.

[13] Chen, Y., Zhou, S. & Li, Q. 2010. Multiobjective topology optimization for finite periodic structures. *Computers & Structures,* 88**,** 806-811.

[14] Jung, Y., Chu, K.T. & Torquato, S. 2007. A variational level set approach for surface area minimization of triply-periodic surfaces. *J. Comput. Phys.,* 223**,** 711-730.

[15] Chang, C., Zhou, S., Chen, Y. & Li, Q. 2012. Characterization of Fluid Dynamic Properties of Schwarz's Primitive Cellular Materials. *World Journal of Engineering,* 7**,** 167-168.

[16] Zhou, S. & Li, Q. 2008. A variational level set method for the topology optimization of steady-state Navier–Stokes flow. *Journal of Computational Physics,* 227**,** 10178-10195.

[17] Guest, J.K. & Prévost, J.H. 2007. Design of maximum permeability material structures. *Computer Methods in Applied Mechanics and Engineering,* 196**,** 1006-1017.

[18] Huang, X. & Xie, Y.M. 2011. Evolutionary topology optimization of continuum structures including design-dependent self-weight loads. *Finite Elements in Analysis and Design,* 47**,** 942-948.

[19] Wang, M.Y., Wang, X. & Guo, D. 2003. A level set method for structural topology optimization. *Computer Methods in Applied Mechanics and Engineering,* 192**,** 227-246.

[20] Takezawa, A., Nishiwaki, S. & Kitamura, M. 2010. Shape and topology optimization based on the phase field method and sensitivity analysis. *J. Comput. Phys.,* 229**,** 2697-2718.

[21] Taboas, J.M., Maddox, R.D., Krebsbach, P.H. & Hollister, S.J. 2003. Indirect solid free form fabrication of local and global porous, biomimetic and composite 3D polymer-ceramic scaffolds. *Biomaterials,* 24**,** 181-94.

[22] Allaire, G. 2002. *Shape Optimization by the Homogenization Method*, Springer.

[23] Allaire, G., Jouve, F. & Toader, A.-M. 2004. Structural optimization using sensitivity analysis and a level-set method. *Journal of Computational Physics,* 194**,** 363-393.

[24] Sussman, M., Smereka, P. & Osher, S. 1994. A level set approach for computing solutions to incompressible two-phase flow. *J. Comput. Phys.,* 114**,** 146-159.

[25] Sethian, J.A. 1999. *Level Set Methods and Fast Marching Methods: Evolving Interfaces in Computational Geometry, Fluid Mechanics, Computer Vision and Materials Science*, Cambridge: Cambridge University Press.

[26] Gomes, J. & Faugeras, O. 2000. Reconciling Distance Functions and Level Sets. *Journal of Visual Communication and Image Representation,* 11**,** 209-223.

[27] Osher, S. & Fedkiw, R.P. 2001. Level Set Methods: An Overview and Some Recent Results. *Journal of Computational Physics,* 169**,** 463-502.

[28] Zhou, S., Li, W. & Li, Q. 2010. Level-set based topology optimization for electromagnetic dipole antenna design. *Journal of Computational Physics,* 229**,** 6915-6930.

[29] Labelle, F. & Shewchuk, J.R. 2007. Isosurface stuffing: fast tetrahedral meshes with good dihedral angles. *ACM SIGGRAPH 2007 papers.* San Diego, California: ACM.

[30] Victoria, M., Querin, O.M. & Martí, P. 2011. Topology design of three-dimensional continuum structures using isosurfaces. *Advances in Engineering Software,* 42**,** 671-679.

[31] Challis, V. 2010. A discrete level-set topology optimization code written in Matlab. *Structural and Multidisciplinary Optimization,* 41**,** 453-464.

[32] Hill, R. 1963. Elastic properties of reinforced solids: Some theoretical principles. *Journal of the Mechanics and Physics of Solids,* 11**,** 357-372.

[33] Sanchez-Palencia, E. 1983. Asymptotic Analysis II — Homogenization method for the study of composite media *In:* VERHULST, F. (ed.). Springer Berlin / Heidelberg.

[34] Wang, X., Mei, Y. & Wang, M.Y. 2004. Level-set method for design of multi-phase elastic and thermoelastic materials. *International Journal of Mechanics and Materials in Design,* 1**,** 213-239.

[35] Edelsbrunner, H. & Shah, N.R. 1996. Incremental Topological Flipping Works for Regular Triangulations. *Algorithmica,* 15**,** 223-241.

[36] Si, H. & Gaertner, K. Meshing Piecewise Linear Complexes by Constrained Delaunay Tetrahedralizations. 14th International Meshing Roundtable, September 2005 2005. 147-163.

[37] Si, H. On Refinement of Constrained Delaunay Tetrahedralizations. 15th International Meshing Roundtable, September 2006 2006.

[38] Fang, Q. & Boas, D. Tetrahedral mesh generation from volumetric binary and gray-scale images. IEEE International Symposium on Biomedical Imaging 2009, 2009. 1142-1145.

[39] Svanberg, K. 1987. The method of moving asymptotes—a new method for structural optimization. *International Journal for Numerical Methods in Engineering,* 24**,** 359-373.

[40] Huang, X., Radman, A. & Xie, Y.M. 2011. Topological design of microstructures of cellular materials for maximum bulk or shear modulus. *Computational Materials Science,* 50**,** 1861-1870.

[41] Challis, V.J. & Guest, J.K. 2009. Level set topology optimization of fluids in Stokes flow. *International Journal for Numerical Methods in Engineering,* 79**,** 1284-1308.

5 Multiobjective Topology Optimisation of Tissue Scaffolds

The viability of a porous tissue scaffold depends on well-maintained oxygen transport and nutrient supply. It is known that the porous architecture of a scaffold plays a critical role in oxygen transportation and tissue regeneration outcome. While past computational studies had designed a range of microstructures with optimised mechanical and fluid dynamics properties, their ability to sustain long term and long distance oxygen supply was rarely investigated. To accurately define and assess the optimal scaffold microstructures, multiobjective topology optimisation was conducted based on effective diffusivity and effective bulk modulus criteria, and through a combined level-set and isosurface method. Following this, an oxygen diffusion simulation was carried out on a selected optimised microstructure and a sample of an unstructured scaffold for comparison.

A range of optimised microstructures with different combinations of diffusivity and effective bulk modulus were to be defined by isosurface modelling. This study aims to demonstrate the benefits of multiobjective topology optimisation for scaffold design involving oxygen transport.

5.1 Introduction

Maintaining adequate oxygen and nutrient supply is the key to maintain a viable environment for tissue regeneration in tissue scaffolds [1, 2]. The structure of tissue scaffolds in particular plays a critical role in nutrient transportation, cell infiltration and mechanical support [2, 3]. The presence of cells is also known to have a considerable effect on oxygen transport [4]. A range of scaffold structural requirements have been so far established in terms of porosity [2,

5, 6], pore size [7] and connectivity [8] to address those design issues. However, merely meeting these basic structural requirements does not guarantee successful tissue regeneration [9-12]. It has been shown that the scaffold topology plays a more influential role in cell migration and nutrient transport, which subsequently determine the outcome of cell distribution and proliferation [8], all together forming a complex biological feedback cycle.

Poor cell infiltration in scaffolds is a major challenge in tissue engineering [13]. The implication is that the practical size of tissue scaffolds is limited by cell viability, which diminishes with increasing scaffold depth and decreasing oxygen concentration. To improve cell infiltration, the effect of scaffold structure has been studied extensively in relation to the regulation of cell migration [5, 6] and vascularisation [7]. Pore connectivity has since been identified as one of the key deciders of the effective mass transport and diffusion in scaffolds [8]. Some common strategies for enhancing nutrient transport include increasing porosity, introducing micro-porous structure (~ 1 μm) [13] and constructing dedicated macro-porous channels for the long distance transport [2]. Meanwhile, the conflict between increasing porosity and maintaining structural strength also has to be taken into account in the design process to ensure that the structural integrity is not compromised [14, 15].

Computational design and topology optimisation has demonstrated fair amount of potential in Tissue Engineering [16]. Topology optimisation has been performed to maximise or to create 2D and 3D microstructures with desired conductivity [17, 18], permeability [19-23], stiffness [19, 24, 25] , and bulk modulus [10, 17, 26]. Some studies have suggested using special mathematical models such as minimal surfaces as the building blocks of tissue scaffolds [8, 27, 28]. The fabrication of microstructures can be done by 3D printing [8, 29].

Even though non-parametric topology optimisation methods are well-established, they usually employ fixed-mesh, voxelised modelling techniques that trade off the model quality

for programming simplicity. The ambiguous nature of voxelised models makes it difficult to fabricate scaffolds that physically and accurately reflect the computational results. There is an obvious need to properly define the optimal microstructure, and bridge the gap between computational design and fabrication through an optimisation process that allows the direct translation of computational results to physical products.

In summary, two key challenges remain in the design of porous tissue scaffolds. The first design challenge is to resolve the conflict between structural and transportation properties; and the second challenge is to address the complex interaction and feedback cycle of structural and biological factors. This study aims to address these two issues by using the smooth isosurface modelling technique and the level-set based topology optimisation, and by conducting oxygen consumption simulation to compare the steady-state cell proliferation in both optimised and non-optimised scaffolds. The multiobjective criteria have been created, aiming to maximise the effective diffusivity and bulk modulus of tissue scaffolds concurrently. The actual performance of the optimised scaffold structure is assessed through an oxygen transportation-consumption simulation, in terms of cell viability and oxygen level, and compared to an unstructured titanium scaffold sample.

5.2 Multiobjective topology optimisation

The ultimate goal of tissue scaffold design is to create a lasting, biologically viable environment. For this purpose multi-objective topology optimisation can be used to improve different scaffold properties simultaneously and resolve any conflict among individual objectives. Whatever biological factors that cannot be accounted for in the optimisation process, cell viability for instance, must be assessed separately. To precisely define and characterise the tissue scaffold models in this part of study, the isosurface modelling

technique developed in Chapter 3 had been again utilised. Also based on this technique, a comparison study had been carried out to assess the cell seeding effectiveness of different scaffold structures.

5.2.1 Geometric representation

This study has employed the smooth topology optimisation procedure that combines both implicit level-set and explicit isosurface modelling techniques, but on a multi-objective platform. In this section the level set topology optimisation method and the combined design criteria for diffusivity and bulk modulus are briefly outlined, which correspond to the structural support and nutrient transport requirements of tissue scaffolds, respectively. The next section will describe in detail the incorporation of isosurface modelling and the modification made to the level set method.

Recalling from Chapter 4 that a level set is a collection of all points of a certain value in space. Such set of points forms a surface in the space, which can be used to represent the boundary of a model. A level set function (LSF) is used to track the surface movement over time. This mathematical set has an explicit counterpart known as the isosurface, which can be extracted from the LSF if the location of the level set is interpolated. Mathematically, the level set is defined as:

$$\Gamma: \varphi(x) = k \tag{5-1}$$

where Γ is the level set, φ is the level set function, x is the coordinate system of the modelling space, and k is a constant value. Let $k = 0$, the level set forms a continuous surface and divides the space into two domains: one is the porous space ($\Omega_f: \varphi(x) < 0$, or space filled by fluid in this design scenario) and the other is the solid material of the tissue scaffold ($\Omega_s: \varphi(x) > 0$).

The evolution of the level-set model is controlled by a velocity function, v_n. Conversely, the velocity function can be created according to the desired change or movement of the level-set model. Given a velocity function, the change in LSF required to induce the desired change is solved numerically in the form of a Hamilton-Jacobi equation:

$$\frac{\partial \varphi}{\partial \tau} + v_n |\nabla \varphi| = 0 \tag{5-2}$$

where $\partial \tau$ is the evolution time, and $|\nabla \varphi|$ is the absolute gradient field of the LSF. In topology optimisation, the rate of movement is determined by the sensitivity function so the evolution always results in a net increase in the effective diffusivity and bulk modulus.

The isosurface modelling technique aims to create an explicit boundary from the structured implicit LSF. The goal of this implementation is to replace the conventional voxelised model with smoother finite element mesh, and to improve the numerical accuracy of sensitivity analysis, volume constraint, surface movement and re-initialisation. The key distinction between these two formats, explicit and implicit, is that isosurface modelling requires the physical location of every point of $\varphi(x) = k$ to be identified. In other words, isosurface represents the actual locations of $\varphi(x) = k$, thus explicit.

The generation of an isosurface takes two steps: mesh extraction and mesh smoothening (Figure 5-1). In the discretised 3D LSF space, all level-set points can be extracted directly through linear interpolation (Figure 5-1 a-b). These points are then connected and patched to form one or more continuous triangulated isosurfaces, which are also the material boundaries. This surface mesh is then smoothened to improve its quality as FE mesh (Figure 5-1 c-d).

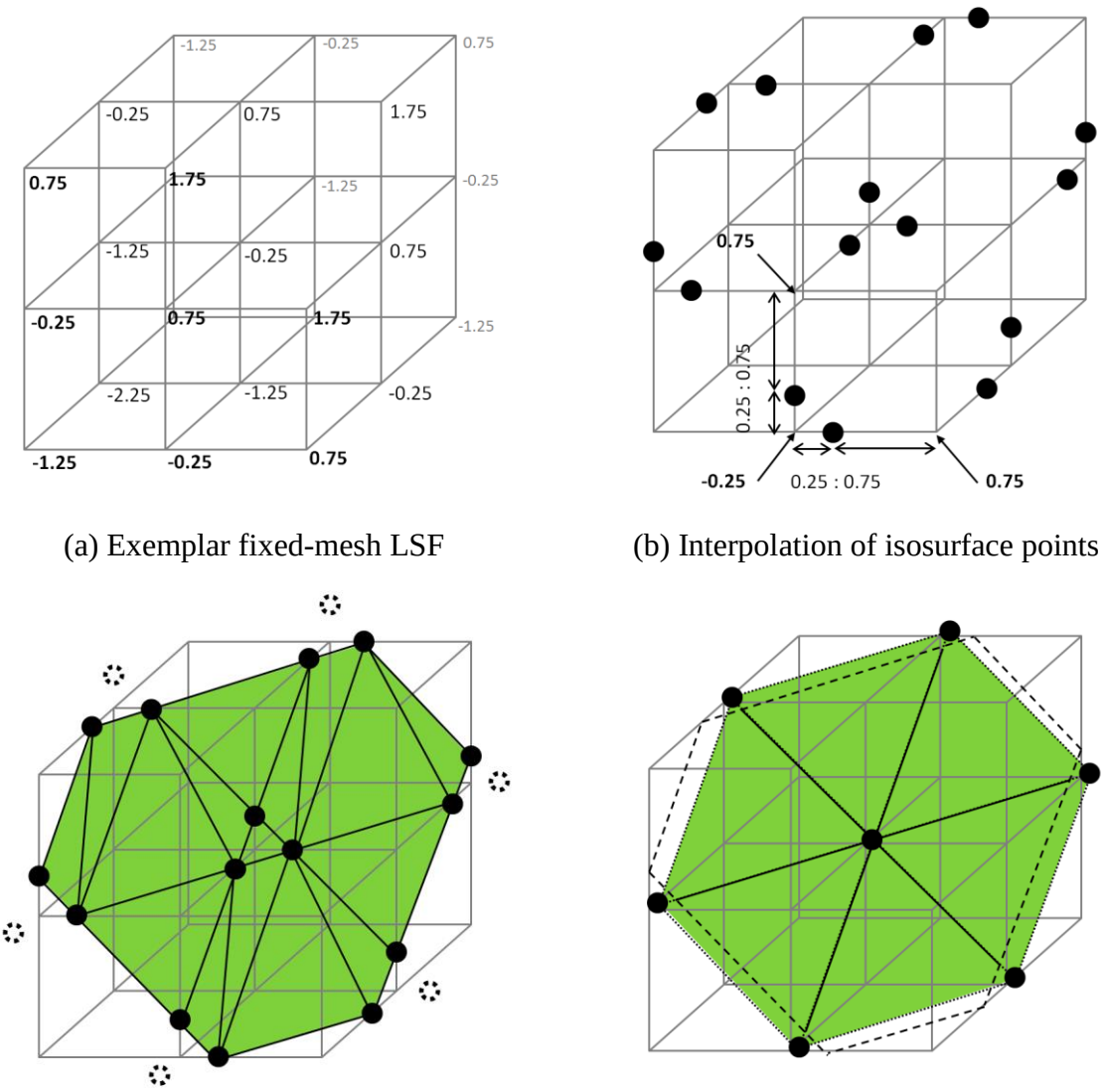

(a) Exemplar fixed-mesh LSF

(b) Interpolation of isosurface points

(c) Face patching with triangles

(d) Mesh smoothing

Figure 5-1. Schematic of the isosurface extraction from a level set function.

Following this, unstructured tetrahedral body mesh is generated on both sides of the isosurfaces to create the 3D FE model. This study has made use of the "iso2mesh" Matlab toolbox [30] and the program, tetgen [31-33] to generate the 3D body mesh. The triangulated surface meshes serve as the foundation for a top-down body mesh generation. Additional points are added to the isosurface by the program to further improve the FE mesh quality. Both the isosurface extraction and the mesh generation are performed every iteration throughout the optimisation process.

5.2.2 Homogenized effective elastic tensor and diffusivity

The effective material properties of a porous material can be computed based on the theory of homogenisation [34]. This involves solving the characteristic response of the representative volume element (RVE) to a unit-strain, followed by the computation of elemental stiffness and diffusivity, and then the summation of the two elemental properties. The homogenised diffusivity can be computed using the following formula:

$$\boldsymbol{D^H} = \frac{1}{V_{RVE}} \int_{\Omega_f} D\left(1 - \frac{\partial u_D}{\partial x}\right) dV \tag{5-3}$$

where $\boldsymbol{D^H}$ is the effective diffusivity of the scaffold, D is the nominal diffusivity of the diffusion media, V_{RVE} is the total volume of the RVE, and u_D is the characteristic concentration obtained by solving the following characteristic equation:

$$\frac{\partial}{\partial x} D\left(I - \frac{\partial u_D}{\partial x}\right) = 0 \tag{5-4}$$

where I is an identity matrix. This equation is solved three times (in x, y and z directions) to obtain three unique responses.

Similarly, the homogenised bulk modulus can be calculated from:

$$\boldsymbol{K^H} = \frac{1}{V_{RVE}} \int_{\Omega_s} \left(1 - \frac{\partial u_K}{\partial x}\right)^T K\left(1 - \frac{\partial u_K}{\partial x}\right) dV \tag{5-5}$$

where $\boldsymbol{K^H}$ is the effective stiffness of the porous structure, K is the nominal stiffness of the solid material, and u_K is the characteristic displacement solution of

$$\frac{\partial}{\partial x} K\left(I - \frac{\partial u_K}{\partial x}\right) = 0 \tag{5-6}$$

where I is an identity matrix. Equation (5-6) is solved three times for three normal strain responses. Subsequently the effective bulk modulus can be calculated:

$$B^H = \frac{1}{9} \sum_{i=1}^{3} \sum_{j=1}^{3} \boldsymbol{K_{i,j}^H}. \tag{5-7}$$

If the effective diffusivity is isotropic, a scalar D^H can be used instead:

$$D^H = \frac{1}{3}\sum_{i=j=1}^{3} \boldsymbol{D_{i,j}^H}. \tag{5-8}$$

This design problem is formulated as a multiobjective optimisation problem, which aims to simultaneously maximise the effective diffusivity and the effective bulk modulus. This operation requires that the effective diffusivity and the effective bulk modulus are normalised. A weight parameter, w, is also assigned to adjust their relative influences to the topology optimisation outcome. Repeating the topology optimisation with different values of w produces a Pareto front ($0 \leq w \leq 1$). The multiobjective function is thereby formulated as:

$$\max \quad J = \frac{D^H}{D_{max}^H} + \frac{B^H}{B_{max}^H} \tag{5-9}$$

$$\text{s.t.} \int_{\Omega_f} dV = V_f$$
$$\frac{D^H B_{max}^H}{B^H D_{max}^H} = \frac{1-w}{w} \quad (0 \leq w \leq 1) \tag{5-10}$$

where D_{max}^H is the maximum achievable effective diffusivity, K_{max}^H is the maximum achievable effective bulk modulus, V_f is the volume constraint of fluid, w is the weight of the normalized bulk modulus, and $(1-w)$ is the weight of the normalized diffusivity. D_{max}^H and B_{max}^H serve as the normalisation factors in Eq. (5-9) and must be determined prior to the multiobjective optimisation. The second condition in the constraint equation (5-10) sets the target, which is the ratio between the normalised effective diffusivity and effective bulk modulus, for each value of w.

5.2.3 Inverse homogenisation using topology optimisation

The topology optimisation method can also be used to design RVE microstructures with desired material properties [35, 36]. In such design scenario, the objective function is formulated in a way that it indicates how close the material properties of current design are to the desired values. The topology is considered optimised when its effective material properties have attained the target numbers. From a macroscopic perspective, it is called the

inverse homogenisation as the effective material properties determine the topology, whereas in homogenisation, topology determines the effective material properties.

5.2.3.1 Targeted stiffness tensor

When designing the microstructure of hard tissue scaffolds, inverse homogenisation technique can be applied to create RVE structure with material properties that match the hard tissue it is replacing. It has been suggested that the stiffness of bone tissue scaffolds should match the host bone [37, 38]. Using the SIMP method and fixed-mesh, an objective function can be formulated in terms of the difference between the targeted stiffness tensor $\boldsymbol{C_{ij}^{*}}$ and the current effective stiffness tensor $\boldsymbol{C_{ij}^{H}}$, subjected to a volume fraction constraint:

$$\begin{cases} \min\limits_{\rho^e} J_S(\rho^e) = \sum\limits_{i,j=1}^{6} \left(\boldsymbol{C_{ij}^{*}} - \boldsymbol{C_{ij}^{H}}(\rho^e)\right)^2 \\ \text{subject to: } 0 < \rho_{min} \le \rho^e \le 1 \\ \dfrac{1}{NE}\sum\limits_{e=1}^{NE}(1-\rho^e) = V_0 \end{cases} \tag{5-11}$$

where ρ is the volume fraction (or "density") of an element, the superscript e denotes elemental property, $\rho_{\min}$ is the minimal allowable density of any element, and NE is the number of elements. $\rho_{min} > 0$, otherwise the model will be singular and unsolvable. The sensitivity of the objective function with respect to the design variable ρ^e is determined by using the adjoint variable method as:

$$\frac{\partial J_S}{\partial \rho^e} = -2\sum_{i,j=1}^{6} r_{ij}\left(\boldsymbol{C_{ij}^{*}} - \boldsymbol{C_{ij}^{H}}(\rho^e)\right)\frac{\partial \boldsymbol{C_{ij}^{H}}(\rho^e)}{\partial \rho^e} \tag{5-12}$$

where r_{ij} is the weight of individual matrix entries, and

$$\frac{\partial \boldsymbol{C_{ij}^{H}}(\rho^e)}{\partial \rho^e} = \sum_{e=1}^{NE}(I - u_i^e)^T \frac{\partial \boldsymbol{C_{ij}^{e}}(\rho^e)}{\partial \rho^e}\left(I - u_j^e\right)dV. \tag{5-13}$$

Each elemental $\boldsymbol{K_{ij}^e}$ value is unique. The method of moving asymptotes (MMA) algorithm [39] is employed to determine the appropriate ρ^e change during the structural evolution.

5.2.3.2 Targeted diffusivity

It has been suggested that designing and using microstructures with low effective diffusivity in places such as cartilage (Malda et al. 2003). In this design scenario, the effective diffusivity can be formulated as an objective, in which the goal is to minimise the difference between the desirable diffusivity $\mathbf{D}^*$ and actual effective diffusivity $\mathbf{D}^{\mathrm{H}}$:

$$\begin{cases} \min_{\rho^e} J_D(\rho^e) = \sum_{i=1}^{3}\left(\boldsymbol{D_{ii}^*} - \boldsymbol{D_{ii}^H}(1-\rho^e)\right)^2 \\ \text{subject to: } 0 < \rho_{min} \le \rho^e \le 1 \\ \frac{1}{NE}\sum_{e=1}^{NE}(1-\rho^e) = V_0 \end{cases}. \tag{5-14}$$

The sensitivity function can be derived directly and the following is obtained:

$$\frac{\partial J_D}{\partial \rho^e} = 2\sum_{i=1}^{3}\left(\boldsymbol{D_{ii}^*} - \boldsymbol{D_{ii}^H}(\rho^e)\right)\frac{\partial \boldsymbol{D_{ii}^H}(1-\rho^e)}{\partial \rho^e}. \tag{5-15}$$

Note that the sensitivity function in this case has the opposite sign to the stiffness sensitivity function since the diffusion domain is the inverted solid domain. Density change therefore has an opposite effect on the diffusivity property.

The stiffness and the diffusivity targets may be combined by summation to form a single objective. In this case, the design outcome aims to match one target property while maximising the other, or aims to match both target properties.

5.2.4 Sensitivity analysis

Let $\alpha = D\left(1-\frac{\partial u_D}{\partial x}\right)$ in Eq. (5-3) and $\alpha = \left(1-\frac{\partial u_K}{\partial x}\right)^T K\left(1-\frac{\partial u_K}{\partial x}\right)$ in Eq. (5-5), the generalized objective functions can be expressed as:

$$J(\varphi) = \frac{1}{V_{RVE}}\int_{\Omega} H(\varphi)\alpha dV \tag{5-16}$$

The time derivative of the objective function can also be written in a general form [40]:

$$\frac{\partial J(u,\varphi)}{\partial \tau} = \int \delta(\varphi)\beta(u,\varphi)v_n|\nabla\varphi|dV \tag{5-17}$$

where $\beta(u,\varphi)$ is some local sensitivity function. Wang et al. had derived the shape derivatives for effective elasticity and effective conductivity in their study, and for a two-phase stiffness problem, the shape derivative of Eq. (5-16) with respect to φ is [41]:

$$\frac{\partial J(u,\varphi)}{\partial \varphi} = -\frac{1}{V_{RVE}}\int \delta(\varphi)\left(1-\frac{\partial u}{\partial x}\right)^T D\left(1-\frac{\partial u}{\partial x}\right)dV \tag{5-18}$$

By chain rule, it can be deduced that $\frac{\partial \varphi}{\partial \tau} = v_n|\nabla\varphi|$. By comparing the time and shape derivatives, $\beta(u,\varphi)$ from Eq. (5-17) can be expressed as:

$$\begin{aligned}\beta(u,\varphi) &= -\frac{1}{V_{RVE}}\left(1-\frac{\partial u}{\partial x}\right)^T D\left(1-\frac{\partial u}{\partial x}\right)\\ &= -\frac{1}{V_{RVE}}\alpha\end{aligned} \tag{5-19}$$

β does not contain an undetermined adjoint variable. Therefore, Eq. (5-17) can be rewritten as:

$$\frac{\partial J(u,\varphi)}{\partial \tau} = -\frac{1}{V_{RVE}}\int \delta(\varphi)\alpha v_n|\nabla\varphi|dV \tag{5-20}$$

Replacing stiffness with diffusivity will yield similar result.

To satisfy the volume constraint, the net change in volume, $\Delta V = \int_\Gamma v_n dS$, must be zero. Therefore, a volume correction term must be introduced to enforce the volume constraint. Let $v_n = -(\alpha+\lambda)$, solve for λ results in the following condition [40],

$$\begin{aligned}\Delta V &= -\int_\Gamma (\alpha+\lambda)dS = 0\\ \lambda &= -\frac{\int_\Gamma \alpha dS}{\int_\Gamma dS}\end{aligned} \tag{5-21}$$

where λ is the volume correction term. $\lambda < 0$ as $\alpha = \left(1 - \frac{\partial u}{\partial x}\right)^T D \left(1 - \frac{\partial u}{\partial x}\right) > 0$. Since dS has already been discretised during the isosurface modelling process, the value of λ can be computed as a surface integral over the isosurface.

Applying $\alpha = -v_n - \lambda$, Eq. (5-20) becomes

$$\frac{\partial J(u,\varphi)}{\partial \tau} = \frac{1}{V_{RVE}} \int \delta(\varphi) v_n^2 |\nabla \varphi| dV + \frac{\lambda}{V_{RVE}} \int \delta(\varphi) v_n |\nabla \varphi| dV \tag{5-22}$$

Due to the volume constraint, $\int \delta(\varphi) v_n |\nabla \varphi| dV = 0$, which leads to:

$$\frac{\partial J(u,\varphi)}{\partial \tau} \geq 0 \tag{5-23}$$

Therefore objective maximisation is guaranteed.

The sensitivity is originally calculated in the unstructured FE domain, whereas the structural evolution occurs in the structured LSF modelling space. For this reason, the sensitivity information must be passed on from the unstructured mesh to the structured LSF system. To do so, firstly, the nodal sensitivity is interpolated from the elemental sensitivity using an inverse distance-weighted method. For each node, the nodal sensitivity is:

$$J_{node} = \frac{\sum_{i=1}^{e} \frac{1}{d_i} J_{element,i}}{\sum_{i=1}^{e} \frac{1}{d_i}} \tag{5-24}$$

where *e* is the total number of elements containing that particular node, and d_i is the distance from the node to the centroid of each element. Due to the large element-to-node ratio in the unstructured mesh, this process is accompanied by some numerical diffusion. Following this operation, the structured LSF sensitivity can be interpolated from the nodal sensitivity through another inverse distance-weighted interpolation:

$$\alpha_{grid} = \sum_{j=1}^{\mathrm{n}} \frac{1}{(d_j + 0.1h)^2} J_{\mathrm{node,j}} \Bigg/ \sum_{j=1}^{\mathrm{n}} \frac{1}{(d_j + 0.1h)^2} \tag{5-25}$$

where n is the total number of nodes around the individual LSF point, and d_j is the distance from the LSF point to each node. Using the squared-weight reduces numerical diffusion. Here adding 0.1 grid space to the distance avoids division by zero in such interpolation process.

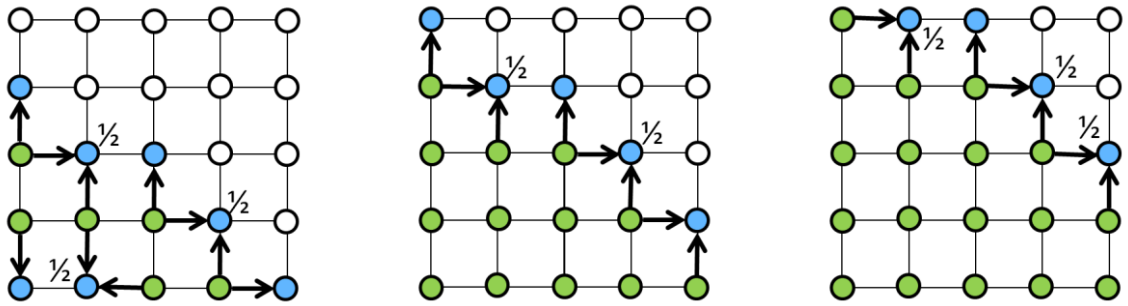

Figure 5-2. Schematic of the iterative flood-filling operation. Green dots represent the points filled by the operation; and blue dots are the points in the von Neumann neighbourhood, to be filled in the next iteration.

A change in topology can only occur if there is a change in sign (+/−) in the LSF. Hence, a regional velocity function that covers the band of $\Gamma: \varphi(x) = 0$ is sufficient to trigger the required structural evolution, since only the points in this band can experience sign-change. The rest of the velocity function can be either disregarded or constructed using an alternative, time-efficient but less accurate algorithm without affecting the overall optimisation. As the aforementioned interpolation process (Eq. (5-24)-(5-25)) already covers the entire band of the isosurface, the result of Eq. (5-25) can be readily used as the velocity function. The flood-filling technique is employed to construct the rest of velocity function as illustrated in Figure 5-2.

Timely re-initialisation of the level set function helps regulate the structural evolution [42]. The re-initialisation aims to regenerate the LSF as a signed-distance function. In this study, this is a straight forward process as the distance between each LSF point and the level-set – isosurface can be computed directly. In addition, the periodic boundary condition and isotropy of RVE is maintained through some numerical operations (see section 4.2.2.2).

5.2.5 Computational viability simulation

In seeded scaffolds, cells occupying the porous space are known to affect the actual effective diffusivity [4]. As a result, the initially scaffold diffusivity may change or deteriorate as the cell population grows and becomes an oxygen transport barrier. To assess the actual optimality of the obtained models, steady-state diffusion tests were conducted and cell viability in two different structures were compared, one optimised and the other non-optimised. In principle, higher oxygen concentration and high cell density are indicators of a better design. The effectiveness of the scaffold design can be assessed in term of cell viability and the steady-state oxygen concentration.

The steady-state oxygen consumption model is governed by the standard diffusion equation:

$$\frac{\partial}{\partial x}\left(D\frac{\partial C}{\partial x}\right)+S=0 \tag{5-26}$$

where C is the oxygen concentration, D is the diffusivity of oxygen in the diffusion medium, and S is the oxygen consumption rate.

To solve this nonlinear equation, it is necessary to correlate both the consumption rate (S) and the oxygen diffusivity (D) to the oxygen concentration (C) or the cell density. Every term in Eq. (5-26) can be expressed as a function of the oxygen concentration (C), which is the only degree of freedom per node. A pre-defined relationship between the oxygen concentration and cell viability is required to assess the viability. In this study, such relationship is derived from the experimental data reported by Radisic et al [43] (Figure 5-3).

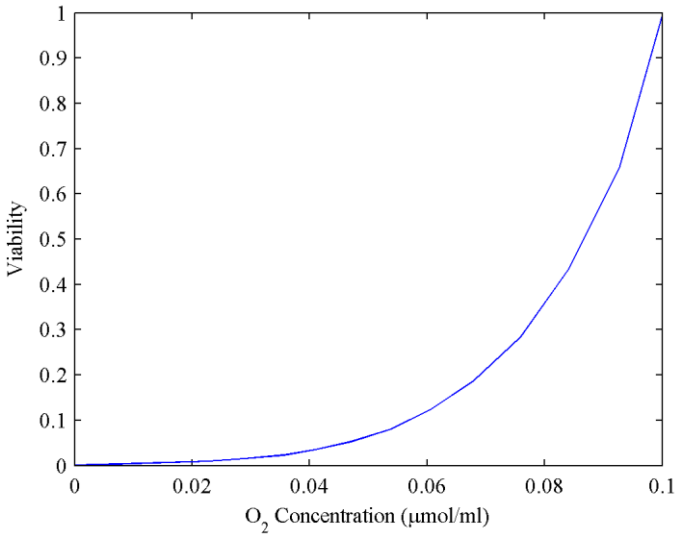

Figure 5-3. Cell viability versus oxygen concentration plot.

The oxygen consumption term from Eq. (5-26) has been implemented as a wall flux boundary condition. The relationship between oxygen consumption and oxygen concentration is governed by the Michaelis-Menten kinetics, and formulated as:

$$S = S_0 N \frac{C}{C + k_m} \tag{5-27}$$

where S is the oxygen flux (consumed), S_0 is the maximum oxygen consumption rate per cell, N is the cell number, and k_m is the Michaelis–Menten constant of half oxygen consumption. This study adopted the set of parameters and material properties of NIH-3T3 cells used by Kang et al. [4]. The maximum oxygen consumption rate S_0 is 7.9×10^{-17} mole/cell/s. The Michaelis–Menten constant k_m is 1.547 μM [44]. In this study, cell densities N of 2.5×10^5 and 1×10^6 cells/cm^3 were used without considering cell proliferation or cell death.

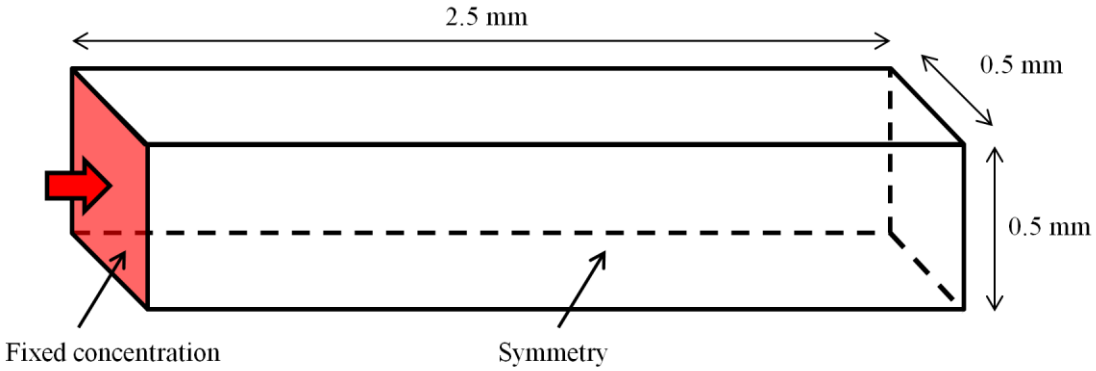

Figure 5-4. Boundary conditions and domain size of the test models. The red boundary is the source with the fixed oxygen concentration.

The simulation was carried out in a 0.5×0.5×2.5 cm^3 modelling domain (Figure 5-4). The optimised scaffold model was created by stacking five optimal cubic RVEs in the direction of oxygen flow (from left to right as illustrated). The non-optimised model was created from the CT-image of a porous tissue scaffold. To simulate the oxygen transport, one face (0.5×0.5 cm^2) of the scaffold model was exposed to a fixed oxygen source at a concentration of 0.1 µmol/ cm^3 (Figure 5-4, red face on the left). The cell distribution on the scaffold internal solid surface was assumed to be initially uniform. To account for the effect of cell deposition on oxygen diffusivity, the porous space occupied by cells was treated as non-diffusive. The resultant fluid diffusivity was calculated based on the simple rule of mixture, i.e. the diffusivity was made directly proportional to the fluid volume fraction. The total non-diffusive volume fraction is equal to the cell number multiplied by the cell volume (1.3×10^{-19} cm^3 / cell [45]).

5.3 Results and discussion

Past studies have applied multiobjective topology optimisation technique to the design of tissue scaffolds, and improved their transportation and mechanical properties [17-23].

However the characterisation of the optimal topology has been problematic due to the use of fixed-mesh modelling in these studies, as FE modelling quality was readily traded off for programming simplicity. A smooth isosurface modelling technique has been thereby proposed and developed, based on the level set method. The primary goal of this study is to accurately define and characterise multiobjective optimisation models with maximised or desired material properties. Additional oxygen consumption simulations have been conducted to assess the optimality of the obtained solutions in terms of cell viability and oxygen concentration.

5.3.1 Isosurface modelling and setup

In this study, the smooth isosurfaces were generated from the structured array of level set function, at a resolution of 37×37×37 (c.f. Figure 5-5). Prior to the volume mesh generation, mesh smoothing was applied to the unrefined isosurface to remove any poorly shaped surface element. The mesh smoothening was carried out through an iterative clean-up process that removed all triangles whose constituting edges fell short of a given tolerance (0.75 × level set grid length). The resultant triangulated surfaces were more evenly sized and spaced after the operation. During the body mesh generation by *Iso2Mesh* [30] and *tetgen* [31-33], additional nodes were added to the isosurface to improve the mesh quality.

An isosurface-based FE model was developed from a CT-image of a tissue scaffold. This model was comparable to the optimised model in terms of pore connectivity, solid integrity, and volume fraction. In this unstructured RVE model, the total volume of isolated or poorly connected pores was about 1-2% of the RVE volume; such void volume was converted and merged into the solid. In the final model, both solid and fluid domains were continuous and each had the volume of 50% of the total volume of the modelling space, the same as the optimised model. The scaffold CT-image, 0.24×0.24×1.2 mm^3 in size, was scaled to

0.5×0.5×2.5 mm^3, at the resolution of 41×41×201. The optimised model was created by stacking five 0.5×0.5×0.5 mm^3 RVEs in a row. In the cell viability assessment, 10% of the total fluid volume was considered occupied by cells, which were considered non-conductive.

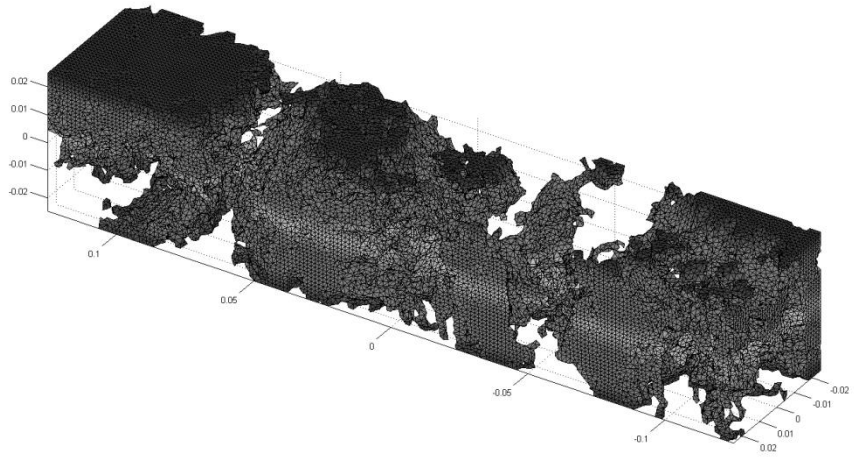

Figure 5-5. The isosurface model of the fluid phase of an unstructured scaffold extracted from a CT-scan image. This model served as the surface mesh of the FEA model.

5.3.2 Topology optimisation

Cubic RVEs were optimised under symmetry, periodicity and isotropy modelling conditions (Figure 5-6a-c). Both solid and fluid volume fractions of the RVEs remained constant at 50% throughout the design process. The starting model used in this optimisation process was a solid cube with three intersecting square channels.

The normalisation of diffusivity and bulk modulus requires the maximum diffusivity and the maximum bulk modulus to be determined first, by running the topology optimisation with w = 0 and w = 1 (Eq. (5-10)), respectively. The maximum effective diffusivity obtained is 0.4 (unit length^2 / s), which coincides with the Hashin-Shtrikman upper bound, whereas the maximum effective bulk modulus obtained is 0.2316 (pressure unit, with Poisson's ratio = 0.3 and elastic modulus E = 1 unit). However in these two cases, there is phase discontinuity in the solid phase and porous phase in the maximum diffusivity and maximum bulk modulus

models, respectively (Figure 5-6(a) and (c). Such discontinuity also implies zero bulk modulus or zero diffusivity. These two cases correspond to the points at two ends of the Pareto front curve (Points A and C in Figure 5-6d). From the design perspective, maximising one material property would compromise the other. In the same figure, the normalised diffusivity and bulk modulus of the unstructured scaffold (CT-image) were marked by Point D, with a diffusivity of 0.2064 (unit length^2 / s) and bulk modulus of 0.1083 (pressure unit), or 51.6% and 46.8% of the maximum achievable diffusivity and bulk modulus, respectively.

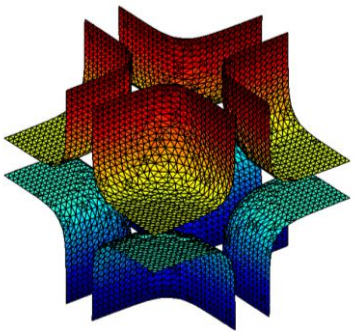

(a) Maximum diffusivity (Point A)

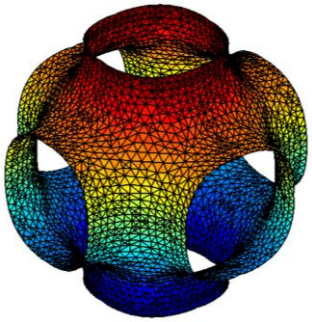

(b) Maximum combination (Point B)

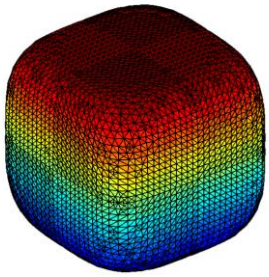

(c) Maximum bulk modulus (Point C)

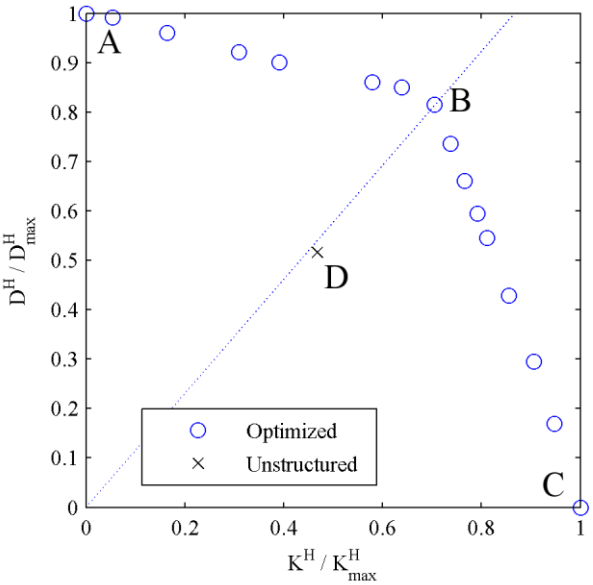

(d) Normalized Pareto front

Figure 5-6. Multiobjective topology optimisation. (a), (b) and (c) are the fluid domains of the optimised models at w = 0, 13/28, 1, respectively. (d) is the Pareto front of the dual-objective optimisation.

The Pareto front in Figure 5-6(d) is generated by varying the weight ratio, $\frac{1-w}{w}$ (Eq. (5-10)). The concave profile reflects the maximisation nature of this problem, in contrast to the convex profile found in other studies that used minimisation formulation [17]. This Pareto front contains two fairly straight segments and an acute change in the gradient at an objective weight of w = 13/28 (Point B). This result shows that there exist some design solutions that have a reasonably high combination of effective diffusivity and effective bulk modulus, with a weight ratio that slightly favours diffusivity (the blue dotted line in Figure 5-6(d)). The optimised models obtained around this weight ratio have 50% higher material properties than those of the unstructured scaffold sample. The optimised topology found in this study agrees with the results obtained in the past optimisation studies [19]. However, the smooth isosurface-based models enable smoother mapping of the Pareto front, compared to the scattered results produced by the voxelised modelling [18]. The optimum design selected for the comparative study in a later section has a weight ratio of 13/28 (Figure 5-6b).

5.3.3 Inverse homogenisation with a diffusivity target

Having determined the maximum achievable value of diffusivity, it was possible to create targets within this value and carry out the inverse homogenisation to build microstructures with designated diffusivity. Using the same volume constraint ($\rho_{solid} = 50\%$), two diffusivity targets were established, one at 50% of the theoretical maximum ($\mathbf{D}^* = 0.50\mathbf{D}^{max}$) and the other at 75% of the theoretical maximum ($\mathbf{D}^* = 0.75\mathbf{D}^{max}$), in which $D^{max} = 0.4$ for $\rho_{solid} = 50\%$ (Table 5-1).

The optimisation results show that there is no unique structural solution if the diffusivity target is lower than the theoretical maximum ($D^{max} = 0.4$). In other words, different RVE structures can be found for the same design criteria. As shown in Table 5-1 a-c, three different initial models had evolved into three distinct structural solutions, which all have the

same effective diffusivity value, $\mathbf{D}^* = 0.2$. Changing the optimisation parameters such as the penalisation factor in SIMP also affected the shape of final solution. It is reasonable to suggest that there exist infinitely many solutions for any diffusivity target as long as $\mathbf{D}^* < 0.4$. Results in Table 5-1a and Table 5-1d show that with different diffusivity targets but the same initial model, the resultant RVE shapes would be similar.

Table 5-1. Inverse homogenisation solutions with different diffusivity targets. Three different initial models had been used: model 1 for cases (a) and (d), model 2 for case (b), and model 3 for case (c).

Target and initial model ($\rho_{avg} = 50\%$)	Optimised base cell	Periodic structure 3×3×3
(a) Initial model 1 $D^* = 0.50D^{max}$ $D^H = \begin{bmatrix} 0.2020 & 0 & 0 \\ 0 & 0.2020 & 0 \\ 0 & 0 & 0.2020 \end{bmatrix}$	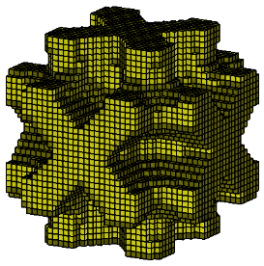	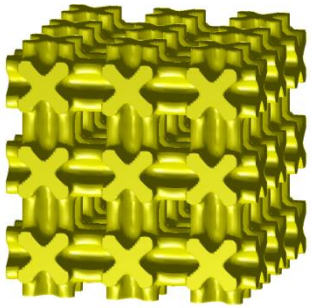
(b) Initial model 2 $D^* = 0.50D^{max}$ $D^H = \begin{bmatrix} 0.2000 & 0 & 0 \\ 0 & 0.2000 & 0 \\ 0 & 0 & 0.2000 \end{bmatrix}$	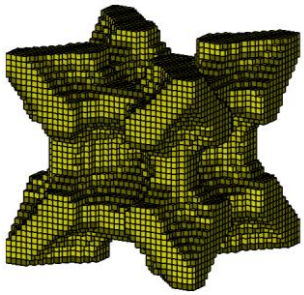	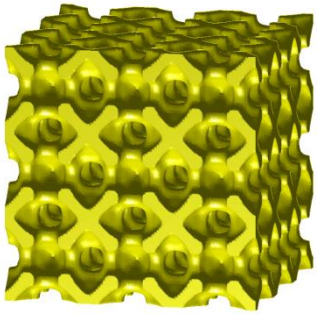
(c) Initial model 3 $D^* = 0.50D^{max}$ $D^H = \begin{bmatrix} 0.2006 & 0 & 0 \\ 0 & 0.2006 & 0 \\ 0 & 0 & 0.2006 \end{bmatrix}$	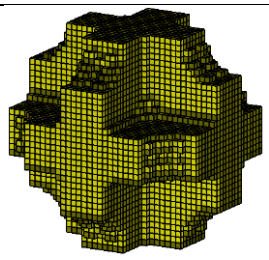	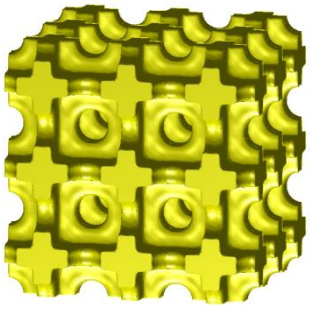

(d) Initial model 1 $D^* = 0.75D^{max}$ $D^H = \begin{bmatrix} 0.2995 & 0 & 0 \\ 0 & 0.2995 & 0 \\ 0 & 0 & 0.2995 \end{bmatrix}$	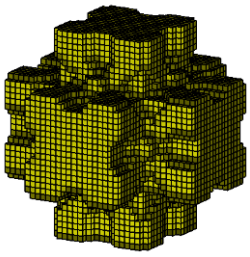	

5.3.4 Combined stiffness and diffusivity target

Alternatively, different property targets would consolidated in a multiobjective topology optimisation. The inverse homogenisation could therefore be carried out with different targets and weight ratios (w) to develop a range of RVE solutions and the Pareto front (Table 5-2), only as a minimisation problem. The results obtained in this study are consistent with results found in the past studies [10]. By comparing Table 5-2 and Figure 5-6, isosurface models show superior quality at the same modelling resolution.

Table 5-2. Optimised topologies with combined stiffness and diffusivity design criteria.

Design with combined stiffness and diffusivity	Optimised base cell	Periodic structure 2×2×2
$w_S = 1.0, w_D = 0.0$ $C_{11}^H = C_{22}^H = C_{33}^H = 0.4412$ $C_{44}^H = C_{55}^H = C_{66}^H = 0.1006$ $D_{11}^H = D_{22}^H = D_{33}^H = 0$	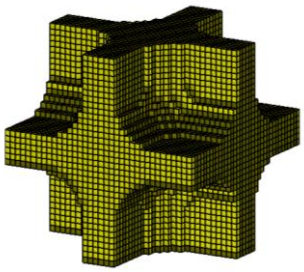	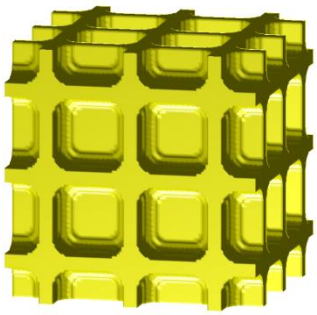
$w_S = 0.92, w_D = 0.08$ $C_{11}^H = C_{22}^H = C_{33}^H = 0.3861$ $C_{44}^H = C_{55}^H = C_{66}^H = 0.0880$ $D_{11}^H = D_{22}^H = D_{33}^H = 0.0269$	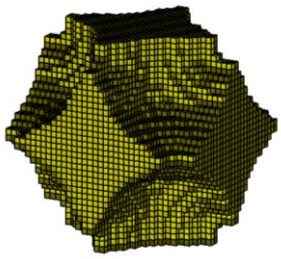	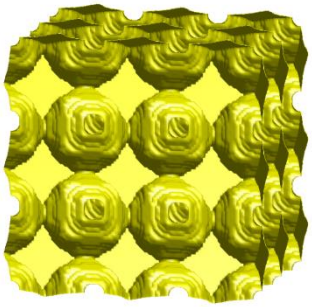

$w_S = 0.64, w_D = 0.36$ $C_{11}^H = C_{22}^H = C_{33}^H = 0.3443$ $C_{44}^H = C_{55}^H = C_{66}^H = 0.0744$ $D_{11}^H = D_{22}^H = D_{33}^H = 0.1538$	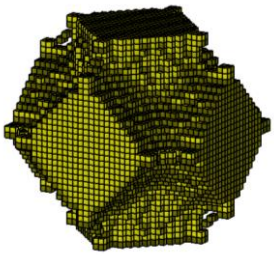	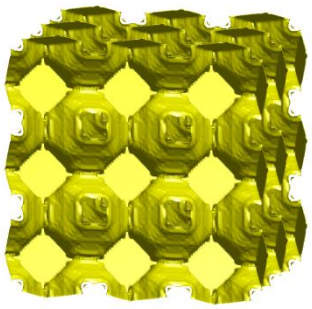
$w_S = 0.48, w_D = 0.52$ $C_{11}^H = C_{22}^H = C_{33}^H = 0.3336$ $C_{44}^H = C_{55}^H = C_{66}^H = 0.0714$ $D_{11}^H = D_{22}^H = D_{33}^H = 0.3237$	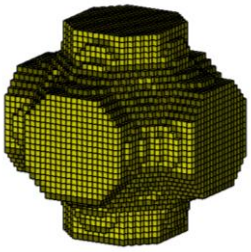	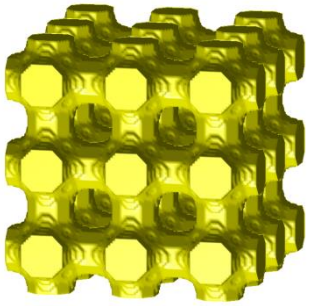
$w_S = 0.0, w_D = 1.0$ $C_{11}^H = C_{22}^H = C_{33}^H == 0$ $C_{44}^H = C_{55}^H = C_{66}^H == 0$ $D_{11}^H = D_{22}^H = D_{33}^H = 0.3975$	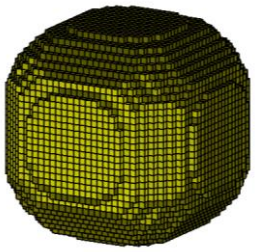	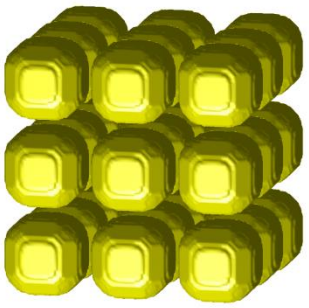

5.3.5 Cell viability assessments

So far, the topology optimisation had been conducted without considering the effect of cells seeding and proliferation on the diffusivity. The actaul cell viability also remained an unknown. To assess the actual improvement brought about by the optimised design, several comparison tests were performed.

The viability assessment results have shown an improved overall viability condition in the optimzed structure (Figure 5-7). With a uniform seeding density of 2.5×10^5 cells/cm^3, the unstructured scaffold shows a steeper drop in the oxygen concentration and a significantly longer proportion of scaffold at the state of hypoxia (depth > 0.1 cm) than that in the optimised structure. Also in the region 0–0.1 cm, the deviation of oxygen concentration (the

width of vertical spread of points) in the unstructured scaffold appears to be much greater. On the other hand, the oxygen drop in the optimised scaffold exhibits some periodic pattern and a narrower deviation, which reflect the structured periodicity of the optimised model.

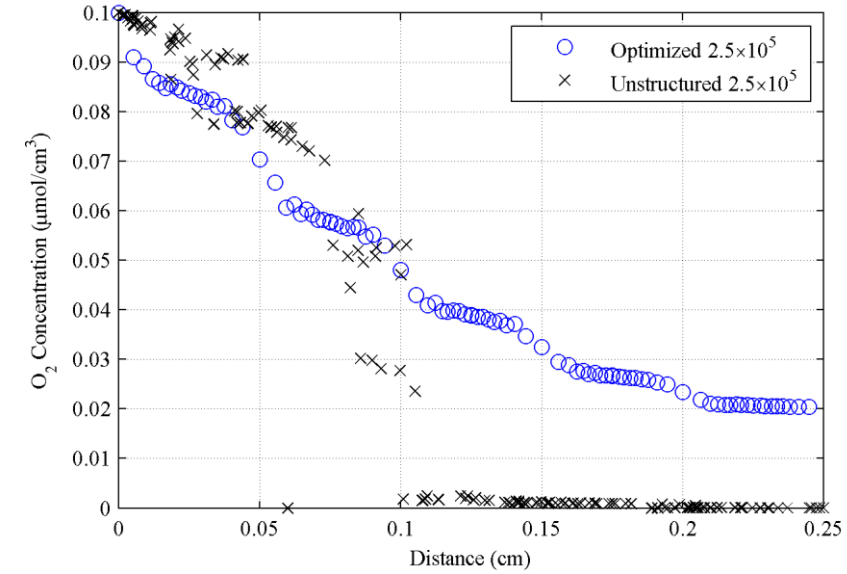

(a)

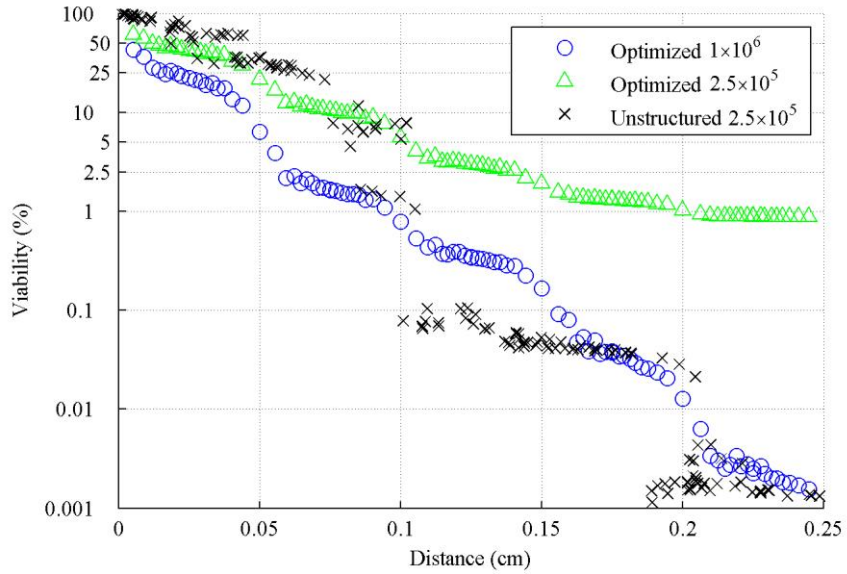

(b)

Figure 5-7. Oxygen concentration profile (a) and viability (b) of the optimised structure and the specimen of unstructured scaffold under uniform seeding condition. The values in the legend indicate cell seeding density.

Figure 5-7b shows that the viability in the unstructured scaffold is up to 20% higher in the region within 0.05 cm from the scaffold surface, compared to that of the optimised scaffold.

At a seeding density of 2.5×10^5 cells/cm^3, the cell viability in the optimised structure drops below 25% at a depth of 0.05 cm; in comparison, the cell viability in the unstructured scaffold drops below 25% at 0.07 cm. However, the viability in both structures drops below 5% at a depth of 0.1 cm, and below 1% at 0.1 cm for the unstructured scaffold and 0.2 cm for the optimised scaffold. Furthermore, the deep scaffold region (> 0.15 cm) is nearly unviable in the unstructured scaffold. Increasing the uniform seeding density to 1×10^6 cells/cm^3 in the optimised scaffold lowered the viability by approximately 20% near the source (< 0.05 cm) and 1% in the deep region (0.25 cm).

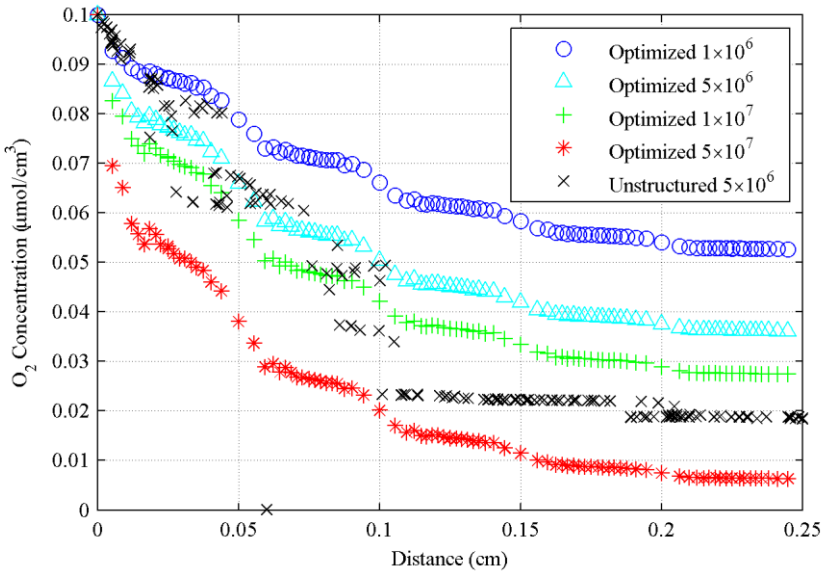

(a) Oxygen concentration

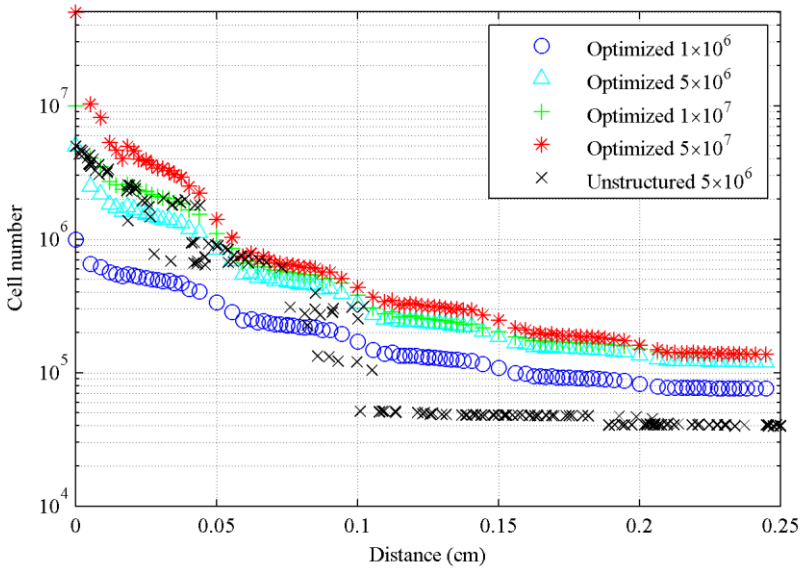

(b) Local cell density

Figure 5-8. Oxygen concentration profiles (a) and cell number (b) of the optimised structure and the unstructured scaffold under variable seeding density condition.

In the second part of this simulation, the cell distribution in tissue scaffolds were assessed without the assumption that seeding density could remain uniform and constant. As the seeding density became a variable, the cell viability was rewritten as a function of oxygen concentration. With these modifications, the resultant cell distribution still showed an improved steady-state oxygen concentration and cell uniformity in the optimzed scaffold (Figure 5-8). It was found that at a maximum cell density of 5×10^6 cells/cm^3, the oxygen concentration as well as the living cell number was more uniform in the optimised scaffolds. The smaller deviation in oxygen concentration and the higher cell number in the optimised scaffold confirmed that optimising effective diffusivity had improved the cell living condition. Figure 5-8 (b) further shows that the deviation in cell number (as in the vertical spread of data points) in the optimised scaffold is much smaller than that in the unstructured scaffold regardless of the maximum seeding density. Changing parameters such as the size of simulation domain, the size of RVE, cell density, oxygen consumption rate, or the boundary conditions had not affected the general oxygen concentration pattern.

As shown in Figure 5-8, it was observed that the cell viability and cell number were sensitive to the seeding density even in the deep scaffold region where the viability could be extremely low. It was found that increasing seeding density from 1×10^7 to 5×10^7 cells/cm^3 resulted in a net decrease in the living cell number in the deep region (> 0.2 cm), due to the worsening hypoxia. It is not clearly shown in the figure that the red line is very slightly lower than the green line for depth greater than 0.2 cm when zoomed in. This suggests a conflict between the maximisation of total cell number and maintaining the uniformity of cell distribution. In other words, cell distribution tends to be more uniform if the cell density is lowered. It was also found that for all tested seeding densities, the oxygen diffusivity across cells did not have a significant effect on the simulation outcome. On the other hand, changing the oxygen diffusivity across fluid would directly affect the oxygen concentration gradient, nevertheless the pattern in the cell distribution profile remained the same.

The relationship between cell viability and structural tortuosity (how twisted pores are) is well-established by the past studies [8]. A closer inspection of this unstructured scaffold model reveals that at a depth of 0.1 cm, there are only three very narrow fluid passages connecting the major pores (Figure 5-5c). Such poor connectivity unsurprisingly coincides with the pattern of the highest oxygen drop shown in Figure 5-7. The 0.1 cm depth also becomes the cut-off depth of viable cell seeding. Other structural irregularities such as highly tortuous and fragmented passages are also found at depths of 0.04 and 0.19 cm (Figure 5-5c). Overall, structural defects have a random distribution, and the results of Figure 5-7 may be characteristic only of the CT-image used in this study. Increasing the sampling dimension of the unstructured scaffold should improve the homogeneity of material properties and the uniformity of oxygen concentration [46]. Nevertheless, this cell distribution assessment highlights the adverse effect of the scaffold tortuosity as well as the benefit of topology optimisation.

These comparison tests have shown that the outcome of cell seeding is influenced by more than just the structural properties. Having the same porosity (50%) and interconnectivity (100%), the optimised scaffold model clearly outperforms the unstructured scaffold in terms of diffusivity, bulk modulus, and cell viability. Therefore the importance of topological characteristics of tissue scaffolds in diffusion-driven cell seeding should not be overlooked. The size and number of narrow pore connection for example, are decisive factors of successful cell infiltration. Design optimisation therefore has helped create a more efficient and more consistent transport environment across the tissue scaffolds.

5.4 Programming considerations

To correctly compute the effective diffusivity and the bulk modulus, both fluid and solid phases must be fully connected and continuous in the modelling space. Otherwise, any unconnected solid part would result in computational singularity, whereas unconnected pores would not be able to contribute to diffusive transport. For these reasons, discontinuities such as voids embedded in the solid were not modelled during the construction of the CT-image-based FE model.

Due to the non-linear nature of the oxygen consumption (Eq. (5-27)), the steady-state oxygen concentration were obtained through an iterative solution method. It was found that increasing the cell number or the oxygen consumption rate per cell would affect the convergence.

In this study, most of the seeding scenarios involved a relatively small volume of cells (~1% volume with the seeding density of 1×10^{7} cells/cm^{3}), thus the volumetric effect of cells on the diffusivity and the oxygen transport efficiency had been marginal. The use of rule of mixture was therefore justified when estimating the effective oxygen diffusivity through fluid.

5.5 Concluding remarks

A porous tissue scaffold should accommodate cell growth and allow efficient nutrient transportation across the entire construct. To achieve this, the pore network must be well-connected to enable cell infiltration and oxygen diffusion. Meanwhile, the mechanical strength and the structural integrity must not be compromised.

This study has formulated the scaffold design problem as a multiobjective optimisation problem, and has incorporated the smooth isosurface modelling technique to improve model definition and numerical accuracy. A renovated level set optimisation method is presented here with modified sensitivity analysis and topology update process. Based on the effective diffusivity and effective bulk modulus criteria, a range of optimal cubic RVE models has been obtained, ranging from the maximum effective diffusivity structure to the maximum effective bulk modulus structure. This set of design solutions are consistent with those voxelised models obtained in the past studies. However, the isosurface modelling technique has demonstrated its higher modelling capacity with more accurately defined microstructures in topology optimisation.

The cell viability simulation has been conducted to evaluate the effectiveness of the optimised scaffold model, in comparison to an unstructured scaffold model constructed from a CT-image. The simulation results confirm that the optimised model provides a more viable environment. The results have also revealed that the connectivity defects and tortuosity in the unstructured model severely impact the effective oxygen transport. In summary, this comparative test makes evident the benefit of having an optimised and well-organized microstructure.

5.6 References

[1] Rose, F.R., Cyster, L.A., Grant, D.M., Scotchford, C.A., Howdle, S.M. & Shakesheff, K.M. 2004. In vitro assessment of cell penetration into porous hydroxyapatite scaffolds with a central aligned channel. *Biomaterials,* 25**,** 5507-14.

[2] Salerno, A., Guarnieri, D., Iannone, M., Zeppetelli, S., Di Maio, E., Iannace, S. & Netti, P.A. 2009. Engineered mu-bimodal poly(epsilon-caprolactone) porous scaffold for enhanced hMSC colonization and proliferation. *Acta Biomater,* 5**,** 1082-93.

[3] Salerno, A., Di Maio, E., Iannace, S. & Netti, P. 2011. Tailoring the pore structure of PCL scaffolds for tissue engineering prepared via gas foaming of multi-phase blends. *Journal of Porous Materials***,** 1-8.

[4] Kang, T.-Y., Kang, H.-W., Hwang, C.M., Lee, S.J., Park, J., Yoo, J.J. & Cho, D.-W. 2011. The realistic prediction of oxygen transport in a tissue-engineered scaffold by introducing time-varying effective diffusion coefficients. *Acta Biomaterialia,* 7**,** 3345-3353.

[5] Silva, M.M., Cyster, L.A., Barry, J.J., Yang, X.B., Oreffo, R.O., Grant, D.M., Scotchford, C.A., Howdle, S.M., Shakesheff, K.M. & Rose, F.R. 2006. The effect of anisotropic architecture on cell and tissue infiltration into tissue engineering scaffolds. *Biomaterials,* 27**,** 5909-17.

[6] Oh, S.H., Park, I.K., Kim, J.M. & Lee, J.H. 2007. In vitro and in vivo characteristics of PCL scaffolds with pore size gradient fabricated by a centrifugation method. *Biomaterials,* 28**,** 1664-71.

[7] Bai, F., Zhang, J.K., Wang, Z., Lu, J.X., Chang, J.A., Liu, J.A., Meng, G.L. & Dong, X. 2011. The effect of pore size on tissue ingrowth and neovascularization in porous bioceramics of controlled architecture in vivo. *Biomedical Materials,* 6.

[8] Melchels, F.P.W., Barradas, A.M.C., van Blitterswijk, C.A., de Boer, J., Feijen, J. & Grijpma, D.W. 2010. Effects of the architecture of tissue engineering scaffolds on cell seeding and culturing. *Acta Biomaterialia,* 6**,** 4208-4217.

[9] Adachi, T., Osako, Y., Tanaka, M., Hojo, M. & Hollister, S.J. 2006. Framework for optimal design of porous scaffold microstructure by computational simulation of bone regeneration. *Biomaterials,* 27**,** 3964-72.

[10] Chen, Y., Zhou, S. & Li, Q. 2011. Microstructure design of biodegradable scaffold and its effect on tissue regeneration. *Biomaterials,* 32**,** 5003-5014.

[11] Hollister, S.J. 2005. Porous scaffold design for tissue engineering. *Nat Mater,* 4**,** 518-24.

[12] Hollister, S.J. 2009. Scaffold design and manufacturing: from concept to clinic. *Adv Mater,* 21**,** 3330-42.

[13] Papenburg, B.J., Liu, J., Higuera, G.A., Barradas, A.M., de Boer, J., van Blitterswijk, C.A., Wessling, M. & Stamatialis, D. 2009. Development and analysis of multi-layer scaffolds for tissue engineering. *Biomaterials,* 30**,** 6228-39.

[14] Lebourg, M., Sabater Serra, R., Mas Estelles, J., Hernandez Sanchez, F., Gomez Ribelles, J.L. & Suay Anton, J. 2008. Biodegradable polycaprolactone scaffold with controlled porosity obtained by modified particle-leaching technique. *J Mater Sci Mater Med,* 19**,** 2047-53.

[15] Nge, T., Nogi, M., Yano, H. & Sugiyama, J. 2010. Microstructure and mechanical properties of bacterial cellulose/chitosan porous scaffold. *Cellulose,* 17**,** 349-363.

[16] Sun, W., Darling, A., Starly, B. & Nam, J. 2004. Computer-aided tissue engineering: overview, scope and challenges. *Biotechnol Appl Biochem,* 39**,** 29-47.

[17] de Kruijf, N., Zhou, S., Li, Q. & Mai, Y.-W. 2007. Topological design of structures and composite materials with multiobjectives. *International Journal of Solids and Structures,* 44**,** 7092-7109.

[18] Chen, Y., Zhou, S. & Li, Q. 2010. Multiobjective topology optimization for finite periodic structures. *Computers & Structures,* 88**,** 806-811.

[19] Guest, J.K. & Prévost, J.H. 2006. Optimizing multifunctional materials: Design of microstructures for maximized stiffness and fluid permeability. *International Journal of Solids and Structures,* 43**,** 7028-7047.

[20] Jung, Y., Chu, K.T. & Torquato, S. 2007. A variational level set approach for surface area minimization of triply-periodic surfaces. *J. Comput. Phys.,* 223**,** 711-730.

[21] Chang, C., Zhou, S., Chen, Y. & Li, Q. 2012. Characterization of Fluid Dynamic Properties of Schwarz's Primitive Cellular Materials. *World Journal of Engineering,* 7**,** 167-168.

[22] Zhou, S. & Li, Q. 2008. A variational level set method for the topology optimization of steady-state Navier–Stokes flow. *Journal of Computational Physics,* 227**,** 10178-10195.

[23] Guest, J.K. & Prévost, J.H. 2007. Design of maximum permeability material structures. *Computer Methods in Applied Mechanics and Engineering,* 196**,** 1006-1017.

[24] Sturm, S., Zhou, S., Mai, Y.W. & Li, Q. 2010. On stiffness of scaffolds for bone tissue engineering-a numerical study. *J Biomech,* 43**,** 1738-44.

[25] Lin, C.Y., Kikuchi, N. & Hollister, S.J. 2004. A novel method for biomaterial scaffold internal architecture design to match bone elastic properties with desired porosity. *Journal of Biomechanics,* 37**,** 623-636.

[26] Kang, H., Lin, C.-Y. & Hollister, S. 2010. Topology optimization of three dimensional tissue engineering scaffold architectures for prescribed bulk modulus and diffusivity. *Structural and Multidisciplinary Optimization,* 42**,** 633-644.

[27] Melchels, F.P.W., Tonnarelli, B., Olivares, A.L., Martin, I., Lacroix, D., Feijen, J., Wendt, D.J. & Grijpma, D.W. 2011. The influence of the scaffold design on the distribution of adhering cells after perfusion cell seeding. *Biomaterials,* 32**,** 2878-2884.

[28] Zhou, S. & Li, Q. 2007. The relation of constant mean curvature surfaces to multiphase composites with extremal thermal conductivity. *Journal of Physics D: Applied Physics,* 40**,** 6083.

[29] Taboas, J.M., Maddox, R.D., Krebsbach, P.H. & Hollister, S.J. 2003. Indirect solid free form fabrication of local and global porous, biomimetic and composite 3D polymer-ceramic scaffolds. *Biomaterials,* 24**,** 181-94.

[30] Fang, Q. & Boas, D. Tetrahedral mesh generation from volumetric binary and gray-scale images. IEEE International Symposium on Biomedical Imaging 2009, 2009. 1142-1145.

[31] Edelsbrunner, H. & Shah, N.R. 1996. Incremental Topological Flipping Works for Regular Triangulations. *Algorithmica,* 15**,** 223-241.

[32] Si, H. & Gaertner, K. Meshing Piecewise Linear Complexes by Constrained Delaunay Tetrahedralizations. 14th International Meshing Roundtable, September 2005 2005. 147-163.

[33] Si, H. On Refinement of Constrained Delaunay Tetrahedralizations. 15th International Meshing Roundtable, September 2006 2006.

[34] Sanchez-Palencia, E. 1983. Asymptotic Analysis II — Homogenization method for the study of composite media *In:* VERHULST, F. (ed.). Springer Berlin / Heidelberg.

[35] Sigmund, O. 1994. *Design of material structures using topology optimisation* PhD Technical University of Denmark.

[36] Sigmund, O. 1994. Tailoring Materials for Specific Needs. *Journal of Intelligent Material Systems and Structures,* 5**,** 736-742.

[37] Catledge, S.A., Clem, W.C., Shrikishen, N., Chowdhury, S., Stanishevsky, A.V., Koopman, M. & Vohra1, Y.K. 2007. An electrospun triphasic nanofibrous scaffold for bone tissue engineering. *Biomedical Materials,* 2**,** 142-150.

[38] Hollister, S.J. 2005. Porous scaffold design for tissue engineering. *Nature Materials,* 4**,** 518-524.

[39] Svanberg, K. 1987. The Method of Moving Asymptotes - a New Method for Structural Optimization. *International Journal for Numerical Methods in Engineering,* 24**,** 359-373.

[40] Wang, M.Y., Wang, X. & Guo, D. 2003. A level set method for structural topology optimization. *Computer Methods in Applied Mechanics and Engineering,* 192**,** 227-246.

[41] Wang, X., Mei, Y. & Wang, M.Y. 2004. Level-set method for design of multi-phase elastic and thermoelastic materials. *International Journal of Mechanics and Materials in Design,* 1**,** 213-239.

[42] Allaire, G., Jouve, F. & Toader, A.-M. 2004. Structural optimization using sensitivity analysis and a level-set method. *Journal of Computational Physics,* 194**,** 363-393.

[43] Radisic, M., Malda, J., Epping, E., Geng, W., Langer, R. & Vunjak-Novakovic, G. 2006. Oxygen gradients correlate with cell density and cell viability in engineered cardiac tissue. *Biotechnology and Bioengineering,* 93**,** 332-343.

[44] Cho, C.H., Park, J., Nagrath, D., Tilles, A.W., Berthiaume, F., Toner, M. & Yarmush, M.L. 2007. Oxygen uptake rates and liver-specific functions of hepatocyte and 3T3 fibroblast co-cultures. *Biotechnology and Bioengineering,* 97**,** 188-199.

[45] Quelle, D.E., Ashmun, R.A., Shurtleff, S.A., Kato, J.Y., Bar-Sagi, D., Roussel, M.F. & Sherr, C.J. 1993. Overexpression of mouse D-type cyclins accelerates G1 phase in rodent fibroblasts. *Genes & Development,* 7**,** 1559-1571.

[46] Grimal, Q., Raum, K., Gerisch, A. & Laugier, P. 2011. A determination of the minimum sizes of representative volume elements for the prediction of cortical bone elastic properties. *Biomech Model Mechanobiol*.

6 Optimisation of Nutrient Transport and Cell Viability

The survival of cells in porous tissue scaffolds relies on efficient and sustained oxygen transport, which is especially important in static culturing conditions. However, cell deposition and proliferation can create diffusion barriers and subsequently affect the oxygen transport across the scaffold construct. Consequently, regional hypoxia and cell death occurs. To improve the cell seeding condition in a scaffold, this study proposes applying method of structural optimisation to the structural design and examine the influence of graded porosity profile on the steady-state cell seeding outcome. The goal of this study is to determine the optimal porosity profile of tissue scaffold for cell growth and viability.

One-dimensional steady-state cell growth simulation has been conducted and the response surface method has been employed to configure the structural profile of scaffold and improve cell living conditions. The optimal scaffold porosity structures for cell growth were to be profiled as a function of depth. The effect of the manipulation of porosity profile on oxygen level and cell viability was then assessed.

6.1 Introduction

Insufficient nutrient supply and ill cell distribution are two major challenges facing the tissue scaffold engineering [1, 2]. Cells in static cultures in particular often suffer from hypoxia as they rely on diffusion to drive oxygen transport [3]. It is known that increasing cell population reduces nutrient transport efficiency [4], which can develop into hypoxia and result in the deterioration of cell vitality in the core region of tissue scaffolds [5]. Consequently, the viable living space shrinks and is limited to the region near the scaffold boundary [6, 7]. It is also suggested that the non-uniform cell deposition across a tissue

scaffold, induced by uneven nutrient distribution, may form a self-imposed transport barrier and further deepens cell distribution deviation [8]. Thus loss in transport efficiency becomes inevitable as the cells populate the pores near the scaffold surface. The solution to sustaining nutrient supply may lie in the structural design of porous tissue scaffolds, which aims to minimise the adverse effect of cell deposition on nutrient supply.

The structural design of tissue scaffolds has been a key research topic with a special focus on the regulation of cell migration [8, 9] and vascularisation [10]. Pore connectivity is commonly used as a design requirement to ensure unimpeded cell infiltration and general mass movement [11]. Some common strategies for promoting cell infiltration include increasing global porosity, introducing micro-porosity (smaller than typical cell size) for the transport of oxygen and chemical species [7], and constructing macro-porous network for nutrient transport and cell migration [2]. While high porosity is preferred due to its apparent benefit to diffusion, short diffusion depth remains a primary limiting factor of how far cells can stay alive from nutrient supply [7]. High porosity also compromises structural strength [12, 13].

A direct solution to the nutrient transport problem is the use of perfusion system. Past studies have demonstrated the effectiveness of advection in overcoming physical transportation barriers, elevating nutrient concentration and improving uniform cell distribution across scaffolds [14]. The significant improvement in both nutrient concentration and cell survival rate makes advection an almost essential condition for cell seeding. However, forced nutrient movement is accompanied by elevated wall shear stress, which could threaten cell attachment and survival [15]. This drawback can potentially negate the benefit of increase nutrient concentration. In a high flow rate scenario, forced fluid flood becomes detrimental to cell survival [14]. For this reason, wall shear stress constraint outweighs the nutrient transport

constraint at a high flow rate. The implementation of perfusion system is therefore double-edged and the benefit is not unlimited.

Past studies have applied topology optimisation on the scaffold microstructures and produced architectures with maximised transport efficiency and mechanical properties [16], and optimised wall shear stress distribution [17]. Functionally graded design has also shown potential in facilitating scaffolded bone remodelling [18]. Despite the success of structure optimisation, the interaction between the topology of tissue scaffolds and the living tissue is rarely used directly as a design criterion [19]. It remains unclear that to what extent the optimisation of microscopic structure can favourably affect the steady state seeding outcome.

To produce more realistic design solutions, the cell activities must be taken into account. This requires incorporating porosity modelling, diffusion-advection computation, and optimisation using cell viability as the design criterion. This optimisation study aims to link the diffusion transport mechanics and the cell proliferation outcome, and to determine the steady-state porosity profile of tissue scaffolds in which cell viability is maximised and the even cell distribution is achieved.

6.2 Optimisation of porosity profile

The importance of scaffold porosity in nutrient transport and cell survival is well recognized in tissue engineering [10, 20]. However, porosity is rarely considered as a design variable in tissue scaffold design. The idea of a functionally graded design in particular, i.e. a scaffold with different porosities at different depths, has yet been fully explored and implemented. This is also unknown whether higher cell survival rate can be achieved by manipulating the diffusion efficiency across scaffolds. To investigate the potential of variable-porosity structure for tissue engineering purposes, this study carries out optimisation on the scaffold

porosity and aims to determine the optimal porosity profile that results in the maximum cell viability.

This structural optimisation seeks improvement in the total cell number, viability and cell infiltration length by altering regional scaffold porosity. The optimisation procedure has two components: the computation of cell proliferation and the optimisation of the porosity profile. The nonlinear diffusion system is firstly solved to predict the steady-state cell density and oxygen concentration [21]. The sensitivity of oxygen concentration, cell number and cell viability to the change in porosity is then determined using the response surface method, and then the porosity profile is updated. This process is performed repeatedly until the objectives can no longer be improved.

6.2.1 Oxygen diffusion-advection modelling

Oxygen diffusion-advection model can be created to simulate changing oxygen concentration over time as a result of oxygen intake by cells. This model represents the scaffold environment that contains tissue scaffold materials, cells and fluid. Cell number and oxygen concentration in the tissue scaffold can be determined, and subsequently be used to predict the final living cell number under different seeding conditions. The model is constructed as shown in Figure 6-1a: a cubic scaffold with homogeneously porous structure is seeded with cells, with only one of the six faces being exposed to an oxygen and nutrient source. All other five surfaces are walls, sealed to disallow transportation in or out of the model. If there is fluid flow, the surface opposite to the source is assumed to be a flow outlet. This system can be effectively translated to a one-dimensional (1D) model in which all variables are formulated as a function of depth, which is the distance to the oxygen source (x, Figure 6-1b).

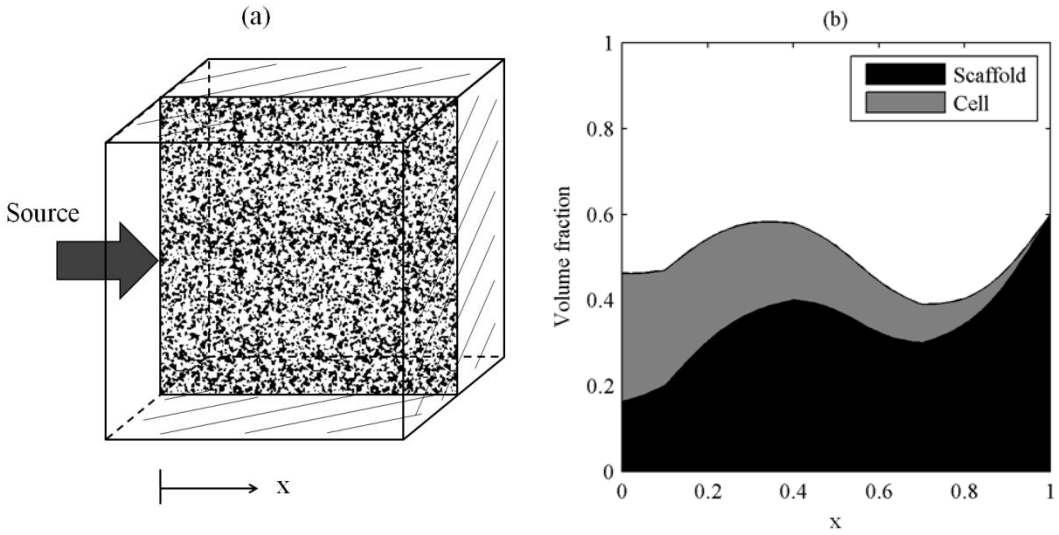

Figure 6-1. Schematic representation of (a) scaffold microstructure and boundary conditions; and (b) volume fraction of various constitutes.

The model has three volumetric constitutes: scaffold, cells, and a purportedly fully-connected, fluid-filled porous space. The porous space is the only constitute that allows diffusion and advection to occur. The porosity is assumed to be homogeneous on the macroscopic level in the non-*x* directions, so that the transport properties do not vary in the non-*x* directions. Based on this assumption, the oxygen diffusivity and permeability can be formulated as a function of *x*-porosity only. The primary design variable is the solid volume fraction (ρ), which is the volume ratio of the modelling space occupied by the scaffold materials; the remaining volume is divided into two fractions according to their effective transport properties: cell volume fraction (v) consisting of cells and the space rendered inaccessible for oxygen transport, and an effective fluid volume fraction that has full fluid diffusivity and conductivity. More precisely, this cell volume fraction value represents the space occupied by cells, which is treated as impermeable in this diffusion-advection system. The solid and the cell volume fraction together form an effective solid volume fraction (ρ^*) which represents the total non-conductive, non-permeable space (Figure 6-2, black and grey regions). The transportation properties of tissue scaffold exist in the fluid phase (Figure 6-2, white region).

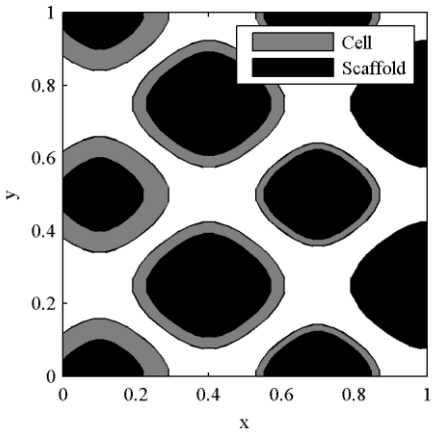

Figure 6-2. Schematic representation of the cell settlement in a tissue scaffold.

The oxygen concentration is the primary degree of freedom in this diffusion-advection model. The steady-state concentration is governed by the following equation:

$$\frac{d}{dx}\left(D\frac{du}{dx}\right) - V\frac{du}{dx} + S = 0 \tag{6-1}$$

where u is the oxygen concentration, D is the oxygen diffusivity across the fluid, V is the fluid flow rate, and S is the oxygen uptake rate. Diffusivity, fluid flow rate and oxygen uptake rate are all directly related to the local cell number and are indirectly related to the oxygen concentration.

The cell volume and oxygen uptake rate are written as functions of u:

$$v = v_0 N(u) \tag{6-2}$$

$$S = S_0 N(u) \times \frac{u}{k_m + u} \tag{6-3}$$

where v is the cell volume fraction (ml/ml), v_0 is the volume of one single cell (ml/cell), N is the local cell density (cells/ml), S_0 is the maximum oxygen uptake rate (mol/cell), and k_m is the Michaelis–Menten constant for half oxygen uptake rate (μM). $\frac{u}{k_m+u}$ can be regarded as the level of cell activity and has a value between 0 and 1.

In this study, the effective diffusivity is formulated as a function of porosity, based on the Hashin-Shtrikman upper bound equation [22]:

$$D = D^* \left[1 - \frac{3(\rho + v)}{2 + (\rho + v)}\right]^p \tag{6-4}$$

where D^* is the nominal diffusivity of oxygen in water, ρ is the solid volume fraction, and p is a penalisation factor. Note that $\rho + v$ is equal to 1 minus the porosity. For $p = 1$, the scaffold architecture is theoretically ideal for diffusion and has the highest possible diffusivity. The p value has been set to 1.2 in this study since the random scaffold microstructure is unlikely to be optimal. The v value may be adjusted if the cells are considered partially-permeable or partially-conductive.

To obtain a deterministic solution in this biological model, it is necessary to pre-define the cell number, *N*, as a function of the oxygen concentration, *u*. The cell viability to oxygen concentration relationship has been derived from the experimental data reported by Radisic et al [23] (Figure 6-3). The non-linear diffusion model is solved iteratively in the order of *u*, *N*, *S*, *D* and lastly *V* until the concentration profile (u) converged. Volume constraint, $\rho_{min} \leq \rho(x) \leq \rho_{max}$, can be applied to restrict the solidity or porosity of scaffold model to a desirable range.

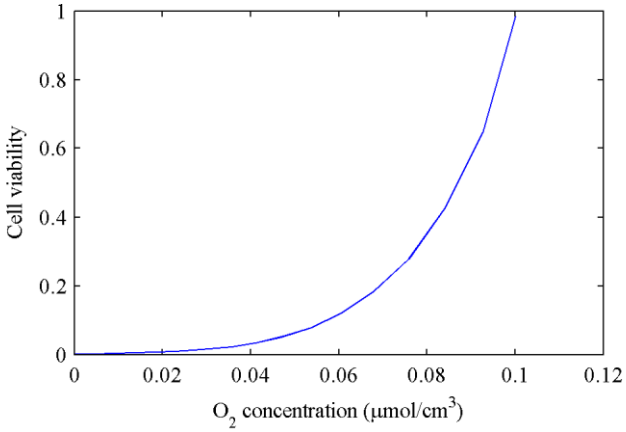

Figure 6-3. Cell viability versus oxygen concentration.

O_2 (µmol/cm^3)	Viability
0	0
0.031566	0.001186
0.045817	0.002348
0.062977	0.004882
0.082868	0.01118
0.105443	0.030186
0.13079	0.104348
0.148053	0.26646
0.155201	0.402484
0.162518	0.621118
0.170063	1

Table 6-1. Estimated cell viability by Radisic et al [30].

In the diffusion models developed in this study, most design constraints have been chosen with the intention to produce generic results that are representative of common cell seeding scenarios. The design space was constructed as a 1 cm^3 cube (Figure 6-1a and Figure 6-2). The concentration on the left boundary (x = 0 cm) was kept at u = 175 μM whereas the right boundary (x = 1 cm) was the flow outlet (see Figure 6-1b). The upper limit (ρ_{max}) and lower limits (ρ_{min}) of the local solid volume fraction were set to 50% and 30%, respectively. The cell volume was assumed to be 1.3×10^{-9} ml/cell [24]. It was also assumed that the maximum number of cells that the peak oxygen concentration (175 μM) could support was 1.61×10^{8} cell/mL and each cell consumed oxygen at a rate of 7.9×10^{-11} μmol/s/cell [25]. The nominal diffusivity, D^*, from Eq. (6-4) is 2.0×10^{-5} (cm^2/s), the same as water. The Michaelis–Menten constant of half oxygen consumption, k_m, is 1.547 μM [25].

6.2.2 Numerical implementation

Since this diffusion-advection system is non-linear, it has to be solved iteratively in a time domain:

$$\frac{du}{dt} = \frac{dD}{dx}\frac{du}{dx} + D\frac{d^2u}{dx^2} - V\frac{du}{dx} + S(x) \tag{6-5}$$

where u is the oxygen concentration, t is the time, D is the diffusion coefficient (diffusivity), V is the flow velocity, and S is the oxygen consumption rate. The flow velocity is constant across the scaffold. Diffusivity and velocity are functions of the total impermeable volume fraction ($\rho^* = \rho + v$) as defined earlier. The flow velocity across a porous tissue scaffold can be calculated based on Darcy's Law [26],

$$\begin{aligned} V &= -\frac{K}{\mu}\frac{dP}{dx} \\ &= -\frac{1}{\int R dx}\frac{1}{\mu}\frac{dP}{dx} \end{aligned} \tag{6-6}$$

where K is the overall scaffold permeability, μ is the fluid viscosity, dP is the pressure change across the scaffold, dx is the scaffold thickness, and R is the local flow resistance. K

is the inverse of the sum of flow resistance. A negative pressure drop has been used to induce flow in the positive-*x* direction.

A simplistic permeability-porosity relationship is formulated based on the Kozeny-Carman equation:

$$K_{local} = \frac{A\varphi^3}{S^2(1-\varphi)^2}. \tag{6-7}$$

where K_{local} is the local permeability, A is a material constant, S is the specific surface area, and φ is the local porosity. To simplify the model, let $A = 1$ and $S = 1$. Local flow resistance R is the inverse of local permeability K_{local},

$$R = \frac{1}{K_{local}} = \frac{(1-\varphi)^2}{\varphi^3}. \tag{6-8}$$

As a function of ρ and v, it can be written as:

$$R = \frac{(\rho+v)^2}{(1-\rho+v)^3}. \tag{6-9}$$

The sizing of time step must obey the Courant–Friedrichs–Lewy condition (CFL condition), which imposes a limit on how much the degree of freedom can be changed per iteration. The time step sizes of all individual terms from the governing equation must be considered:

$$\begin{aligned} dt_1 &= \frac{h_0 h}{V} \\ dt_2 &= \frac{h_0 h}{\max(D)} \\ dt_3 &= \frac{h_0 h}{\max\left(\frac{dD}{dx}\right)} \\ dt &= \min(dt_1, dt_2, dt_3) \end{aligned} \tag{6-10}$$

where h is the length of the finite-difference mesh, and h_0 is the desired step size. $0 \leq h_0 \leq 1$.

6.2.3 Optimisation by response surface method

This structural optimisation aims to optimise cell seeding efficiency in tissue scaffolds at the steady state. The optimisation algorithm consists of two processes, namely the oxygen consumption simulation and the optimisation (Figure 6-4). Three design objectives are (1) increasing total cell number, (2) increasing overall survivability, and (3) reducing oxygen concentration drop. Various combinations of design objectives, seeding mode, and oxygen transportation have been tested as listed in (Table 6-2).

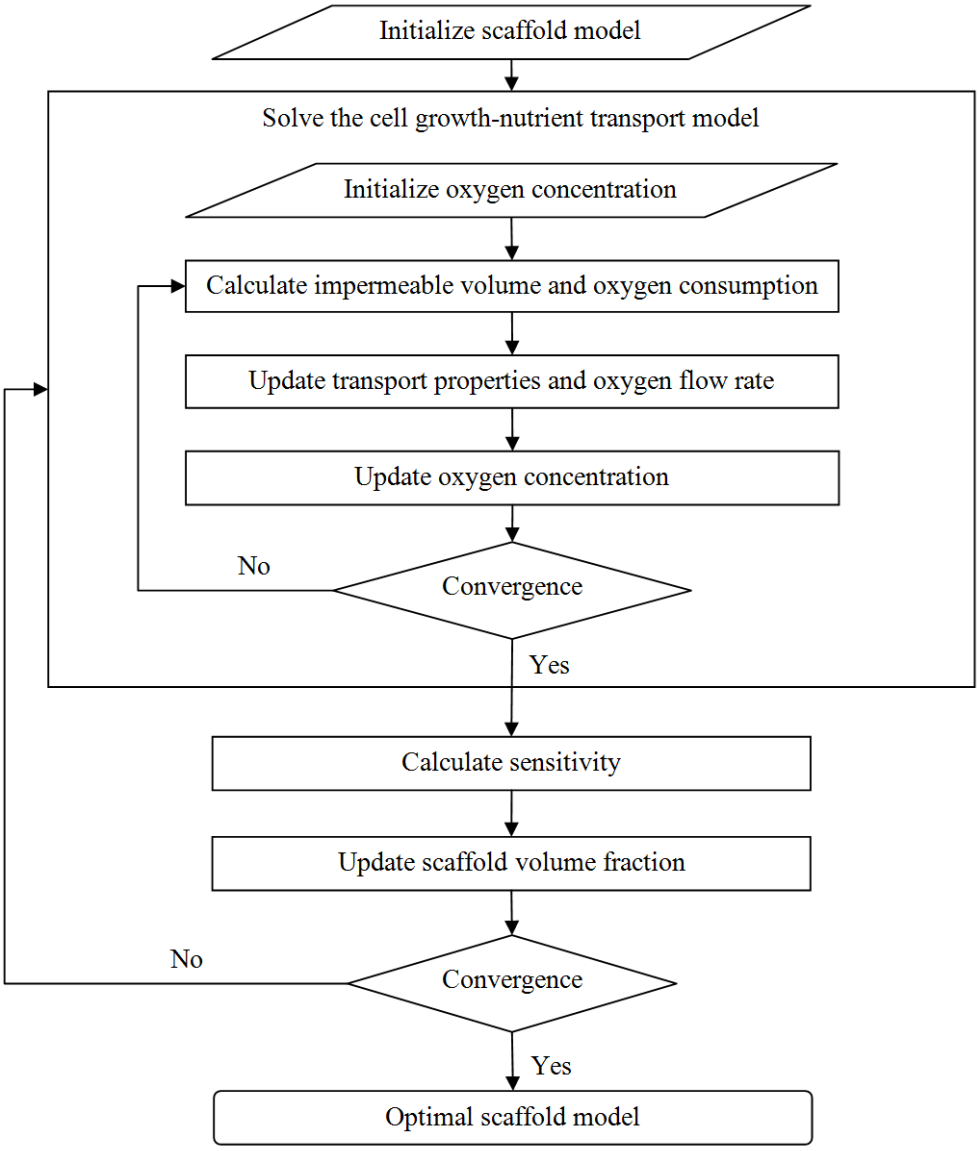

Figure 6-4. Process of response surface optimisation.

Table 6-2. A list of optimisation scenarios.

Scenario	Objective	Seeding density	Oxygen transportation
(1)	Maximise cell number	Oxygen-dependent	Diffusion-advection
(2)	Maximise viability	Constant	Diffusion-advection
(3)	Maximise viability	Constant	Diffusion
(4)	Minimise compliance	Oxygen-dependent	Diffusion
(5)	Minimise compliance	Constant	Diffusion

In the first design scenario where the cell density is a function of oxygen concentration, the objective function is formulated based on the total cell number, as:

$$\begin{aligned} Maximise: J(\rho) &= \int N(u)dx \\ Subject\ to: \frac{\int \rho dx}{l} &= V_S \end{aligned} \tag{6-11}$$

where $N(u)$ is the local number of living cells, l is the thickness of the scaffold, and V_S is the volume constraint of the scaffold material. The maximum value of N is 1.61×10^8 (cells/ml).

In uniform cell seeding scenario, an objective function can be formulated based on the cell survivability as follows:

$$Maximise: J(\rho) = \int \min(N(u), N_0)dx \tag{6-12}$$

where N_0 is the original seeding density, and $N(u)$ is the viable cell density if cell number were u-dependent. The difference between this and the previous formulations is that the uniform seeding density N_0 is much lower than 1.61×10^8 (cells/ml) (see Table 6-2).

Another possible viability measure is the drop in oxygen concentration. In this case, the objective function is the diffusion compliance:

$$Mimimise: J(\rho) = \int \frac{du}{dx}^T D \frac{du}{dx} dx \tag{6-13}$$

In this paper, the solid volume fraction was solved using the response surface method with full factorial design. The entire design domain was discretised into 7 to 8 nodes, each node

represented a ρ variable. The complete ρ profile was interpolated from these nodes using piecewise cubic Hermite interpolating polynomial (PCHIP) and spline interpolation. To satisfy the volume constraint as well as the upper (ρ_{max}) and lower (ρ_{min}) porosity limits, the change in ρ must satisfy:

$$\rho_{i+1} = max\left(min\left(\rho_i + \left(a\frac{dJ}{d\rho_i} + b\right), \rho_{max}\right), \rho_{min}\right) \tag{6-14}$$

where a and b are two scaling terms that satisfy the following condition:

$$max(|\rho_{i+1} - \rho_i|) = h_i \tag{6-15}$$

where h_i is the desirable step size of ρ during the i^{th} iteration. Noted that $\frac{dJ}{d\rho_i}$ is the desirable change in porosity, the polynomial $a\frac{dJ}{d\rho_i} + b$ adjusts the actual change in porosity at individual points. The values of a and b are found through an iterative process:

$$\begin{aligned} a &= a \times \frac{h_i}{max(|\rho_{i+1} - \rho_i|)} \\ b &= b + [mean(\rho_{i+1}) - V_S] \end{aligned} \tag{6-16}$$

The step size is scaled in every iteration step to improve solution convergence:

$$h_{i+1} = h_i \times k, (0 < k \leq 1) \tag{6-17}$$

6.3 Results and discussion

Poor cell proliferation in tissue scaffolds is usually a result of inadequate oxygen supply. Ironically, growing cell population is a potential oxygen transportation barrier. To address such dilemma in tissue scaffold design, optimisation on the structural profile of scaffolds was carried out, and the steady-state cell seeding outcome under different seeding conditions was simulated.

A range of diffusion-advection models of porous tissue scaffold were constructed as one-dimensional finite-difference models. Each model was 1 cm in length. All models were initialised with a uniform scaffold solid volume fraction (ρ) of 40% and the volume fraction

sum across the scaffold was constant throughout the structural optimisation. The maximum and minimum allowable ρ values were set to 50% and 30%. Five different seeding scenarios involving three optimisation objectives were created and simulated. The objectives were to (1) maximise the cell number at steady state, (2) maximise the cell viability and (3) minimise the diffusion compliance. Models with different fluid flow rates or different cell seeding densities were tested and compared.

6.3.1 Maximisation of cell number with perfusion

In the first design scenario where the cell number is oxygen-concentration-dependent, the optimised profiles of solid volume fraction differ drastically among models with different perfusion rates (Figure 6-5). It can be seen in Figure 6-6, the structural evolution is directly affected by pressure drop and perfusion rate. In the design scenario where the pressure drop (dP) is 400 Pa, the final ρ^* profile is essentially a straight line (black dotted line), which gives the lowest total flow resistance. In the absence of fluid flow (dP = 0), the cell number is low and the cell volume is negligible. Reducing the flow rate reduces the cell volume as well as the uniformity of cell distribution. In that case, reducing flow resistance becomes less important.

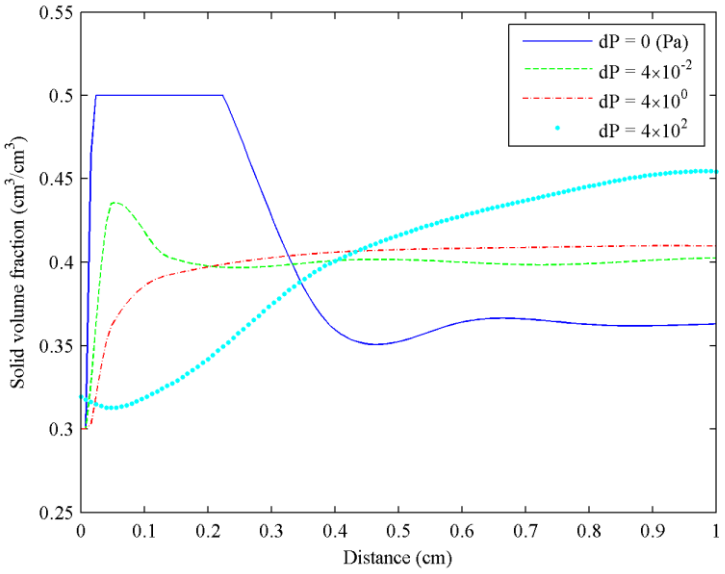

Figure 6-5. The optimised ρ profiles of the tissue scaffold under non-uniform seeding condition (Figure 6-1). Different pressure drops (dP) were applied to different induce perfusion rate.

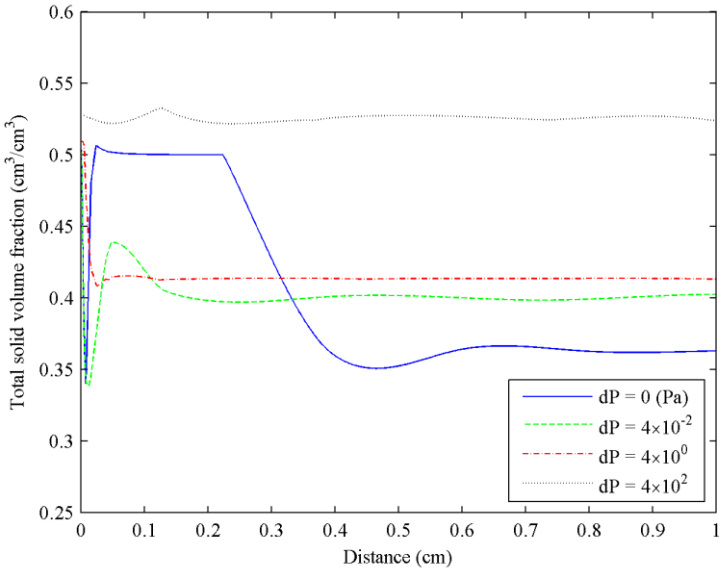

Figure 6-6. The total solid volume fractions (ρ^*) of the optimised tissue scaffolds under non-uniform seeding condition (Figure 6-1).

The objective number had increased steadily over the course of structural optimisation (Figure 6-7a) and converged before the ρ profile started to converge (Figure 6-7b, 50th iteration) Nevertheless, running extra iterations produced a more characteristic ρ profile

(Figure 6-7b, 200th iteration), even though the objective number has already reached the maximum value.

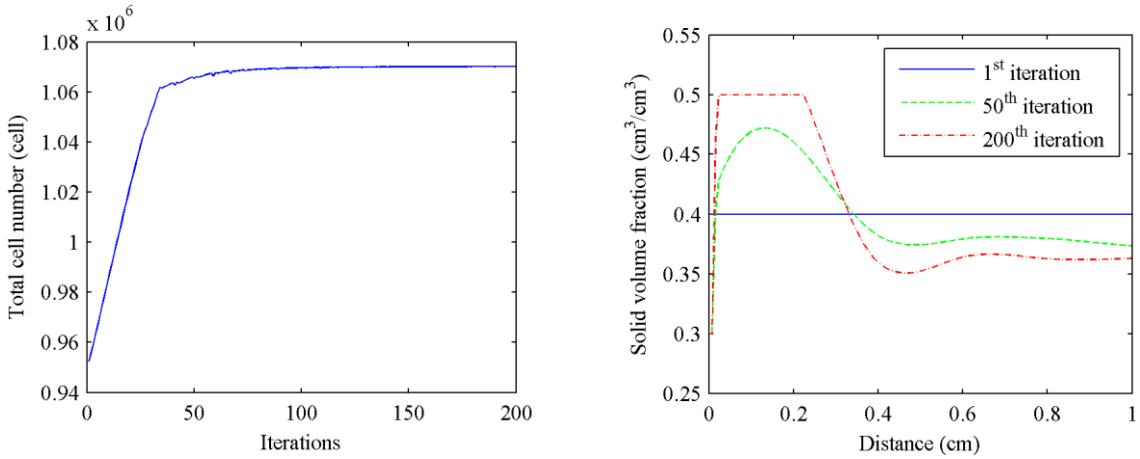

(a) (b)

Figure 6-7. The convergence history of the non-uniform seeding of dP = 0 model.

6.3.2 Maximisation of viability with perfusion

Under uniform seeding condition and viability criterion (Eq. (6-12)), the ρ profile acquired shapes similar to the ones obtained under non-uniform seeding condition and cell number criterion (Figure 6-8). However, the segment of the no-perfusion model that reaches the maximum ρ limit is significantly shorter. The fluctuation in the ρ profile is also more pronounced, although it is likely a numerical artefact of the spline interpolation. In general, the ρ value rises rapid from minimum to maximum over a short distance, and drops back to the initial average value ($\rho = 0.4$). The minimisation of flow resistance again dominates the structural evolution of the high perfusion models, and the resultant ρ^* profiles are largely uniform except the shallow region (distance < 0.3 cm).

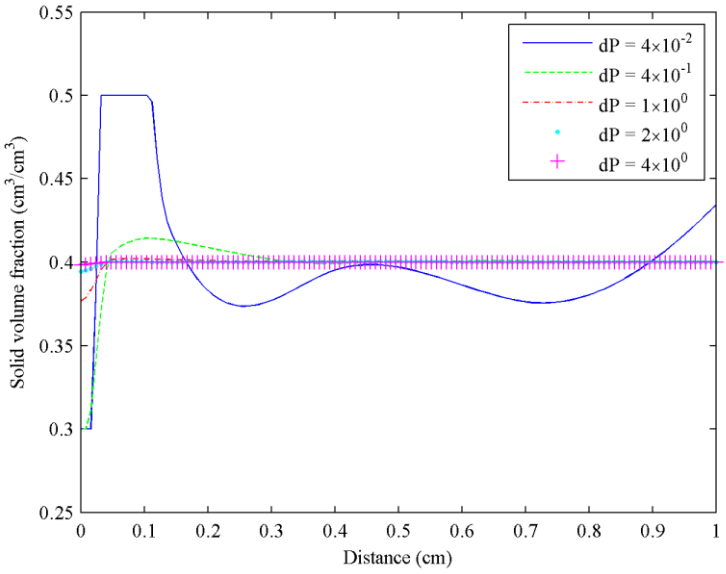

Figure 6-8. The optimised ρ profiles of the tissue scaffold under uniform seeding condition. Different pressure drops (dP) were applied.

Figure 6-9a shows that increasing perfusion rate, by means of increasing pressure drop, directly prevents the living cell density from dropping. However, the increase in the objective number is almost negligible in the high perfusion case (Figure 6-9b). This suggests that optimisation is ineffective if the perfusion rate is high enough.

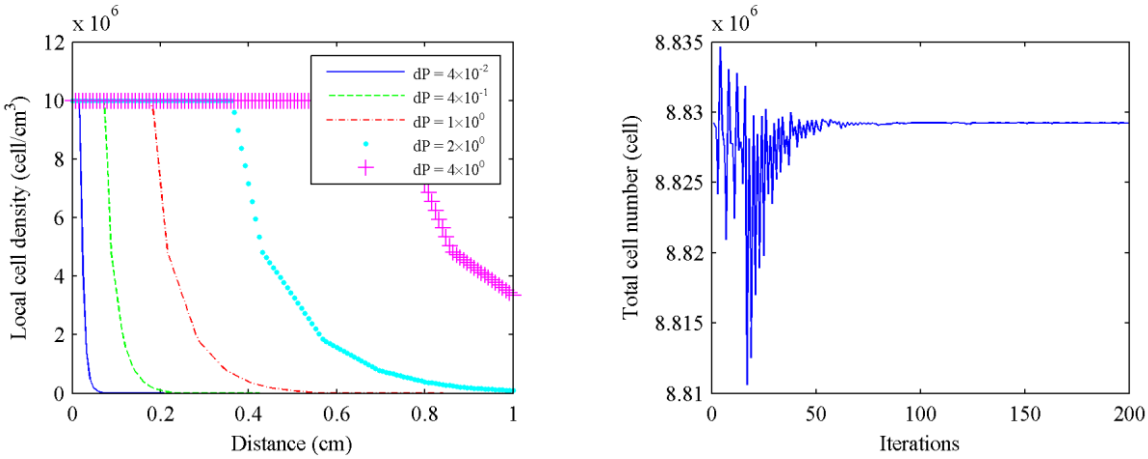

Figure 6-9. The local cell density profiles of the tissue scaffold at different perfusion rates.

6.3.3 Maximisation of viability without perfusion

The optimisation of the ρ profiles under uniform cell seeding condition has produced distinctive profile shapes (Figure 6-10). The results are signified by four segments of extreme

and alternating porosity. Between individual segments is either a steep increase or a steep decrease in the ρ value. Such "stepped" transition has become more apparent as the number of iterations increases over the optimisation process. During the simulation, the formation these "steps" occurred progressively, starting from the source region (x = 0) in the beginning and moving towards the deep region (x = 1) in the end. Such trend coincided with magnitude of the sensitivity function and had persisted since the sensitivity function changed little over the duration of the optimisation process. The local structural evolution ended as the ρ value reached the upper or lower limit. On the other hand, the change in ρ in the deepest scaffold region, where the sensitivity was close to zero, was primarily driven by the volume constraint in response to the changing volume fraction in the shallower scaffold region.

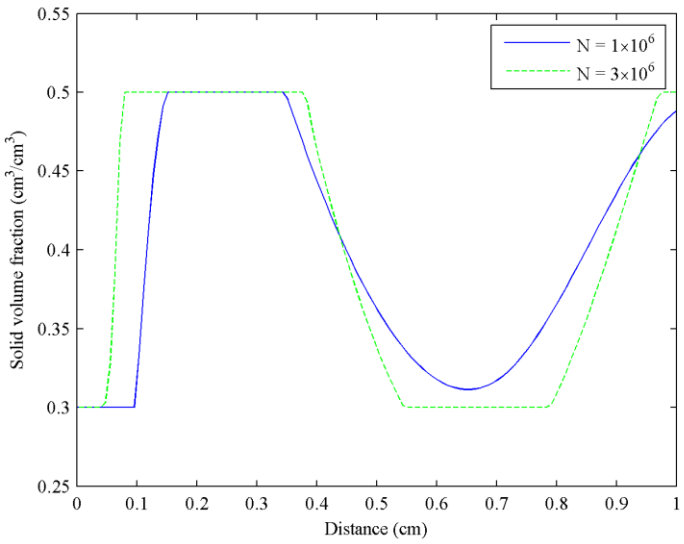

Figure 6-10. The optimised ρ profiles of the tissue scaffold under uniform seeding condition. Different cell seeding densities (N) were applied.

6.3.4 Minimisation of diffusion compliance with variable seeding density

The use of diffusion compliance criterion has also yield a unique ρ profile (Figure 6-11). Four distinct ρ segments can be identified: next to the nutrient source is the maximum ρ segment, followed by a minimum segment, an intermediate segment and finally a maximum segment. The curved profile in the intermediate segment might have been a result of spline

interpolation and non-smooth N-u relationship (Figure 6-3). Increasing the weight of PCHIP interpolation could reduce the curvature and the overshoot, but at a cost of convergence speed.

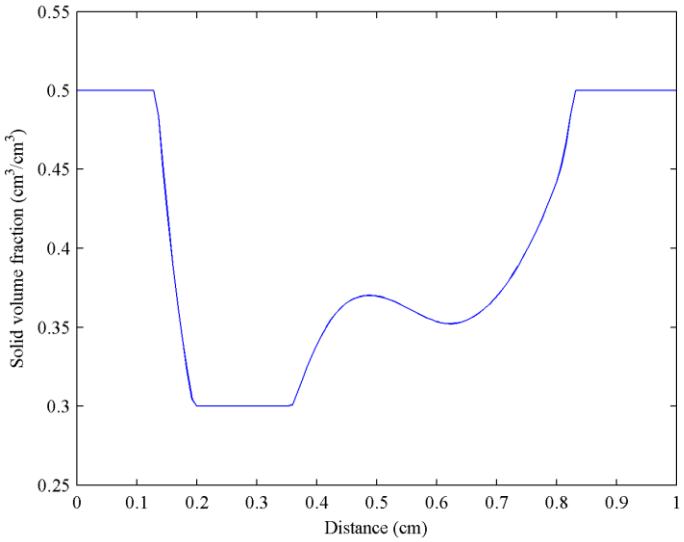

Figure 6-11. The optimised ρ profiles of the tissue scaffold under non-uniform seeding condition (Figure 6-1). No pressure drop was applied.

In this optimisation scenario, a moderate increase in oxygen concentration was observed in the shallower scaffold region (distance < 0.4 cm), whereas the deeper region appeared unaffected (Figure 6-12). Such localized improvement implies that the influence of design optimisation on the deeper scaffold region is limited. Thus, the cells that could actually benefit from the enhanced viability were limited to those living close to the nutrient source. In the region where oxygen concentration and cell viability was low since the beginning of optimisation, the living condition has not improved. In fact, the local oxygen level in the very deep region experienced a mild drop as a result of decreasing diffusivity.

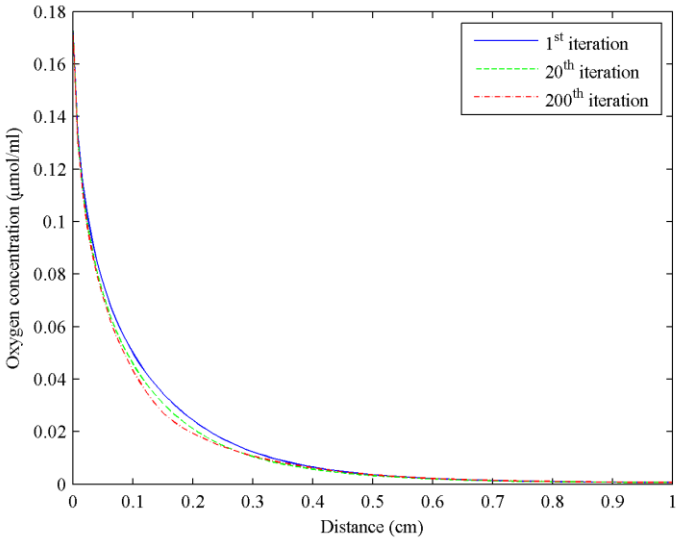

Figure 6-12. The evolution of steady-state oxygen concentration profiles of the diffusion compliance model though the structural optimisation.

6.3.5 Minimisation of diffusion compliance with uniform seeding density

Figure 6-13 shows the characteristic "step" ρ profiles at three different uniform seeding densities. The lengths of individual ρ segments are inversely related to the seeding density. If viability is defined as the depth of scaffold where the oxygen concentration drops to approximately zero, the viability of scaffold is about 0.35 cm at a seeding density of 3×10^5 cell/ml, 0.2 cm at 1×10^6 cell/ml, and 0.1 cm at 3×10^6 cell/ml (Figure 6-14). Beware that the viable depth depends not only on the seeding density but also on the scaffold thickness. Increasing the seeding density and the thickness will significantly reduce the cell viability in a static culture.

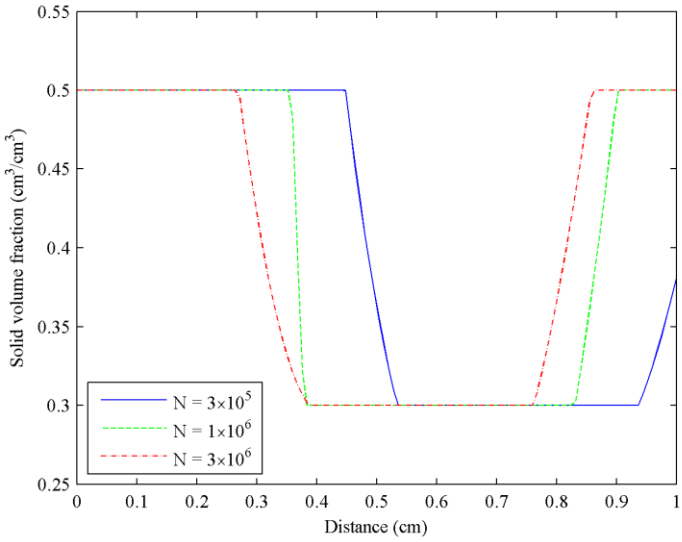

Figure 6-13. The optimised ρ profiles of the tissue scaffold under uniform seeding condition. Different cell seeding densities (N) were applied.

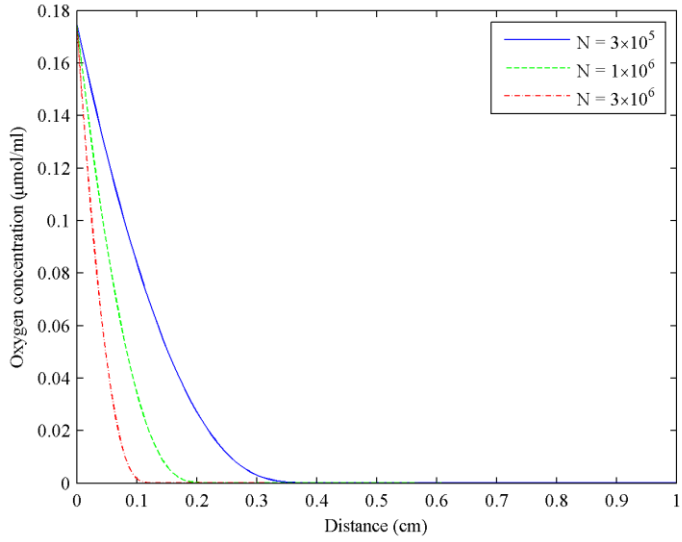

Figure 6-14. The steady-state oxygen concentration profile of the optimising diffusion compliance model under uniform seeding condition.

Overall, using scaffolds with graded and depth-dependent porosity profile can improve seeding outcome and diffusion condition. The improvement in cell viability and cell number are concurrent. However, it was found that the cell infiltration depth and viability are very limited in static culturing condition as manipulating the porosity in the deep scaffold region makes little impact on the cell growth outcome. Static culture with diffusion transport can only support cell life up to a seeding density and to a certain depth. The depth restriction

implies that there exists a limit to the practical thickness of tissue scaffolds, in which seeded cells can stay alive over a long period of time.

In summary, cell number, cell survivability and the overall oxygen concentration in porous tissue scaffolds can be improved by using graded-porosity designs. Additional tests have shown that scaling the cell volume (v_0, Eq. (6-2)), oxygen uptake rate (S_0, Eq. (6-3)), and penalisation factor (p, Eq. (6-4)) made little impact on the final optimisation outcome. The diffusivity property of cells also has little influence on the final results if the cell density is lower. It was found that the non-linear nature of this biological model and convergence issue had indirectly limited the maximum and the minimum cell density that could be simulated. Nevertheless, the simulation conditions used in this study are representative of tissue scaffolding in general.

The oxygen concentration plots and the cell viability profiles presented in this chapter are generally consistent with the past findings [6, 7]. However the actual effect of variable porosity on cell viability cannot be validated since no experimental study has been done on scaffolds with strategically graded porosity, experiments are also outside the scope of this research. Therefore this study recommended further investigation of tissue scaffolds with graded porosity.

6.4 Programming consideration

The response surface method was used for the reason that an analytical expression of the sensitivity could not be derived directly from the non-linear diffusion equation. As the full factorial design of the response surface method was rather expensive to perform, the number of ρ variables to eight was limited to eight points. The ρ profile of the whole scaffold model was interpolated using the PCHIP and the spline methods. Two of such modelling nodes were

placed outside the simulation space of the tissue scaffold, allowing the manipulation of ρ gradient near the modelling boundaries (x = 0 or x = 1).

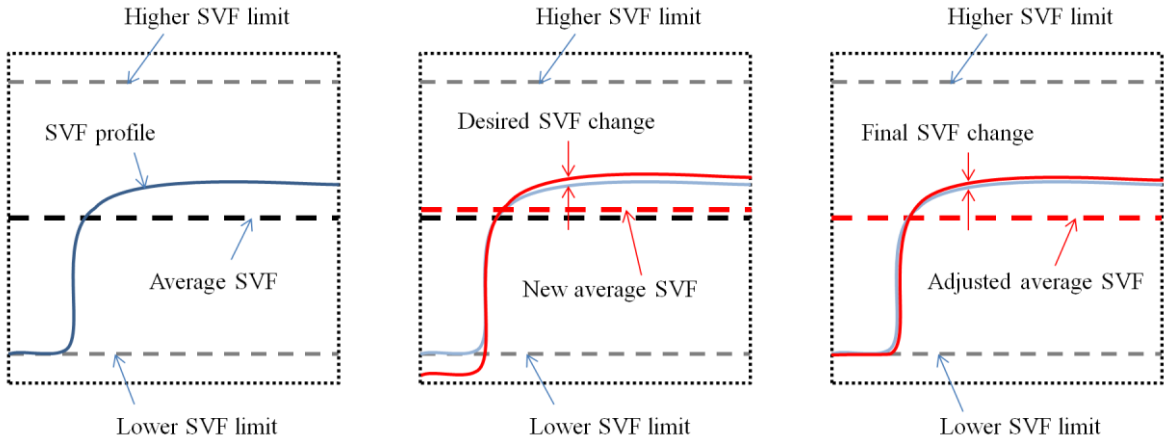

(a) Original (b) Updated (c) Final

Figure 6-15. Schematic illustration of the update of the ρ profile.

The structural evolution could slow down when the high sensitivity regions with low ρ values reached the lower ρ limit (Figure 6-15a). When that happened, the ρ profile could not be updated based on the desired ρ change, otherwise the volume constraint would be violated (Figure 6-15b). To satisfy the volume constraint, only the part of ρ profile with low sensitivity was allowed to move (Figure 6-15c). As a result, the actual ρ update would be much slower than planned. To maintain a reasonable ρ evolution pace, the change in ρ must be scaled up (Eq. (6-16)).

6.5 Concluding remarks

The optimal structures for cell survival in tissue scaffold have been characterised in terms of graded porosity. The results show that improved cell seeding outcome can be achieved through the manipulation of porosity profile. The configuration of porosity/solid volume fraction profile depends on the cell seeding mode, perfusion rate as well as the design objective. The thickness of individual porosity layers and the resultant oxygen concentration largely depends on the seeding condition. The seeding density also determines the practical

thickness of tissue scaffolds. The porosity of the deep scaffold region is less critical and may be compromised to meet the volume constraint. Overall, this design strategy has significantly improved the long-distance diffusion transport across the scaffold but has limited effect on advection-dominated transport system.

While the simulation results have shown that perfusion can effectively improve nutrient transportation rate, it was found the structural optimisation process could not improve the effectiveness of perfusion much further. The influence of structural optimisation on nutrient transport diminishes with increasing perfusion rate.

6.6 References

[1] Rose, F.R., Cyster, L.A., Grant, D.M., Scotchford, C.A., Howdle, S.M. & Shakesheff, K.M. 2004. In vitro assessment of cell penetration into porous hydroxyapatite scaffolds with a central aligned channel. *Biomaterials*, 25**,** 5507-14.

[2] Salerno, A., Guarnieri, D., Iannone, M., Zeppetelli, S., Di Maio, E., Iannace, S. & Netti, P.A. 2009. Engineered mu-bimodal poly(epsilon-caprolactone) porous scaffold for enhanced hMSC colonization and proliferation. *Acta Biomater*, 5**,** 1082-93.

[3] Yu, P., Lee, T.S., Zeng, Y. & Low, H.T. 2009. Fluid dynamics and oxygen transport in a micro-bioreactor with a tissue engineering scaffold. *International Journal of Heat and Mass Transfer*, 52**,** 316-327.

[4] Kang, T.-Y., Kang, H.-W., Hwang, C.M., Lee, S.J., Park, J., Yoo, J.J. & Cho, D.-W. 2011. The realistic prediction of oxygen transport in a tissue-engineered scaffold by introducing time-varying effective diffusion coefficients. *Acta Biomaterialia*, 7**,** 3345-3353.

[5] Malda, J., Woodfield, T.B., van der Vloodt, F., Kooy, F.K., Martens, D.E., Tramper, J., van Blitterswijk, C.A. & Riesle, J. 2004. The effect of PEGT/PBT scaffold architecture on oxygen gradients in tissue engineered cartilaginous constructs. *Biomaterials*, 25**,** 5773-80.

[6] Ishaug, S.L., Crane, G.M., Miller, M.J., Yasko, A.W., Yaszemski, M.J. & Mikos, A.G. 1997. Bone formation by three-dimensional stromal osteoblast culture in biodegradable polymer scaffolds. *J Biomed Mater Res*, 36**,** 17-28.

[7] Papenburg, B.J., Liu, J., Higuera, G.A., Barradas, A.M., de Boer, J., van Blitterswijk, C.A., Wessling, M. & Stamatialis, D. 2009. Development and analysis of multi-layer scaffolds for tissue engineering. *Biomaterials*, 30**,** 6228-39.

[8] Silva, M.M., Cyster, L.A., Barry, J.J., Yang, X.B., Oreffo, R.O., Grant, D.M., Scotchford, C.A., Howdle, S.M., Shakesheff, K.M. & Rose, F.R. 2006. The effect of

anisotropic architecture on cell and tissue infiltration into tissue engineering scaffolds. *Biomaterials,* 27**,** 5909-17.

[9] Oh, S.H., Park, I.K., Kim, J.M. & Lee, J.H. 2007. In vitro and in vivo characteristics of PCL scaffolds with pore size gradient fabricated by a centrifugation method. *Biomaterials,* 28**,** 1664-71.

[10] Bai, F., Zhang, J.K., Wang, Z., Lu, J.X., Chang, J.A., Liu, J.A., Meng, G.L. & Dong, X. 2011. The effect of pore size on tissue ingrowth and neovascularization in porous bioceramics of controlled architecture in vivo. *Biomedical Materials,* 6.

[11] Melchels, F.P.W., Barradas, A.M.C., van Blitterswijk, C.A., de Boer, J., Feijen, J. & Grijpma, D.W. 2010. Effects of the architecture of tissue engineering scaffolds on cell seeding and culturing. *Acta Biomaterialia,* 6**,** 4208-4217.

[12] Lebourg, M., Sabater Serra, R., Mas Estelles, J., Hernandez Sanchez, F., Gomez Ribelles, J.L. & Suay Anton, J. 2008. Biodegradable polycaprolactone scaffold with controlled porosity obtained by modified particle-leaching technique. *J Mater Sci Mater Med,* 19**,** 2047-53.

[13] Nge, T., Nogi, M., Yano, H. & Sugiyama, J. 2010. Microstructure and mechanical properties of bacterial cellulose/chitosan porous scaffold. *Cellulose,* 17**,** 349-363.

[14] Koch, M.A., Vrij, E.J., Engel, E., Planell, J.A. & Lacroix, D. 2010. Perfusion cell seeding on large porous PLA/calcium phosphate composite scaffolds in a perfusion bioreactor system under varying perfusion parameters. *J Biomed Mater Res A,* 95**,** 1011-8.

[15] Bettahalli, N.M.S., Steg, H., Wessling, M. & Stamatialis, D. 2011. Development of poly(l-lactic acid) hollow fiber membranes for artificial vasculature in tissue engineering scaffolds. *Journal of Membrane Science,* 371**,** 117-126.

[16] Chen, Y.H., Zhou, S.W. & Li, Q. 2009. Computational design for multifunctional microstructural composites. *International Journal of Modern Physics B,* 23**,** 1345-1351.

[17] Chen, Y., Zhou, S., Cadman, J. & Li, Q. 2010. Design of cellular porous biomaterials for wall shear stress criterion. *Biotechnology and Bioengineering,* 107**,** 737-746.

[18] Lin, D., Li, Q., Li, W., Zhou, S. & Swain, M.V. 2009. Design optimization of functionally graded dental implant for bone remodeling. *Composites Part B: Engineering,* 40**,** 668-675.

[19] Chen, Y., Zhou, S. & Li, Q. 2011. Microstructure design of biodegradable scaffold and its effect on tissue regeneration. *Biomaterials,* 32**,** 5003-5014.

[20] Salerno, A., Di Maio, E., Iannace, S. & Netti, P. 2011. Tailoring the pore structure of PCL scaffolds for tissue engineering prepared via gas foaming of multi-phase blends. *Journal of Porous Materials***,** 1-8.

[21] Truscello, S., Schrooten, J. & Van Oosterwyck, H. 2011. A computational tool for the upscaling of regular scaffolds during in vitro perfusion culture. *Tissue Eng Part C Methods,* 17**,** 619-30.

[22] Hashin, Z. & Shtrikman, S. 1962. A Variational Approach to the Theory of the Effective Magnetic Permeability of Multiphase Materials. *Journal of Applied Physics,* 33**,** 3125-3131.

[23] Radisic, M., Malda, J., Epping, E., Geng, W., Langer, R. & Vunjak-Novakovic, G. 2006. Oxygen gradients correlate with cell density and cell viability in engineered cardiac tissue. *Biotechnology and Bioengineering,* 93**,** 332-343.

[24] Quelle, D.E., Ashmun, R.A., Shurtleff, S.A., Kato, J.Y., Bar-Sagi, D., Roussel, M.F. & Sherr, C.J. 1993. Overexpression of mouse D-type cyclins accelerates G1 phase in rodent fibroblasts. *Genes Dev,* 7**,** 1559-71.

[25] Cho, C.H., Park, J., Nagrath, D., Tilles, A.W., Berthiaume, F., Toner, M. & Yarmush, M.L. 2007. Oxygen uptake rates and liver-specific functions of hepatocyte and 3T3 fibroblast co-cultures. *Biotechnology and Bioengineering,* 97**,** 188-199.

[26] Shimko, D.A., Shimko, V.F., Sander, E.A., Dickson, K.F. & Nauman, E.A. 2005. Effect of porosity on the fluid flow characteristics and mechanical properties of tantalum scaffolds. *J Biomed Mater Res B Appl Biomater,* 73**,** 315-24.

7 Design and Optimisation of Fractal Vasculature

Effective nutrient transportation is critical to cell survival in tissue scaffold engineering. In the absence of blood vessels and other advection transport measures, cells in a scaffold often suffer from hypoxia. The hypoxic condition is especially dire in a pure diffusion environment. In this regard, natural vascular systems and their fractal patterns have inspired the design of artificial vasculature in tissue scaffolds. In this chapter, the design problem of artificial vasculature has been carried out as a topology optimisation problem with diffusion criterion. Solid isotropic material penalisation (SIMP) method was employed. The topology optimisation was performed in square (2D) and cubic (3D) modelling spaces, with a fluid phase that has a high diffusivity and a solid phase that has a low diffusivity. A range of optimised models had been thereafter obtained by using different fluid and solid diffusivity values. It was found that with a very low solid diffusivity, the optimised fluid phases resemble natural vascular systems and exhibit certain degree of fractality. Increasing solid diffusivity or increasing surface flux at the modelling boundary reduced the resultant fractality. The link between optimality and fractality was found to be case-specific, generally associated with low diffusivity, high volumetric oxygen consumption, and low surface flux.

7.1 Introduction

Sustained and efficient nutrient transport is crucial to the tissue regeneration and the long-term viability of cells in porous tissue scaffolds. It has also been found that, diffusion transport alone cannot maintain an adequate oxygen level across tissue scaffolds of large size, and is further hindered by the cell settlement in the porous space [1, 2] (also see Chapter 6). Decreasing diffusivity has been correlated to increasing cell population, which encumbers the nutrient movement that keeps cells alive inside a scaffold [3] and threatens cell viability across a construct [4].

In natural tissues, blood vessels address the demand of nutrient by acting like a source. The branching of blood vessels improves their spatial coverage and reduces the distance between individual cells and the vessels. Similarly in tissue scaffolds, vascularisation creates an internal nutrient supply that facilitates tissue regeneration [5]. The development of the vasculature system through a tissue scaffold during the tissue regeneration process, or the lack of it, will determine whether the oxygen level in any part of the construct can be sustained [6]. Considering the absence of vascular system in typical tissue scaffolds in vitro, the introduction of artificial vasculature may improve certain aspect of cell viability and growth [7]. For this reason, artificial vasculature emerges as a strategy to tend the need of mass transportation and oxygen conduction [8].

To tackle the nutrient transportation problems from a structural perspective, topology optimisation methods can be utilised to create complex and non-intuitive structures that resemble blood vessel network. Topology optimisation has already been used in transport-related design problems such as the design of fluid channels [9, 10] and permeable microstructure [11]. Computational design optimisation also has been applied to solve diffusion-related problems on both microscopic [12, 13] and macroscopic levels [14]. Moreover, complete and realistic vascular branching networks have been generated using the constrained constructive optimisation [15].

Fractal is a special design focus in this study. Naturally occurring fractal patterns found in ice crystal, coastline [16], and blood vessel network [17] has fascinated mathematicians and artists alike. Although the optimality of these fractal patterns is largely up for debate, biologically-inspired materials is becoming a popular area of research for those who seek natural solutions [18]. The key challenge in this field of work is the lack of proof of optimality. On one hand, it is unclear whether fractal patterns can potentially be optimal. On

the other hand, it is yet known whether some well-known optimal solutions are fractal. To gain a better understanding of the nature of optimality and fractal patterns, the cause and effect of fractalisation must be determined.

A multi-scale optimisation on the diffusion transport in tissue scaffolds has been conducted. The goals of this study are: (1) to design a vasculature network for optimal nutrient transport by means of topology optimisation, and (2) to establish any possible relationship between optimality and fractality under the steady-state diffusion condition. This relationship will help elucidate the much speculated self-optimising nature of vascular system [19]. Design from a fractal perspective also gives rise to the prospect of a comprehensive tissue scaffolding solution, which encompasses both macroscopic and microscopic transportation mechanisms on a continuous scale.

7.2 Optimisation of vascular structure

Introducing artificial macroscopic channels to scaffolds is shown to be an effective technique in supporting cell colonisation in tissue scaffolds [20, 21]. To take advantage of such technique at their maximum potential, the application of topology optimisation in the design of vasculature system was proposed. Following the optimisation, the hypothetical optimality of natural blood vessel system was assessed from an engineering design point of view.

7.2.1 Diffusion optimisation under uniform oxygen consumption

The aim of this study is to design an artificial vasculature system for tissue scaffolds. It is assumed that the scaffolds are uniformly seeded with cells under a steady-state diffusion condition, where cells consume oxygen at a constant rate (Figure 7-1). To prevent hypoxia, the artificial vasculature should be designed in a way to ensure maximum oxygen delivery and concentration.

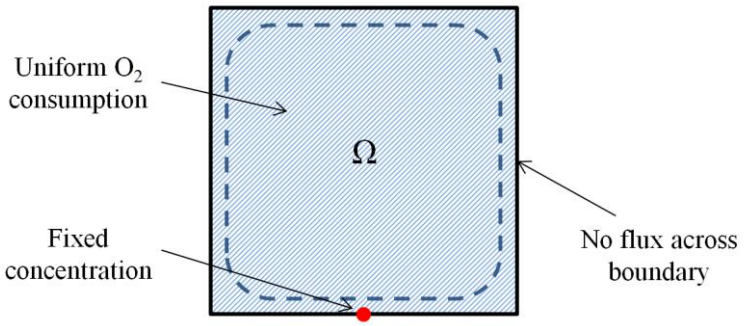

Figure 7-1. Boundary and load conditions in design models with uniform oxygen consumption.

This design problem can be formulated as a two-phase problem with void/fluid as the conductive phase and solid as the less-conductive phase (Figure 7-2). In this study, it is assumed that oxygen enters the scaffold through a point-source where the oxygen concentration level is maintained at a constant level. The void/fluid phase is given a nominal diffusivity value of 1 unit. The solid phase is considered partially conductive, and allows diffusion to occur at a lower rate (<1). The topology optimisation is to be conducted in various scenarios, each with a different oxygen diffusivity value of the solid phase.

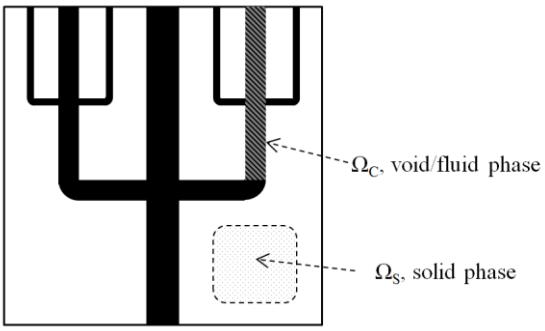

Figure 7-2. Schematic sketch of the artificial vasculature.

The objective of this topology optimisation is to minimise the diffusion compliance, J, which is expressed as:

$$\begin{aligned} &\text{Minimise: } J = \int_{\Omega} \frac{\partial u^T}{\partial x} D \frac{\partial u}{\partial x} d\Omega \\ &Subject\ to: \int_{\Omega} \rho_C d\Omega \leq \Omega_{\text{void}} \end{aligned} \tag{7-1}$$

where u is the concentration, D is the diffusivity coefficient or matrix, Ω denotes the design domain, $d\Omega$ is the volume, ρ_C is the local void volume fraction, and Ω_{void} is the total void volume fraction constraint. The void volume is presumably filled with fluid. Such objective formulation is identical to the thermal compliance, which is a measure of thermal conductivity [13]. The diffusivity coefficient is a function of fluid-solid volume fraction. Assuming that the fluid and solid phases have nominal diffusivity of D_V and D_s, respectively, the effective local diffusivity D of partially-solid material can be expressed as:

$$D(\rho) = D_s + (D_V - D_s) \times {\rho_V}^p, \tag{7-2}$$

where p is the penalisation factor. This power-law relationship between volume fraction and diffusivity has followed the Solid Isotropic Material with Penalisation (SIMP) principle [22].

The diffusion system at the state of equilibrium is governed by Fick's law,

$$-D\frac{\partial^2 u}{\partial x^2} = f_b, \tag{7-3}$$

where f_b is the body force and its value is a constant. The oxygen consumption is volumetric and can be appropriately represented by the body force term.

7.2.2 Applying oxygen consumption as surface flux

Oxygen consumption can also be applied as surface flux across the modelling boundary, or as a combination of flux and body force, as illustrated in Figure 7-3. In this case, flux can be considered as the oxygen demand of the neighbouring tissue just outside the design domain. Therefore, oxygen is drawn out of the modelling domain.

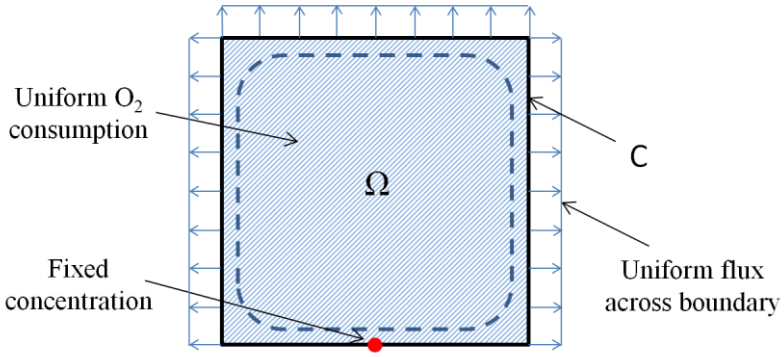

Figure 7-3. Boundary and load conditions in design models with surface flux. C denotes the location where load f_c (flux) is applied.

To model the additional oxygen consumption, a flux term is added to the governing equation:

$$-D\frac{\partial^2 u}{\partial x^2} = f_b + f_c \tag{7-4}$$

$$\int_{\Omega} f_b d\Omega + \int_{c} f_c d\Omega = F \tag{7-5}$$

where f_c is the flux across the modelling boundary, and F is the sum of oxygen consumption. The total oxygen consumption, F, is a constant value. Neither the flux nor the body force can be negative anywhere in the modelling space. Different design scenarios can be created with different combinations of f_b and f_c values.

7.2.3 Zooming and re-optimisation

To investigate the local material distribution and improve the clarity of regional vasculature pattern, a small section of model can be taken and re-optimised at a higher resolution. As illustrated in Figure 7-4, a section, Ω_1, is taken from the original model, Ω_0. The resolution of Ω_1 is increased to match that of the original model. Concentration degree of freedom (DoF) on all internal boundaries of the new model is fixed (marked in red). The concentration is interpolated from the original DoF solution along the internal boundaries.

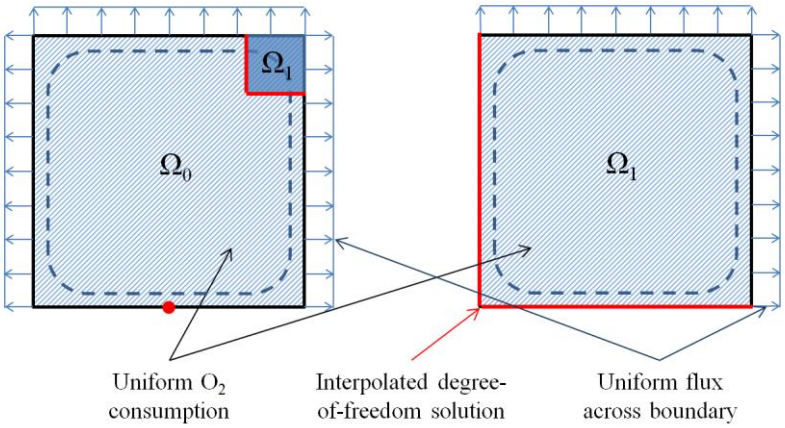

Figure 7-4. The boundary and load conditions of a new local design model.

7.3 Results and discussion

Maintaining even nutrient distribution and transport is a common challenge in tissue scaffold engineering. The design of macroscopic channels and vasculature network has been proposed as a potential solution to enhance the transport environment and improve cell viability in tissue scaffolds [7, 8, 23]. Based on this concept, a scenario of topology optimisation known to produce models exhibiting characteristics of vasculature was created [13, 14]. The optimised vascular structures were examined to determine their fractality through model-scaling and re-optimisation. Using these results, it can be deduced whether the optimal structures are truly fractal, or conversely, whether the fractal nature of vasculature network is essential to achieving optimality.

7.3.1 Volumetric oxygen consumption

In Chapter 6, it has been demonstrated that the scaffold porosity can be used as a design variable in structural optimisation. The results shows that manipulating the porosity profile can effectively increase the overall cell survivability, even though such success does not fully resolve the viability problem. Here porosity is used as a design variable for the creation of macroscopic vasculature-like porous network.

In this chapter, a two-phase design problem has been formulated, in which one phase represents the artificial vasculature and the other represents the solid scaffold material. Topology optimisation was performed to manipulate the solid material distribution of the vascular system. The overall impedance to diffusion transport was minimised by minimising the diffusivity compliance. Design models were discretised into 125×125 structured finite element models; each element has solid volume fraction of 65% at the beginning of the simulation, at the same time a 65% total volume constraint was imposed. The Method of Moving Asymptote (MMA) solver [24] was employed to solve this optimisation problem. Different combinations of oxygen diffusivity and consumption models had been tested. The sink (consumption) was formulated as a combination of uniform body force and surface flux, which signified the volumetric oxygen demand inside the simulation domain and the oxygen demand outside the domain, respectively.

Vasculature-like structures had been successfully generated through the topology optimisation. Complex branch patterns have formed naturally in optimisation scenarios that involved only volumetric oxygen demand, as shown in Figure 7-5. Starting in a modelling space filled with intermediate material ($\rho = 65\%$ in every element), solid elements ($\rho \to 1$) and fluid elements ($\rho \to 0$) gradually materialised and became distinguishable over time. Using a high penalisation factor helped remove the intermediate density elements ($0 < \rho < 1$), and allowed the models to evolve into two distinct phases. The fluid elements self-arranged into channelled system regardless of the diffusivity value. As the fluid phase sharpened, small auxiliary channels spawned along their larger parent channels like branches. In some cases, many generations of channels formed and self-arranged in a fractal fashion (Figure 7-5 g-i). In most scenarios, toward the end of topology optimisation there remained a small percentage of intermediate elements at the interface of two material phases. Increasing the penalisation factor or increasing the modelling resolution reduced the grey band

thickness. Removing this intermediate phase became increasingly challenging as D_s decreases, which resulted in the development of finer channels and the increasingly complex solid-fluid boundary. The end result in the $D_s = 10^{-8}$ case closely resembles the models found in an earlier study in term of branching pattern [13]. Decreasing D_s value unsurprisingly led to increasing diffusivity compliance and a steeper concentration drop across the model (Figure 7-6).

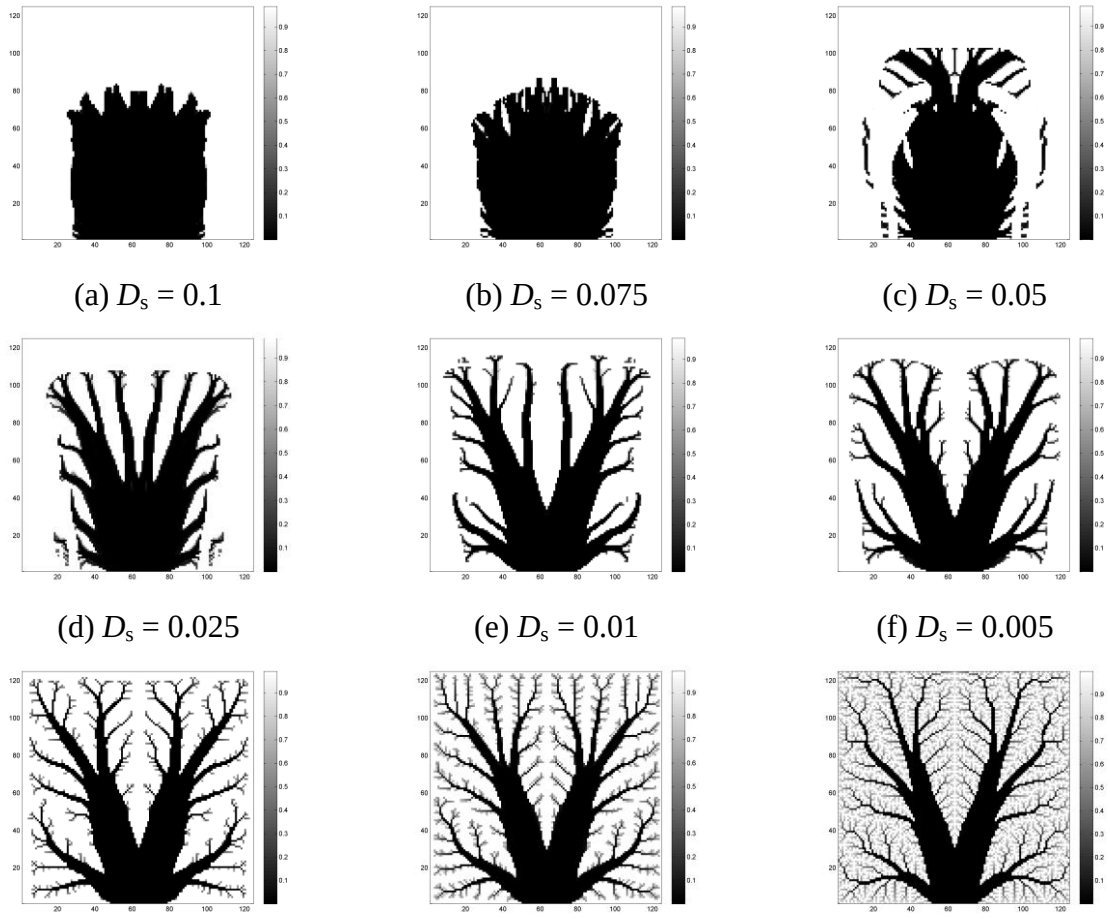

(a) $D_s = 0.1$ (b) $D_s = 0.075$ (c) $D_s = 0.05$

(d) $D_s = 0.025$ (e) $D_s = 0.01$ (f) $D_s = 0.005$

(g) $D_s = 0.0025$ (h) $D_s = 0.00125$ (i) $D_s = 10^{-8}$

Figure 7-5. Optimised models with different oxygen diffusivities through the solid phase (white region). The total fluid volume fraction (black region) is 35%. No flux was applied on the boundary of design domain.

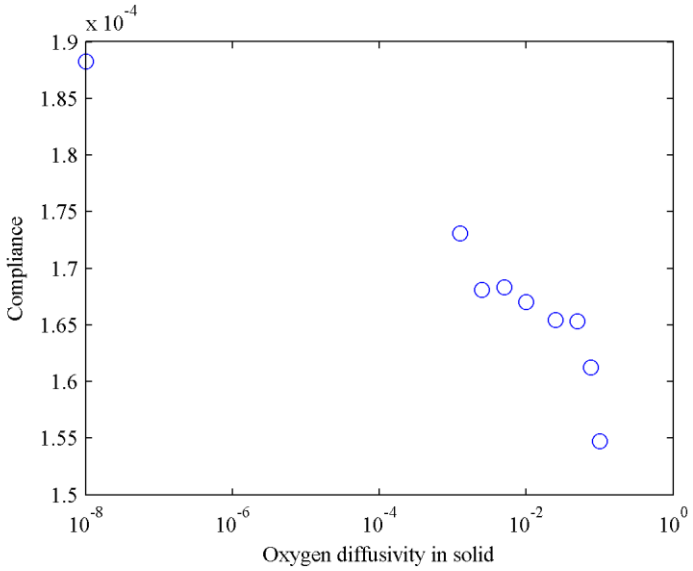

Figure 7-6. Compliance versus oxygen diffusivity through the solid phase, D_s.

In the optimised $D_s = 10^{-8}$ model, the total fluid volume fraction decreases across the design domain (Figure 7-7). Notably, when plotted as a function of distance from the source point (x=0, y=0), the fluid volume appears to drop exponentially (Figure 7-7a). When plotted against the distance from the source surface (y=0), the drop appears to be linear (Figure 7-7b).

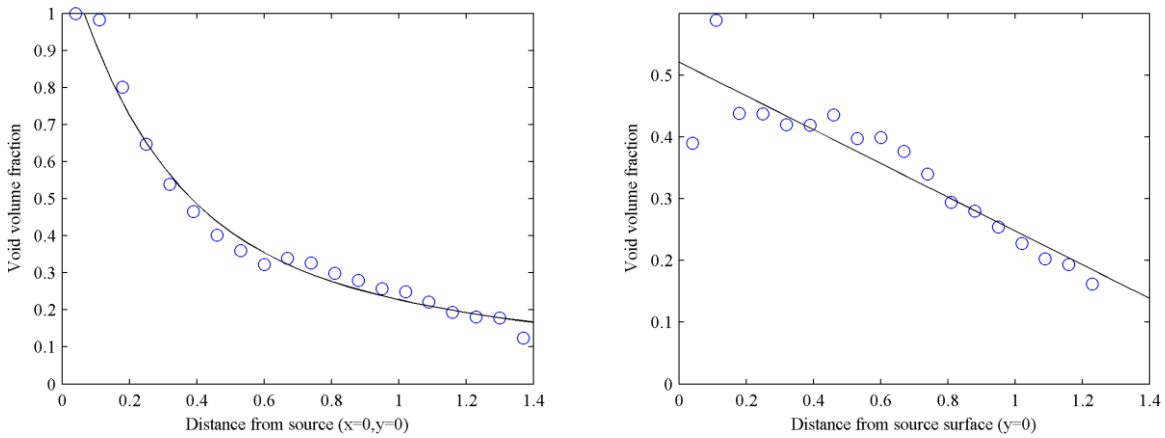

(a) Distance from the point source (x=0, y=0)

(b) Distance from the y = 0 surface

Figure 7-7. Fluid volume fraction versus diffusion distance. Here, the fluid volume fraction is the sum of fluid volume (area of the black region) divided by the total volume (total area). The model is case (i) of Figure 7-6, where $D_s = 10^{-8}$.

A small section of the low solid diffusivity model $D_s = 10^{-8}$ was up-scaled in term of mesh density to allow a closer inspection of the branch structure and re-optimisation (Figure 7-8). In this process, the top-right corner of original model was taken with five times increase in resolution, and re-optimised (Figure 7-8 a-b ×5). The process was repeated to further improve image quality (Figure 7-8 b-c ×25, c-d ×125, and d-e ×625). Remarkably, all optimised local (scaled) models contain ubiquitous branch structure, which suggested fractality (Figure 7-8 a-e). Throughout the zooming and optimisation process, new and finer branches had kept emerging regardless of how small the extracted model was. On the scale of ×625, self-similarity can be clearly observed (Figure 7-8e). Note that the size of the model in Figure 7-8d is the same as the size of single square element in Figure 7-8a (every model has a resolution of 125-by-125). This shows that the fractal fluid channels are presented in the grey pixel at the top right corner of the original model. Repeatedly zooming in and re-optimising had revealed the local material distribution that could not have been defined due to the resolution limit. When the same operation was performed on non-fractal models, for example, zooming and re-optimising the higher solid diffusivity model, $D_s = 10^{-2}$ (Figure 7-5e), the material boundary had only been smoothened and sharpened but no fractal pattern had emerged (Figure 7-8f). In comparison, the fluid network in the local $D_s = 10^{-8}$ model shows obviously better spatial coverage than that of the zoomed-in $D_s = 10^{-2}$ model. This result demonstrates that fractality is not a numerical artefacts created by the zooming process, and reaffirms the obvious fact that only fractal topology shows fractal patterns on all levels.

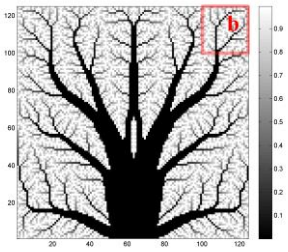

(a) $D_s = 10^{-8}$, zoom: ×1

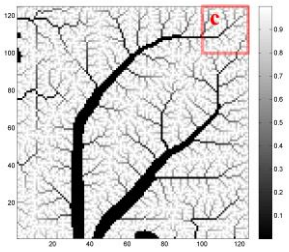

(b) $D_s = 10^{-8}$, zoom: ×5

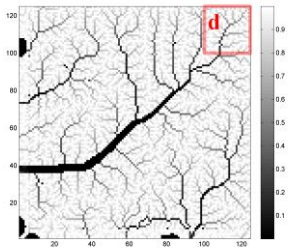

(c) $D_s = 10^{-8}$, zoom: ×25

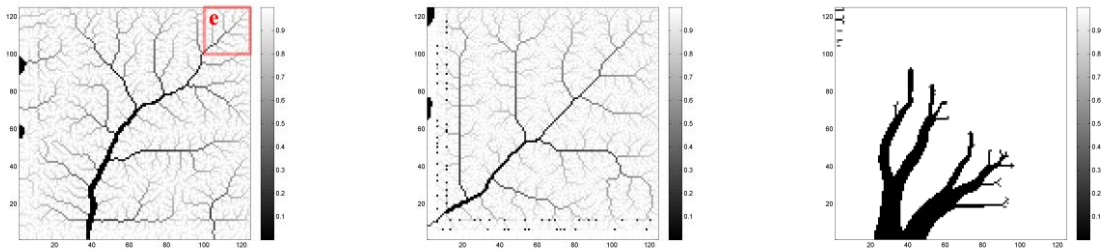

(d) $D_s = 10^{-8}$, zoom: ×125 (e) $D_s = 10^{-8}$, zoom: ×625 (f) $D_s = 10^{-2}$, zoom: ×5

Figure 7-8. Enhanced local images of optimised channel network show infinite branching pattern. Each subsequent image is a re-optimised partial model of its predecessor. The top-right corner of each original model (a-d, 25×25 pixel) is zoomed in by 500% (b-e, 125×125 pixels) and re-optimised as a new model. (f) is the zoom-in image of $D_s = 10^{-2}$ model, which shows no fractal pattern.

It was found that the resultant fractal shapes were sensitive to the choice of design parameters. Using different MMA parameters or initial models could result in some degree of deviation in the final topological (compare Figure 7-5i and Figure 7-8a). For this reason, the zoomed and re-optimised images could deviate when using a different set of design parameters.

Some topological anomalies emerged during the re-optimisation process. These numerical artefacts include isolated material spots, artificial spots and lines along the interpolated boundary. Large black spots in Figure 7-8b-e are examples of the isolated void, forming in the region where the DoF boundary condition was imposed. Artificial spots and lines emerged along the borders where discrete volume constraints were applied (black dots and lines in Figure 7-8d-e). Nevertheless, the re-optimised fluid phase distribution conformed well to the original image where it was taken. Only the light grey areas, i.e. pixels that are mostly solid, re-arranged to form a new fluid network (compare Figure 7-8a with b, and b with c). Generally, the DoF boundary condition and the volume constraint are believed to be responsible for the formation of these numerical artefacts in the zoomed-in models. Anyhow, using the scaled original images (Figure 7-8a-d, red square) as the initial models produced fairly conformal results. Using a uniformly grey image as the initial model would otherwise

result in very different material distribution and break the material/DoF connectivity at the modelling boundary.

Recursion, which is a main feature of fractal, is manifested in the formation of diffusion barrier. In this specific model, the solid phase with extremely low diffusivity ($D_s = 10^{-8}$) has acted as diffusion barrier and emerged concurrently with void channel. Throughout the optimisation process, long continuous solid walls formed across the design domain and practically divided it into many sub-domains as illustrated in Figure 7-9. As diffusion could occur between across the walls, the solid structure in each sub-domain evolved independently, in which shorter walls formed and further divided each sub-domain into smaller domains (Figure 7-9b-c). This process had repeated and had been self-driven as formation of wall ($\rho \rightarrow 1$) always occurred in conjunction with formation of diffusion passage ($\rho \rightarrow 0$) due to the volume constraint.

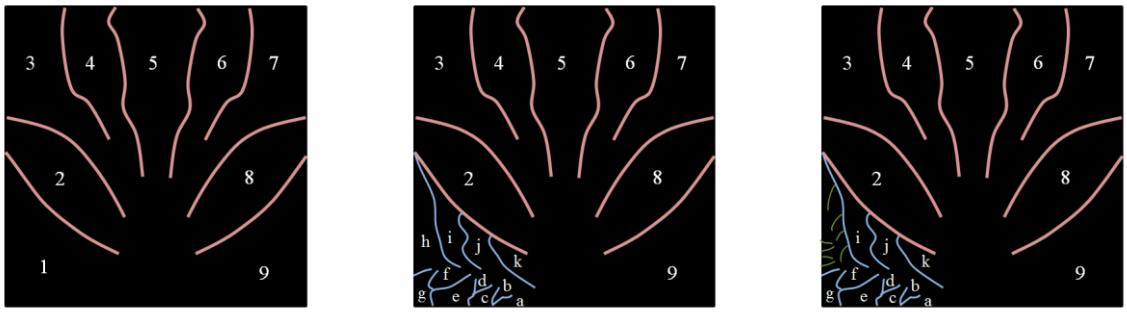

(a) Primary division (b) Secondary division (c) Tertiary division

Figure 7-9. Effective flux boundary of the diffusion network. These lines depict major solid barriers that divide the transportation network into independent zones. (a) Each primary zone (1-9) contains only one primary channel. (b) Each secondary zone (a-k) contains only one secondary channel, and so on.

Self-similarity, which is another feature of fractal, is signified by the similar branching pattern in every divided domain and on every level (Figure 7-8 and Figure 7-9). The branching behaviour is attributed to the need of spatial coverage of the transport system. It is obvious that multiple thin channels provide a better spatial coverage than one thick channel.

Such spatial coverage has the apparent advantage of minimising the distance between any point in the design space and the nutrient supply stream. It has been reported that in human body, most cells live within 200 microns from the nearest capillary and 200 microns is about the longest viable diffusion distance in cell culture [25, 26]. Hence, minor branches are found everywhere in similar spatial arrangement.

The branching and fractal pattern was also observed in the models where oxygen consumption was only imposed on the solid phase (Figure 7-10). The resultant models showed no significant difference in topology when compared to their uniform oxygen consumption counterparts, but with slightly thinner fluid network and improved spatial coverage. Such topological difference was attributed to the fact that the fluid phase no long consumed oxygen, and reaching out into the deep solid area was essential to reduce diffusion gradient and compliance. The material distribution among the models with different D_s values appeared to be more consistent. The results also show an increasing fractality as the D_s value decreases.

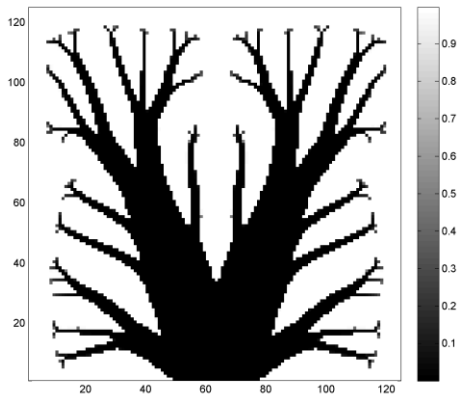

(a) D_s = 0.01

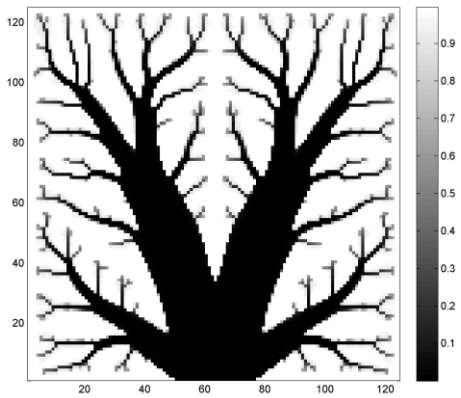

(b) D_s = 0.0025

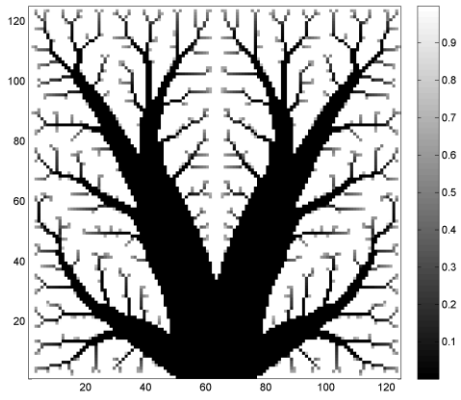

(c) D_s = 0.00125

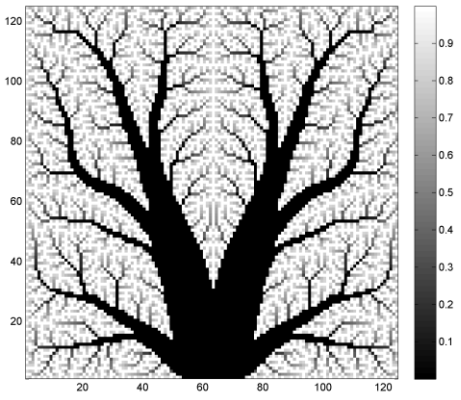

(d) $D_s = 10^{-8}$

Figure 7-10. Optimised models with different oxygen diffusivities, D_s. The imposed body force is directly proportional to the solid volume fraction. The total fluid volume fraction (black region) is 35%. There was no surface flux across the modelling boundary.

The fluid channels did not grow all the way through the body-force-only models. Furthermore, the optimal channel length and branching pattern were found to depend on D_s. In high solid diffusivity models ($D_s \gg 0.01 \times D_f$), the branches tended to be shorter and offered less spatial coverage since the solid phase already allowed certain degree of diffusion. In contrast, the channels in low solid diffusivity models ($D_s \ll 0.01 \times D_f$) almost reached the modelling boundary at the end of optimisation. If fluid were to flow through these constructs, the solid edges of these images must be cropped (Figure 7-11). In that case, each model should be cropped by a different percentage according to the thickness of the solid layer. High solid-diffusivity models were trimmed by a greater amount. Individual images were also sharpened to create higher black-and-white contrast using different lightness thresholds, so that the volume fraction constraint was satisfied. High solid-diffusivity models required lower thresholds, meaning that most nearly-black (nearly-fluid) elements were considered as solid (white).

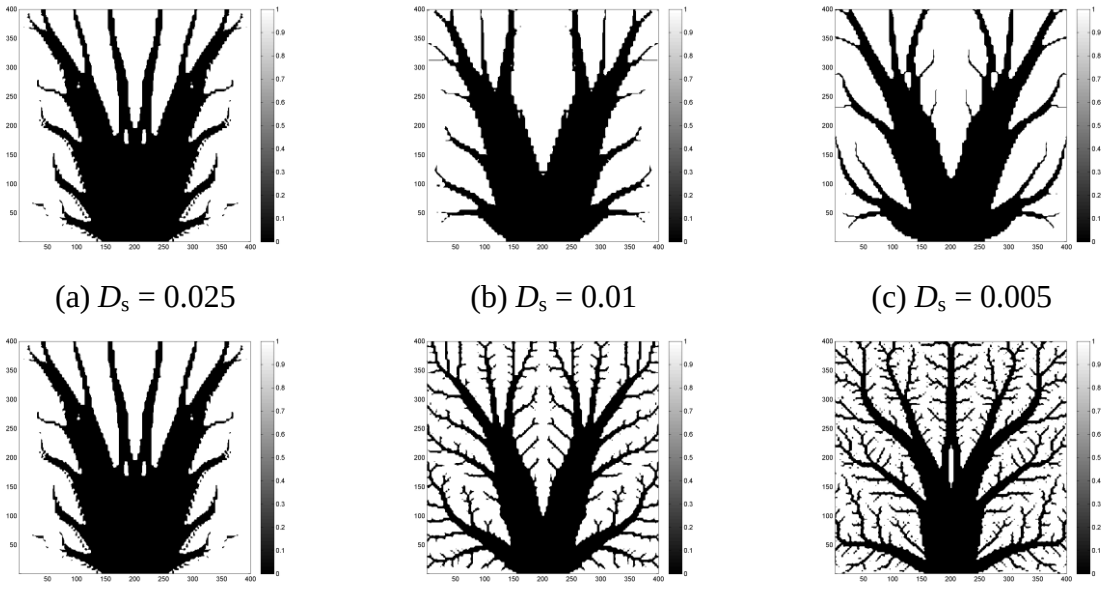

(a) D_s = 0.025 (b) D_s = 0.01 (c) D_s = 0.005

(d) D_s = 0.0025 (e) D_s = 0.00125 (f) D_s = 10^{-8}

Figure 7-11. Cropped and sharpened images with different oxygen diffusivities. The total fluid volume fraction (black region) is 40% in all models.

Image sharpening could compromise phase continuity. The formation of fine channels and isolated solid and fluid regions were observed in the sharpened low D_s models (e.g. Figure 7-11f). It was found that with a nearly zero D_s (e.g. Figure 7-11f), fractality could increase indefinitely. Consequently, the newer generations of channels became thinner than the pixel size (consider Figure 7-9c). As it is impossible to increase the model resolution indefinitely, grey elements would always present regardless of modelling setting. The channels became infinitely thin as D_s approaches zero, and were filtered out during image processing.

It is important to note that the significant amount of intermediate material (grey elements) found in the final models is not an indication of poor convergence. In fact, these grey pixels reflect the nature of fractal pattern, particularly in the low resolution models. As demonstrated in Figure 7-8a-e, fluid network exists on all levels and covers every single pixel. Increasing the penalisation factor of the SIMP method in topology optimisation reduces the "greyness", but it does not eliminate their existence. Increasing the modelling resolution has also shown limited influence, and is only effective in improving the black-and-white

contrast if the optimal pattern is non-fractal (e.g. Figure 7-8f). Changing other modelling and optimisation parameters affects only the resultant material distribution but not the level of fractality. Knowing that the optimal distribution is fractal, attempting to remove such pattern is actually counterproductive to the optimisation effort. Therefore, the "greyness" should be recognised as a characteristic of the optimised diffusion model rather than a convergence problem.

Fluid movement has not been taken into account in this design process. Based on the diffusion design criterion, the transport systems are optimised for steady-state diffusion only. Nevertheless, the design scenarios presented here are a reasonable analogue of pressure-driven fluid transport system such as plant roots and leaf veins. The point source term is an analogue of water absorption through roots and water supply to leaves. The mass transport of nutrients and oxygen in permeable media follows similar principle that governs diffusive mass movement. Therefore the design models and the solutions are consistent with natural transport phenomena.

The results however may not be representative of a forced perfusion system due to the difference in nature between creeping flow and forced advection. Unlike diffusion, advection rate can be increased by increasing pressure. Increasing advection rate alone can minimise global concentration gradient to any desirable level regardless of the size of model. Even though a design constraint can be imposed on the fluid flow rate or the wall shear stress level [27], the wall shear stress can be easily reduced by scaling up the channel size. Such scalability implies that it is easier to upscale mass transport by simply increasing fluid flow rate and channel size than trying to modify the vasculature. As a result, advection transport can largely outweigh diffusion transport and quantitatively makes diffusion a less influential

factor. Furthermore, the boundary condition of an advection problem is very different from the point-source boundary condition used in a diffusion-driven system.

The intermediate material phase in the optimised models can become a problem when it comes to manufacturing. Multiphase topology optimisation normally expects the results that contain only pure material phases. However, the advancing multi-material printing technology has made it possible to fabricate structures with intermediate materials [28]. Although not topologically ideal, structures with such materials exhibit better phase continuity. Such technology may eliminate some problems regarding the manufacturability of intermediate materials to some extent. However, considering that void or fluid is not a printable phase, this manufacturing technique cannot be applied.

7.3.2 Oxygen flux across boundary of design space

In the second part of this study, the flux boundary condition was introduced and its impact on topology optimisation was assessed. As seen in Figure 7-12, the most apparent effect of this new oxygen demand was that fluid channels went all the way across the design space. It was found that increasing the proportion of oxygen uptake through flux reduced fractality, and improved the connection of channel network between the source and the boundary. By conducting the aforementioned zooming and re-optimising process, it was found that the branching pattern would not become fractal if body force was zero (Figure 7-12a-b). However, as long as the body force was non-zero, fractal pattern would emerge, especially in models with very low diffusivity (note the light-grey elements in Figure 7-12d, f, h, j and l). Nonetheless, the relative amount of surface flux affects the complexity of branching pattern, channels size, and number of dead-end channels (Figure 7-12e, g, i and k).

Flux:Body force	D_s = 0.00125	$D_s = 10^{-8}$
100%:0%	 (a)	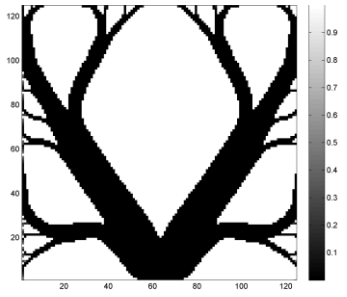 (b)
90%:10%	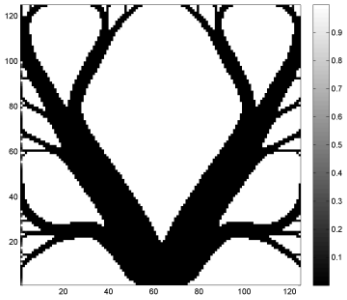 (c)	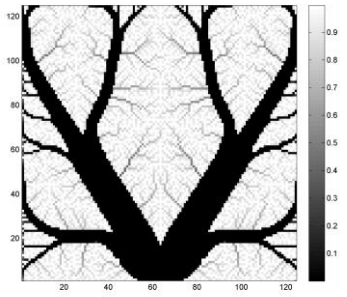 (d)
75%:25%	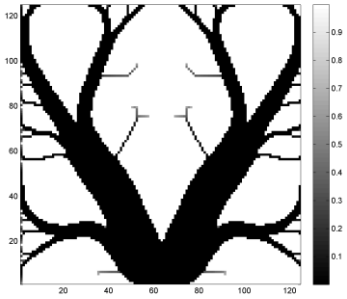 (e)	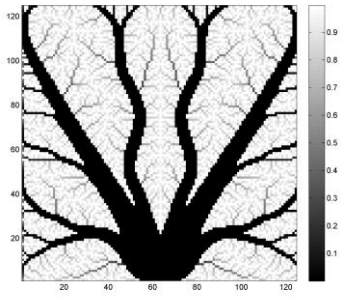 (f)
50%:50%	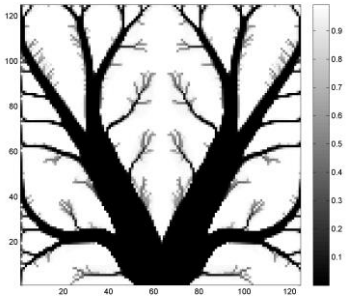 (g)	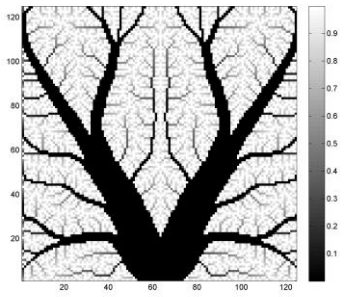 (h)

25%:75%	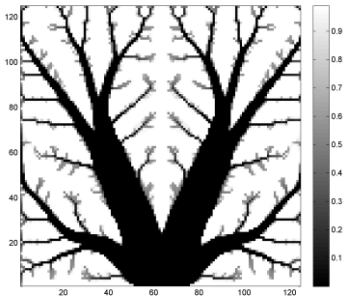 (i)	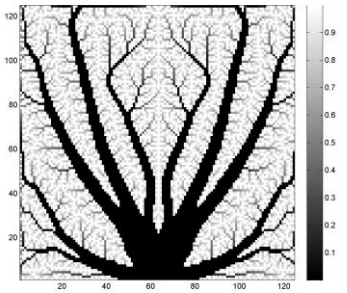 (j)
10%:90%	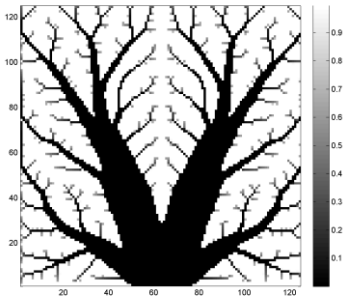 (k)	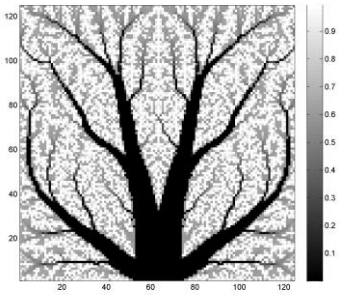 (l)

Figure 7-12. Optimised models with different flux to body-force ratios and oxygen diffusivities in the solid phase. The total fluid volume fraction (black region) is 35%.

In the high-flux low-body-force scenarios, the optimised structures appear in a common shape regardless of the diffusivity through the solid phase (compare Figure 7-12 a and b). The branched channel pattern could only be obtained if D_s was sufficiently low ($D_s < 0.01$, compared to Figure 7-13). Otherwise, the fluid phase would acquire a "bulb" shape (Figure 7-13a, $D_s = 0.1$) similar to the results found in the body-force-only simulations (Figure 7-5a-c). In other words, a model developed a bulb-shaped fluid phase with a high D_s value and a branched channel network with a low D_s value. A branched pattern can be either fractal or non-fractal whereas the bulb pattern is always non-fractal. It has become apparent that both the development and the fractalisation of channel network pattern are strongly related to the oxygen diffusivity in the less conductive phase, namely the solid phase in this study.

Flux:Body force 100%:0%	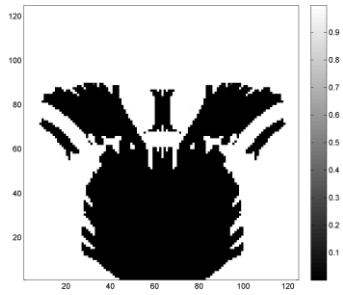 (a) D_s = 0.1	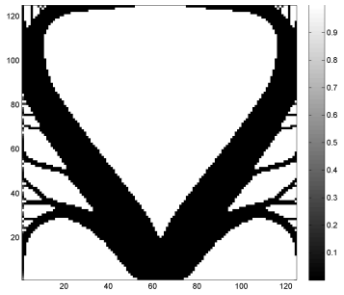 (b) D_s = 0.01

Figure 7-13. Optimised models with different solid diffusivities, D_s, under surface-flux condition only. The total fluid volume fraction (black region) is 35%.

7.3.3 3D volumetric oxygen consumption

The topology optimisation in 3D under body force condition has also yielded the characteristic branching pattern, as shown in Figure 7-14. With relatively high oxygen diffusivity in the solid phase, branching did not occur (Figure 7-14a). Reducing the oxygen diffusivity has resulted in the development of branched fluid phase (Figure 7-14b-d). The optimised model with a very low oxygen diffusivity shows that the fluid channels cover the entire modelling domain.

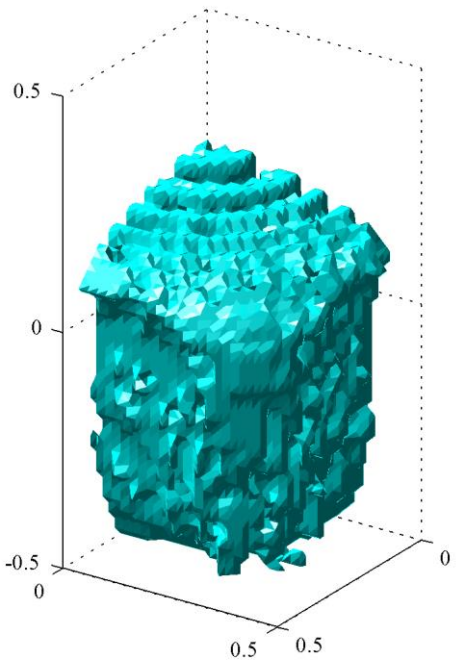

(a) D_s = 0.05

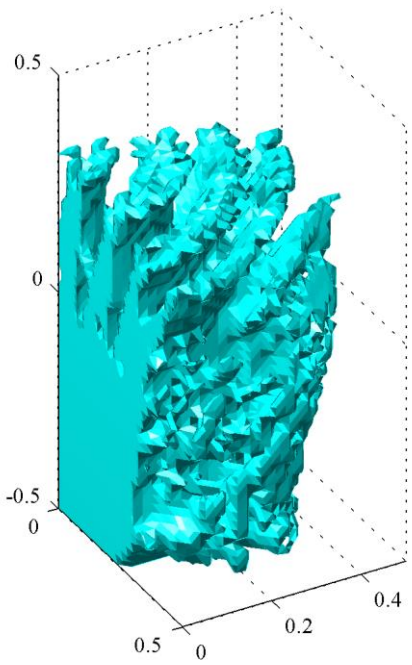

(b) D_s = 0.01

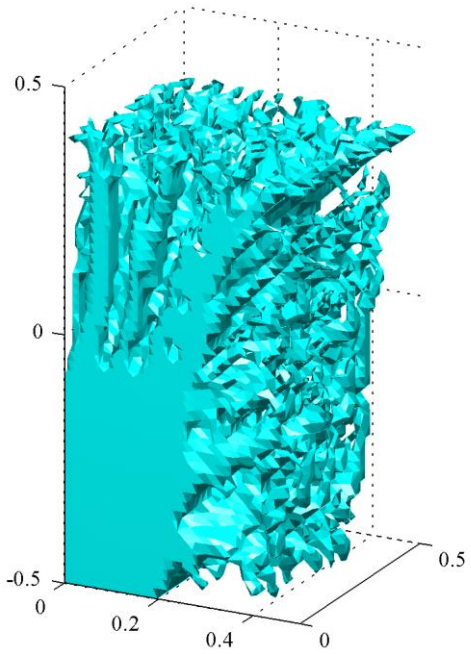

(c) D_s = 0.001

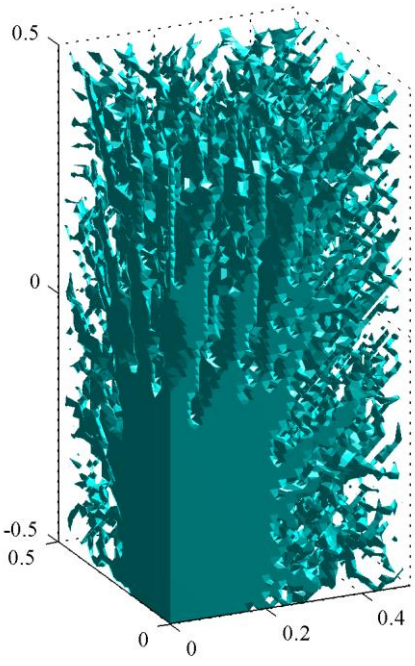

(d) $D_s = 10^{-8}$

Figure 7-14. Quarter-model view of the optimised 3D models with different oxygen diffusivities through solid, D_s. The source point is at the bottom corner (x,y,z) = (0,0,-0.5) of the quarter model. The total fluid volume fraction (cyan region) is 35%.

The cross-sectional plots in Figure 7-15 reveal the material distribution and possible degree of fractality. It was found that only low oxygen diffusivity models contained a significant amount of intermediate materials (red and yellow pixels in Figure 7-15d), whereas the high solid diffusivity models contained distinct solid and fluid phases and little intermediate phase. This result is consistent with the findings in 2D optimisation scenarios, and thus strengthens the supposed link between solid diffusivity, fractality and branching pattern.

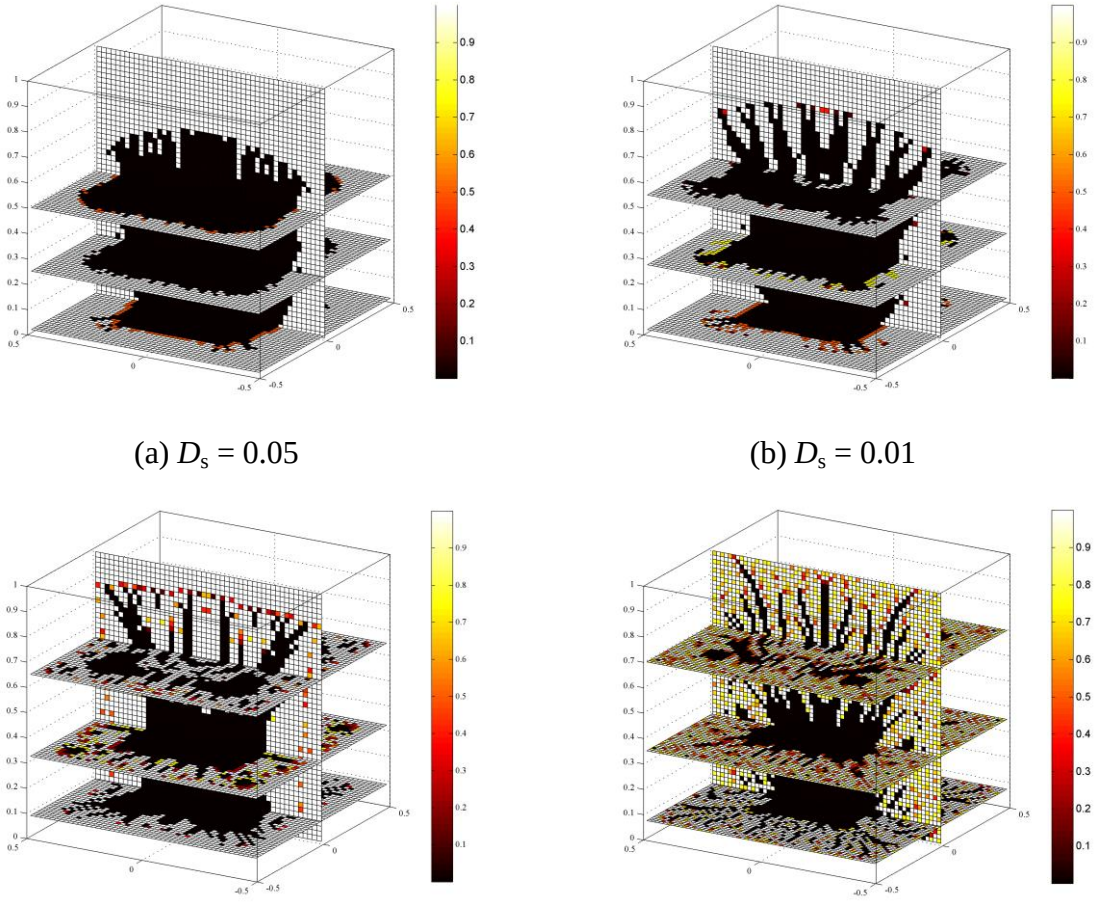

(a) D_s = 0.05 (b) D_s = 0.01

(c) D_s = 0.001 (d) $D_s = 10^{-8}$

Figure 7-15. Cross-sectional view of the optimised 3D vasculature with different oxygen diffusivities through solid, D_s. Elements with different solid volume fractions are illustrated with different colours. The total fluid volume fraction (black and coloured regions) is 35%.

Special results have been obtained by imposing a partial body force condition and the no-flux boundary condition (Figure 7-16). A tree/roots-shaped structure has been produced by applying the uniform oxygen consumption only to the upper half of the modelling space.

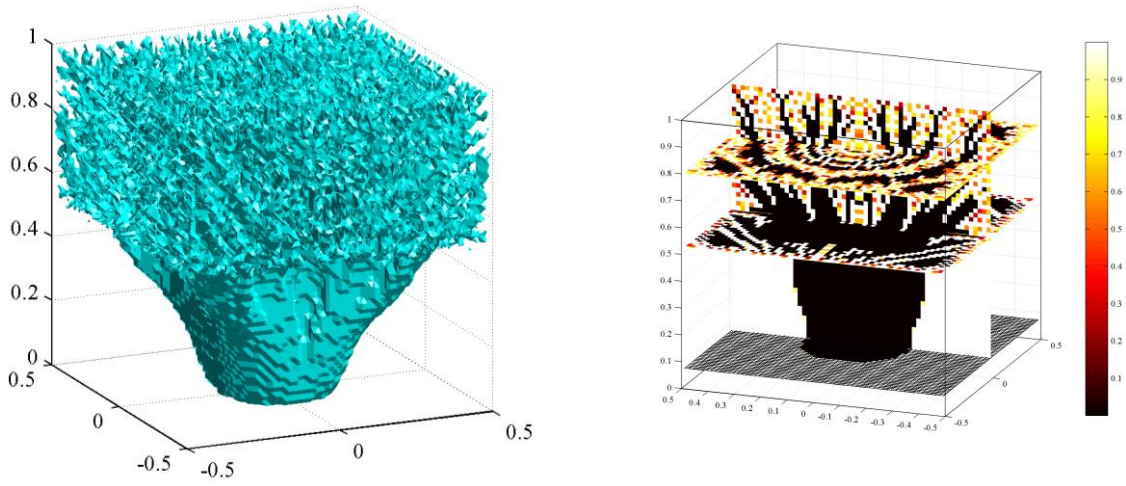

(a) Isosurfcae view (b) Cross-sectional view

Figure 7-16. Cross-sectional view of the optimised 3D models ($D_s = 10^{-8}$) with partial oxygen consumption. Oxygen consumption is only applied to the upper half of the modelling space, 0.5 <= z <= 1. $D_s = 10^{-8}$. The total fluid volume fraction (black and coloured regions) is 35%.

7.4 Programming consideration

Despite having clarified the link between fractal and the presence of intermediate material phase, convergence has remained a major problem in this part of topology optimisation study. The drastic difference in sensitivity among individual elements has been identified as the primary cause of two convergence problems, which are the instability of structural evolution and the sluggish convergence. Instability is prevalent in the low diffusivity models in which fractal pattern were obtained. The fractal nature implies difficulty in measuring sensitivity accurately since many elements are in the intermediate material phase, and contain complex solid and fluid network on a smaller scale. As a result, the structural evolution can become unstable as the phase state of some elements alternate undecidedly between solid and fluid. This numerical oscillation had been observed and was found to propagate across the modelling space, and result in divergence of some of the simulations. Furthermore, the SIMP formulation is a numerical technique employed to improve phase contrast, with an ultimate goal to rid of all intermediate-phase elements. It however is not designed to measure the

actual sensitivity of intermediate phase. As a result, the sensitivity of intermediate elements may not have been accurately determined.

On the other hand, sluggish convergence has encumbered the 3D optimisation effort by impeding individual elements from reaching their optimal states, whether they are solid or fluid. Sluggish convergence has been found to be associated with sensitivity and volume constraint. In this study, an element with high sensitivity became more fluid while an element with low sensitivity became more solid. Once an element attained a completely fluid state, its high sensitivity would no longer initiate volumetric change. This became a significant issue when a small number of elements with extremely high sensitivity were preventing the majority of elements with extremely low sensitivity from evolving (see Table 7-1 for a numerical example). If the sensitivity was not properly adjusted, it could hinder further structural evolution (Table 7-1, compare Adjustments 1 and 2).

Table 7-1. Exemplar volume update and possible approaches to meet the volume constraint.

Initial data Hypothetically, if there are 1002 elements in one model and the sensitivity analysis shows:				
	Element #1	Element #2	Element #3-#1002	Average
Volume (current)	99%	65%	64.966%	65%
Sensitivity	10	0.1	0.0901	0.1
Sensitivity (adjusted)	9.9	0	-0.0099	0
Volume update (proposed max change = 10%)				
Volume change	10%	0	-0.01%	0
Volume (new)	99%+10% = 109%	65%+0 = 65%	64.966%-0.01% = 64.956%	65%
Volume (constraint)	100%	65%	64.956%	64.991%
Volume change (actual)	100%-99% = 1%	0%	-0.01%	-9% (not satisfied)

Adjustment 1 (proposed max change = 1%)				
Volume change	1% (lower)	0	-0.001% (lower)	0
Volume (new)	99%+1% = 100%	65%+0 = 65%	64.966%-0.001% = 64.965%	65%
Volume (constraint)	100%	65%	64.965%	65%
Volume change (actual)	1% (lower)	0%	-0.001% (lower)	0 (satisfied)
Adjustment 2 (proposed max change = 9%)				
Volume change	1% (lower)	9% (higher)	-0.01%	0
Volume (new)	99%+1% = 100%	65%+9% = 74%	64.966%-0.01% = 64.956%	65%
Volume (constraint)	100%	74%	64.956%	65%
Volume change (actual)	1% (lower)	9% (higher)	-0.01%	0 (satisfied)
Sensitivity (effective)	0.09121 (lower)	0.1	0.0901	0.09011
Sensitivity (adjusted)	0.001099	0.009889	-0.00001099	0 (satisfied)

As shown in the example, some sensitivity and volume adjustments should be made not only to satisfy the volume constraint, but also to maintain the rate of structural evolution. The actual change in elemental volume would most certainly deviate from the sensitivity if the evolution rate was to be maintained.

The built-in adjustment mechanism in the MMA solver could cope with the 2D sensitivity issues but not so well in the 3D situations. Additional adjustments were made to augment the volume constraint system. In this study, the sensitivity value of individual elements was capped by one upper limit and one lower limit. The upper limit was determined by the sensitivity of the element whose volume changed the most in the previous time step (in the example above, Element #2 increased most). The lower limit was determined by the sensitivity of the element whose volume changed the least (or most negative) in the previous time step (in the example above, Element #3-#1002 decreased most). As the solid volume fraction of Element #1 has reached 100%, its sensitivity in the following iteration will be

limited by the sensitivity of Element #2. In fact in the current iteration, the effective sensitivity of Element #1 only has to be a fraction of the sensitivity of Element #2.

7.5 Concluding remarks

Sustained nutrient transport is recognised as the key to successful tissue scaffolding. The diffusive movement must be maintained spatially and temporally to ensure cell viability. Inspired by the efficiency of natural vascular systems in nutrient transport and their fractal pattern, this topology optimisation study was carried out to design and optimise artificial vasculature system and to determine if there exists a link between optimality and fractality.

From the 2D and 3D optimisation results, it is concluded that fractal is an optimal structural pattern in diffusion transportation systems under uniform oxygen consumption. The fractal pattern is more recognisable in scenarios involving high uniform body force and low diffusivity. Lowering the oxygen diffusivity in the solid phase will result in higher degree of fractality. The architecture of the optimised models resembles natural vascular transport systems found in plants and animals. Moreover, it is deduced that the intermediate material phase is actually part of the solution, rather than an un-converged numerical transition between two major phases.

7.6 References

[1] Malda, J., Rouwkema, J., Martens, D.E., le Comte, E.P., Kooy, F.K., Tramper, J., van Blitterswijk, C.A. & Riesle, J. 2004. Oxygen gradients in tissue-engineered Pegt/Pbt cartilaginous constructs: Measurement and modeling. *Biotechnology and Bioengineering,* 86**,** 9-18.

[2] Radisic, M., Malda, J., Epping, E., Geng, W., Langer, R. & Vunjak-Novakovic, G. 2006. Oxygen gradients correlate with cell density and cell viability in engineered cardiac tissue. *Biotechnology and Bioengineering,* 93**,** 332-343.

[3] Kang, T.-Y., Kang, H.-W., Hwang, C.M., Lee, S.J., Park, J., Yoo, J.J. & Cho, D.-W. 2011. The realistic prediction of oxygen transport in a tissue-engineered scaffold by introducing time-varying effective diffusion coefficients. *Acta Biomaterialia,* 7**,** 3345-3353.

[4] Mekala, N.K., Baadhe, R.R. & Potumarthi, R. 2014. Mass transfer aspects of 3D cell cultures in tissue engineering. *Asia-Pacific Journal of Chemical Engineering,* 9**,** 318-329.

[5] Qu, D., Li, J., Li, Y., Gao, Y., Zuo, Y., Hsu, Y. & Hu, J. 2011. Angiogenesis and osteogenesis enhanced by bFGF ex vivo gene therapy for bone tissue engineering in reconstruction of calvarial defects. *J Biomed Mater Res A,* 96**,** 543-51.

[6] Landman, K.A. & Cai, A.Q. 2007. Cell proliferation and oxygen diffusion in a vascularising scaffold. *Bull Math Biol,* 69**,** 2405-28.

[7] Rose, F.R., Cyster, L.A., Grant, D.M., Scotchford, C.A., Howdle, S.M. & Shakesheff, K.M. 2004. In vitro assessment of cell penetration into porous hydroxyapatite scaffolds with a central aligned channel. *Biomaterials,* 25**,** 5507-14.

[8] Mesallati, T., Buckley, C.T., Nagel, T. & Kelly, D.J. 2011. Introducing Microchannels into Chondrocyte-Seeded Agarose Hydrogels Influences Matrix Accumulation in Response to Dynamic Compression and TGF-beta 3 Stimulation. *In:* ELHAJ, A. & BADER, D. (eds.) *8th International Conference on Cell & Stem Cell Engineering.*

[9] Guest, J.K.P., Jean H 2006. Topology optimization of creeping fluid flows using a Darcy–Stokes finite element. *International Journal for Numerical Methods in Engineering,* 66**,** 461-484.

[10] Challis, V.J. & Guest, J.K. 2009. Level set topology optimization of fluids in Stokes flow. *International Journal for Numerical Methods in Engineering,* 79**,** 1284-1308.

[11] Guest, J.K. & Prévost, J.H. 2007. Design of maximum permeability material structures. *Computer Methods in Applied Mechanics and Engineering,* 196**,** 1006-1017.

[12] Chen, Y., Zhou, S. & Li, Q. 2011. Microstructure design of biodegradable scaffold and its effect on tissue regeneration. *Biomaterials,* 32**,** 5003-5014.

[13] de Kruijf, N., Zhou, S., Li, Q. & Mai, Y.-W. 2007. Topological design of structures and composite materials with multiobjectives. *International Journal of Solids and Structures,* 44**,** 7092-7109.

[14] Chen, Y., Zhou, S. & Li, Q. 2010. Multiobjective topology optimization for finite periodic structures. *Computers & Structures,* 88**,** 806-811.

[15] Bui, A.V., Manasseh, R., Liffman, K. & Šutalo, I.D. 2010. Development of optimized vascular fractal tree models using level set distance function. *Medical Engineering & Physics,* 32**,** 790-794.

[16] Sapoval, B., Baldassarri, A. & Gabrielli, A. 2004. Self-Stabilized Fractality of Seacoasts through Damped Erosion. *Physical Review Letters,* 93**,** 098501.

[17] West, G.B., Brown, J.H. & Enquist, B.J. 1997. A General Model for the Origin of Allometric Scaling Laws in Biology. *Science,* 276**,** 122-126.

[18] Cadman, J., Chang, C.-C., Chen, J., Chen, Y., Zhou, S., Li, W. & Li, Q. 2013. Bioinspired lightweight cellular materials - Understanding effects of natural variation on mechanical properties. *Materials Science and Engineering: C,* 33**,** 3146-3152.

[19] Murray, C.D. 1926. The Physiological Principle of Minimum Work: I. The Vascular System and the Cost of Blood Volume. *Proceedings of the National Academy of Sciences of the United States of America,* 12**,** 207-214.

[20] Salerno, A., Guarnieri, D., Iannone, M., Zeppetelli, S., Di Maio, E., Iannace, S. & Netti, P.A. 2009. Engineered mu-bimodal poly(epsilon-caprolactone) porous scaffold for enhanced hMSC colonization and proliferation. *Acta Biomater,* 5**,** 1082-93.

[21] Salerno, A., Di Maio, E., Iannace, S. & Netti, P. 2011. Tailoring the pore structure of PCL scaffolds for tissue engineering prepared via gas foaming of multi-phase blends. *Journal of Porous Materials***,** 1-8.

[22] Auriault, J.L. 1983. Effective macroscopic description for heat conduction in periodic composites. *International Journal of Heat and Mass Transfer,* 26**,** 861-869.

[23] Silva, M.M., Cyster, L.A., Barry, J.J., Yang, X.B., Oreffo, R.O., Grant, D.M., Scotchford, C.A., Howdle, S.M., Shakesheff, K.M. & Rose, F.R. 2006. The effect of anisotropic architecture on cell and tissue infiltration into tissue engineering scaffolds. *Biomaterials,* 27**,** 5909-17.

[24] Svanberg, K. 1987. The method of moving asymptotes—a new method for structural optimization. *International Journal for Numerical Methods in Engineering,* 24**,** 359-373.

[25] Ishaug, S.L., Crane, G.M., Miller, M.J., Yasko, A.W., Yaszemski, M.J. & Mikos, A.G. 1997. Bone formation by three-dimensional stromal osteoblast culture in biodegradable polymer scaffolds. *J Biomed Mater Res,* 36**,** 17-28.

[26] Papenburg, B.J., Liu, J., Higuera, G.A., Barradas, A.M., de Boer, J., van Blitterswijk, C.A., Wessling, M. & Stamatialis, D. 2009. Development and analysis of multi-layer scaffolds for tissue engineering. *Biomaterials,* 30**,** 6228-39.

[27] Chen, Y., Zhou, S., Cadman, J. & Li, Q. 2010. Design of cellular porous biomaterials for wall shear stress criterion. *Biotechnology and Bioengineering,* 107**,** 737-746.

[28] Michalatos, P. & Payne, A. 2014. *3D printing material distributions* [Online]. Tasman Machinery. [Accessed 11/20 2014].

8 Conclusions and Future Work

8.1 Summary

This fire-part study has demonstrated that the material properties and cell viability of tissue scaffolds can be improved through numerous design approaches. The material properties of tissue scaffolds can be optimised independently to the point of theoretical optimum, or simultaneously to meet multidisciplinary design requirement (Figure 8-1). Also, cell viability can be significantly enhanced under diffusion-dominated condition.

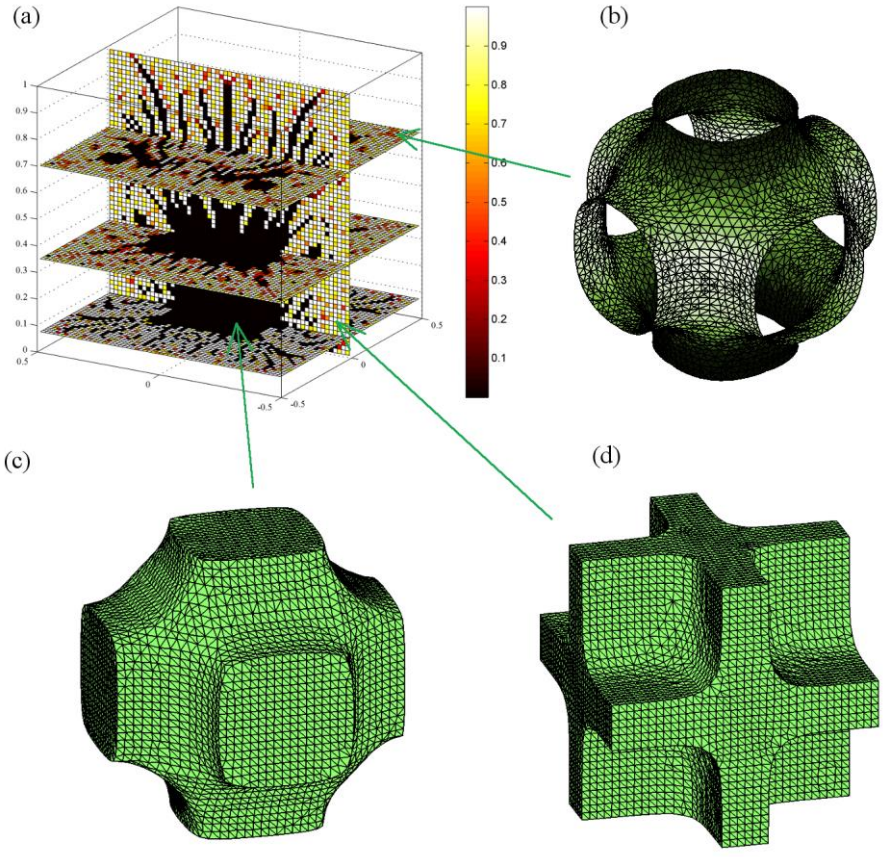

Figure 8-1. A multi-scale design of tissue scaffold with optimised permeability, diffusivity, bulk modulus and cell viability. RVE model (b) is recommended for the intermediate porosity region. RVE model (c) is recommended for the high porosity region. RVE model (d) can be used in the low porosity region.

The major achievements of this study are:

- The development of high quality models of tissue scaffolds.

- The clarification of the optimal structures of tissue scaffolds in terms of:
    - effective diffusivity,
    - effective bulk modulus,
    - effective permeability,
    - steady-state cell viability,
    - steady-state cell number, and
    - steady-state oxygen concentration.
- Demonstrating the effectiveness of topology optimisation on improving cell viability in diffusion-dominated and advection-dominated systems.
- The validation of optimality of fractal vascular systems.

This thesis was a five-part study. The first part of this study (Chapter 3) was the formulation of the high quality isosurface modelling technique. The isosurface modelling process was automated and implemented in the level-set-based topology optimisation. This technique showed robustness and capability in converting complex CT-images and mathematical models to smooth finite element meshes. The resultant meshes exhibited decent quality, suitable for the subsequent finite element analysis and topology optimisation procedure. The isosurface models were written in the stereolithography format, which could be readily used in solid freeform fabrication. Isosurface modelling as a tool for topology optimisation was further demonstrated in the next two parts of study.

The second part of this study (Chapter 4) was the single objective optimisation of tissue scaffolds and the characterisation of optimal structures. The RVE of tissue scaffolds with optimised bulk modulus, diffusivity and permeability were found using the level set method and the isosurface modelling technique. The incorporation of isosurface modelling was proven beneficial, showing significant improvements in model quality, numerical accuracy,

and smoother convergence when the results were compared to those obtained from conventional approaches. The proposed topology optimisation technique appropriately filled the gap in topology optimisation in CFD.

The third part of this study (Chapter 5) was the multiobjective optimisation of tissue scaffold structures. A range of optimal cubic RVE models were obtained, ranging from the maximum effective diffusivity structure to the maximum effective bulk modulus structure. The optimal intermediate model was found to be similar but not exactly the same as the Schwarz's primitive surface, which was suggested the optimal shape by past studies. Further cell viability test provided evidence that the optimised RVE design offered a more viable environment than a scaffold with random microstructure.

The forth part of the study (Chapter 6) was the optimisation of the porosity profile of tissue scaffolds. The results revealed that to improve the final cell seeding outcome, non-uniform porosity structures were required. The resultant porosity patterns depended on a number of technical factors including seeding density, seeding uniformity, perfusion rate and the design objective. Overall, the manipulation of porosity profile had shown significant influence on the cell survivability in a diffusion-dominated environment. Besides topology optimisation, a number of facts were also deduced:

- Advection, or perfusion, was found crucial to the sustainability of oxygen level in a tissue scaffold that was one centimetre in size, or larger.
- Topology optimisation as a design technique had shown limited influence on the cell survivability in an advection-dominated environment.
- The practical size or the thickness of a tissue scaffold, in term of cell survivability, could be predicted if the desired seeding density was given.

This knowledge can help us decide whether a scaffold size is viable to begin with, and if topology optimisation will make a significant different in the final seeding outcome.

The last part of the study (Chapter 7) was a multi-scale design and optimisation of artificial vascular system. A clear connection between optimality and fractality of material distribution was established through the steady-state diffusion simulation. However, such relationship was found only to exist in situations where the scaffold material was virtually non-conductive and the volumetric oxygen consumption was the primary force. On the other hand, optimal vascular networks with low degree of fractality or with no observable fractality were found in situations where surface flux was dominant, and in scenarios where scaffold material allowed diffusion to occur within itself, even at an extremely slow rate. In conclusion, the results support the conjecture that natural vascular systems acquire their fractal shapes through the process of self-optimisation.

Finally, this thesis has presented not only a comprehensive design of tissue scaffolds for load-bearing and nutrient transportation purposes, but also explored how biological responses could trigger beneficial or adverse feedback cycles that can lead to cell death or self-optimisation. The driven mechanisms of both engineering and biological optimisations were explained. This research is a demonstration of the benefit of computational investigation in tissue engineering and scaffold design.

8.2 Recommendations for future works

In this thesis, all problems were formulated and solved as deterministic problems to simplify the solution process. However, biological processes usually involve some degree of uncertainty. In the context of design of tissue scaffolds, taking into account the uncertainty in cell proliferation outcome should produce more realistic solutions. Design under uncertainty is therefore a potential area for future investigation.

The scope of this study has been limited by the availability of mathematical models of biological systems. A re-investigation or a reformulation of the optimisation method is necessary if any of the following models is improved or new models are made available in the future:

1. cell growth rate as a function of oxygen concentration,
2. cell death rate as a function of oxygen concentration,
3. diffusion model for space partially occupied by cells, and
4. the determination of effective diffusivity and stiffness of fractal materials.

To our knowledge there is no study on time-dependent optimisation of tissue scaffolds. All results obtained in this study were also optimised at the steady state only. The development of time-dependent models of biological system will be crucial to the investigation of real-time cell proliferation and the biological effect of topology.

Finally, experiments are necessary to verify and validate the optimality of the computational designs. The primary factors that have been preventing this from taking place in this five-part study are the cost and the ability to manufacture the prescribed microstructures at the desired scale. Nevertheless, solid freeform fabrication is a promising and suitable technique for the production of structured tissue scaffolds. The development and integration of precision solid freeform fabrication in tissue engineering is highly anticipated.